THE DETERMINATION OF THE OPTICAL CONSTANTS OF SOME SILICATE GLASSES AT MILLIMETRE AND SUBMILLIMETRE WAVELENGTHS

A Thesis submitted by

JAMES ROBERT BIRCH

to the University of London

in the Faculty of Science

for the degree of Doctor of Philosophy

Department of Physics

Queen Mary College

December 1978

The determination of the optical constants of some silicate glasses at millimetre and submillimetre wavelengths

by

J.R.Birch

ABSTRACT

This work has two interlocking themes. It is primarily concerned with the development of precise, broad band, Fourier transform spectrometric techniques for the determination of the optical constants of solids at millimetre and submillimetre wavelengths. One such technique cannot easily accomodate the wide range of optical constants found in solids, leading to specimens which range from the virtually transparent to the virtually opaque, and it was therefore necessary to develop transmission and reflection techniques. The intercomparison of these techniques, their particular experimental difficulties and susceptibilities to random and systematic error, was performed by using each method to determin the optical constants of soda lime silica glass over as wide a spectral range as possible. Previous to this work there had been no systematic study of this important material at these wavelengths and, thus, this investigation gave the second theme of this work, the quantitative determination of the optical constants of soda lime silica glass at millimetre and submillimetre wavelengths.

The results of this study are presented in four chapters. First, in chapter 5, power transmission Fourier transform spectrometry has been used to investigate the spectral variation of the optical constants of the glass between 3 and 50cm^{-1}, using an analysis of channel spectra to give the refractive index. This chapter also contains the results of measurements made with a grating instrument between 1000 and 4000cm^{-1}. Secondly, in chapter 6, the results of the first direct determinations of the optical constants by dispersive transmission Fourier transform spectrometry are presented and shown to indicate the presence of a hitherto unknown loss process below 20cm^{-1} that is tentatively associated with a similar process previously observed in fused silica. Thirdly, in chapter 7, dispersive reflection Fourier transform spectrometry has been used to determin the optical constants up to 360cm^{-1}, well into the mid-infrared region of opacity of this glass. The results of chapters 6 and 7 provide the first quantitative description of the optical constants of this glass betweem 3 and 360cm^{-1}. Finally, in chapter 8, the dispersive reflection measurements are extended to simple binary and ternary silicate glasses, and these results used to identify the contributions to the mid-infrared absorption of the metal ions associated with the various metal oxide additives of the glass. From this it was possible to account for all of the absorption in soda lime silica glass as a superposition of contributions from the near-infrared bands of the SiO_2 network of the glass and the four main metal ions.

ACKNOWLEDGEMENTS

Many colleagues and friends have helped in the gestation of this work, not only through their discussions of its contents, but also through their advocacy of perserverance. In particular, I am grateful to Dr C.C.Bradley, my supervisor at the National Physical Laboratory, for his advice during the first stages of this work, and for his continual interest since leaving the Laboratory; to Professor D.H.Martin of Queen Mary College for helpful discussions on the progress of the work; to all my colleagues, past and present, in the Division of Electrical Science at the National Physical Laboratory for the assistance that they have given to this work by their many actions and words; and, finally, to the late Dr J.E.Chamberlain who first introduced me to the many pleasures and subtleties of dispersive Fourier transform spectrometry.

INDEX

CHAPTER 1

INTRODUCTION

The work described in this thesis is concerned with the development of precise broad band techniques for the determination of the optical constants of solids between 3 mm and 25 μm wavelength, a portion of the electromagnetic spectrum variously known as the infrared, far infrared or submillimetre region. The optical constants are a pair of numbers for each frequency which describe the manner in which the phase and amplitude of an electric field vector change as it propagates through a medium and, when combined as the real and imaginary parts of a complex number, are alternatively known as the complex refractive index. Knowledge of this complex refractive index is of particular value as it is, ultimately, dependent on the structure of the medium so that the interpretation of its frequency variation is a powerful technique for the investigation of material structure and the physical phenomena occurring in them.

The systematic investigation of the infrared spectral region has its origins in the work of Rubens in the period beginning around 1890 [1, 2] when he and his co-workers developed quantitative spectroscopic techniques for wavelengths longer than about 25 μm and applied them to the study of the optical properties of a variety of materials. Although subsequent workers further refined and devloped these techniques, introducing such innovations as the echelette grating [3], the mercury arc source [4] and spark generators [5, 6]. The development of truly precise techniques for the longer wavelength region beyond 50 μm did not occur until the late 1950s with the practical realisation of the techniques of Fourier transform

spectrometry [7,8] following the enunciation of the throughput advantage possessed by instruments having cylindrical symmetry by Jacquinot [9,10] and of the multiplex advantage by Fellgett [11,12], combined with the development of high speed digital computers. There was then a large expansion in infrared spectrometry, partly recorded by the bibliographies of Palik [1, 2] and Bloor [13], in which a vast amount of information on the power transmission and reflection properties of all phases of matter was gathered and used in the investigation and interpretation of such diverse problems as molecular dynamics of gases and liquids, lattice dynamics of crystalline solids, energy band structure of solids, plasma diagnostics, atmospheric pollution and astronomy.

Many of the spectra so obtained have been analysed using a variety of approximate expressions of differing degrees of complexity and applicability to give the optical constants of the materials studied with correspondingly different errors, both random and systematic. The requirement for approximate expressions results from the fact that usually one has only one experimentally determined quantity, the power reflection or transmission, from which to derive the two optical constants, an intractable problem. There are, of course, ways around this. Arguments based on causality [14, 15], for example, can be shown to lead to the Kramers-Kronig relations [16, 17] between the optical constants and enable both to be found from a single spectroscopic measurement over a sufficiently wide spectral range. Generally speaking, however, such methods are far from satisfactory and the recent development of dispersive Fourier transform spectrometry has made them redundant, at least for wavelengths longer than 20 μm. In dispersive Fourier transform spectrometry the specimen is introduced into

one arm of a two beam interferometer and from a comparison of the modulus and phase spectra transformed from interferograms recorded with and without the specimen in place both the amplitude attenuation and phase shift caused by the specimen can be derived. Thus, one now has two measured quantities and these can be solved directly for the optical constants.

A phase sensitive interferometer is obviously essential for such measurements and in the visible region instruments such as the Jamin, Mach-Zehnder[18] and Rayleigh interferometers have been used extensively to measure the real refractive indices of gases and liquids using quasi-monochromatic light. The application to broad band infrared measurements described above, although feasible at any time since Michelson derived his original instrument[19], did not take place until after the establishment of conventional Fourier transform spectrometry and occurred in 1963 when Chamberlain, Gibbs and Gebbie[20] published the real refractive index spectrum of crystal quartz between 20 and 55 cm^{-1}. Following this, the subject was developed by transmission measurements on transparent solids, liquids and gases by Chamberlain and co-workers at NPL[21-23] and on transparent and opaque solids and on gases by Bell and co-workers at Ohio State University[24-27]. More recently, several other groups have become involved in the field and dispersive measurements are now made over a wide range of frequencies and temperatures on materials varying from the transparent to the opaque. The recent developments relevant to this work are discussed in more detail in the two chapters on dispersive measurements, 6 and 7.

The present work evolved out of a requirement to have available a range of precise measurement techniques to determine not only the optical constants of a specimen but also its power transmission and reflection properties between about 3 mm and 25 μm wavelength, which region we shall loosely call the millimetre and submillimetre wavelength region. Thus, it was necessary to develop dispersive transmission and reflection techniques and to use and refine conventional power transmission techniques to enable meaningful comparisons to be made between all three. Although considerable effort was put into developing normal incidence power reflection techniques [28-30] these will not be discussed in this work as they were largely superseded by the development of the corresponding dispersive technique.

In order to facilitate this development of techniques and to aid in their intercomparison it was necessary to choose a material, or class of materials, to study, whose optical constants were such that within the millimetre and submillimetre wavelength region there would be at least one region of virtual transparency and one of virtual opacity. This would give the following three distinct spectral regions of interest:

(i) The region of transparency where power and dispersive transmission techniques can be used and intercompared.

(ii) The region of opacity where dispersive reflection techniques can be used.

(iii) The intermediate region of heavy absorption, but not compete opacity, where there is a phase shift on reflection substantially different from π radians so that both reflection and transmission techniques can be used and intercompared.

There are many classes of solids that fulfill this requirement. Crystalline materials such as the alkali halides or high purity group 2-6 and 3-5 semiconductors all have intense reststrahlen bands at the frequency of the transverse optic phonon. These provide localised regions of high reflectivity and absorption with transparency in the wing regions. Alternatively, the plasma resonance in doped elemental semiconductors such as germanium or silicon would provide low frequency regions of high absorption with transparency increasing to higher frequency away from the resonance. Such materials were not, however, chosen for two main reasons. Firstly, they are all fairly well characterised systems whose physics is usually well understood and, secondly the use of crystalline materials implies possible anistrophies, which would require the use of plane polarised radiation, a complication that was avoided in this work even though the polarising

interferometer of Martin and Puplett makes its inclusion relatively simple. The material chosen instead for this study was soda lime silica glass having the approximate composition of ordinary window glass. Although glass is a material that is produced, used and wasted in vast amounts the physics of it, and of amorphous materials in general, are not as well understood of those of other, more ordered, condensed phases, and the amount of quantitative spectroscopic data published on it at millimetre and submillimetre wavelengths is extremely limited.

That this material should satisfy our requirements for regions of transparency and opacity is apparent from figure 1.1 which shows the power transmission spectra of several specimens of soda lime silica glass below 40 cm^{-1} and above 1000 cm^{-1}. The rapid transmission cutoffs at 40 and 1000 cm^{-1} clearly indicate the presence of a region of intense absorption in the mid-infrared optical region. The structure on the spectrum of the 0.25 mm

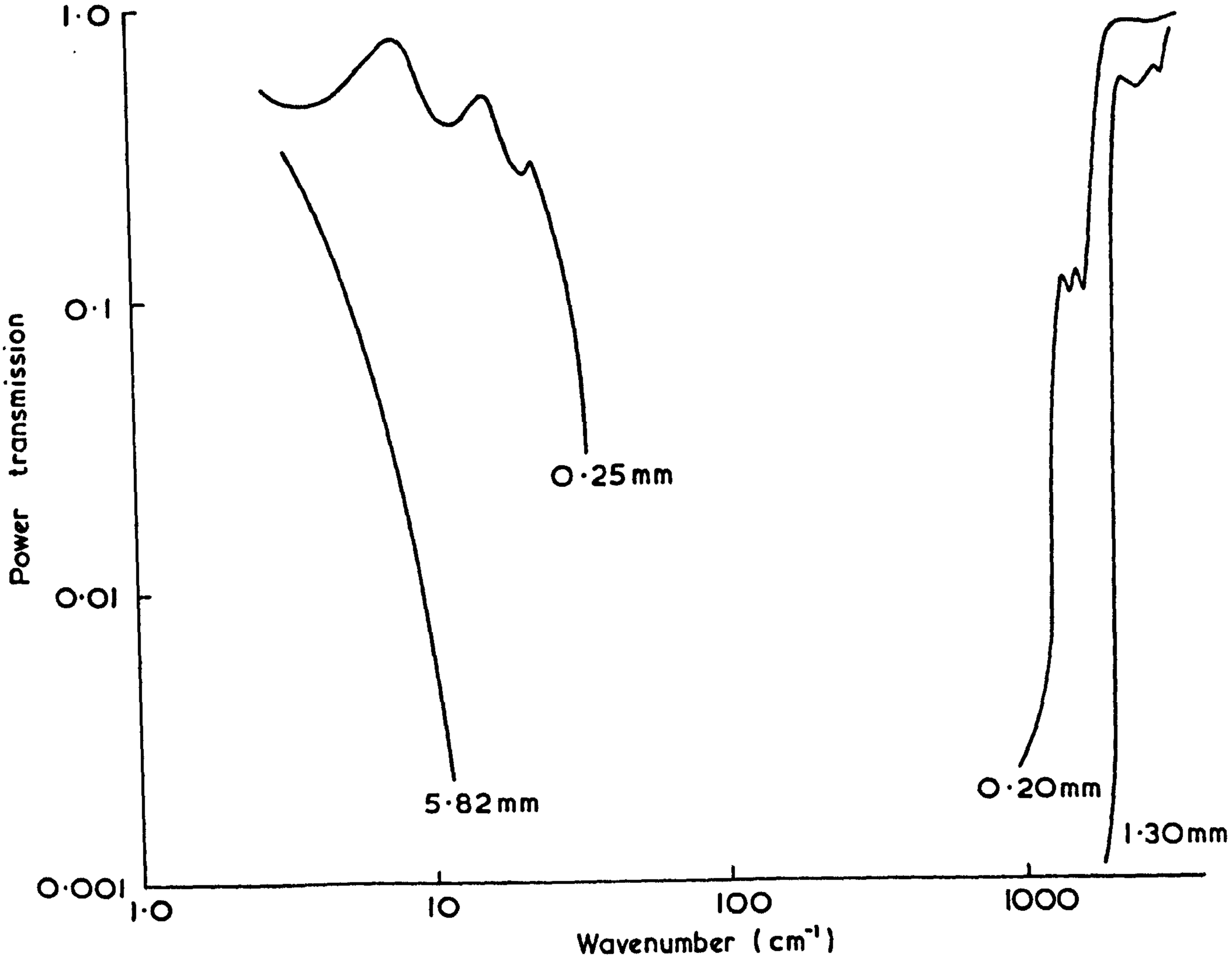

Fig.1.1. The power transmission spectra of several soda lime silica glass specimens in the wings of the infrared absorption region at 293K.

specimen below 30 cm^{-1} is due to interference between rays that have undergone multiple internal reflections within it, while the structure on the high wavenumber curves is associated with OH absorption bands[32]. The origins of this region of opacity are fairly well understood in general terms; the absorption above 400 cm^{-1} is mainly due to four vibrational modes of the SiO_2 network of the glass at about 445, 670, 750 and 975 cm^{-1}, while the absorption below 400 cm^{-1} is usually assigned to the sum of contributions from the low frequency wings of these SiO_2 bands with those of vibrational modes of the various ions, introduced by the metal oxide additives of the glass, against the SiO_2 network.

Although the presence of this region of intense absorption had long been realised (see, for example, Jenkins and White[33]) very little quantitative data on the optical constants associated with it were available. The region between 4 and 45 cm^{-1} had been studied in transmission by several workers[34-38] at various temperatures with a lack of consistency between the results, while the qualitative measurements of Exarhos and Risen[39] on a mechanically ground specimen of the binary glass $Na_2O.SiO_2$ dispersed in a polyethylene matrix provided the first demonstration of the vibrational mode of the Na ion in a silicate glass. In reflection, measurements have been made on the high wavenumber side of the region by Sweet and White[40] and by Aronson and Strong[41]. More recently, Ellis et al[42] have shown that after allowance is made for the absorption associated with the loss processes of the SiO_2 network of the glass an intense, broad absorption feature centred about 100 cm^{-1} remains, which they tentatively associate with the presence of the metal ions Na and Ca.

Thus, apart from its usefulness as a standard reference material for the intercomparison of the various measurement techniques developed during this study, the optical constants of soda lime silica glass at millimetre and submillimetre wavelengths were sufficiently unknown for this work to provide useful data with which to resolve past inconsistencies and unknowns. The results of this determination of the optical constants of this glass are presented in chapters 5, 6 and 7. In chapter 5 the millimetre, submillimetre and near infrared power transmission measurements are discussed and it is shown that the temperature variation of the long wavelength absorption coefficient is strongly frequency dependent, resolving some inconsistencies between earlier measurements [35-38]. In chapter 6 the optical constants of the millimetre and submillimetre regions are again derived, this time by dispersive transmission measurements, and compared with those of the previous chapter. At millimetre wavelengths a strong dispersion in the real refractive index is found, which led to the identification of a previously unknown loss process in the glass. In chapter 7 dispersive reflection techniques have been used to measure the optical constants in the opaque region up to 360 cm^{-1} and, by the subtraction of the calculated contribution from the mid-infrared SiO_2 bands, the total absorption associated with the metal ions introduced with the metal oxide aditives is clearly identified. Finally, in chapter 8, dispersive reflection measurements are presented for simple binary and ternary silicate glasses which enabled characteristic oscillator parameters to be assigned to the vibrational modes of the various metal ions, and, by using these parameters it was possible to account for all of the loss due to the metal ions in soda lime silica glass in chapter 7 as the superposition of classical damped harmonic oscillators associated with Al, Na, Ca and Mg ions. During the course of this works some of the results presented in chapters 5, 6 and 7 have been published [108,157,158].

Notation and units have often been a matter of controversy in electromagnetism. Within the present work it has been the author's intention to adhere to SI units with two exceptions, both for reasons of common spectroscopic usage. Thus, the unit of inverse wavelength, the wavenumber, is expressed in cm^{-1}, and the power absorption coefficient in neper cm^{-1}. The use of the dimensionless neper in the latter follows the preference of Chamberlain and Chantry[233] as a way of distinguishing between power absorption coefficient and absorbance by indicating that the former has been derived from the natural logarithm of a ratio.

CHAPTER 2

ELECTROMAGNETIC QUANTITIES

2.1 INTRODUCTION

The interaction of a plane monochromatic electromagnetic wave with a finite isotropic medium can be fully characterised by three parameters: the optical constants of the medium, jointly known as the complex refractive index, the frequency of the radiation and a factor describing the shape or form of the medium which, in its most tractable form, would be the thickness of a plane parallel specimen. The total amplitude attenuation and phase shift of the rays transmitted through and reflected from the specimen can be calculated from these parameters. This chapter, therefore, will show how the concept of a complex refractive index arises from Maxwell's equations for an homogeneous absorbing medium, deriving the form of the relationship between it and the conductivity, permeability and permittivity of the medium before describing the complex form of the Fresnel formulae for the reflection and transmission of an interface between two dissimilar media and their limiting values for cases of practical interest.

Throughout this article the electromagnetic field vectors are shown as complex quantities in order to simplify the representation of the phase relationships between different waves. Similarly, the conductivity, permeability and permittivity are shown as being complex in order that allowance can be made for phase relationships that might exist between current density and electric field, magnetic induction and magnetic field, and electric displacement and electric field.

2.2 THE COMPLEX REFRACTIVE INDEX

When Maxwell's equations are solved for a medium of relative permittivity $\hat{\varepsilon}'$, relative permeability $\hat{\mu}$, and conductivity $\hat{\sigma}$ the electric field vector $\underline{\hat{E}}$ is found to satisfy the wave equation [44, 45]

$$\nabla^2 \underline{\hat{E}} - \hat{\sigma}\mu_0\hat{\mu}\frac{\partial \underline{\hat{E}}}{\partial t} - \mu_0\varepsilon_0\hat{\mu}\hat{\varepsilon}'\frac{\partial^2 \underline{\hat{E}}}{\partial t^2} = 0 \qquad \ldots (2.1)$$

Where ε_0 and μ_0 are the permittivity and permeability of free space and t is time. The relative permittivity has been written with a prime to distinguish it from another permittivity to be introduced in the following section. A similar expression holds for the magnetic field vector, but we only consider electric field behaviour by limiting the discussion to non-magnetic materials in which the magnetic field does not couple strongly with the medium. The plane wave

$$\underline{\hat{E}} = \underline{\hat{E}}_0 \exp i(\underline{\hat{\gamma}}.\underline{r} - \omega t) \qquad \ldots (2.2)$$

having angular frequency ω and wave vector $\underline{\hat{\gamma}}$ with $\underline{r}$ the distance vector, is a solution of equation 2.1 if

$$\underline{\hat{\gamma}}.\underline{\hat{\gamma}} = \omega^2\hat{\mu}\mu_0\left(\varepsilon_0\hat{\varepsilon}' + \frac{i\hat{\sigma}}{\omega}\right) \qquad \ldots (2.3)$$

The phase velocity of the plane wave of equation 2.2 is the velocity of propagation of a wavefront of constant phase

$$\underline{\hat{\gamma}}.\underline{r} - \omega t = \text{constant} \qquad \ldots (2.4)$$

and is, therefore, $\partial r/\partial t$ in

$$\underline{\hat{\gamma}}.\frac{\partial \underline{r}}{\partial t} = \omega \qquad \ldots (2.5)$$

For an homogenous material the real and imaginary parts of the wavevector are parallel and lie in the direction of propagation. Equations 2.3 and 2.5 may therefore be re-arranged to give the phase velocity of the wave as

$$\frac{\delta r}{\delta t} = \left\{\mu_0\hat{\mu}\left[\varepsilon_0\hat{\varepsilon}' + \frac{i\hat{\sigma}}{\omega}\right]\right\}^{-1/2} \qquad \ldots (2.6)$$

but, by definition, this must be the velocity of light in the material. Hence the refractive index is complex and given by

$$\hat{n} = c\sqrt{\mu_0\hat{\mu}\left[\varepsilon_0\hat{\varepsilon}' + \frac{i\hat{\sigma}}{\omega}\right]} \qquad \ldots (2.7)$$

where c is the speed of light in vacuum. The role played by $\hat{n}$ can be seen by writing it interms of its real and imaginary parts

$$\hat{n} = n + ik \qquad \ldots (2.8)$$

and substituting for equations 2.3, 2.7 and 2.8 into 2.2 to give

$$\hat{\underline{E}}_x = \hat{\underline{E}}_0 \exp(-i\omega t)\ \exp(\pm\frac{k\omega x}{c})\exp(\frac{i}{\pm}\frac{n\omega x}{c}) \qquad \ldots (2.9)$$

where propagation is now considered to be in a specific direction, x . If the negative sign is chosen for the second exponential, and the corresponding positive sign for the third, equation 2.9 becomes

$$\hat{\underline{E}}_x = \hat{\underline{E}}_0 \exp(-i\omega t)\ \exp(-\frac{k\omega x}{c})\ \exp(\frac{i}{}\frac{n\omega x}{c}) \qquad \ldots (2.10)$$

and represents a homogeneous plane wa ve attenuated in the positive x direction with its phase advancing as x increases. The imaginary part, k , of $\hat{n}$ is therefore a dissipative term and is known as the absorption index. The real part, n , of $\hat{n}$ is known as the real refractive index, but is often called just the refractive index.

2.3 THE COMPLEX RELATIVE PERMITTIVITY

Equation 2.7 for the complex refractive index may be written in the form

$$\hat{n}^2 = c^2 \mu_0 \hat{\rho} \varepsilon_0 \hat{\varepsilon} \qquad \ldots (2.11)$$

to introduce the unprimed complex relative permittivity

$$\hat{\varepsilon} = \hat{\varepsilon}' + \frac{i\hat{\sigma}}{\omega \varepsilon_0} \qquad \ldots (2.12)$$

including the effects of all processes determining the amplitude and phase of the polarisability [46]. In the rest of this work the term complex relative permittivity will refer to this unprimed quantity. In the case of an insulator $\hat{\sigma} = 0$ and

$$\hat{\varepsilon} = \hat{\varepsilon}' \qquad \ldots (2.13)$$

As $c^2 = (\mu_0 \varepsilon_0)^{-1}$, equation 2.11 reduces to

$$\hat{n}^2 = \hat{\rho} \hat{\varepsilon} \qquad \ldots (2.14)$$

which is known as Maxwell's formula, and for a non-magnetic medium this reduces to the familiar form

$$\hat{n}^2 = \hat{\varepsilon} \qquad \ldots (2.15)$$

as $\hat{\rho}$ goes to unity.

If the real and imaginary parts of $\hat{\varepsilon}$ are written in the form

$$\hat{\varepsilon} = \varepsilon' + i\,\varepsilon'' \qquad \ldots (2.16)$$

the following relationships between the real and imaginary parts of $\hat{n}$ and $\hat{\varepsilon}$ are simply derived

$$\varepsilon' = n^2 - k^2 \qquad \ldots (2.17)$$

$$\varepsilon'' = 2nk \qquad \ldots (2.18)$$

$$n^2 = \frac{\sqrt{(\varepsilon')^2 + (\varepsilon'')^2} + \varepsilon'}{2} \qquad \ldots (2.19)$$

$$k^2 = \frac{\sqrt{(\varepsilon')^2 + (\varepsilon'')^2} - \varepsilon'}{2} \qquad \ldots (2.20)$$

2.4 REFLECTION AND TRANSMISSION AT AN INTERFACE

The first sections of this chapter have dealt with the propagation of a plane wave through an isotropic medium. With a finite specimen it becomes necessary to include the effects of the interfaces between that medium and its surroundings on the propagation of the wave. These will depend critically on the shape of the specimen and the geometry of the situation but the starting point for any attempt to analyse such a system must be Fresnel's equations.

2.4.1 FRESNEL'S EQUATIONS

Fresnel's equations relate the amplitude attenuation and phase shift suffered by an electromagnetic wave on reflection from, and transmission through, a plane interface between two semi infinite media to their optical constants, the angle of incidence and the polarisation of the incident wave. They are derived from the boundary conditions which apply at the interface and are usually given as real quantities [45] by assuming transparent media, but in their most general form they are the complex quantities described in the following four equations [46]

$$\hat{r}_\perp = \frac{\hat{n}_1 \cos\hat{\theta}_1 - \hat{n}_2 \cos\hat{\theta}_2}{\hat{n}_1 \cos\hat{\theta}_1 + \hat{n}_2 \cos\hat{\theta}_2} \qquad \ldots (2.21)$$

$$\hat{r}_{//} = \frac{\hat{n}_1 \cos\hat{\theta}_2 - \hat{n}_2 \cos\hat{\theta}_1}{\hat{n}_1 \cos\hat{\theta}_2 + \hat{n}_2 \cos\hat{\theta}_1} \qquad \ldots (2.22)$$

$$\hat{t}_{\perp} = \frac{2\hat{n}_1 \cos\hat{\theta}_1}{\hat{n}_1 \cos\hat{\theta}_1 + \hat{n}_2 \cos\hat{\theta}_2} \qquad \ldots (2.23)$$

$$\hat{t}_{\parallel} = \frac{2\hat{n}_1 \cos\hat{\theta}_1}{\hat{n}_1 \cos\hat{\theta}_2 + \hat{n}_2 \cos\hat{\theta}_1} \qquad \ldots (2.24)$$

In these $\hat{r}$ is the amplitude reflection coefficient and $\hat{t}$ the amplitude transmission coefficient for the incident wave polarised perpendicular ($\perp$) and parallel ($\parallel$) to the plane of incidence. The subscript 1 refers to the medium from which the wave is incident onto the interface, and the subscript 2 to the other medium. $\hat{\theta}_1$ and $\hat{\theta}_2$ are the angles of incidence and refraction, which are related by the complex form of Snell's law.

$$\hat{n}_1 \sin\hat{\theta}_1 = \hat{n}_2 \sin\hat{\theta}_2 \qquad \ldots (2.25)$$

In the special case of normal incidence, with which this work is concerned, $\hat{\theta}_1$ and $\hat{\theta}_2$ are real and zero and the Fresnel equations simplify to

$$\hat{r}_{\perp} = \hat{r}_{\parallel} = \hat{r}_{12} = \frac{\hat{n}_1 - \hat{n}_2}{\hat{n}_1 + \hat{n}_2} \qquad \ldots (2.26)$$

and, $$\hat{t}_{\perp} = \hat{t}_{\parallel} = \hat{t}_{12} = \frac{2\hat{n}_1}{\hat{n}_1 + \hat{n}_2} \qquad \ldots (2.27)$$

with the subscript order signifying incidence from medium 1. It follows that for incidence from medium 2

$$\hat{r}_{21} = -\hat{r}_{12} \qquad \ldots (2.28)$$

and, $$\hat{t}_{21} = \frac{\hat{n}_2 \hat{t}_{12}}{\hat{n}_1} \qquad \ldots (2.29)$$

2.4.2 EXPONENTIAL FORM OF FRESNEL'S EQUATIONS

The form in which the Fresnel equations were discussed in the previous section is not the most useful as it does not explicitly separate the attentuation and

and phase shift terms. A more convenient form uses the following exponential notation. The complex attenuation of an electric field vector on reflection at normal incidence from an interface is written in the form

$$\hat{r}_{12} = r_{12} \exp i\, \phi^{r}_{12} \qquad \ldots (2.30)$$

which explicitly shows the attenuation, r_{12}, and phase, ϕ^{r}_{12}, terms. It is readily shown from 2.8 and 2.26 that

$$r^2_{12} = \frac{(n_1^2 - n_2^2 + k_1^2 - k_2^2)^2 + 4(n_2 k_1 - n_1 k_2)^2}{\left[(n_1 + n_2)^2 + (k_1 + k_2)^2\right]^2} \qquad \ldots (2.31)$$

and,

$$\tan \phi^{r}_{12} = \frac{2(n_2 k_1 - n_1 k_2)}{n_1^2 - n_2^2 + k_1^2 - k_2^2} \qquad \ldots (2.32)$$

As the reflected and incident waves are in the same medium, equation 2.31 represents the power reflection coefficient of the interface.

When the initial medium is a vacuum $\hat{n}_1 = 1 + i0$ and equations 2.31 and 2.32 reduce to their more familiar forms

$$r^2_{12} = \frac{(n_2 - 1)^2 + k_2^2}{(n_2 + 1)^2 + k_2^2} \qquad \ldots (2.33)$$

and,

$$\tan \phi^{r}_{12} = \frac{-2k_2}{1 - n_2^2 - k_2^2} \qquad \ldots (2.34)$$

The phase changes that occur on reflection from transparent and opaque media can be derived from the limiting behaviour of 2.34 as $k_2 \to 0$ and ∞. In the former case

$$\lim_{k_2 \to 0} \phi^{r}_{12} = \lim_{k_2 \to 0} \arctan \frac{-2k_2}{1 - n_2^2} \qquad \ldots (2.35)$$

and, in the latter,

$$\lim_{k_2 \to \infty} \phi^{r}_{12} = \lim_{k_2 \to \infty} \arctan \frac{-2}{-k_2} \qquad \ldots (2.36)$$

As $n_2 > 1.0$ both angles lie in the third quadrant and in their limits tend to π radians. The result for the opaque medium is of particular relevance to the dispersive reflection measurements of chapter 7 where the complex reflectivity of an unknown specimen is compared to that of a metallised surface.

When the wave is incident onto a vacuum from a more dense medium, so that $\hat{n}_2 = 1 + i0$, the phase change on reflection is given by

$$\tan \phi_{12}^{r} = \frac{2k_1}{n_1^2 + k_1^2 - 1} \qquad \ldots (2.37)$$

and in the limits of transparent and opaque media ϕ_{12}^{r} now goes to zero.

In a similar manner to the above analysis of $\hat{r}_{12}$ it is easily shown that the exponential form for $\hat{t}_{12}$

$$\hat{t}_{12} = t_{12} \exp \phi_{12}^{t} \qquad \ldots (2.38)$$

leads to the expressions

$$t_{12}^2 = 4 \cdot \frac{\left[n_1(n_1+n_2) + k_1(k_1+k_2)\right]^2 + (n_2k_1 - n_1k_2)^2}{\left[(n_1+n_2)^2 + (k_1+k_2)^2\right]^2} \qquad \ldots (2.39)$$

and,

$$\tan \phi_{12}^{t} = \frac{n_2k_1 - n_1k_2}{n_1(n_1+n_2) + k_1(k_1+k_2)} \qquad \ldots (2.40)$$

While r_{12}^2 is the power reflectivity of the interface between the two media, t_{12}^2 is not its power reflectivity. In particular, for $n_1 > n_2$, t_{12}^2 can exceed unity. This is because the incident and transmitted rays are in media of different permittivities. The correct power transmission of the interface is $1 - r_{12}^2$.

The phase change on transmission for incidence from a vacuum is

$$\phi_{12}^{t} = \text{arc tan} \frac{-k_2}{1+n_2} \qquad \ldots (2.41)$$

and, for practical values of $\hat{n}_2$, is in the fourth quadrant close to zero.

Similarly, for incidence onto a vacuum

$$\phi_{12}^{t} = \arctan \frac{k_1}{n_1(n_1+1) + k_1^2} \qquad \ldots(2.42)$$

For transparent media the angles represented by 2.41 and 2.42 tend to zero.

2.5 WAVENUMBER, ABSORPTION COEFFICIENT AND PROPAGATION FACTOR

In broad band spectrometry at millimetre and submillimetre wavelengths the angular frequency of a wave and the absorption index of a medium are not widely used terms. It is more common to characterise a wave by its reciprocal wavelength, known as wavenumber, $\tilde{\nu}$, and related to the angular frequency by

$$\tilde{\nu} = \frac{\omega}{2\pi c} \qquad \ldots (2.43)$$

The attenuation of a wave by a medium is usually described by the power absorption coefficient

$$\alpha = 4\pi\tilde{\nu}k \qquad \ldots (2.44)$$

Using 2.43 and 2.44 to rewrite equation 2.10 for a plane wave leads to

$$\hat{E}_x = \hat{E}_0 \exp(-i\omega t) \exp(-\frac{\alpha x}{2}) \exp(i2\pi n\tilde{\nu}x) \qquad \ldots (2.45)$$

and it is clear that the radiation intensity falls to a fraction $1/e$ in a distance $1/\alpha$. It is convenient to define here for later reference the complex propagation factor $\hat{a}$ as

$$\hat{a} = \exp(-\frac{\alpha x}{2}) \exp(i2\pi n\tilde{\nu}x) \qquad \ldots (2.46)$$

which represents the complex transmission factor of a wave which has propagated over a distance x in a medium, and does not include interface

effects. Equation 2.45 therefore simplifies to

$$\hat{\underline{E}}_x = \hat{a}\,\hat{\underline{E}}_0 \exp -i\omega t \qquad \ldots (2.47)$$

2.6 ELECTRIC FIELD, POWER AND INTENSITY

This chapter has been developed in terms of the electric field vector. In the theory of the two beam interferometer introduced in chapter 3 radiation intensity is used. This is the time average of the energy flux in the direction of propagation, or the power crossing unit area in the direction of propagation. In practise the radiation detectors used respond to the radiation power, which will be proportional to the radiation intensity if the beam profile is uniformly illuminated.

CHAPTER 3

FOURIER TRANSFORM SPECTROMETRY

3.1 INTRODUCTION

The work described in this thesis is concerned with the derivation of the optical constants of solids from transmission or reflection measurements made with the techniques of Fourier transform spectrometry (FTS). In this chapter, therefore, the basic principles of FTS at millimetre and submillimetre wavelengths are outlined and discussed. This is not performed in great depth, more detailed descriptions can be found in the books of Chantry[47] and Bell[48], and the forthcoming one of Chamberlain[49].

3.2 THE ÉTENDUE AND MULTIPLEX ADVANTAGES

Broad band spectroscopic measurements at millimetre and submillimetre wavelengths are more difficult than in many other spectral regions due to the weak thermal sources that must be used. FTS is now generally accepted as the best technique for such measurements because of two advantages which it posseses over the alternative techniques of prism and grating spectrometry.

The first of these is the étendue, or throughput, advantage described by Jacquinot[9,10] which refers to the large radiation throughput possessed by an interferometer as a consequence of its cylindrical symmetry. In prism and grating spectrometers the radiation throughput is small as narrow slits must be used to achieve adequate resolving powers. Chamberlain[50] has illustrated this point for instruments having equal transmission factors by calculating that the luminosities, and hence throughputs, of prism, grating and interferometric spectrometers are in the ratio of 1 : 7 : 2000.

The second advantage is Fellgett's multiplex advantage[11,12] which applies to detector-noise-limited spectrometers. It arises from the difference between the sequential observation of spectral elements in a dispersive (i.e. grating or prism) instrument and their simultaneous observation in an interferometric one. In its most simple formulation the multiplex advantage results in the interferometric spectrum having a signal-to-noise ratio that is $\sqrt{M}$ times that of a dispersive instrument, given identical ovservation times and where M is the number of spectral elements to be observed. There is presently some controversy about the correct value of the improvement factor.[51-53] At near infrared and visible wavelengths where photon noise generally predominates over detector noise the multiplex advantage is lost, although the étendue advantage is not.

There are additional advantages in the use of interferometric spectrometry that are consequential to the étendue and multiplex advantages. These include the attainment of high resolving powers, high spectral accuracy and short experimental times and have been discussed by Bell[48].

3.3 THE THEORY OF FTS

A Fourier transform spectrometer has two major components, a two beam interferometer and the digital computer used to compute the Fourier components of the intensity delay pattern produced by the interferometer. In this section the relationship between the experimentally accessible quantity, the interferogram, and the required quantity, the power spectrum, are derived. The description is in terms of integral equations for continuous data between infinite limits, and the practical limitations imposed by the necessary use of real data are briefly considered.

In a two beam interferometer the source radiation is divided into two beams which propagate along separate paths to be recombined in some manner at a detector. The optical path difference between these beams is altered and the variation in detected power caused by the interference of the two partial beams is recorded as a function of this path difference. In the following the simple wave theory of chapter 2 is used to derive the relationship between the detected power interference pattern and its corresponding power spectrum.

Consider an interferometer of the type shown schematically in figure 3.1. The radiation from the source is incident upon an inclined beamdivider having a complex reflectivity $\hat{r}_\bullet$ and a complex transmission $\hat{t}_\bullet$ for the incident radiation at the particular angle of incidence. The two waves so produced* are known as the partial waves and propagate to the plane reflectors M_1 and M_2, are reflected and return to the beamdivider where they recombine to give rise to one wave returning to the source and one propagating on to the detector. The two reflectors, M_1 and M_2, are distance $0.5x_1$ and $0.5x_2$, respectively, from the centre of the beamdivider and M_2' is the image of M_2 in the beamdivider, as seen from the detector. If the source is monochromatic the plane wave incident on the beamdivider is given by equation 2.45 and, for an evacuated interferometer, this becomes

$$\hat{\underline{E}}_x = \hat{\underline{E}}_o \exp(-i\omega t) \exp(i2\pi\tilde{\nu} x) \qquad \ldots (3.1)$$

---

*This method of creating the partial waves is common to all interferometers of the Michelson type and is known as division of the amplitude of the incident wave. The partial waves can also be formed by division of the wavefront of the incident wave using instruments such as lamella grating interferometers. [8, 54, 55] These will not be considered as they do not lend themselves to dispersive Fourier transform measurements.

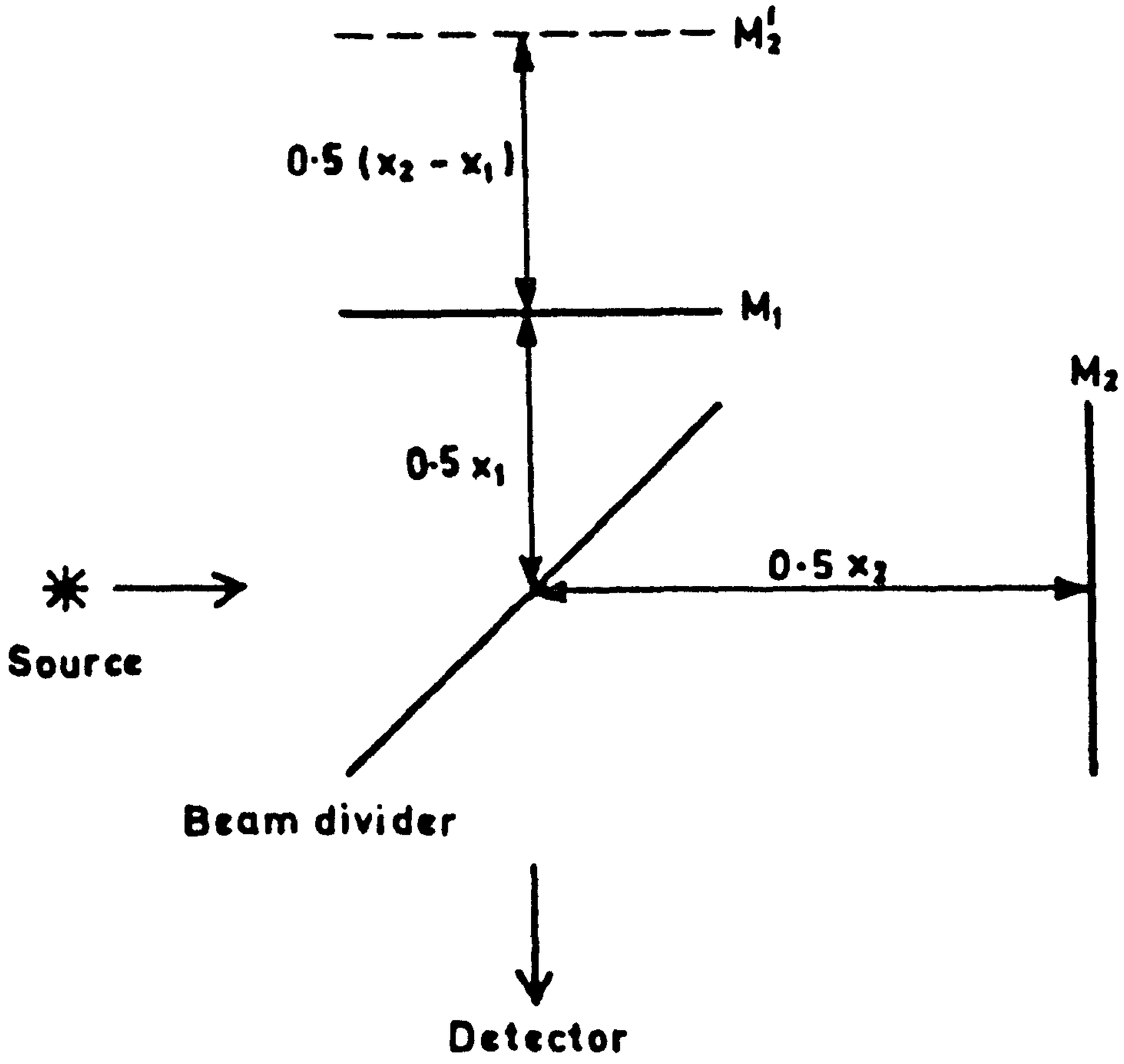

Fig.3.1. Schematic representation of a two beam interferometer.

By Young's principle of superposition [33] the electric field vector at the detector will therefore be

$$\hat{\underline{E}}\,(X_1, X_2) = \hat{\underline{E}}_o\,\hat{r}_o\,\hat{t}_o \exp i\pi\left[\exp i2\pi\tilde{\nu}X_1 + \exp i2\pi\tilde{\nu}X_2\right] \quad ..(3.2)$$

where X_1 is the total distance travelled by the partial beam reflected from M_1 as it propagates from the source to the detector, with X_2 the same for the other beam. The factor $\exp i\pi$ comes from the reflectivity, $1.0\exp i\pi$, of M_1 and M_2 and although not relevant at this stage it is included as it is of prime importance when dispersive reflection spectrometry is considered. The temporal phase term, $\exp(-i\omega t)$, is implicitly included in $\hat{\underline{E}}_o$ as experimental detectors only respond to the time averaged value of the radiation power.

If M_1 is fixed and M_2 allowed to move along an axis perpendicular to itself we can introduce the optical path difference, x, given by

$$x = X_2 - X_1 = x_2 - x_1 \quad \ldots (3.3)$$

so that 3.2 can be written in the form

$$\hat{\underline{E}}(x) = -\hat{\underline{e}}_o\left[1 + \exp(i2\pi\tilde{\nu}\,x)\right] \quad \ldots (3.4)$$

where $\hat{\underline{e}}_o$ is the complex vector

$$\hat{\underline{e}}_o = \hat{\underline{E}}_o\,\hat{r}_o\,\hat{t}_o \exp i2\pi\tilde{\nu}X_1 \quad \ldots (3.5)$$

The radiation intensity, $i(x)$, at the detector will be proportional to the [49] time average of the energy flux, so that

$$i(x) = \frac{\varepsilon_o c}{2}\left\langle|\hat{\underline{E}}(x)|^2\right\rangle \quad \ldots (3.6)$$

where the brackets $\langle\ \rangle$ denote the time average. This leads to

$$i(x) = \varepsilon_o c\left\langle|\hat{\underline{e}}_o|^2\right\rangle(1 + \cos 2\pi\tilde{\nu}\,x) \quad \ldots (3.7)$$

At zero path difference $x=0$ and the intensity is

$$i(o) = 2\varepsilon_o c\left\langle|\hat{\underline{e}}_o|^2\right\rangle \quad \ldots (3.8)$$

Thus, the intensity, $i(x)$, as a function of the optical path difference can be written as the sum

$$i(x) = \frac{I(o)}{2} + \frac{I(o)}{2} \cos 2\pi\tilde{\nu}x \qquad \ldots (3.9)$$

of a constant term and one varying cosinusoidally with x. The x- dependent term can be written in the form

$$I_o(x) = I(o) \cos 2\pi\tilde{\nu}x \qquad \ldots (3.10)$$

where $I_0(x)$ represents the value of the detected power at x path difference and, when recorded in some analogue form over a range of values of x, is known as the interferogram. If the radiation source were polychromatic, radiating at all wavenumbers from zero to infinity, equation 3.10 could be expressed as

$$I_0(x) = \int_0^\infty S_o(\tilde{\nu}) \cos 2\pi\tilde{\nu}x \, . \, d\tilde{\nu} \qquad \ldots (3.11)$$

where $S_0(\tilde{\nu})$ is the detected power in the wavenumber interval $\tilde{\nu}$ to $\tilde{\nu} + d\tilde{\nu}$. In a real interferometer the modulation technique, misalignment of optics and phase asymmetries, among other things, lead to an interferogram that may not be symmetric about $x = 0$, and it is convenient to generalise 3.11 to include sine and cosine components

$$I_0(x) = \int_0^\infty \hat{S}_o(\tilde{\nu}) \exp(-i2\pi\tilde{\nu}x) d\tilde{\nu} \qquad \ldots (3.12)$$

If this is generalised to include negative wavenumbers [49,56] its complex Fourier transform leads to the following expression for the complex spectrum

$$\hat{S}_o(\tilde{\nu}) = S_o \exp i\phi_o = \int_{-\infty}^{\infty} I_o(x) \exp(i2\pi\tilde{\nu}x) dx \qquad \ldots (3.13)$$

having modulus S_0 and phase ϕ_0 that will both be functions of wavenumber. This is the basic equation of FTS relating the recorded interferogram to the

computed spectrum. In its numerical evaluation the sine and cosine transforms

$$q(\tilde{\nu}) = S_o \sin \phi_o = \int_{-\infty}^{\infty} I_o(x) \sin 2\pi\tilde{\nu} x \, . \, dx \qquad \ldots (3.14)$$

and

$$p(\tilde{\nu}) = S_o \cos \phi_o = \int_{-\infty}^{\infty} I_o(x) \cos 2\pi\tilde{\nu} x \, . \, dx \qquad \ldots (3.15)$$

are separately evaluated and then combined to give the modulus and phase spectra

$$S_o = \sqrt{q(\tilde{\nu})^2 + p(\tilde{\nu})^2} \qquad \ldots (3.16)$$

and

$$\phi_o = \arctan\left\{\frac{q(\tilde{\nu})}{p(\tilde{\nu})}\right\} \qquad \ldots (3.17)$$

Equation 3.17 for the phase only gives the principal value of ϕ_o, lying between $\pm\pi/2$ radians. This can be extended to $\pm\pi$ radians by using the signs of the sine and cosine transform to determine which quadrant the angle falls in.

The equations developed above are the basic equations relating the computed spectra to the recorded interferogram in the case of ideal, continuous and infinite data. More rigorous treatments including the effects of real, discrete data and the effects of noise are available in the literature[47-49, 57-64]. In the remainder of this section we shall consider semi-qualitatively some aspects of the limitations imposed by real data. The modifying effects that the insertion of a specimen into the interferometer has on the interferogram and the computed spectra will be considered in detail in the following chapter with the development of the concept of the complex insertion loss of a specimen[65].

3.3.1 INSTRUMENTAL LINE SHAPE

The equations for the complex spectra of the previous section were derived assuming a continuous interferogram observed over an infinite range of path

differences, whereas in practice it is discretely sampled over the finite range $-D \leqslant x \leqslant D$. In this section we shall consider the spectral broadening that results from this truncation. The discrete sampling causes aliasing of the spectrum and places limitations on the highest frequency radiation that can be present in the detected spectrum if systematic errors are to be avoided. [47-49, 58, 62]

The practical result of the truncation at $x = \pm D$ is that the computed spectrum $\hat{S}_o'(\tilde{\nu})$ differs from the ideal spectrum described by equation 3.13, the two being related by

$$\hat{S}_o'(\tilde{\nu}) = \hat{S}_o(\tilde{\nu}) \; * \; A(\tilde{\nu}, D) \qquad \ldots (3.18)$$

where the asterisk denotes convolution [66]. The function $A(\tilde{\nu}, D)$ has a finite width, thereby broadening any discrete feature in the spectrum, and is known as the instrumental line shape, or the spectral window, of the interferometer. Its functional form may be derived by considering the response of the interferometric spectrometer to a monochromatic input recorded over a finite range of path differences. The interferogram from such an input of wavenumber $\tilde{\nu}_o$ would be

$$I(x) = 0 \qquad D < |x| \qquad \ldots (3.19)$$

and,

$$I(x) = I(0) \cos(2\pi\tilde{\nu}_o x - \phi_o) \qquad D \geqslant |x| \qquad \ldots (3.20)$$

including a term ϕ_o to allow for phase asymmetry. It is easily shown that this leads to computed sine and cosine spectra

$$q'(\tilde{\nu}) = -I(0) \sin\phi_o \left[\frac{\sin 2\pi(\tilde{\nu}_o + \tilde{\nu})D}{2\pi(\tilde{\nu}_o + \tilde{\nu})} - \frac{\sin 2\pi(\tilde{\nu}_o - \tilde{\nu})D}{2\pi(\tilde{\nu}_o - \tilde{\nu})} \right] \qquad \ldots (3.21)$$

and,

$$p'(\tilde{\nu}) = I(0) \cos\phi_o \left[\frac{\sin 2\pi(\tilde{\nu}_o + \tilde{\nu})D}{2\pi(\tilde{\nu}_o + \tilde{\nu})} + \frac{\sin 2\pi(\tilde{\nu}_o - \tilde{\nu})D}{2\pi(\tilde{\nu}_o - \tilde{\nu})} \right] \qquad \ldots (3.22)$$

which are to be compared with the ideal values given by equations 3.14 and 3.15. The modulus spectrum calculated from 3.21 and 3.22 is

$$S'_{\sigma}(\tilde{\nu}) = I(o).D\left[\left\{\text{sinc2}\ (\tilde{\nu}_{\sigma}+\tilde{\nu})D\right\}^2 + \left\{\text{sinc2}\ (\tilde{\nu}_{\sigma}-\tilde{\nu})D\right\}^2 + 2\ \text{sinc}\ 2(\tilde{\nu}_{\sigma}+\nu_{\sigma})D.\text{sinc}\ 2(\tilde{\nu}_{\sigma}-\tilde{\nu})D.\left\{\cos^2\phi_{\sigma}-\sin^2\phi_{\sigma}\right\}\right]^{\frac{1}{2}} \quad \ldots (3.23)$$

where the sinc function

$$\text{sinc}\ 2XD = \frac{\sin\ 2\pi XD}{2\pi XD} \quad \ldots (3.24)$$

has a broad peak of unity height at XD = 0 and oscillates about zero with decreasing amplitude as |XD| increases. For positive wavenumbers the contribution of the sinc function in ($\tilde{\nu}_{\sigma}+\tilde{\nu}$) rapidly tends to zero and equation 3.23 becomes

$$S'_{\sigma}(\tilde{\nu}) = I(o).D.|\text{sinc}\ 2(\tilde{\nu}_{\sigma}-\tilde{\nu})D| \quad \ldots (3.25)$$

Thus, the form of the instrumental line shape, for the modulus spectrum, is found to be

$$A(\tilde{\nu},D) = D.|\text{sinc}\ 2\tilde{\nu}\ D| \quad \ldots (3.26)$$

3.3.2 WEIGHTING AND RESOLUTION

In many applications the oscillating side lobes of the instrumental line shape can lead to undesirable spurious features in the computed spectrum. The side lobes are associated with the abruptness of the truncation at $x = \pm D$ and can be suppressed by multiplying the recorded interferogram by a function that gradually falls to zero at the extreme path difference values. This process is known as weighting and is always accompanied by an increase in the width of the instrumental line shape, leading to decreased resolving power. The spectrum computed from a weighted interferogram is said to have been apodised.

The weighting functions in general use are symmetric about zero path difference and decrease monotonically from that position, although for the special case of dispersive FTS Parker and Chambers[67] use an asymmetric function to emphasize the dispersive structure occurring at positive path differences in the interferogram. The function used in this work has been the cosine-squared function

$$\cos^2 \frac{\pi x}{2D} \qquad \ldots (3.27)$$

and the advantages and disadvantages of the use of this particular form have been considered for the special case of gas spectrometry by Burroughs and Harries[68], who have shown for strong lines that the effects of pressure broadening and saturation can be equivalent to interferogram weighting, which is thus not required. More recently Norton and Beer[69] have discussed a new class of algebraic weighting functions having the general form

$$\sum_{i=0}^{n} C_i \left(1 - {}^{x}/_{D}\right)^i \qquad \ldots (3.28)$$

where the sum

$$\sum_{i=0}^{n} C_i = 1.0 \qquad \ldots (3.29)$$

and n does not, in general, exceed 4, which they claim to have close to optimum properties in terms of suppressing the side lobes without excess loss of resolution.

The effects of truncation and weighting are to introduce a finite spectral resolution into the computed spectrum. Several definitions of this are in use and, although it has recently been shown that these are all over-optimistic,[70] we shall use two definitions that have long been in common use and that are adequate for the broad spectral features studied in this work. Thus, for an un-weighted interferogram recorded between the limits $D \geqslant |x|$ the wave-

number resolution in the computed spectrum is taken to be

$$\Delta\tilde{\nu} = \frac{1}{2D} \qquad \ldots (3.30)$$

The effect of the cosine-squared weighting is to approximately double the width of the instrumental line shape. Thus, the weighted, or apodised, resolution becomes

$$\Delta\tilde{\nu} = \frac{1}{D} \qquad \ldots (3.31)$$

The resolution of an interferometer cannot be continually decreased by recording interferograms to ever larger values of D as suggested by 3.30 and 3.31. There is a fundamental limit restricting this due to the limiting solid angle of the interferometer [47, 48], but this occurs for resolutions whose numerical values are much lower than those used in this work.

3.4 THE TWO BEAM INTERFEROMETER

In this section we shall describe the basic interferometer used for the transmission measurements of chapter 5 and from which the dispersive interferometers of chapter 6 and 7 were developed. There are several commercial interferometers available for the submillimetre spectral region and these are described in the books of Chantry [47], Bell [48] and Kimmitt [71]. The design of these commercial instruments tend to be similar in so far as their optics tend to be mounted on a common baseplate in a vacuum chamber and their operation is designed for the non-specialist often incorporating built-in filters, automatic beamdivider change-over and pre-set alignment. These are obviously desirable features of any commercial instrument but they result in a lack of flexibility in terms of non-standard applications. The basic instrument used for this work was the NPL modular cube interferometer [72] which differs significantly from these former instruments.

All the optical elements, source, collimator, mirrors, lenses, beamdividers and detector are mounted separately in their own small modules. These bolt together onto a central cube housing the beamdivider. This modular form allows interferometers that have widely differing configurations to be constructed from the same basic units. Thus, the interferometer can be tailored to very specific applications, leading to more efficient use of the source energy and experimental time, and as a result has been responsible for recent developments in the dispersive FTS of solids [73, 74], liquids [75], and gases [76, 77], conventional high resolution studies of the pure rotation spectra of gases [78], and fusion plasma diagnostics [79], as well as being the basic instrument of the Gebbie-NPL group since the early 1960s [80].

3.4.1 INTERFEROMETRIC HARDWARE

The optical configuration of the NPL interferometer is shown schematically in figure 3.2. The radiation source was a 125W mercury vapour arc in a quartz envelope which was operated from a current stabilised dc source [81]. This has been found to give improved performance in the spectral region below 250 cm^{-1} where the quartz envelope is transparent and the radiation emitted by the lamp predominently comes from the plasma. The source radiation was collimated by a two mirror system incorporating one off-axis concave mirror and then incident at 45^{o} on the beamdivider in the main body of the interferometer. The beamdivider was a stretched Melinex* film with its thickness chosen to suit the spectral range under investigation. The partial beams transmitted and reflected by the beamdivider propagate along their respective interferometer arms to recombine back at the beamdivider. Two recombined beams leave the interferometer, one focussed onto the detector and one returning to the source. The latter is not generally used,

---

*I.C.I. trade name for polyethylene terephthalate

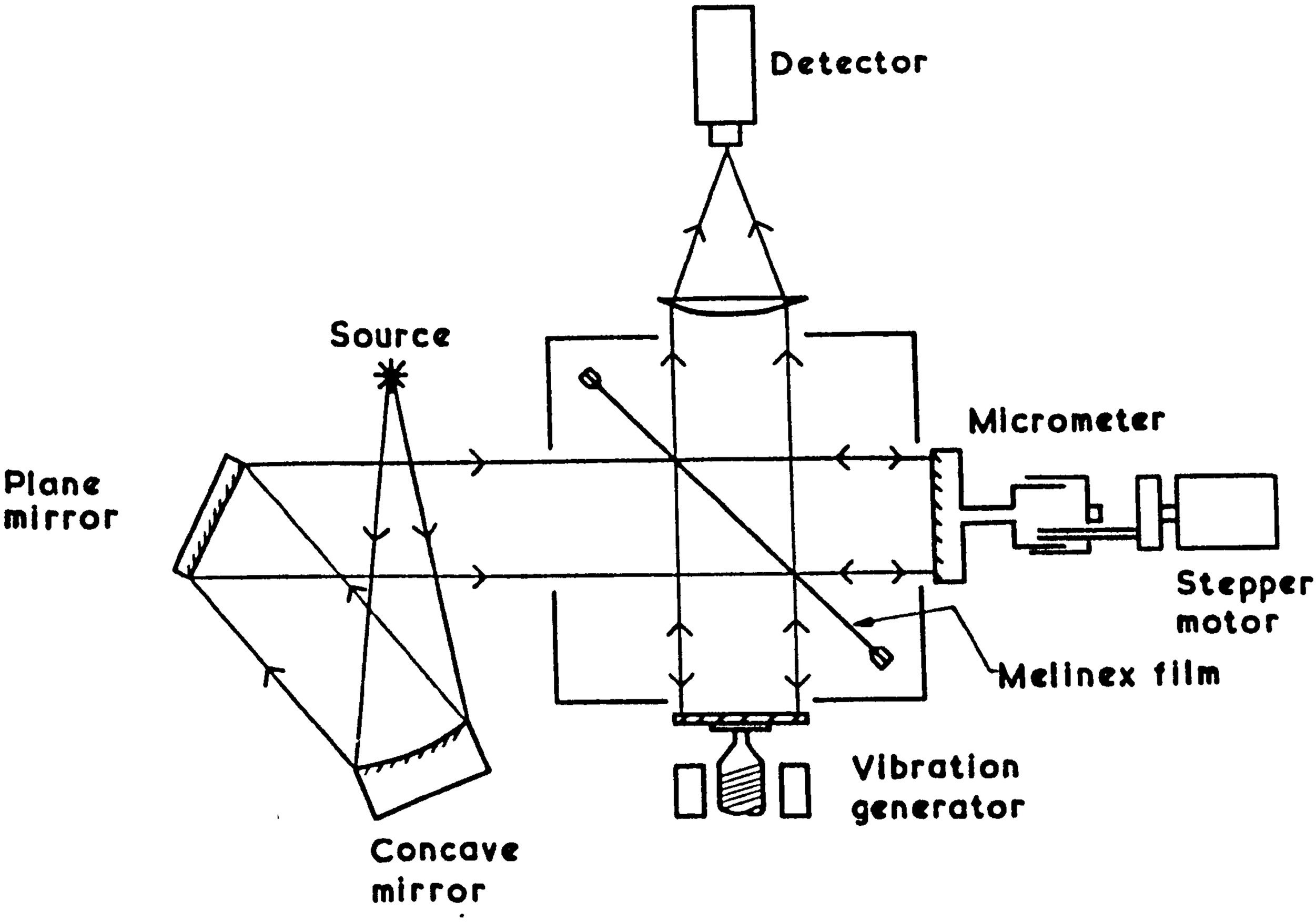

Fig.3.2. Optical layout of the basic NPL modular cube interferometer.

although interferometers have been constructed which make use of both [82,83]. Plane mirror reflectors were used in the arms of the interferometer, one mounted on a step-driven micrometer to produce the path difference variation while the other was mounted on a vibration generator so that phase modulation [84-86] of the radiation within the interferometer could be used.

The pitch of the micrometer driven mirror was 0.5 mm and had a 50 mm travel. It was driven by a synchronous stepping motor which could be controlled to give 12.5, 25, 50, 100 or 200 steps per revolution, corresponding to path intervals of 80, 40, 20, 10 or 5 μm.

3.4.2 MODULATION

Most submillimetre wavelength interferometric experiments have been performed using amplitude modulation of the source radiation to facilitate the detection and recording of the interferogram in spite of the serious disadvantages associated with the method. In particular, the detected signal contains a constant term (equation 3.9) that contains no useful spectral information and which restricts the full use of the dynamic range of the spectrometer system. Some authors [87,88] have devised amplitude modulation schemes in which this constant term is suppressed by chopping the radiation in one arm of the interferometer only, but these are complicated systems requiring careful setting up. Phase modulation, on the other hand, recently applied to the submillimetre wavelength region by Chamberlain [84-86], offers a simple way of achieving the same result and simultaneously improving the throughput of the interferometer. A small periodic movement is given to the normally fixed interferometer mirror, modulating the path difference in the interferometer and synchronous detection of the detector output signal at the modulation frequency is used. Thus, only radiation

that has been interferometrically modulated is recorded in the analogue output of the interferometer thereby removing the constant term. When sinusoidal phase modulation is used the computed modulus spectrum includes a wavenumber - dependent Bessel function of the first order as a factor, the phase spectrum is shifted by $\pi/2$ radians and, in a detector-noise-limited system, the signal-to-noise ratio of the interferogram is increased by a factor of nearly two over the corresponding amplitude modulation case. In the spectral domain the effect of the Bessel function is to cause the intensity to exceed that of the amplitude modulation case over the wavenumber range [85]

$$0.13\tilde{\nu}_m \leqslant \tilde{\nu} \leqslant 0.89\tilde{\nu}_m \qquad \ldots (3.32)$$

where $\tilde{\nu}_m$ is the wavenumber where the Bessel function first goes to zero, after $\tilde{\nu} = 0$. The wavenumber $\tilde{\nu}_m$ is related to the amplitude, $\flat$, of the sinusoidal modulation by

$$\tilde{\nu}_m = \frac{0.58}{\flat} \qquad \ldots (3.33)$$

This dependence on the modulation amplitude allows phase modulation to be used as a coarse spectral band pass filter. Thus, for a given beamdivider the higher or lower wavenumbers may be emphasized by appropriate choice of the modulation amplitude. Usually, however, the interferometer is operated with the amplitude set to give maximum detected signal, which approximately corresponds to the situation when the maximum of the Bessel function coincides with that of the interferometer transmission spectrum.

In the early application of phase modulation techniques it was customary to mount the modulating mirror on a small loudspeaker coil [84,86] which had low power consumption at the amplitudes and frequencies ($\sim 16Hz$) required for use with Golay cells. However, during the course of this work [29,30] we

have found these to be inadequate at the much higher amplitudes and frequencies ($\sim 200Hz$) used with liquid helium cooled detectors at low wavenumbers. They have several mechanical resonances at these frequencies, are unstable at large amplitudes and have a tendency to jam or seize up after prolonged operation. A commercial vibration generator* of a more rugged construction was found to be an adequate alternative.

3.4.3 SPECTRAL RANGE

The spectral range over which an interferometer operates is determined by four factors, the source emission spectrum, the transmission spectra of its lenses and filters, the spectral responsivity of the detector and the efficiency with which the beamdivider transfers the source energy to the detector. Fleming[89] has called this the spectral transfer coefficient of the beamdivider and it is the dominant factor determining the band pass of the interferometer. It has a periodic variation with wavenumber due to the interference of the multiply-reflected rays within it, rising from zero at zero wavenumber, passing through a maximum and falling to zero again. This repeats, with decreasing efficiency, to higher wavenumbers, but it is normal practice to only work with the first lobe. Noise and the finite digitisation of the interferogram reduce the useful spectral range even further, typically to be within the wavenumbers of the first lobe at which the power has fallen to about 0.1 of that at the maximum of the band pass. This might extend to 80% of the first lobe.

The variation of spectral range associated with beamdivider thickness has been discussed by Chamberlain et al[90] and is illustrated in figure 3.3.

The upper set of curves represent the modulus spectra obtained from a two

---

* Type 101, Ling Dynamic Systems, Royston, Hertfordshire

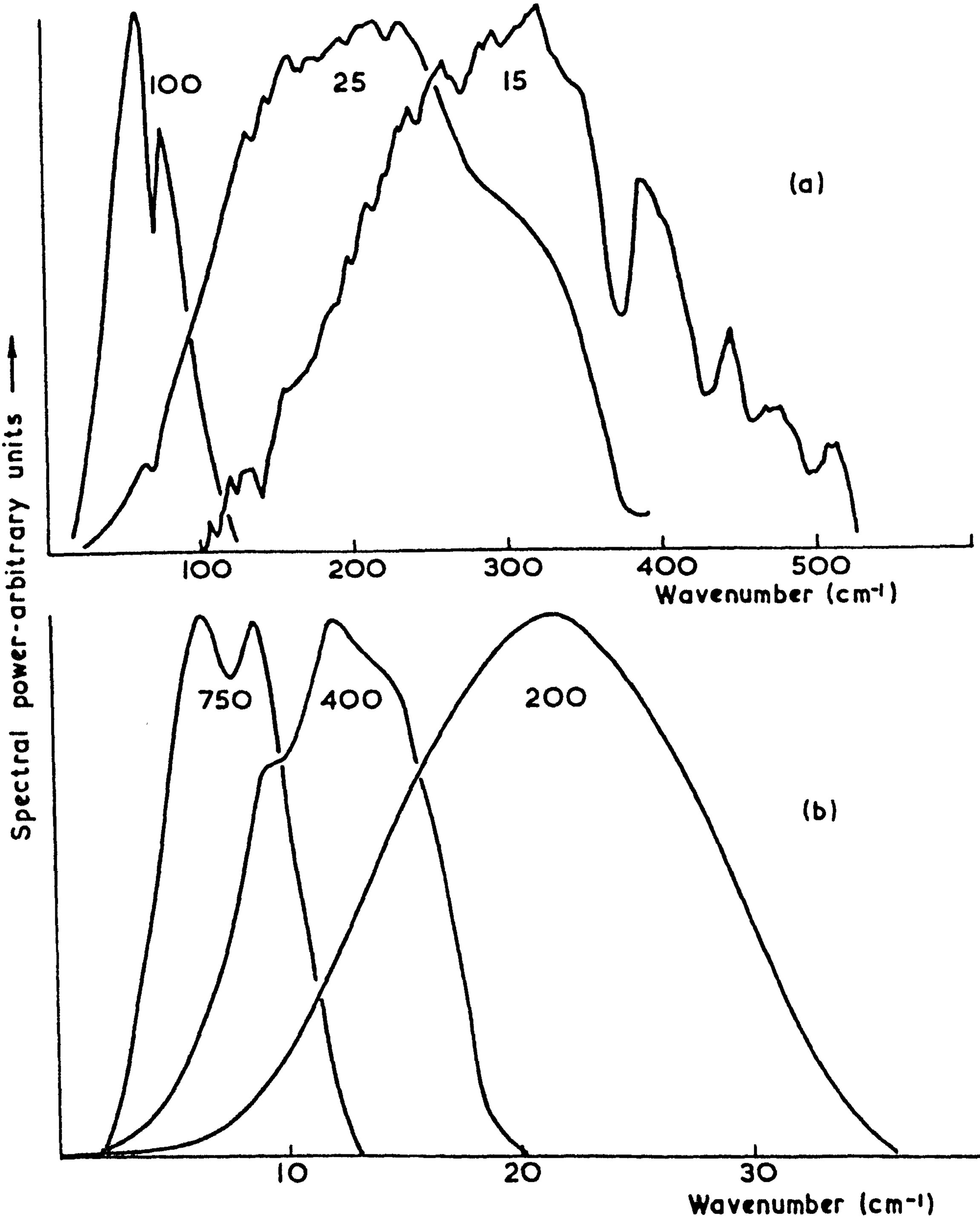

Fig.3.3. Typical modulus spectra obtained with different thickness dielectric beamdividers.

beam interferometer having 15,25 and 100 gauge* melinex beamdividers. The first two were recorded with a diamond window Golay cell, the last with a quartz window Golay cell. The thinnest, 15g (3.8 μm), beamdivider spectrum would have been usable between about 150 and 500 cm^{-1}. The structure on the high wavenumber side of its spectrum is due to absorption bands in the melinex. The sharp line in the 100g beamdivider spectrum results from the 73 cm^{-1} band of polyethylene, used in the condensing lenses of the interferometer. At wavenumbers below 30 cm^{-1} the source radiation is decreasing rapidly in intensity and it is usual to use liquid helium cooled detectors for this spectral region. Figure 3.3b shows detected spectra corresponding to 200,400 and 750g beamdividers recorded using a Rollin-type liquid helium cooled indium antimonide photoconductor [91,92]. The spectral response of this detector cuts offsharply above 40 cm^{-1}, but is extremely sensitive in the millimetre wavelength region about 10 cm^{-1}. All of the spectra of figure 3.3 were recorded using phase modulation and illustrate the major disadvantage of the use of thin film dielectric beam-dividers, that to cover a wide spectral range it is necessary to make measurements with several beamdividers. This is avoided in the polarisation interferometer of Martin and Puplett [31] which uses wire grid beamdividers, and has a more uniform spectral response out to a wavenumber inversely proportional to the grid spacing.

3.4.4 DETECTORS

During the course of this work different detectors were used to suit the spectral region and experimental conditions. Above 30 cm^{-1} room temperature Golay cells were used, the quartz-windowed type below 250 cm^{-1}, so that the opacity of the quartz at higher wavenumbers could act as a natural short wavelength filter, and the diamond-windowed type for the region above

* Gauge is an imperial measure for thin film thickness
100 gauge $\equiv$ 10^{-3} inch $\equiv$ 25.4 μm

250 cm^{-1}. Below 30 cm^{-1} liquid helium cooled indium antimonide detectors of both the Rollin-[91,92] and Putley-type[93,94] were used. The Rollin-type operates in zero magnetic field, as opposed to the Putley-type of detector, and can therefore be made into the more compact detector and was consequently more frequently used, although the Putley was used for continuous measurements from millimetre wavelengths to about 100 cm^{-1} requiring a cooled detector because of its broader spectral response.

3.4.5 DATA RECORDING AND PROCESSING

The a.c. voltage analogue of the detected interferogram was passed through a low noise amplifier into a phase sensitive detector to obtain a dc voltage proportional to the interferogram intensity at the modulation frequency. In the earliest measurements of this work this was converted into 8 bit binary form and stored on paper tape for subsequent processing. With the improvement of instrumental techniques the interferogram signal-to-noise ratios exceeded the 255:1 resolution available in binary form and the interferograms were subsequently recorded on paper tape in Isocode-7 format scaled between $\pm$ 11999 to give an intensity resolution of 1 part in 23999.

The Fourier transformation of the interferograms took place on an Elliot 905 computer. The binary coded interferograms were transformed using a machine code program based on the Chebyshev recursion formula* whilst the Isocode ones used the fast Fourier transform procedure based on the Cooley-Tukey algorithm[95].

---

* Written by Dr J.E.Gibbs of the Division of Electrical Science, NPL

CHAPTER 4

THE RELATIONSHIPS BETWEEN THE COMPLEX INSERTION LOSS AND THE OPTICAL CONSTANTS

4.1 INTRODUCTION

The object of the type of spectroscopic measurement described in this work is the derivation of the optical constants of a specimen from the quantity that is measured in a particular FTS experiment. The ease with which this may be performed, and the accuracy of the calculated optical constants, are critically dependent on the type of experiment performed, which is, in itself, dictated by the degree of transparency of the specimen. Gases are the easiest materials to deal with as their low refractive indices generally allow interface effects[65] to be ignored in the calculation of the optical constants; liquids are the next easiest as the variable thickness of a specimen allows techniques to be used which suppress interface contributions[76,77]; solid specimens are the most difficult as their relatively high refractive indices and fixed thicknesses mean that interface effects need to be explicitly allowed for[75,96-107].

In this chapter the basic equations for the transmission and reflection spectra of a plane parallel specimen are derived, the relationship between these quantities and the complex insertion loss, which is the measured quantity, is considered, and the methods by which the optical constants may be derived from the complex insertion loss discussed. The use of non-parallel specimens is not considered as the measured quantity then becomes dependent on the experimental geometry, which is not easily allowed for in calculations.

4.1.1 THE COMPLEX INSERTION LOSS

When a specimen is introduced into a two beam interferometer, either in the exit beam or one of the partial beams, the quantity that is determined from the ratio of the complex specimen spectrum and the complex reference spectrum is known as the complex insertion loss of the specimen [65] and is written

$$\hat{L}(\tilde{\nu}) = L(\tilde{\nu}) \exp i \phi_L(\tilde{\nu}) \qquad \ldots (4.1)$$

It is, therefore, the complex factor by which the detected complex spectrum is changed by the introduction of the specimen and, thus, will be a function both of the optical properties of the specimen and of those of whatever it replaced when it was introduced into the interferometer. It should not be confused with the complex transmission and reflection coefficients of the specimen. These are the complex factors relating the emergent to the incident electric field amplitudes, and are unaffected by the attenuations and phase shifts associated with the material replaced by the specimen. As the complex insertion loss depends upon the position of the specimen in the interferometer it is more correctly called the complex positional insertion loss.

4.1.2 DISPERSIVE AND NON-DISPERSIVE MEASUREMENTS

There are four broad band spectrometric experiments that can be performed on solids with the intention of deriving information concerning their optical constants. One can perform power transmission, power reflection, dispersive transmission and dispersive reflection experiments. In a power, or non-dispersive, experiment the specimen is placed in the exit beam of the interferometer in such a way that its power reflection or transmission is determined. The measurement will be characteristic of all the rays internally reflected within the specimen and the symmetry of the measurement, with both beams

of the interferometer passing through the specimen, means that all phase information is generally lost, although some will be present if a channel spectrum is resolved. This loss of phase information results in power transmission measurements mainly being used to determine the power absorption coefficient of the specimen via a variety of approximate expressions, and in power reflection measurements being combined with a Kramers-Kronig analysis to construct the phase information.

In the dispersive measurement the specimen is placed in one of the partial beams of the interferometer so that there is an asymmetry between the two beams. This allows the amplitude attenuation and phase shift caused by the specimen to be determined, from which both optical constants can be calculated. Thus, the dispersive experiment provides more information than the non-dispersive one, allowing the optical constants to be calculated exactly without recourse to approximate expressions, but, as we shall see, this can only be achieved through the use of very stable interferometers, especially for reflection measurements, so that meaningful phase spectra are obtained.

4.1.3 TRANSPARENCY AND OPACITY, THE CHOICE OF AN EXPERIMENT

The choice of whether to use a transmission or a reflection experiment is largely governed by the product of the power absorption coefficient and the thickness of the specimen, although the refractive index is a consideration. In a very loose manner a specimen may be classified as transparent if it transmits a sufficient fraction of the radiant energy incident on it for an accurate transmission measurement to be made. Depending on the experimental conditions this could correspond to a power transmission as low as 10^{-3}. In theory, of course, a specimen can always be made sufficiently thin for it to become transparent but, at some point, the effects of the internally

reflected rays become important and distort the transmission, and it can be difficult to create extremely thin films whose properties correspond to those of the bulk medium. In practice, we have found from our power transmission measurements on glasses [108] (see following chapter) that consistent values of the power absorption coefficient from measurements on different thin specimens are only possible for $\alpha \lesssim 150$ Neper . cm^{-1}. For higher values quite large systematic differences result.

4.2 THE TRANSMISSION AND REFLECTION OF A LAMELLA

In this chapter we shall be concerned with discussing the relationship between the quantity that is measured in a Fourier transform spectrometric experiment and the optical constants of the specimen. This will be with relation to plane parallel or lamellar specimens and it is first necessary to derive the expressions for the complex, and power, transmission and reflection coefficients of such a specimen.

For a lamella of refractive index n_2 immersed in a medium of refractive index n_1 the total complex transmission, $\hat{T}_{12}$, and reflection, $\hat{R}_{12}$, coefficients of it are given, for a perfect lamella, by the infinite sums of all the partial waves transmitted through, or reflected from, it. Hence

$$\hat{T}_{12} = \hat{t}_{12}\hat{a}_2\hat{t}_{21} + \hat{t}_{12}\hat{a}_2^3\hat{r}_{21}^2 t_{21} + \hat{t}_{12}\hat{a}_2^5\hat{r}_{21}^4\hat{t}_{21} + \ldots . \qquad \ldots (4.2)$$

and

$$\hat{R}_{12} = \hat{r}_{12} + \hat{t}_{12}a_2^2\hat{r}_{21}\hat{t}_{21} + \hat{t}_{12}\hat{a}_2^4\hat{r}_{21}^3\hat{t}_{21} + \ldots . \qquad \ldots (4.3)$$

where $\hat{t}_{12}$, $\hat{t}_{21}$, $\hat{r}_{12}$, $\hat{r}_{21}$ are the various Fresnel transmission and reflection coefficients of the interfaces between the two media (equations 2.26, 2.27) and $\hat{a}_2$ is the complex propagation factor for a distance equal to the thickness of the lamella (equation 2.46). The first term in 4.2 is the single pass transmission of the lamella, and that of 4.3 is its front surface reflection.

Equations 4.2 and 4.3 can be summed with the aid of 2.28 and 2.29 to give

$$\hat{T}_{12} = \frac{\hat{a}_2 (1 - \hat{r}_{12}^2)}{1 - \hat{a}_2^2 \hat{r}_{12}^2} \quad \ldots (4.4)$$

and

$$\hat{R}_{12} = \frac{\hat{r}_{12} (1 - \hat{a}_2^2)}{1 - \hat{a}_2^2 \hat{r}_{12}^2} \quad \ldots (4.5)$$

which, by use of the exponential forms of $\hat{r}_{12}$ and $\hat{a}_2$ (equations 2.30 and 2.46) can be expended into the forms derived by Bell [46]. These four equations are the basic equations governing dielectric measurements on solids and, depending on the particular experiment, either the series or the summed forms may be preferred. Thus, for some dispersive measurements, in which the phase sensitivity of the interferometer resolves the contributions of the internally reflected rays into spearate interference signatures, only a few terms of the series forms may be used.

4.2.1 POWER TRANSMISSION AND REFLECTION

The power transmission and reflection coefficients of a lamella will be the

modulus-squared of the corresponding complex expression, equation 4.3 or 4.4. Therefore, the power transmission of the lamella is given by

$$T_L = \frac{r^{-2} + r^2 - 2\cos 2\phi^r}{(ar)^{-2} + (ar)^2 - 2\cos 2(\phi^r + \phi^a)} \quad \ldots (4.6)$$

and its power reflection by

$$R_L = \frac{a^{-2} + a^2 - 2\cos 2\phi^a}{(ar)^{-2} + (ar)^2 - 2\cos 2(\phi^r + \phi^a)} \quad \ldots (4.7)$$

In these, r and ϕ^r refer to the complex reflectivity r_{12} of the Fresnel reflectivity given by equations 2.30, 2.31 and 2.32, although the subscripts have been omitted for convenience. Similarly a and ϕ^a represent the modulus and phase of the complex propagation factor, so that, from equation 2.46, we obtain

$$a = \exp -\frac{\alpha x}{2} \quad \ldots (4.8)$$

$$\text{and} \quad \phi^a = 2\pi n \tilde{\nu} x \quad \ldots (4.9)$$

These equations, 4.6 and 4.7, are perfectly general for any lamella and apply for all angles of incidence provided that the appropriate functional form for the Fresnel reflectivity is used, and that the thickness is replaced by $x / \cos\theta_2$ where θ_2 is the angle of refraction in the lamella.

4.2.2 THE CHANNEL SPECTRUM

As the phase angle ϕ^a of equation 4.9 is linearly dependent on wavenumber. The cosine terms in it appearing in equations 4.6 and 4.7 for T_L and R_L are periodic in wavenumber and lead to a periodicity in the transmission and

reflection spectra of the lamella. This periodic portion of the spectrum is known as the channel spectrum of the specimen, and the optical constants of the lamella can be derived from its amplitude and periodicity. This aspect is considered later in this chapter, in section 4.3.2.

46, 109-113

The channel spectrum is not always observed experimentally for a variety of reasons. The intensity resolution of the spectrometer may be insufficient to resolve the amplitude variations, the surfaces of the lamella may be rough or non-parallel and the spectral resolution of the spectrometer may be too large to resolve adjacent features. Under any of these circumstances the measured lamella spectrum will not be adequately described by equations 4.5 and 4.6, and in this section we shall consider the form that the correct expressions take. If the specimen is rough or uneven then it is not easy to allow for the effects of this in a general form. We shall, instead, consider the specific, but often met, case of inadequate spectral resolution. Figure 4.1 represents the rays propagating through a lamella specimen placed at the exit aperture of a two beam interferometer. The rays from the fixed and moving mirror arms are incident on the lamella from the left and, after multiple internal reflections emerge as the rays a1, a2, a3 etc and b1, b2, b3 etc. If the interferogram were recorded to infinite path differences it would consist of an infinite series of interference signatures spaced by approximately

$$2\bar{n}x \qquad \ldots (4.10)$$

in path difference, where $\bar{n}$ is the mean refractive index of the material in the spectral region being studied. In this situation the measured power transmission would correspond to T_L of equation 4.6. If the channel spectrum is to be unresolved the range of path differences recorded must be res-

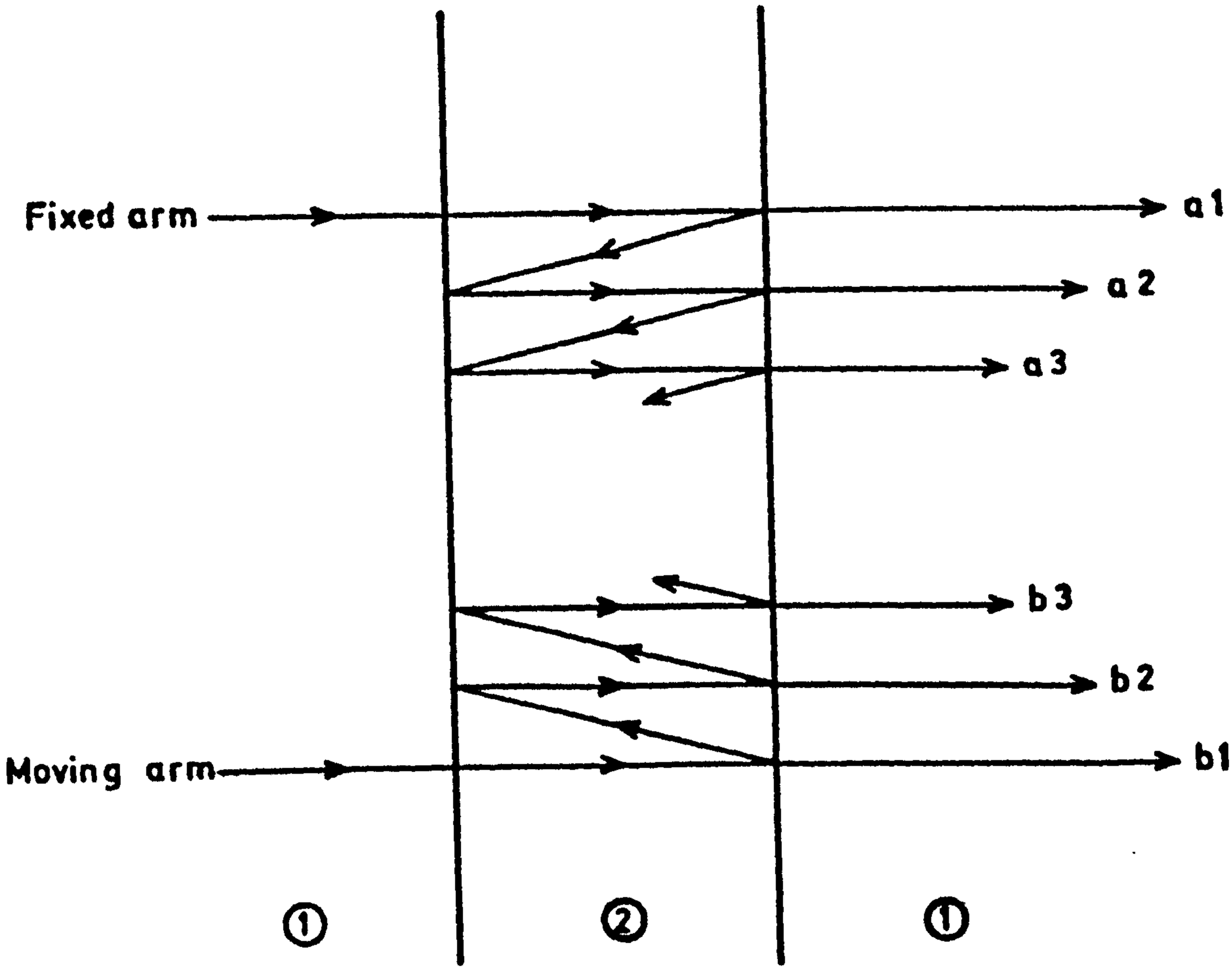

Fig.4.1. The internally reflected rays of a lamella placed at the exit aperture of a two beam interferometer.

tricted so that only the zero path difference interference signature is present. This will consist of the power interferograms due to interference between the pairs of rays

a1 and b1, a2 and b2, a3 and b3 etc

all having a unique maximum at zero path difference. Therefore, the measured power transmission would be the infinite sum

$$\tilde{T}_L = \left|(1-\hat{r}_{12}^2)\,\hat{a}_2\right|^2 + \left|(1-\hat{r}_{12}^2)\,\hat{a}_2^3\,\hat{r}_{21}^2\right|^2 + \left|(1-\hat{r}_{12}^2)\hat{a}_2^5\hat{r}_{21}^4\right|^4+\ldots \qquad \ldots (4.11)$$

with the corresponding series for the power reflection

$$\tilde{R}_L = \left|\hat{r}_{12}\right|^2 + \left|(1-\hat{r}_{12}^2)\,\hat{a}_2^2\,\hat{r}_{21}\right|^2 + \left|(1-\hat{r}_{12}^2)\hat{a}_2^4\,\hat{r}_{21}^3\right|^2+\ldots \qquad \ldots (4.12)$$

The first terms of 4.10 and 4.11 represent the single pass power transmission and the front surface power reflection respectively. When these series are summed they become

$$\tilde{T}_L = \frac{a^2\,(1-2r^2\cos 2\phi^r + r^4)}{1 - a^4\,r^4} \qquad \ldots (4.13)$$

and

$$\tilde{R}_L = \frac{r^2\,(1-2r^2a^4\cos 2\phi^r + a^4)}{1 - a^4\,r^4} \qquad \ldots (4.14)$$

where the subscripts have again been omitted, but remain implicit in the order 1,2 for r and ϕ^r. These are equivalent to the forms derived by Bell[46] from averaging T_L and R_L over one cycle of ϕ^a to simulate the loss of phase information.

4.3 POWER TRANSMISSION MEASUREMENTS

Power transmission measurements are probably the most frequently performed spectrometric measurements on solids and their purpose is generally to derive the power absorption coefficient, α, from the measured insertion loss, $L(\tilde{\nu})$, which in this instance will now be a real quantity. As the exact

relationship between these two quantities cannot be expressed in the form

$$\alpha = f(L(\tilde{\nu}), n) \qquad \ldots (4.15)$$

where n is the real refractive index, various approximate expressions have been developed for the purpose of evaluating α from $L(\tilde{\nu})$. In this section we shall show how the insertion of a specimen at the exit aperture of the interferometer modifies both the recorded interferogram and the computed spectrum, and then consider the use of the more common of the approximate expressions, before showing how the optical constants may be derived from the channel spectrum.

4.3.1 INSERTION OF A SPECIMEN

A lamellar specimen of medium 2 is placed at the exit aperture of an interferometer containing medium 1 in such a manner that both partial beams pass through it before reaching the detector. Following the arguments of section 3.3 it may be shown that the recorded interferogram changes from that of the empty interferometer, equation 3.12, to become

$$I_s(x) = \int_{-\infty}^{\infty} |\hat{T}|^2 \, S_o(\tilde{\nu}) \exp -(i2\pi\tilde{\nu}x) \, . \, d\tilde{\nu} \qquad \ldots (4.16)$$

where $\hat{T}$ is the complex transmission factor of the specimen that is appropriate to the particular measurement. This would be the factor $\hat{T}_{12}$ of equation 4.4 if a channel spectrum were resolved, if not then $|T|^2$ would represent the phase averaged power transmission $\tilde{T}_L$ of equation 4.13. In either case the phase of the Fourier components of the interferogram have not been changed by the introduction of the specimen. Thus, the symmetry of the measurement has lost the phase of $\hat{T}$. The complex spectrum computed from equation 4.16 is

$$\hat{S}_s(\tilde{\nu}) = |\hat{T}|^2 \hat{S}_o(\tilde{\nu}) \qquad \ldots (4.17)$$

so that the ratio of the modulus spectrum of this with that of equation 3.13 gives

$$\frac{|\hat{S}_s(\nu)|}{|\hat{S}_o(\nu)|} = |\hat{T}|^2 \qquad \ldots(4.18)$$

the generally quoted result that the ratio of the modulus spectra obtained with and without the specimen in place gives its power transmission coefficient.

This formulation is somewhat misleading as it hides, by an assumption, an important point. In the derivation of equation 4.16 it is implicitly assumed that the amount of medium 1 displaced by the specimen is non-absorbing. This is so for a vacuum instrument, and a good assumption for an unevacuated one at submillimetre wavelengths. However, when we consider dispersive experiments it is vital to explicitly include the effects of the displaced medium 1, whether or not it is absorbing, in order to allow for its displaced phase. Thus, for consistency with the following sections we rewrite equation 4.18 as

$$\frac{|\hat{S}_s(\nu)|}{|\hat{S}_o(\nu)|} = \frac{|\hat{T}|^2}{|\hat{T}_u|^2} \qquad \ldots(4.19)$$

where $\hat{T}_u$ is the complex transmission factor of the displaced thickness of medium 1 immersed in itself, and, from equations 2.26 and 4.4, as $\hat{r}_u = 0$, it is apparent that $\hat{T}_u = \hat{a}$, the complex propagation factor. As no phase changes occur in this measurement the factor

$$\frac{|\hat{T}|^2}{|\hat{T}_u|^2} \qquad \ldots(4.20)$$

is the complex insertion loss of the specimen for this measurement, and in this case is real.

One further point that arises from our discussion of finite data and the instrumental line shape in section 3.3.1 is that equation 4.19 should strictly speaking be written

$$\frac{|\hat{S}_s(\nu)|}{|\hat{S}_o(\nu)|} = \frac{[|\hat{T}|^2 . |\hat{S}_o(\nu)|] * A(\nu, D)}{[|\hat{T}_{11}|^2 . |\hat{S}_o(\nu)|] * A(\nu, D)} \quad \ldots (4.21)$$

to include the effect of the instrumental line shape. If both $|\hat{T}|$ and $|\hat{T}_{11}|$ are smoothly varying functions of wavenumber then it is reasonable to take equation (4.19) as correct. If, however, $|\hat{T}|$ has sharp features in it care must be exercised in analysing the ratio of the modulus spectra.

4.3.2 ANALYSIS OF THE CHANNEL SPECTRUM

If the specimen interferogram has been recorded to sufficiently large path difference values (greater than 2nd, where d is the lamella thickness) the transmission spectrum that is measured will contain a channel spectrum as discussed in section 4.2.2. The period of this has been used by many authors (see, for example[44,109,116-117]) as a means of determining the real refractive index and, more recently, Loewenstein and Smith[110-113] have developed a method for extracting the power absorption coefficient from the amplitude of the channel fringes. In this section we shall derive the simple equations relating the real refractive index to the spectral positions of the local maxima and minima of the channel spectrum.

Equation 4.6 for the full power transmission coefficient of the lamella shows that a local maximum in the transmission occurs when

$$\cos 2(\phi^r + \phi^a) = 1.0 \qquad \ldots(4.22)$$

and a local minimum when

$$\cos 2(\phi^r + \phi^a) = -1.0 \qquad \ldots(4.23)$$

Thus, the channel spectrum period is dependent upon both n and k, which is not often stated, although the small values of k met in most transmission experiments means that the period is usually determined by n alone. Equations 4.22 and 4.23 can be written in the form

$$2(\phi^r + 2\pi n \tilde{\nu}_{max} d) = 2m\pi \qquad \ldots(4.24)$$

for the maximum, and

$$2(\phi^r + 2\pi n \tilde{\nu}_{min} d) = (2m+1)\pi \qquad \ldots(4.25)$$

for the minimum, where m=0,1,2 etc. and d is the lamella thickness.

As they stand these cannot be solved for n if $\tilde{\nu}$ and m are known from experiment. However, in a transmission experiment k is usually very small and $\phi^r \rightarrow \pi$, so that 4.24 and 4.25 simplify to

$$2 n \tilde{\nu}_{max} d = m \qquad \ldots (4.26)$$

and

$$2 n \tilde{\nu}_{min} d = \frac{2m+1}{2} \qquad \ldots (4.27)$$

Thus, if $\tilde{\nu}_{max}$ or $\tilde{\nu}_{min}$ are measured, and the order number m is known, the refractive index can be calculated unambiguously from a single feature, or an average taken over several periods. At millimetre and submillimetre wavelengths the order number is usually known, but if it is not n is often found by rearranging 4.26 or 4.27 to relate it to the spacing of adjacent maxima or minima. Moss[109] has pointed out that this is only valid if the refractive index has no linear dependence on wavelength.

The approach that has been used in this work when studying different thickness specimens of the same material has been to take the spectral position, $\tilde{\nu}_m$, of the maxima and minima of the channel fringes for all the specimens and form the product $2 d \tilde{\nu}_m$ where d is the appropriate thickness value. If the order number is known, equations (4.26) and (4.27) show that the points so formed should fall on the curve

$$m = (2 d \tilde{\nu}_m)\, n (\tilde{\nu}) \qquad \ldots (4.28)$$

If the refractive index is constant over the spectral range studied a least-squares straight line fit to the data yields its value.

In a similar manner to the above, the problem of the channel spectra seen in reflection can be analysed for the spectral positions of the local maxima and minima. If the same assumptions are made then it is found that the maxima

occur at wavenumbers given by

$$2\,n\tilde{\nu}_{max}\,d = \frac{2m+1}{2} \qquad \ldots (4.29)$$

and the minima by

$$2\,n\tilde{\nu}_{min}\,d = m \qquad \ldots (4.30)$$

where m is again integral, m = 0, 1, 2 etc. Thus, the period of the channel spectrum seen in reflection is the same as that seen in transmission, with a transmission maximum occurring at the same wavenumber as a reflection minimum and vice versa.

Loewenstein and Smith [110-113] have shown that the contrast of a channel spectrum seen in reflection exceeds that in transmission for refractive indices up to ~ 3.8. As most transparent materials fall into this category they have developed a reflection technique for the derivation of the complex refractive index from the zeroes in a difference spectrum formed from the reflectivity spectrum of a specimen measured with and without sufficient resolution to resolve the channel spectrum. It has the advantage that the position of a zero crossing is easier to locate than that of a turning point, and their experimental values are generally in good agreement with those of other workers. However, it suffers from the major disadvantage of any channel spectrum technique of being very limited in resolving power. The refractive index can only be determined at the maxima and minima of the channel spectra and if one requires values that are closely spaced in wavenumber it is necessary to work with thick specimens.

4.3.3 APPROXIMATE EXPRESSIONS FOR THE POWER ABSORPTION COEFFICIENT

In the previous section we considered how the real refractive index may be determined from a power transmission spectrum exhibiting a channel spectrum

due to interference between the rays multiply reflected within it. If the power absorption coefficient is required it is more usual to measure the power transmission spectrum with a sufficiently low resolving power that the channel spectrum is not resolved. Under these conditions the measured transmission corresponds to $\tilde{T}_L$ of equation 4.13. This cannot be solved directly for α from $\tilde{T}_L$ as it first requires knowledge of n, and then an iterative approach, to derive α. There are, however, three approximate forms of 4.13 that allow for more straightforward solutions, and in this section we shall consider all three and the systematic errors that result from their use.

The first approximation is to assume that k, the absorption index, is small in a transmission experiment, which is fairly reasonable, so that the reflection phase shift, ϕ^r, goes to π radians. Under these conditions 4.13 simplifies to

$$\tilde{T}_L = \frac{a^2 (1 - r^2)^2}{1 - a^4 r^4} \qquad \ldots (4.31)$$

which can be written in the form of a quadratic in a^2 having the roots

$$e^{\alpha x} = \frac{(1-r^2)^2 \pm \sqrt{(1-r^2)^4 + 4r^4 \tilde{T}_L^2}}{2 \tilde{T}_L} \qquad \ldots (4.32)$$

Choosing the positive sign as α must be real, and writing R for r^2, leads to

$$\alpha = \frac{1}{x} \ln \left[\frac{(1 - R)^2 + \sqrt{(1-R)^4 + 4R^2 \tilde{T}_L^2}}{2 \tilde{T}_L} \right] \qquad \ldots (4.33)$$

which is the widely-used form given by Moss [109]. It can be solved directly for α provided that n is independently known and k is sufficiently less than n for R to be given by

$$R = \left[\frac{n - 1}{n + 1} \right]^2 \qquad \ldots (4.34)$$

instead of the full form, equation 2.33.

The second approximate form of $\tilde{T}_L$ is formed by further assuming that $1 \gg a^4 r^4$ so that 4.31 reduces to

$$\tilde{T}_L = a^2 (1 - r^2)^2 \qquad \ldots (4.35)$$

This is equivalent to saying that there are no multiple internally reflected rays within the lamella, and the transmission corresponds to a single pass of the lamella with the ray suffering reflection losses only as it enters and leaves the specimen. The power absorption coefficient can be extracted from 4.35 in the form

$$\alpha = \frac{1}{x} \ln \left[\frac{(1 - R)^2}{\tilde{T}_L} \right] \qquad \ldots (4.36)$$

with the same approximation applying for R as in 4.33. The major disadvantage of using either 4.33 or 4.36 is the requirement for independent measurement, or knowledge, of n. The final approximation removes this restriction by using measurements on specimens of different thicknesses, x_1 and x_2. It assumes that the contributions from any internally reflected rays are absent so that each transmission is given by 4.35. If this is so, the ratio of the two transmission coefficients gives

$$\alpha = \frac{1}{x_1 - x_2} \ln \left[\frac{\tilde{T}_2}{\tilde{T}_1} \right] \qquad \ldots (4.37)$$

The three expressions, 4.33, 4.36 and 4.37 are the most commonly used approximations in power transmission spectrometry. In appendix 1 we consider the errors that are introduced by their use, the results which can be summarised by the following:

(i) If the refractive index of the specimen is known α should be calculated using the first approximation, equation 4.33. For wavenumber-thickness products greater than unity this will generally give rise to systematic errors less than $\pm\ 10^{-4}$ (fractional), and it may, therefore, be

considered to be an exact solution.

(ii) If the refractive index is unknown α should be found from measurements on two specimens using equation 4.37. The ratio of the specimen thicknesses should lay in the range 0.25 to 0.75, and the calculated value of α can then be corrected in association with the curves of figure A1.4 to reduce the computation errors. It is always unadvisable to correct for large systematic error and the thicknesses should be chosen so that these are expected to be small

(iii) Large errors can result from the use of the second expression, 4.36. The first, 4.33, should always be used in preference to it, especially as both require knowledge of the real refractive index.

4.4 POWER REFLECTION MEASUREMENTS

Of the four types of spectroscopic experiment considered in section 4.1.2 power reflection measurements are the most difficult to analyse for the complex refractive index, and are usually only performed when the absorption is so high that transmission measurements cannot be made. The optical constants cannot, in general, be derived from a single reflectivity measurement over a limited spectral range as approximate expressions of the form

$$\alpha = f(R, n) \qquad \ldots (4.38)$$

analogous to those used in transmission do not exist, mainly because, unless $k \gtrsim n$, R is very insensitive to α. Several techniques, based on measurements at two angles of incidence or two polarisations together with the use of precomputed charts to derive the optical constants exist, [118-120] but these have not been applied at millimetre and submillimetre wavelengths. A Kramers-Kronig dispersion analysis [14-17, 121,122] of the reflection spectrum can be used to construct the phase spectrum, but data must be collected over a wide spectral

range and high radiometric accuracy is required to avoid serious phase errors.

There are, also, experimental situations in which the use of the relationship [123-127] may be incorrect or fail. Alternatively, internal reflection spectrometry [128-130] will give the optical constants, but its implementation at millimetre and submillimetre wavelengths is difficult and has not been attempted.

Due to these difficulties of analysis the most general application of reflection measurements at millimetre and submillimetre wavelengths is in the characterisation of the reflectivity of a surface or a specimen. There are however specific measurement problems where power reflection spectrometry can give important quantitative information. In the study of semiconductors, for instance, the position and shape of the plasma resonance are parameters from which the free charge carrier number density and mobility can be derived. [131-143]

4.5 DISPERSIVE TRANSMISSION MEASUREMENTS

In a dispersive FTS measurement the specimen is placed into one arm of a two beam interferometer. If this is the fixed mirror arm the effect of the dispersion of the specimen is to shift the zero path difference fringe to positive path differences and to distort it. This shifted asymmetric interferogram now contains the phase information that is missing from a non-dispersive measurement and the following analysis shows how this arises. It will be assumed that the radiation in the fixed mirror arm passes through the specimen twice, once before and once after reflection at the fixed mirror.

Proceeding then in the manner of sections 3.3 and 4.3.1, the electric field vector at the detector for a monochromatic input would be

$$\hat{E}_s(x) = -\hat{e}_o \left[T^2 \exp i (2\phi^T - 4\pi\tilde{\nu} d) + \exp i 2\pi\tilde{\nu} x \right] \qquad \ldots (4.39)$$

for a specimen of thickness d. In this equation the complex transmission factor of the specimen for a single pass has been written in the form

$$\hat{T} = T \exp i\phi^T \qquad \ldots (4.40)$$

to be consistent with the notation introduced in equation 4.16. Thus, it has not yet been specified whether-or-not a channel spectrum has been resolved. The term $-4\pi\tilde{\nu}d$ in the first exponent of equation 4.39 represents the loss of the phase shift of the vacuum displaced by the specimen. It follows that the radiation intensity at the detector is

$$i_s(x) = \frac{i(0)}{4}\left\{1+T^4\right\} + \frac{i(0)}{2} T^2 \cos\left\{2\pi\tilde{\nu}x - (2\phi^T - 4\pi\tilde{\nu}d)\right\} \qquad \ldots (4.41)$$

If this is generalised to a polychromatic source, and we introduce the complex exponential notation again, the full x - dependent interferogram becomes

$$I_s(x) = \int_{-\infty}^{\infty} T^2 \hat{S}_o(\tilde{\nu}) \exp -i\left\{2\pi\tilde{\nu}x - (2\phi^T - 4\pi\tilde{\nu}d)\right\} d\tilde{\nu} \qquad \ldots (4.42)$$

Thus, the Fourier inversion of this leads to the complex specimen spectrum

$$\hat{S}_s(\tilde{\nu}) = T^2 \exp i(2\phi^T - 4\pi\tilde{\nu}d).\ \hat{S}_o(\tilde{\nu}) \qquad \ldots (4.43)$$

The ratio of the complex spectra of equations 4.43 and 3.13 therefore gives the complex insertion loss of the specimen for this double-pass dispersive transmission experiment as

$$\hat{L}(\tilde{\nu}) = T^2 \exp i(2\phi^T - 4\pi\tilde{\nu}d) \qquad \ldots (4.44)$$

If one deals separately with the modulus and phase spectra one therefore obtains T^2 from the ratio of the modulus spectra

$$T^2 = \frac{|\hat{S}_s(\tilde{\nu})|}{|\hat{S}_o(\tilde{\nu})|} \qquad \ldots (4.45)$$

and the phase of $\hat{T}$ from the difference of the phase spectra

$$2\phi^T = ph\left\{\hat{S}_s(\tilde{\nu})\right\} - ph\left\{\hat{S}_o(\tilde{\nu})\right\} + 4\pi\tilde{\nu}d \qquad \ldots (4.46)$$

This development has implicitly assumed that the origins of computation used for the transformation of the two interferograms were identical. In practice, the origin of computation for the specimen interferogram is usually shifted to coincide with its displaced bright fringe to minimise phase branching. An important aspect of this is discussed in section 6.3.

4.5.1 THE NATURE OF THE DISPERSIVE INTERFEROGRAM

Due to the phase sensitivity of the dispersive interferometer the dispersive interferogram is radically different from the non-dispersive one, being the sum of an infinite number of interference signatures from six distinct sources. In this section we shall consider the effects that these have on the interferogram and how many of the signatures can be suppressed by careful positioning of the specimen.

Consider, then, the upper half of figure 4.2 which represents a plane parallel specimen in the fixed arm of a two beam interferometer. Its thickness is d and its rear surface is a distance D from the fixed mirror M and parallel to it. Without the specimen in place the recorded, phase-modulated, interferogram would be of the form shown schematically in part (a) of the figure, having a unique signature at zero path difference. With the specimen in place the interferogram has the form shown in (b). The ray r reflected at the front surface of the specimen gives rise to the interference signature i (r) at path difference

$$x_r = \delta_r - 2(D + d) - (2\tilde{\nu})^{-1} \qquad \ldots (4.47)$$

where δ_r is due to the Fresnel phase shift on reflection at the specimen and the term in $(2\tilde{\nu})^{-1}$ arises from the π radians phase shift experienced by the other partial ray on reflection at the moving mirror. The rays that undergo multiple internal reflections and leave through the front surface (r_1, r_2, r_3 etc) give rise to the signatures i (r_1) etc. These are approximately equispaced with i (r) and i (r_1) separated by an amount

$$\Delta x_r = 2nd + (\delta_T + \delta'_T) + (\delta'_r - \delta_r) \qquad \ldots (4.48)$$

in path difference, where δ_T is due to the phase shift on transmission across the interface into the specimen, δ'_T on transmission out of the specimen and

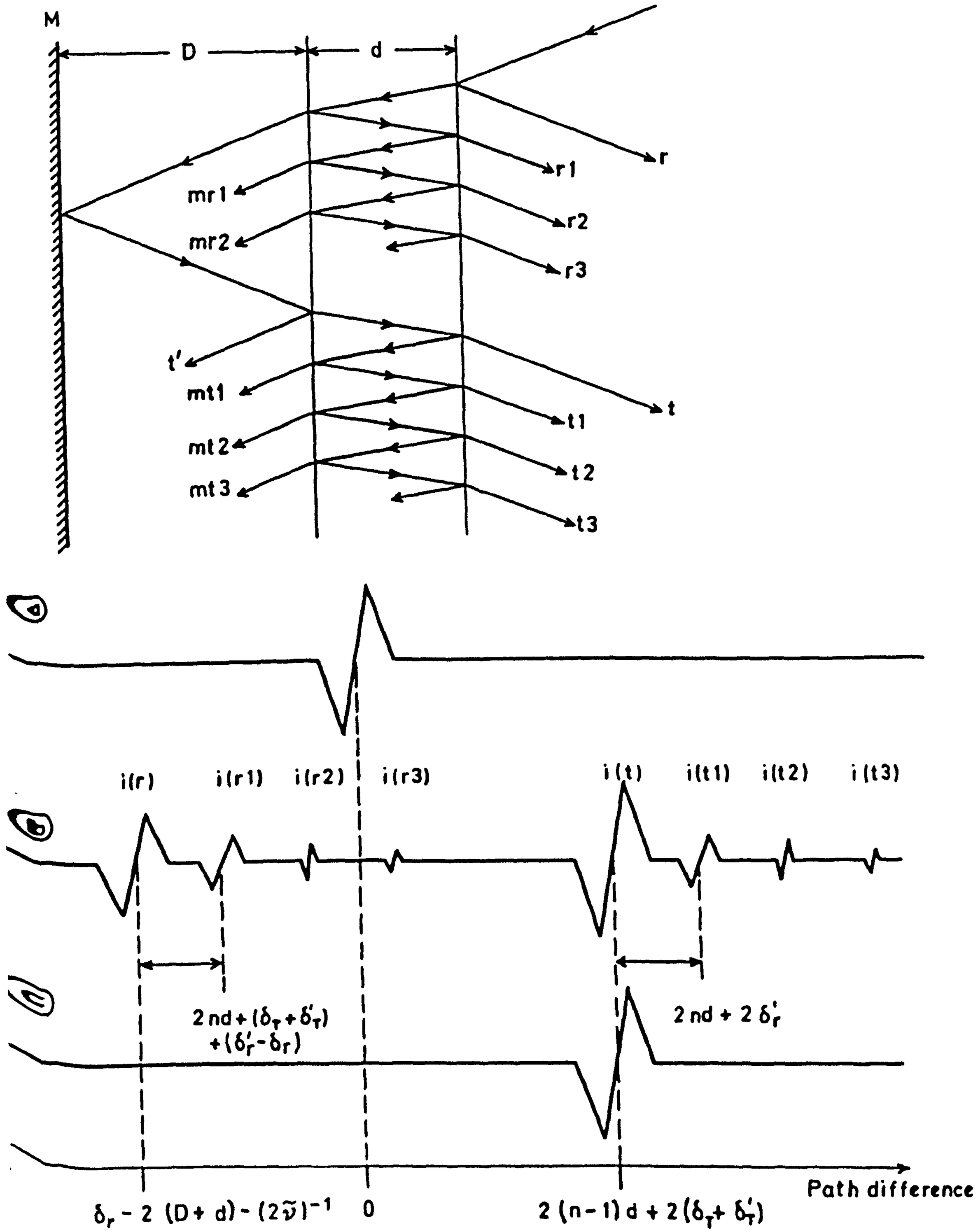

Fig.4.2. The origin of the various interference signatures in a dispersive transmission experiment.

S_r' on an internal reflection. In a similar manner, the ray t that has passed directly through the specimen, been reflected at the mirror and traversed the specimen again will cause the signature i(t) at path difference

$$x_t = 2(n-1)d + 2(\delta_r + \delta_r') \qquad \ldots (4.49)$$

and leads to the series of internally reflected signatures i(t1), i(t2), i(t3) etc, with i(t1) displaced from i(t) by

$$x_t = 2nd + 2S_r' \qquad \ldots (4.50)$$

The signatures due to the rays mr1, mr2 etc that have been internally reflected, leave the specimen through its rear surface to be reflected at M and re-enter the specimen will be another equispaced series superimposed on the i(t1) etc series provided that the shifts δ_r, δ_r', δ_r and δ_r' are small compared to 2nd, which will usually be the case. The signature due to t′ reflected from the rear surface of the specimen will be at

$$x_t' = 2D + 2(n-1)d + \delta_r + 2(S_r + S_r') + (2\sigma)^{-1} \qquad \ldots (4.51)$$

while those from mt1, mt2, mt3 etc will be at even greater path differences.

The presence of all of these signatures means that the optical constants are not related to the computed spectrum in a straightforward manner. Ideally, one only requires the i(t) signature. This is possible in the study of liquids with the subtraction technique developed by Chamberlain [97,107] or the iterative techniques of the Leiden group [98-105]. These all require measurements on at least two thicknesses of the material under study, and with the specimen in good optical contact with the mirror. As such they are not applicable to solids, and the specimen interferogram for solids is simplified by making the distance D, between the specimen and the mirror, sufficiently large (~30-40mm) that the i(r) signatures do not fall within the range of recorded path differences.

The i(t1) etc signatures may be similarly suppressed if the specimen thickness is such that the maximum path difference value used, x_{max}, is less than the separation, 2nd + $2S_r'$ of i(t) and i(t1). With these two conditions realised the specimen interferogram simplifies to that shown in part (c) of figure 4.2, from which the optical constants may be extracted as discussed in the following section.

4.5.2 DERIVATION OF THE OPTICAL CONSTANTS

In this section the numerical procedures used to derive the optical constants from the measured complex insertion loss are derived. This is done with reference to the configuration of the previous section in which the specimen interferogram only contains the direct beam signature i(t). Thus the complex transmission factor $\hat{T}$ relevant to these measurements is

$$\hat{T} = (1 - \hat{r}_{12}^2)\,\hat{a}_2 \qquad \ldots (4.52)$$

If the measurement is performed in a vacuum environment we can use the appropriate Fresnel equation, 2.26, to rewrite equation 4.52 in terms of the complex refractive index of the specimen

$$\hat{T} = \frac{4\hat{n}}{(1+\hat{n})^2} \cdot \hat{a} \qquad \ldots (4.53)$$

where the subscript 2 is now taken as implicit. Thus, from equation 4.45 we can derive the following relationship between the observed ratio of the modulus spectra and the optical constants

$$\frac{|\hat{S}_s(\tilde{\nu})|}{|\hat{S}_o(\tilde{\nu})|} = \frac{16\,e^{-\alpha d}}{((1+n)^2+k^2)^4} \cdot \left\{\left[n\left\{(1+n)^2+k^2\right\}+2k^2\right]^2 + k^2\left[1-n^2-k^2\right]^2\right\} \ldots (4.54)$$

In a similar manner equation 4.53 could be expanded to give an expression for ϕ^T to substitute into equation 4.46, but this leads to a cumbersome expression.

It is more elegant to express ϕ^T as the sum of the individual phase shifts experienced by the ray on its four transmissions across the boundaries of the specimen. Thus, from equations 4.46, 2.41 and 2.42

$$ph\{\hat{S}_s(\tilde{\nu})\} - ph\{\hat{S}_o(\tilde{\nu})\} = 2.\left[\arctan -\frac{k}{1+n} + \arctan \frac{k}{n(n+1)+k^2}\right] + 4\pi\tilde{\nu}(n-1)d \quad \ldots (4.55)$$

Rearranging equations 4.54 and 4.55 leads to the following expressions for the real refractive index, n, and the power absorption coefficient, α, in terms of the two measured quantities the modulus spectra ratio and the phase spectra difference.

$$n = 1 + \frac{1}{4\pi\tilde{\nu}d} \cdot \left\{\Delta_t - 2.\left[\arctan -\frac{k}{1+n} + \arctan \frac{k}{n(n+1)+k^2}\right]\right\} \ldots (4.56)$$

and,

$$\alpha = \frac{1}{d} \cdot \ln \left[\frac{16.\left\{\left[n\left\{(1+n)^2+k^2\right\} + 2k^2\right]^2 + k^2\left[1-n^2-k^2\right]^2\right\}}{\left\{(1+n)^2+k^2\right\}^2 \cdot \frac{|\hat{S}_s(\tilde{\nu})|}{|\hat{S}_o(\tilde{\nu})|}}\right] \ldots (4.57)$$

where Δ_t has been written for the measured phase difference

$$\Delta_t = ph\{\hat{S}_s(\tilde{\nu})\} - ph\{\hat{S}_o(\tilde{\nu})\} \quad \ldots (4.58)$$

As n and α appear on both sides of equations 4.56 and 4.57, they cannot be solved exactly, given the measured values of d, Δ_t and the modulus ratio. The following iterative procedure is therefore used.

Firstly, an approximate refractive index value, n_o, is calculated by ignoring the phase shifts that occur on transmission through the interfaces of the specimen

$$n_o = 1 + \frac{\Delta_t}{4\pi\tilde{\nu}d} \quad \ldots (4.59)$$

This is used to give an approximate value for the power reflection of the specimen surfaces

$$R_o = \left[\frac{1 - n_o}{1 + n_o}\right]^2 \qquad \ldots (4.60)$$

An approximate α-value can now be calculated by assuming that the reflection losses occur as power, rather than amplitude, losses. Hence

$$\alpha_o = \frac{1}{d} \ln \left[\frac{(1 - R_o)^2}{\frac{|\hat{S}_s(\tilde{\nu})|}{|\hat{S}_o(\tilde{\nu})|}}\right] \qquad \ldots (4.61)$$

leading to the absorption index

$$k_o = \alpha_o / 4\pi\tilde{\nu} \qquad \ldots (4.62)$$

With these approximate n_o - and k_o - values corrected n - and k - values, n_1 and k_1 can be calculated using the full equations 4.56 and 4.57 and the whole process repeated until the iterated values converge to the required level of accuracy.

In practice there is usually no need to iterate more than twice as the uncorrected values, n_o and k_o, lie close to the limiting values for most specimens. This is considered with regard to real measurements in section 6. The lack of sensitivity to an iterative solution is not surprising in view of the typical experimental conditions. The phase shift of the specimen is usually dominated by the term $4\pi\tilde{\nu}nd$, which can easily exceed 100 radians, and approximating equation 4.57 by 4.61 implies the assumption that

$$\left[1 - \left[\frac{1-n}{1+n}\right]^2\right]^2 \simeq 16.\frac{\left\{\left[n\{(1+n)^2 + k^2\} + 2k^2\right]^2 + k^2\left[1 - n^2 - k^2\right]^2\right\}}{\left\{(1+n)^2 + k^2\right\}^4} \qquad \ldots (4.63)$$

which is a good assumption for the small k - values not in most transmission experiments.

4.6 DISPERSIVE REFLECTION MEASUREMENTS

In a dispersive reflection experiment the front surface of the specimen exactly replaces the surface of the fixed mirror of the interferometer and its dispersion has a similar effect to that of the specimen in a dispersive transmission experiment. The only difference is that as the phase shift on reflection is considerably less than that on transmission the shift of the zero path difference fringe is much smaller, being a few micrometres at most, compared to several millimetres or more, in the transmission case.

Thus, the electric field at the detector when such a reflecting specimen is in the interferometer would be

$$\hat{E}_s(x) = -\hat{e}_o \left[R \exp i(\phi^R - \pi) + \exp i2\pi\tilde{\nu}x \right] \quad \ldots (4.64)$$

where the complex reflection factor of the specimen has been written

$$\hat{R} = R \exp i\phi^R \quad \ldots (4.65)$$

without specifying whether the measurements resolves only the front surface reflected ray or some of the internally reflected rays as well. The term $-\pi$ in equation 4.64 arises from the phase shift of π radians that occurs on reflection at the moving mirror. The radiation intensity at the detector is, therefore,

$$i_s(x) = \frac{i(0)}{4}\left\{1 + R^2\right\} + \frac{i(0)}{2} \cdot R \cdot \cos\left\{2\pi\tilde{\nu}x - (\phi^R - \pi)\right\} \quad \ldots (4.66)$$

and, once again generalising to a polychromatic source and complex exponential notation gives the x - dependent interferogram

$$I_s(x) = \int_{-\infty}^{\infty} R \cdot \hat{S}_o(\tilde{\nu}) \exp -i\left\{2\pi\tilde{\nu}x - (\phi^R - \pi)\right\} \cdot d\tilde{\nu} \quad \ldots (4.67)$$

The Fourier inversion of this leads to the complex specimen spectrum

$$\hat{S}_s(\tilde{\nu}) = R \exp i(\phi^R - \pi) \cdot \hat{S}_o(\tilde{\nu}) \quad \ldots (4.68)$$

and the ratio of this complex spectrum with that of the reference measurement, equation 3.13, therefore gives the complex insertion loss for this specimen in this dispersive reflection experiment as

$$\hat{L}(\tilde{\nu}) = R \exp i(\phi^R - \pi) \qquad \ldots (4.69)$$

Dealing separately with the modulus and phase spectra then leads to the following relations for R and in terms of the measured quantities

$$R = \frac{|\hat{S}_s(\tilde{\nu})|}{|\hat{S}_o(\tilde{\nu})|} \qquad \ldots (4.70)$$

and,

$$\phi^R = ph\{\hat{S}_s(\tilde{\nu})\} - ph\{\hat{S}_o(\tilde{\nu})\} + \pi \qquad \ldots (4.71)$$

There are two points to note about the derivation of these last two equations. Firstly, in deriving equation 4.64 it was assumed that the reflectivity of the moving mirror of the interferometer was $1.0 \exp i\pi$, that of a perfect reflector. Metallic reflectors, with their finite conductivities, are not perfect reflectors and in chapter 7 an absolute method for the determination of complex reflectivity is discussed, and used to consider how the behaviour of some typical laboratory mirrors departs from this ideal situation. Secondly, it is interesting to note an important difference between dispersive and non-dispersive reflectivity measurements. We have seen above that in the former it is the amplitude reflectivity, R, that is measured while, in the latter measurement the power reflectivity, R^2, is determined. Thus, in regions of very low reflectivity where $R \gg R^2$ there is considerable advantage in signal level to be gained from dispersive measurements.

4.6.1 THE NATURE OF THE DISPERSIVE INTERFEROGRAM

There are significant differences between a dispersive reflection and a dispersive transmission interferogram. Firstly, in the reflection measurement

the fixed mirror is replaced by the specimen so that the rays mr1, t′ and mt1 etc of figure 4.2, that pass through the rear surface of the specimen are lost to the experiment. Secondly, one would usually only perform a reflection experiment when the specimen is so opaque that the easier transmission experiment is not possible. The internally reflected rays r1, r2, r3 etc would then be strongly attenuated and not observed, even if they fell inside the range of recorded path differences. In a dispersive reflection experiment, therefore, it is usual for the specimen interferogram to only show one interference signature, that characteristic of the front surface reflection.

4.6.2 DERIVATION OF THE OPTICAL CONSTANTS

If the specimen interferogram is only characteristic of the front surface reflection as discussed in the previous section the measured complex reflection factor $\hat{R}$ of equation 4.64 will be the Fresnel reflectivity of that surface, and for incidence from a vacuum equation 2.26 gives this as

$$\hat{r}_{12} = \frac{1 - \hat{n}_2}{1 + \hat{n}_2} \qquad \ldots (4.73)$$

One now sees the unique value of dispersive reflection FTS, inverting equation 4.73 gives

$$\hat{n}_2 = \frac{1 - \hat{r}_{12}}{1 + \hat{r}_{12}} \qquad \ldots (4.74)$$

and it is apparent that the real and imaginary parts of $\hat{n}_2$ can be exactly calculated from 4.74 without approximate or iterative solutions. Separating equation 4.74 into its real and imaginary parts leads to the following expressions for the real refractive index and the absorption index

$$n_2 = \frac{1 - r_{12}^2}{1 + r_{12}^2 + 2r_{12}\cos\phi_{12}^r} \qquad \ldots (4.75)$$

and

$$k_2 = \frac{-2r_{12}\sin\phi^r_{12}}{1 + r_{12}^2 + 2r_{12}\cos\phi^r_{12}} \qquad \ldots (4.76)$$

As ϕ^r_{12} is greater than, or equal to π radians, $\sin\phi^r_{12}$ in equation 4.76 is negative and k_2 takes a positive value.

CHAPTER 5

POWER TRANSMISSION MEASUREMENTS

5.1 INTRODUCTION

Due to their experimental simplicity power transmission measurements are the most frequently performed broad-band spectroscopic measurement. In this chapter the instrumentation for such measurements at room and liquid helium temperatures is briefly introduced and the results of measurements on soda lime silica glass specimens below 50 cm^{-1} are used to compare some of the techniques discussed in chapter 4 for deriving the optical constants from the measured power transmission. Finally, for completeness, the results of some near-infrared transmission measurements taken with a grating spectrometer are introduced. The analysis of both these sets of measurements enables the optical constants of the glass in the long and short wavelength wings of the mid-infrared band to be characterised.

5.2 INSTRUMENTATION AND PERFORMANCE

The instrumentation used for power transmission measurements at room and liquid helium temperatures was, essentially, the modular interferometer described in section 3.4.1 This has been discussed in detail in that chapter and in other publications [72,47] and in this section some aspects of its performance below 50 cm^{-1}, the main spectral region of interest in this chapter, that have not been previously considered will be discussed.

In the room termperature measurements the specimen was always introduced into the collimated beam at the exit aperture of the interferometer, before the condensing lens. This avoided effects due to defocussing and ambiguities in the effective specimen thickness caused by the use of converging radiation. [145]

This was not possible at liquid helium temperatures where light-pipe optics were used. Also, in the room temperature measurements, no attempt was made to stabilise the temperature of the specimen. This presented no problem for soda lime silica glass, but some materials undergo phase transitions at temperatures close to 300K, PTFE at 292K for example [146], and temperature control would be needed for precise measurements on such materials.

Throughout this work polyethylene or TPX [147] lenses were used as the condensing element for the radiation detector of the interferometer, although both materials become quite heavily absorbing above $100\ cm^{-1}$. Recent measurements with a Pfund all-reflecting condensing system [148] instead of polymer lenses have shown that the detected radiation intensity can be increased by a factor increasing from unity at $50\ cm^{-1}$ to greater than 30 by $300\ cm^{-1}$, although care has to be taken to avoid detector non-linearities and aliasing problems due to the increased radiation flux at the detector.

5.2.1 SPECTRAL REPRODUCIBILITY

In power transmission measurements the mechanical stability of the interferometer is not as important a consideration as it is in dispersive measurements, where the phase spectrum is required. Thus, measures to stabilise the interferometer were not generally necessary, although two precautions were found to be worthwhile implementing. These were to water cool both the housing of the mercury arc lamp and the Golay cell detector, when used. The first of these avoided the mechanical vibrations that can result from forced air cooling using a fan, while the second avoided temperature induced changes in the responsivity ($\sim$ 1% per ^{o}C) of the Golay cell.

With these precautions taken, and using phase modulation, high quality interferograms could be consistently obtained for the spectral region below 50 cm^{-1}. This is illustrated in figure 5.1 which shows two typical interferograms recorded during this work. Their quality may be quantified by their signal-to-noise ratio which is taken as the ratio of the maximum-to-minimum intensity variation across zero path difference to the standard deviation of the intensity at a constant path difference value. The first of these two interferograms, (a), was recorded with a 750g melinex beamdivider and a liquid helium cooled Rollin detector with a 0.3s time constant in the phase sensitive detector. The spectral range was restricted to wavenumbers below $10cm^{-1}$ by the use of a double-sided diffraction filter of the type described by Kimmitt[71], and based on the work of Möller and McKnight[149]. This is the most difficult spectral region for broad-band spectrometry due to the low source power levels, but the signal-to-noise ratio of the interferogram is sufficiently high ($\sim$ 400:1) for precise studies. The second interferogram illustrated, (b), was recorded with the same detector and a 200g melinex beamdivider, with the spectral range now extending to about $50cm^{-1}$, the cut-off of the detector. The time constant was 0.1s and the increased power levels from the source lead to a signal-to-noise ratio of about 5000:1. The quality of this interferogram is apparent from the insert which shows, on an expanded ordinate scale, the structure on the main interferogram above it, and on which the noise is only just resolved.

It is difficult to quantitatively transform from noise in the interferogram domain to noise in the spectral domain, but, qualitatively, the effect of our typical interferogram noise may be seen by the reproducibility of spectra computed from nominally identical interferograms. This is illustrated in figures 5.2 and 5.3 for the two spectral ranges represented by the interferograms of figure 5.1. In figure 5.2 the upper graph, (a), shows the superimposition of three

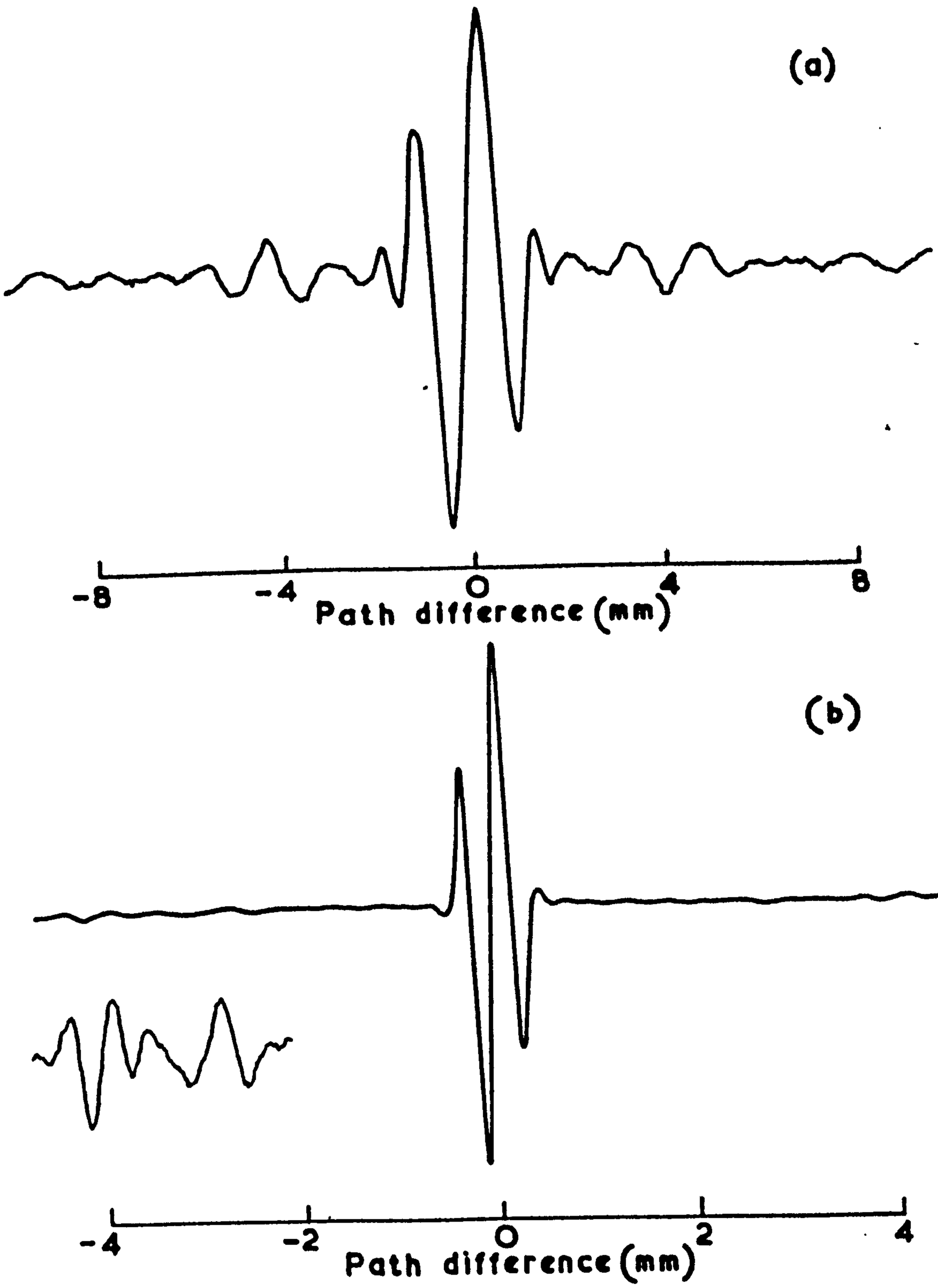

Fig.5.1. Typical interferograms obtained with (a) 750g and (b) 200g dielectric beamdividers in the interferometer.

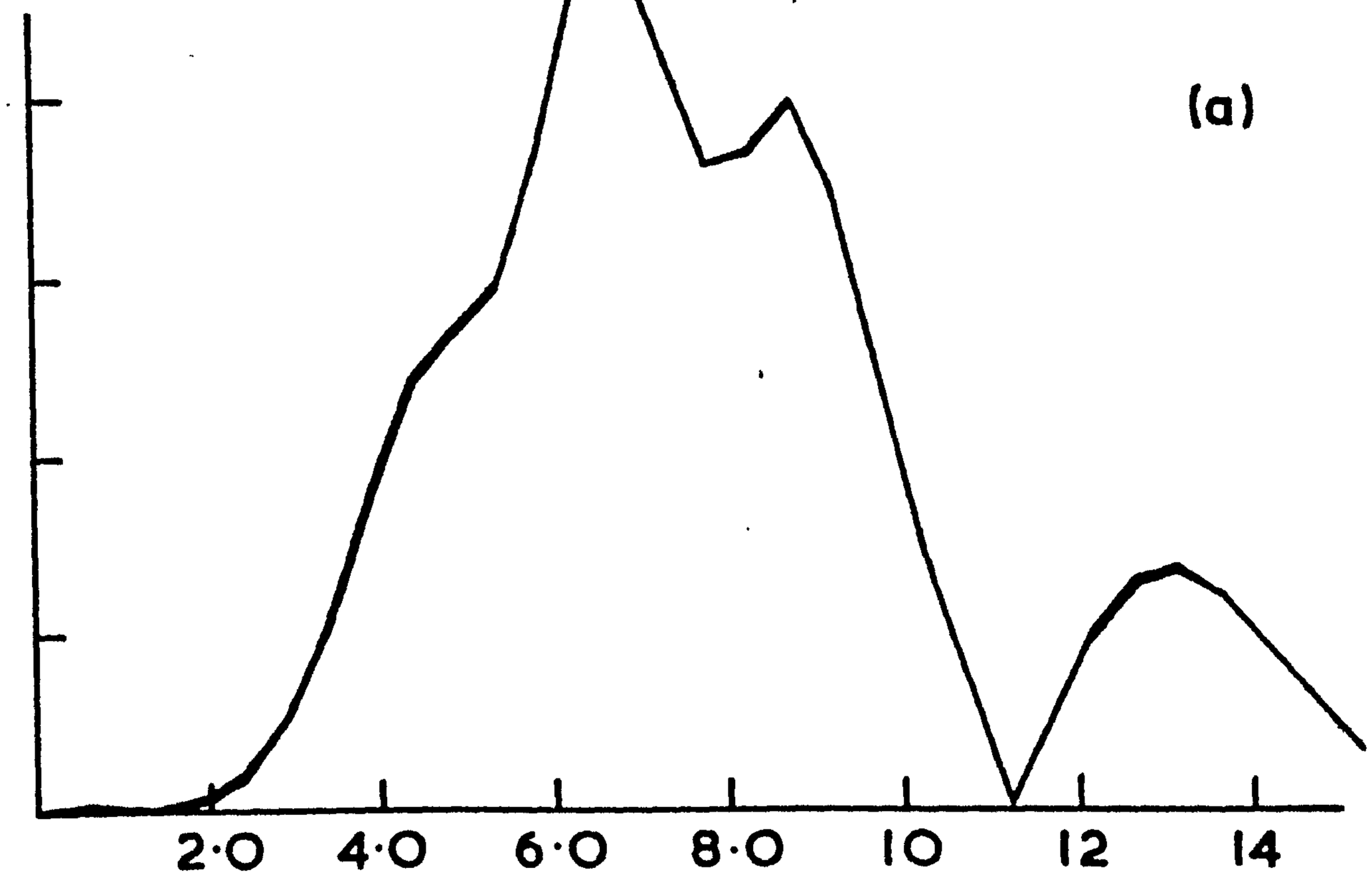

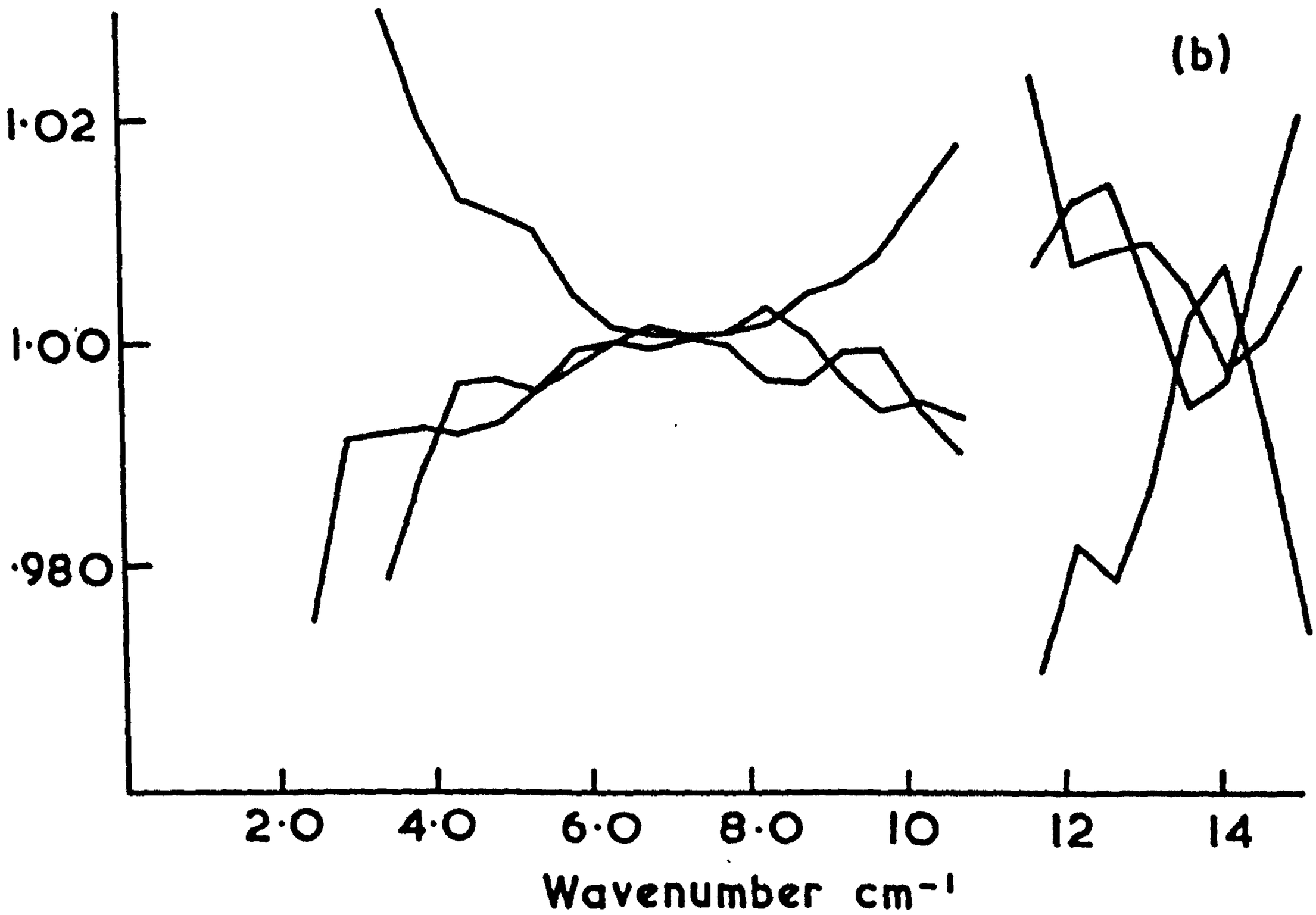

Fig.5.2. Illustrating the reproducibility of modulus spectra recorded with a 750g beamdivider.

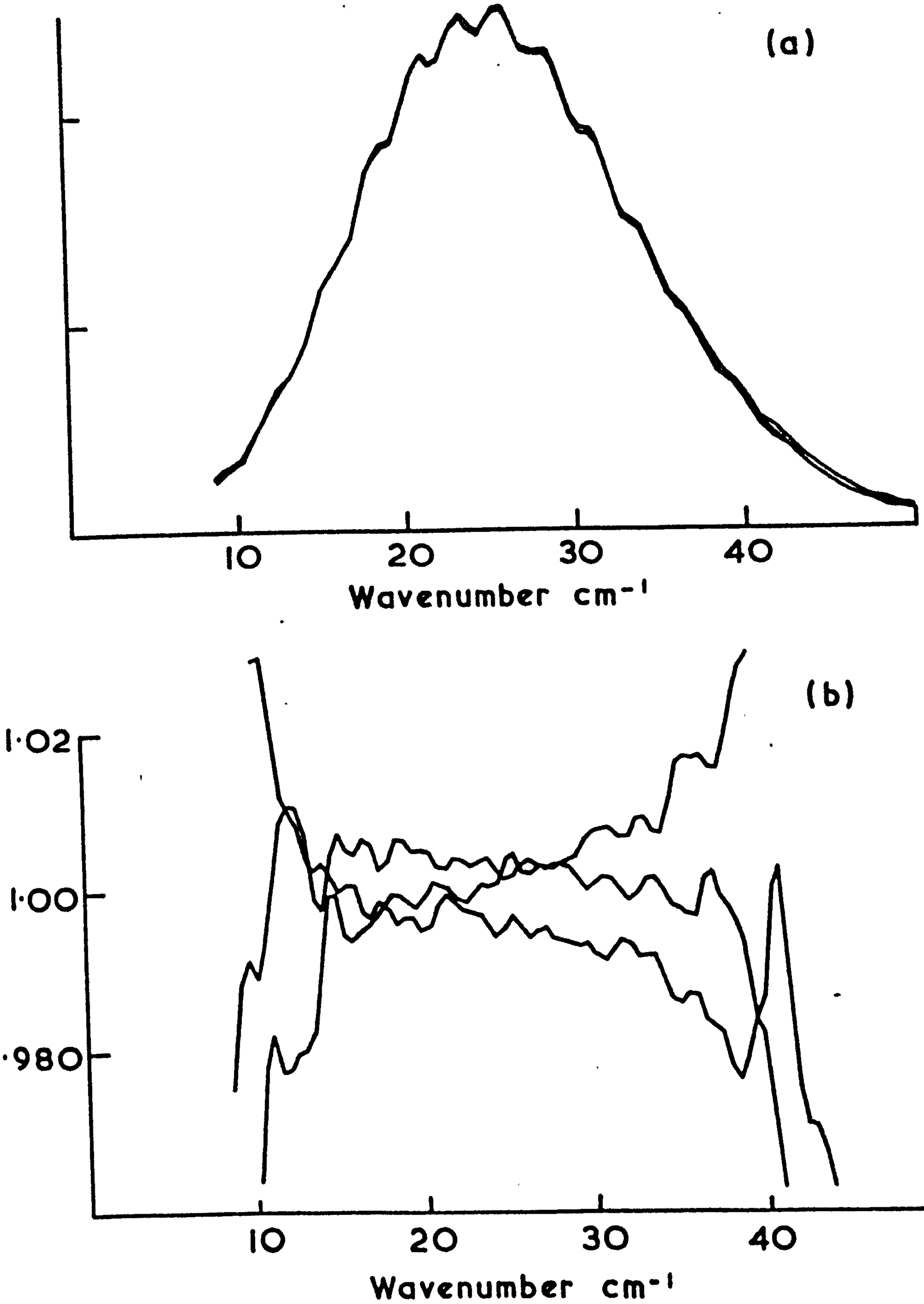

Fig.5.3. Illustrating the reproducibility of modulus spectra recorded with a 200g beamdivider.

modulus spectra computed to 1 cm^{-1} apodised resolution from separate interferograms similar to that of figure 5.1 (a). The zero in all three at 11.2 cm^{-1} corresponds to the first zero of the phase modulation characteristic, that due to the beamdivider was at 15 cm^{-1}. The three closely reproduce each other and the differences between them are more apparent from figure 5.2 (b) which shows the ratio of each against the average of all three. Over most of the useful spectral range below 11 cm^{-1} they fall within $\pm$ 1% of each other. The gap at 11 cm^{-1} is where the ratios depart significantly from unity due to the low power levels. In a similar manner the curves of figure 5.3 correspond to three spectra computed to 1 cm^{-1} apodised resolution from interferograms similar to that of figure 5.1 (b). The periodic structure is a channel spectrum due to the interference signature at 4 mm path difference seen in 5.1 (b). This vanishes in the ratios of figure 5.3 (b) and again, over most of the spectral range, the reproducibility is about $\pm$ 1%. Most of the difference between the ratios of figure 5.3 (b) is systematic, and was due to the fact that the measurements were taken shortly after the detector was filled with liquid helium, at a time when its responsivity had not stabilised. The level of random variation on these ratios is considerably less than $\pm$ 1%, being more like $\pm$ 0.25%.

5.2.2 LIQUID HELIUM TEMPERATURES

The power transmission of a specimen at liquid helium temperatures may be measured in one of two configurations. The specimen may be mounted on a cold finger cooled by contact with a liquid helium reservoir, or by immersion in liquid helium. The former is the most versatile as a wide range of specimen temperatures may be achieved by the use of various cryogenic liquids, but it suffers from the disadvantage that the detector cannot usually be mounted in the specimen area, so that it is necessary to have windows into and out of the cryostat, leading to increased signal losses. In the latter technique the

detector is also immersed in the liquid helium, near to the specimen. This technique was used for these measurements and as the apparatus was not significantly different from those of other workers only a brief description is given.

The exit beam of the interferometer was focussed into the cryostat through a thin polyethylene window sealing the entrance of a 0.8 m long light pipe. The lower end of this was immersed in liquid helium and, over its length, its bore tapered from 12 to 6 mm diameter. The detector assembly was supported at the lower end of the light pipe. The specimen holder was about 50 mm above the detector assembly and consisted of a flat brass plate, 9.5 mm thick, in the shape of a quarter circle. Three 8 mm diameter holes were drilled through this, at the same radius, and the plate could be rotated into a 10 mm gap in the light pipe, at a point where its bore was 8 mm diameter, so that the axis of any of the holes was coincident with that of the light pipe. Specimens were gravity held in place in the holder by a small lip at the bottom of each hole, and, during one helium fill, measurements could be made on two specimens with the third hole acting as the reference position. It was important that the third hole be used as the reference position, rather than removing the holder completely from the light pipe. The radiation in the light pipe is not collimated and undergoes many wall reflections. Thus, if the holder were removed no allowance would be made for the light guiding effect of its walls and the background spectrum would not be characteristic of the specimen measurement. The magnitude of this light guiding effect may be seen from figure 5.4 which shows the ratio of modulus spectra recorded at 4.2K without and with the holder in place and representing, therefore, the relative power transmission of the gap. At the longest wavelengths, where the radiation diverges strongly from the end of the light pipe the effective transmission of

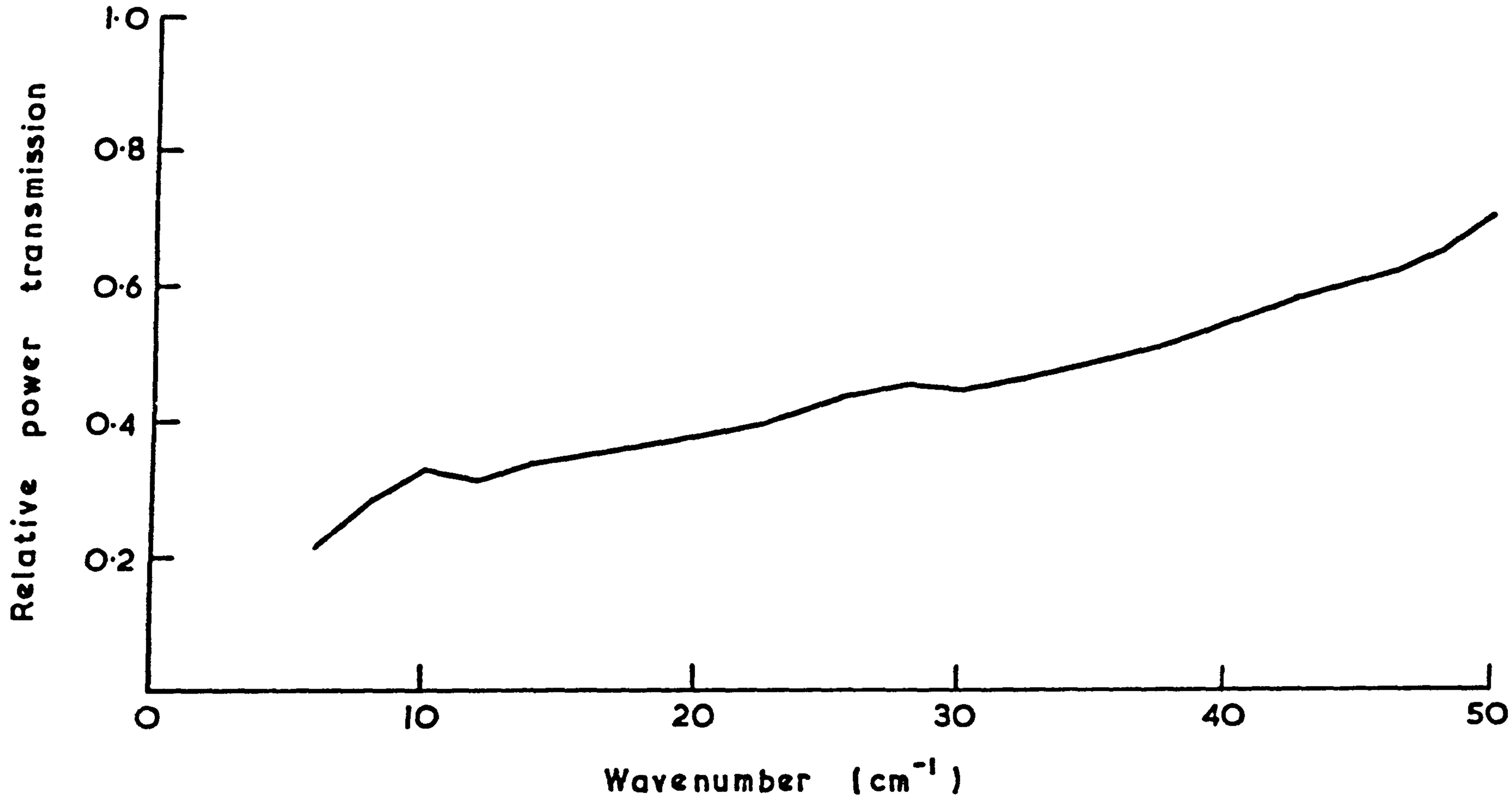

Fig.5.4. Illustrating the light guiding effect of a short section of circular brass pipe.

gap is only 0.2 of that of the specimen holder. The divergence decreases with wavelength and by 50 cm^{-1} the transmission of the gap has risen to 0.65 of that of the holder.

Measurements with this apparatus were made with either a Rollin- or a Putley-detector. The Rollin-detector tended to be used between 3 and 50 cm^{-1} at any temperature between 1.8 and 4.2K by varying the pressure of the gas over the liquid surface between about 12 and 760 torr [150]. Outside of this spectral range, up to 90 cm^{-1}, the Putley-detector was used, but only at its operating temperature of ~ 1.8K.

It is usual practice to have a thin black polyethylene filter at the entrance to the light pipe to prevent visible and near infrared radiation reaching the detector and giving a spurious signal due to direct band gap excitation. It was found to be additionally necessary to insert a similar filter in the liquid helium bath between the specimen and the detector. This was particularly so for specimens that exhibited low loss in the far-infrared, but were opaque in the near-infrared. Under these circumstances the near infrared flux reaching the detector element varied enormously with the specimen in or out of the light pipe. In the situation of reduced flux with the specimen in the light pipe the detector resistance would increase, leading to an increase in responsivity that made it possible to measure power transmissions apparently in excess of unity. Use of the second filter avoided this.

5.3 PREVIOUS MEASUREMENTS ON SODA LIME SILICA GLASS

Very little quantitative data on the optical constants of soda lime silica glass in the millimetre and submillimetre wavelength region was available at the beginning of this study. In 1965 Mashkovich and Demeshina [34] published power transmission measurements indicating the presence of an absorption

feature near to 16 cm^{-1} and power reflection measurements which showed a constant reflectivity of about 0.18 between 10 and 100 cm^{-1}. If $n \gg k$ this would correspond to a refractive index close to 2.5. It was, however, apparent from their data that the absorption feature could have been due to internal interference effects, and this was confirmed by the subsequent measurements of Dianov et al[37], between 5 and 20 cm^{-1}, on one of the specimens of the earlier authors. The results of Dianov et al showed that the absorption coefficient increased monotonically with wavenumber, and that at 5 cm^{-1} it also increased linearly with increasing temperature between 100 and 300K, with its value at 300K being almost twice that at 100K. They also showed that the refractive index at 5 cm^{-1} increased from 2.52 at 100K to 2.56 at 300K. Their measurements were in contrast to those of Hadni et al[35,36] showing that both the absorption coefficient and the refractive index were independent of temperature above 50 cm^{-1}. Intermediate between these sets of authors were the measurements of Bagdade and Stolen[38] between 10 and 45 cm^{-1}. These authors found a refractive index of 2.6 at room temperature, and describe the absorption coefficient as temperature independent between 107K and room temperature, although their detailed measurements show that at 34 cm^{-1} it in fact increased by an amount equivalent to about 3.3 $Np.cm^{-1}$. Bagdade and Stolen also found that the absorption coefficient at room temperature varies as the square of the wavenumber between 10 and 45 cm^{-1} in general agreement with the theories of Vinogradov[151] and Schlömann[152] for low frequency absorption in a disordered charge system. The results of this chapter will show that the temperature dependence of the absorption coefficient is wavenumber dependent. Thus, at millimetre wavelengths the absorption coefficient is strongly temperature-dependent, becoming temperature-independent by 50 cm^{-1}.

5.4 COMPOSITIONAL ANALYSIS OF SPECIMENS

The chemical composition of soda lime silica glass can vary within fairly broad limits and in table 5.1 the major constituents of the glasses studied in these power transmission measurements are listed*. As the variation in the amounts of the major constituents present in these specimens was not great, no attempt was made to correlate this with variations in the measured optical constants. The effects of composition on the complex refractive index are considered in the dispersive reflection measurements of chapter 8.

5.5 THE REFRACTIVE INDEX BELOW 40 cm^{-1}

The refractive index below 40 cm^{-1} was determined at 293, 4.2 and 1.8K from the spectral positions of the maxima and minima of the channel spectra seen in transmission measurements on six specimens having thicknesses between 0.152 and 1.305 mm. All of the measurements were taken with a Rollin detector, and no differences could be measured between the optical constants at 1.8 and 4.2K. Figures 5.5 and 5.6 show typical power transmission spectra, figure 5.5 being at 293K and 5.6 at 4.2K. Several qualitative conclusions about the optical constants can be immediately drawn from these spectra:

(i) For each temperature the period of the channel spectrum is virtually constant, so that within the precision of these measurements the refractive index will not appear to be significantly dispersed.

(ii) There is a region of intense absorption above 50 cm^{-1}.

---

* The analysis was performed by Mr G.W.Smith of the Division of Chemical Standards, NPL, except for that of the 1.692 and the 3.088 mm specimens, which was provided by Dr G.W.F.Pardoe of Pilkington Brothers Ltd. These specimens were also used in the dispersive transmission measurements

SPECIMEN THICKNES(mm)	MEASUREMENT TEMPERATURE	SiO_2	Na_2O	CaO	MgO	K_2O	Sb_2O_5	ZnO	PbO	R_2O_3*	TRACE+	TOTAL
0.152, 0.215, 0.270 0.710, 1.310	1.8/4.2/293K	69.80	11.90	8.90	4.80	0.45	-	-	-	3.90	-	99.75
0.148, 0.199	Near infrared 293K											
0.246	293K	70.70	11.06	-	-	-	4.4	4.6	7.1	-	Ag, Al, Ca, Cr, Fe, K, Sn, Ti	97.86
1.305	293K	71.10	15.50	6.65	4.50	0.38	-	-	-	-	Al, Cr, Cu Fe, V	98.13
1.692	293K	72.6	12.9	8.4	4.0	0.6	-	-	-	1.22	-	99.72
3.088	293K	72.80	13.00	9.00	3.2	0.6	-	-	-	0.991	-	99.591
5.82	293K	71.00	13.80	8.50	3.60	0.65	-	-	-	-	Al, Cr, Cu, Fe, Mn, Ni, Sn, Ti, V	97.55
6.16	293K	71.50	14.00	12.70	trace	trace	0.4	-	-	-	Al, Cr, Cu, Fe, Pb	98.60

Table 5.1 Compositional analysis of the glass specimens used in the transmission measurements of this, and the following, chapter. The figures shown are the compositional percentage weight.
*R_2O_3 essentially represents Al_2O_3, for the 3.088mm specimen this breaks up into 0.9% Al_2O_3 and 0.091% Fe_2O_3
+ Trace elements found spectrographically.

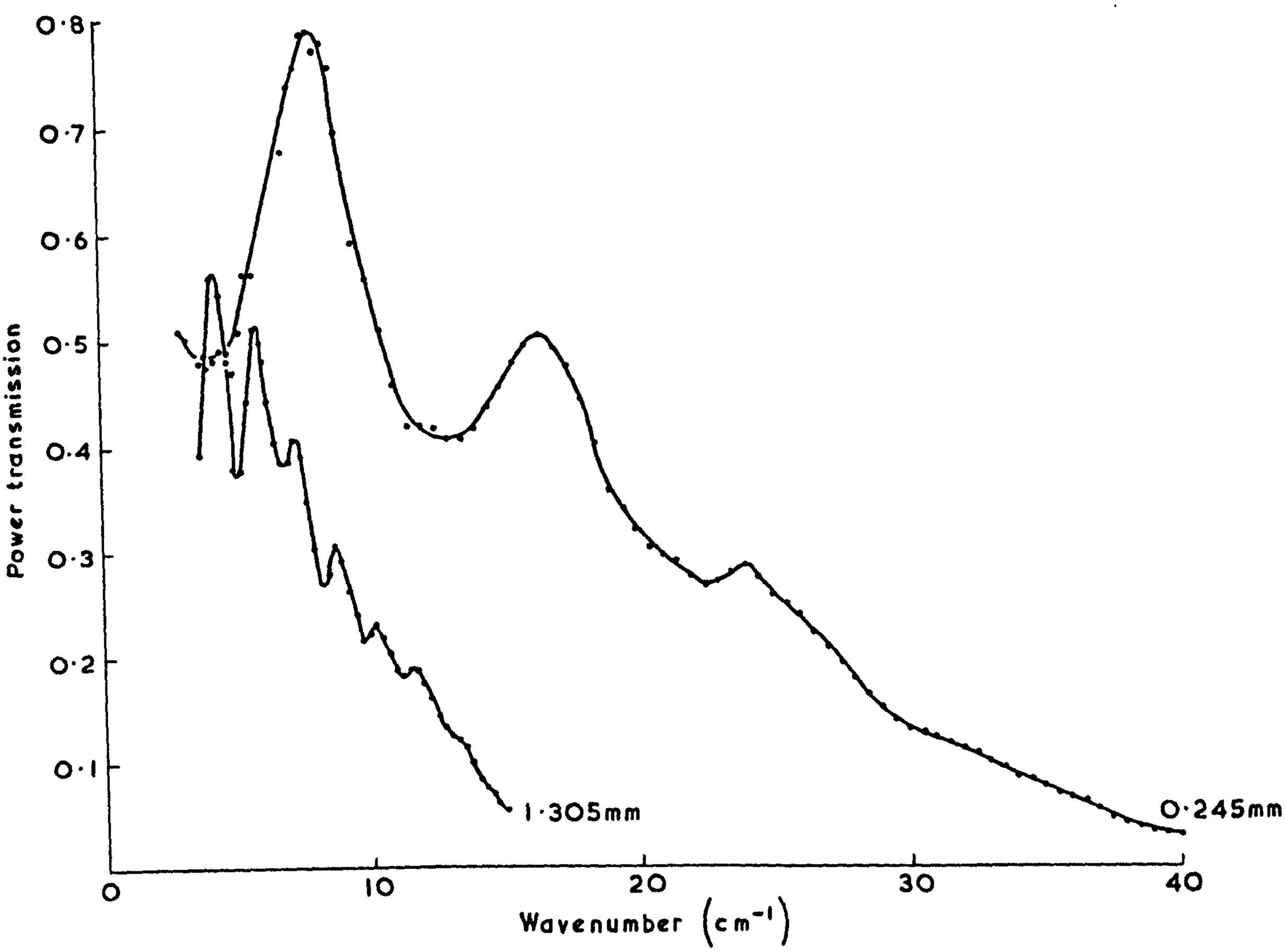

Fig.5.5. The power transmission spectra of two thicknesses of soda lime silica glass below 40cm^{-1} at 293K.

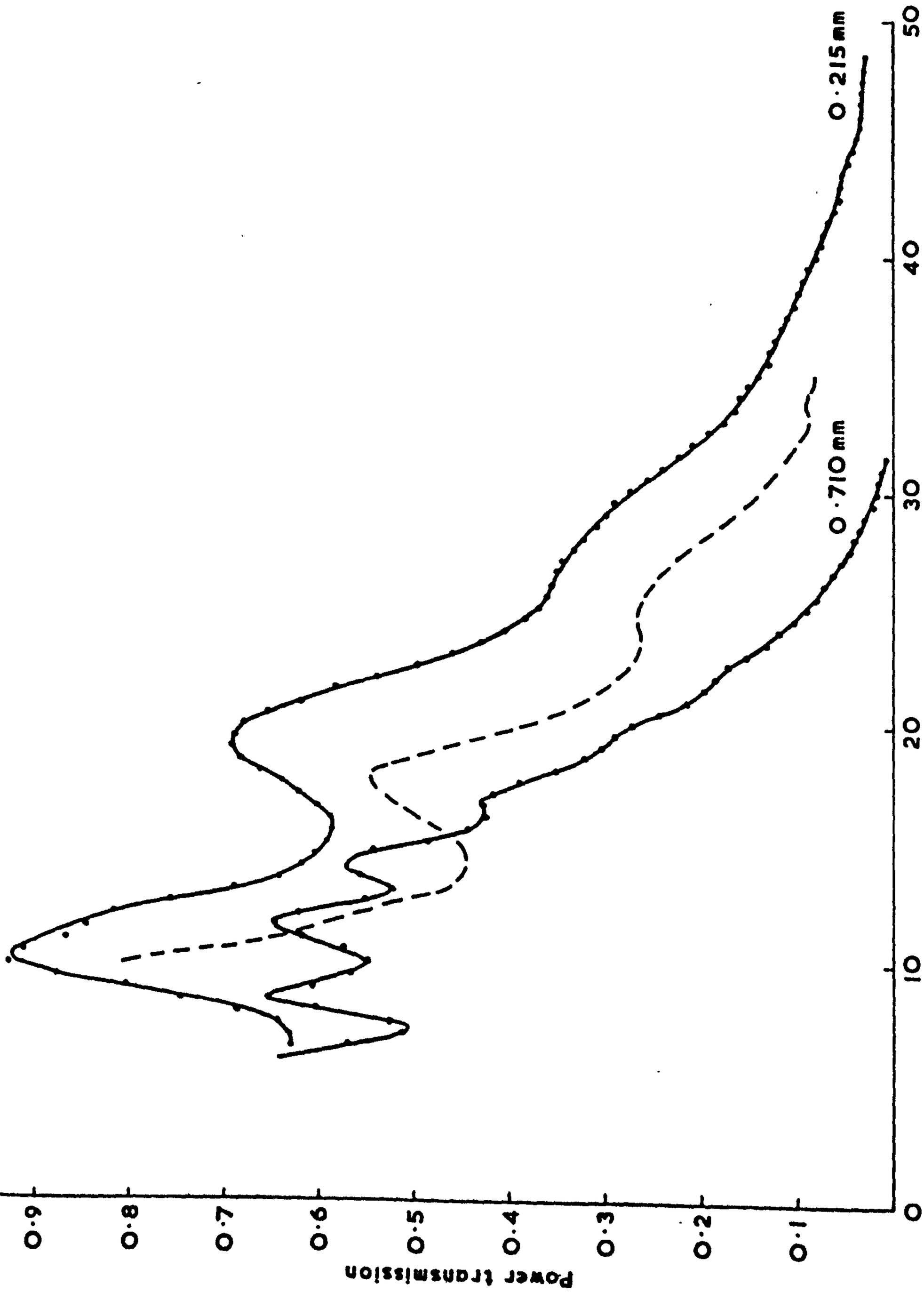

Fig.5.6. The power transmission spectra of two thicknesses of soda lime silica glass below 50cm^{-1} at 4.2K.

(iii) Both parts of the complex refractive index decrease with decreasing temperature. This is seen from the dashed curve in figure 5.6 which represents the power transmission of the 0.215mm specimen at 293K. Its transmission and channel spectrum period both increase on cooling.

The refractive index in both temperature ranges was determined from the experimental data by the two techniques described in section 4.3.2. Firstly, for each interference fringe to which an order number could be assigned n was calculated from equation 4.26 or 4.27, as appropriate, and then by application of the least-squares straight line fit represented by equation 4.28.

5.5.1 DETERMINING THE ORDER NUMBER

For the thinner specimens it was always possible to unambiguously assign an order number to a fringe in their channel spectra by visual inspection. Thus, for the transmission spectrum of the 0.245mm specimen shown in figure 5.5, the maximum at 8.1 cm^{-1} has the order number $m = 1.0$, and the minimum at 12.6 cm^{-1} corresponds to $m = 1.5$. With the thicker specimens, however, such as the 1.305 mm one of figure 5.5, a more systematic approach was used even though a reasonable guess could be made. The interference fringe at the lowest wavenumber was given the reduced order number $m' = 0$ if a maximum or 0.5 if a minimum. If the dispersion in the material is small a plot of the wavenumber $\tilde{\nu}_m$ associated with m' against m' can be extrapolated back to give a negative value of m' at zero wavenumber. It is easily shown that the magnitude of this is the correction to be added to the reduced order number to give the correct scale, m. This is illustrated in figure 5.7 for the 1.305mm specimen. The lack of dispersion is apparent from the good fit to a straight line, and $m' = -3$ at $\tilde{\nu}_m = 0$, so that in figure 5.5 the maximum at 4.35 cm^{-1} takes the order number

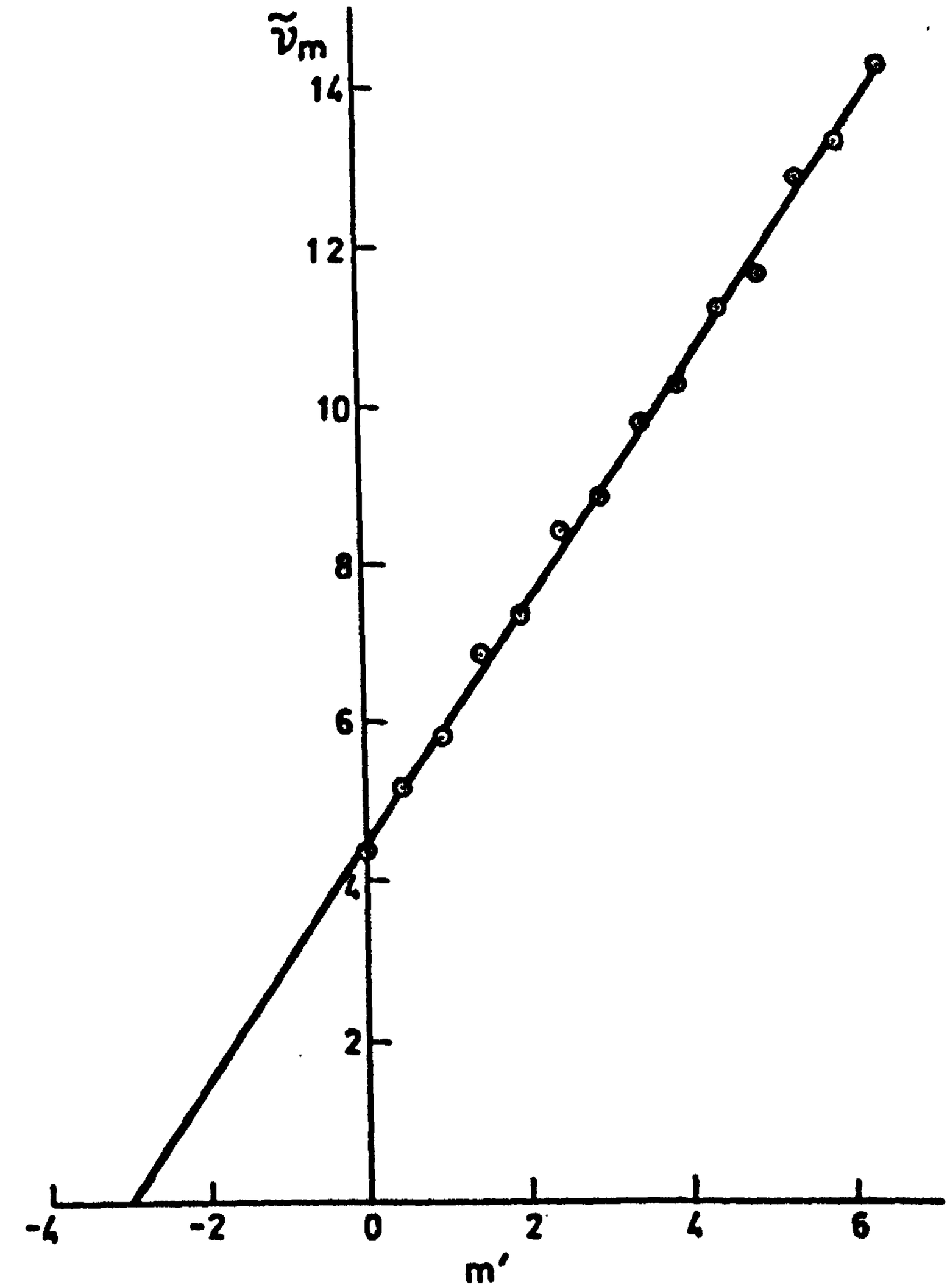

Fig.5.7. Reduced order number against wavenumber for the 1.305mm specimen at 293K.

m = 3. This procedure will only be valid at submillimetre wavelengths, where the order number is low, and only if the measured spectra have good signal-to-noise ratios.

5.5.2 THE REFRACTIVE INDEX

With the order number of each maxima and minima of all the spectra used in these measurements identified, the refractive index spectra of figure 5.8 were calculated by the application of equations 4.26 and 4.27 to each feature in the channel spectrum. In calculating the refractive index for the liquid helium measurements the effects of thermal contraction were allowed for by taking $4.5 \times 10^{-6}\ K^{-1}$ as the effective coefficient of linear expansion for soda lime silica glass between 4.2 and 293 K. This is the mean of the 283K value ($9 \times 10^{-6}\ K^{-1}$) and that for liquid helium temperatures ($\sim 0 \times 10^{-6} K^{-1}$) given by White[153].

The scatter at both temperatures is too large to establish the presence, or otherwise, of any spectral variation, and the 293K point at 22 cm^{-1} is, in particular, obviously low. In figure 5.5 we see that the transmission spectrum of this specimen has a shallow minimum about 22 cm^{-1}, and a small intensity error would easily lead to a mis-identification of $\tilde{\nu}_m$, causing the depression of the calculated n-value. Mean values of n were calculated over the entire spectral range, giving rise to

$$n_{293} = 2.544 \pm 0.082 \qquad \ldots (5.1)$$

and

$$n_{4.2} = 2.477 \pm 0.102 \qquad \ldots (5.2)$$

where the error limits are the standard deviations of the points forming each mean. Thus, the refractive index at each temperature has been determined with a random error of about 4 parts in 10^2. The mean values are shown

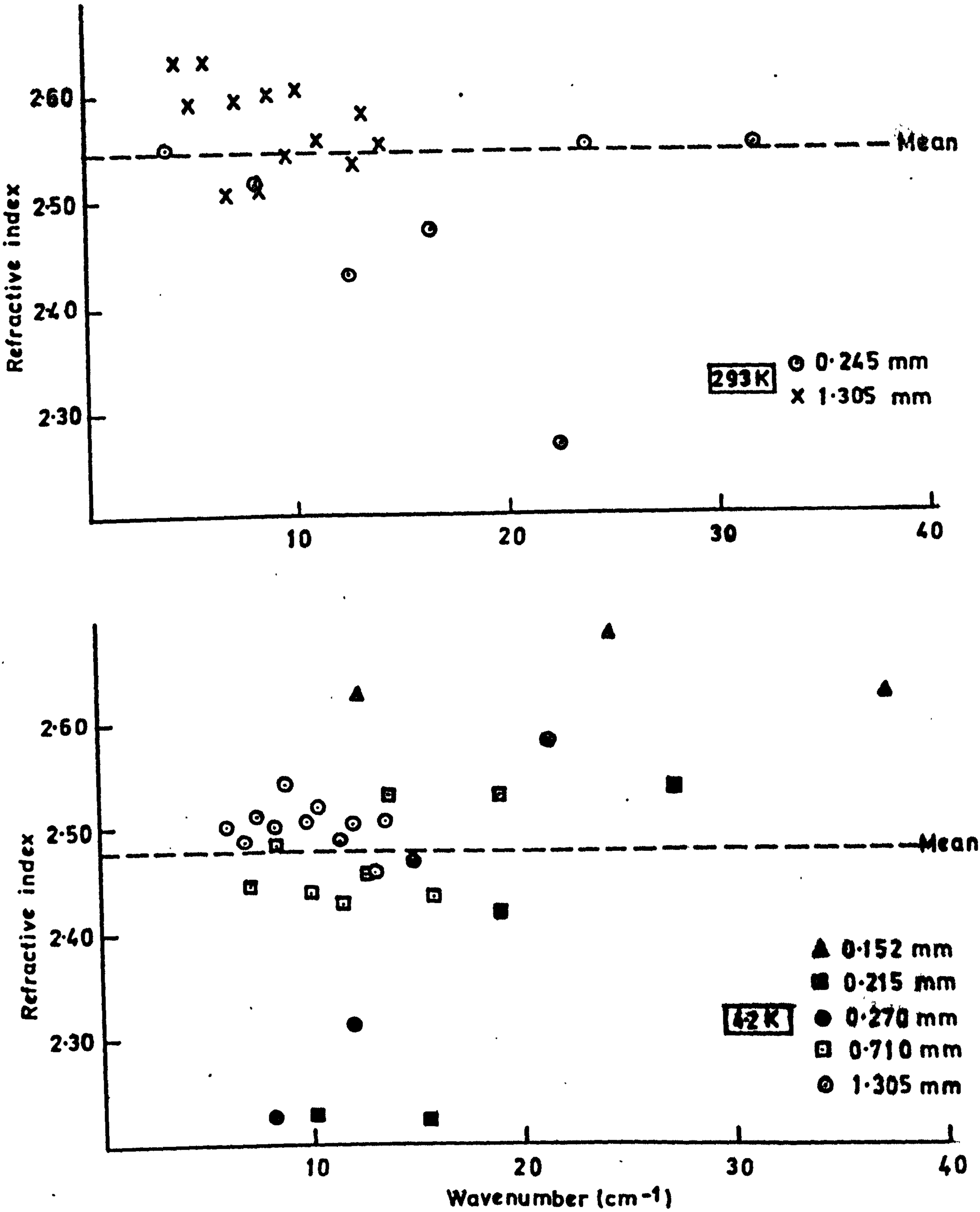

Fig.5.8. Refractive index spectra of soda lime silica glass at 293K and 4.2K, determined from the positions of local maxima and minima in channel spectra.

as the dashed lines in figures 5.8 (a) and (b). The low temperature results, where several thin specimens were used, illustrate a major systematic error in this type of determination, that due to the thickness measurement. The calculated values of the refractive index of the 0.152 mm specimen, the thinnest used, (shown as Δ) are systematically much higher than the mean value, and this displacement would be accounted for by an error of 8.5 μm in the thickness measurement. This is quite possible for a micrometer determination or a non-plane parallel specimen.

In the alternative technique, discussed in section 4.3.2, the order number m was plotted against the product $2d\tilde{\nu}_m$ for all the channel spectra of all the specimens. These are shown in figure 5.9 for both temperatures and it is apparent, especially for the low temperature results where five specimens were used, that for a given order number the product $2d\tilde{\nu}_m$ is approximately constant, as expected. The straight lines are the best fits to each data set found by a least-squares analysis and, in figure 5.9(a), the point most distant from the best fit, that at m = 2.5, is the 22 cm^{-1} point previously discussed. Equation 4.28 shows that if the material is non-dispersive the refractive index will be the gradient of the straight line through the measured points, and we therefore derive that

$$n_{293} = 2.586 \pm 0.022 \qquad \ldots (5.3)$$

and

$$n_{4.2} = 2.513 \pm 0.017 \qquad \ldots (5.4)$$

i.e. that in this analysis, using the same basic data as for the results 5.1 and 5.2, n has been determined with a random error of about 5 parts in 10^3, an order of magnitude smaller than the earlier method achieved. The differences between the two sets of values for the refractive indices are shown in

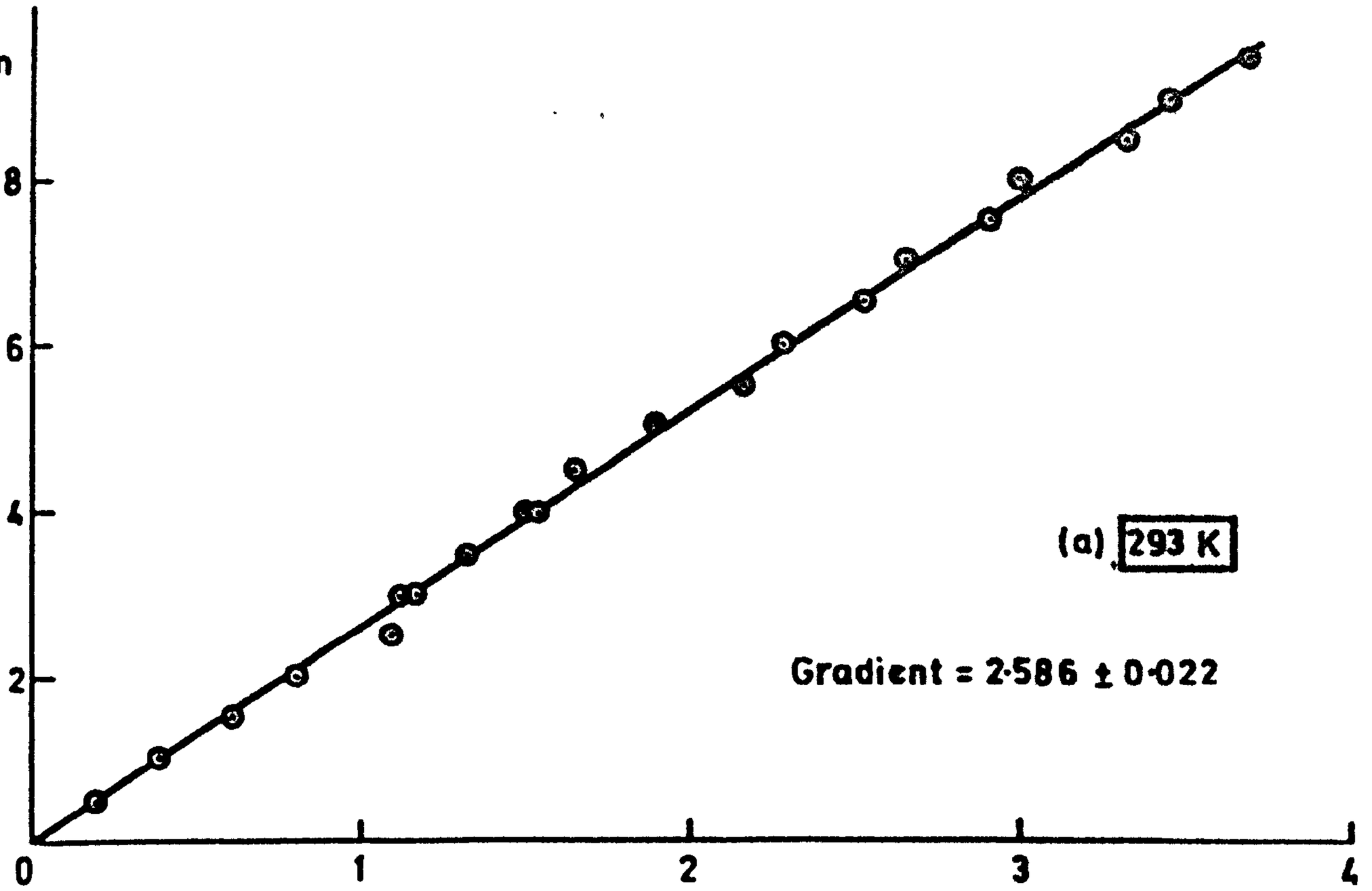

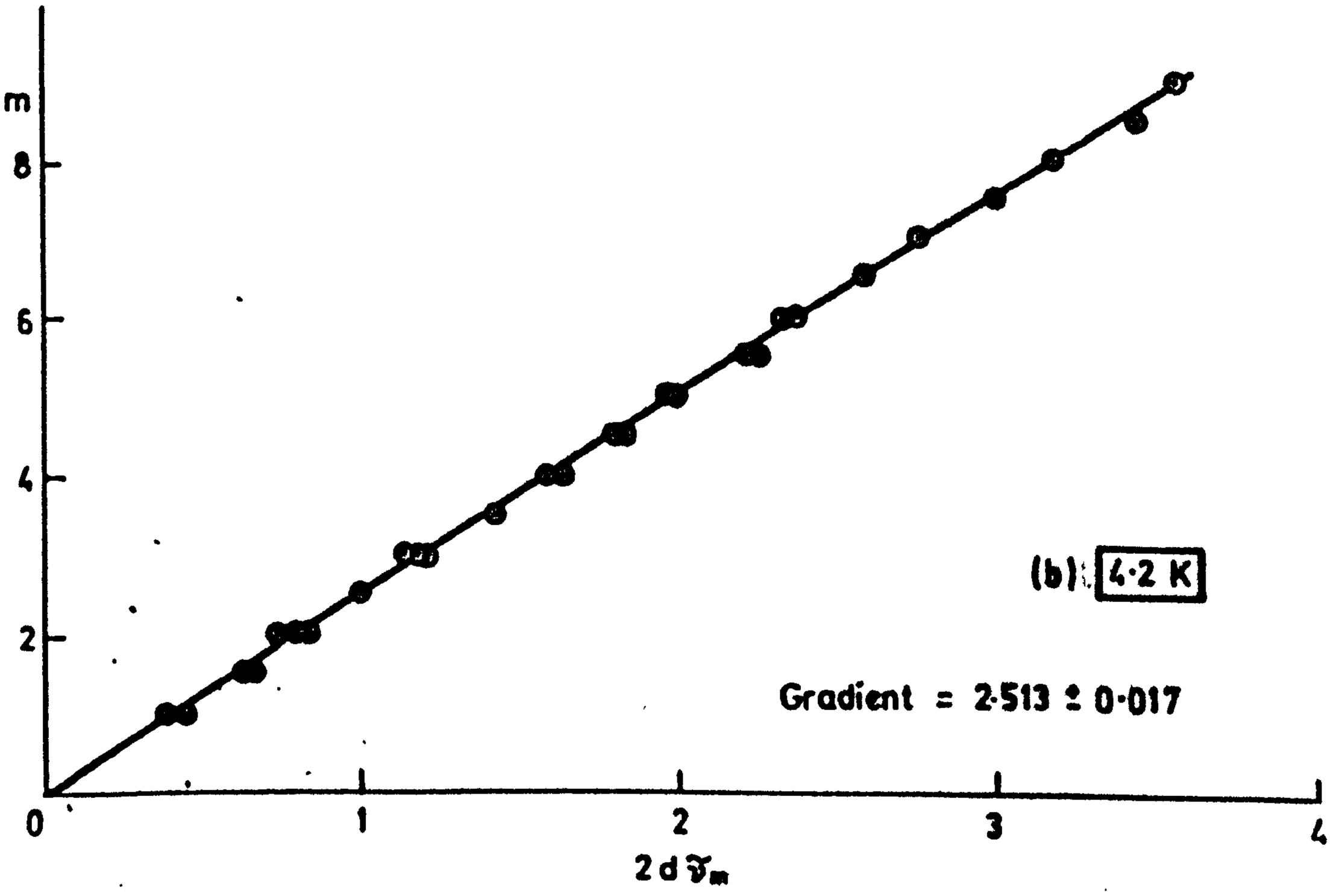

Fig.5.9. Channel spectrum order number m plotted against $2\tilde{\nu}_m d$ for both temperatures.

table 5.2. The value due to the arithmetic mean is lower for both temperatures than that given by the least-squares method by about 1.5% in addition to the difference in the level of the random errors. Although these differences are small, they are significant in comparison

Temp.(K)	n-mean	n-least squares	Difference*	%Difference+
293	2.544 ± 0.082	2.586 ± 0.022	0.042	1.6
4.2	2.477 ± 0.102	2.513 ± 0.017	0.036	1.4

Table 5.2 The differences between the refractive index values ascribed to the glass specimens by the two methods of analysis.
* least-squares minus mean
+ as a percentage of the least-squares value.

with dispersive measurements as these will have much smaller error limits.

In the following section it is shown that the least squares value is expected to be the more correct of the two. We have therefore used these to plot figure 5.10 showing the temperature variation of the mean refractive index between 4 and 40 cm^{-1}. The straight line is drawn between the 4.2 and 293K points to provide a qualitative indication of the variation only. The point at 77K, 2.52 ± 0.02, is from the measurements of Dianov et al[37] at 5 cm^{-1} and, within the limits of experimental error, agrees with the trend indicated by our measurements. Bagdade and Stolen[38] gave $n_{293} = 2.6$ between 10 and 45 cm^{-1}. This is within the error limits of the present measurements but, as it was derived from only three features in a channel spectrum, is considered liable to be in error.

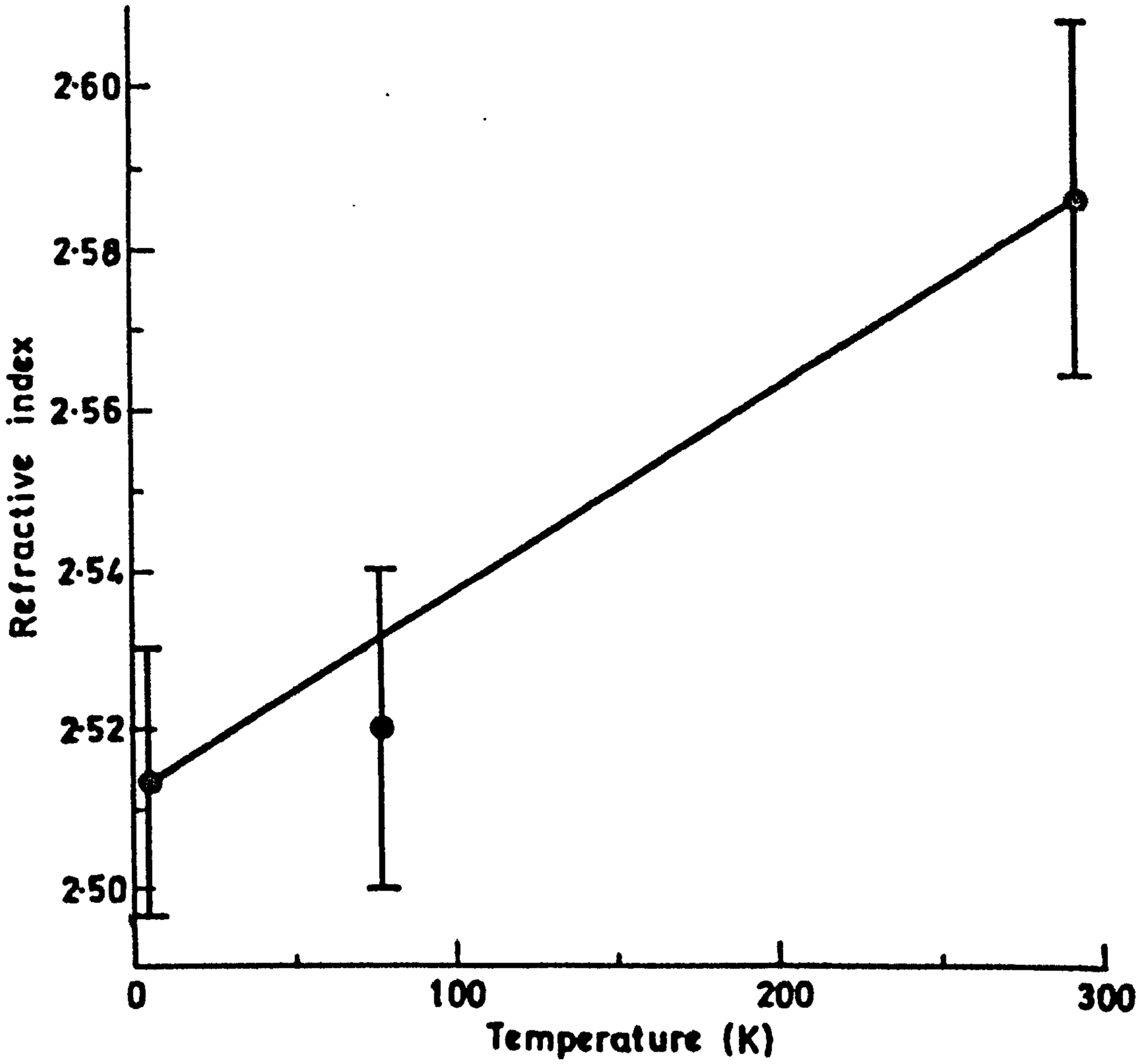

Fig.5.10. Temperature variation of the mean refractive index of soda lime silica glass between 4 and 40cm^{-1}.

5.5.3 THE DIFFERENCES BETWEEN THE TWO METHODS

The differences between the refractive index values determined from the same experimental data by the two methods arise from the different role played by error in the spectral position $\tilde{\nu}_m$. The refractive index values determined from N experimental observations would be

$$n_1 = \frac{1}{N} \sum_N \frac{m}{2d\tilde{\nu}_m} \quad \ldots (5.5)$$

for the mean-method, and

$$n_2 = \frac{\sum_N m}{\sum_N 2d\tilde{\nu}_m} \quad \ldots (5.6)$$

for the least-squares method. In deriving equation 5.6 it has been assumed that there is no error in m and that the best fit to the experimental data $(m, 2d\tilde{\nu}_m)$ passes through the point $(0,0)$[154]. In the absence of error in $\tilde{\nu}_m$ the two methods are equivalent and

$$n_1 = n_2 = n_o = \frac{m}{2d\tilde{\nu}_m} \quad \ldots (5.7)$$

where n_o is the true value of the refractive index. If, instead, there is an error Δ_m in the determination of $\tilde{\nu}_m$, the quantities

$$n_1' = \frac{1}{N} \sum_N \frac{m}{2d(\tilde{\nu}_m + \Delta_m)} \quad \ldots (5.8)$$

and

$$n_2' = \frac{\sum_N m}{\sum_N 2d(\tilde{\nu}_m + \Delta_m)} \quad \ldots (5.9)$$

are evaluated instead. In an experimental situation $\Delta_m/\tilde{\nu}_m$ would be less than unity and the difference between the evaluated and true value given by

the mean method can be expanded by the binomial theorem as

$$n_1' - n_o = \frac{n_o}{N} \sum_N \left\{ - \frac{\Delta_m}{\tilde{\nu}_m} + \left(\frac{\Delta_m}{\tilde{\nu}_m}\right)^2 - \left(\frac{\Delta_m}{\tilde{\nu}_m}\right)^3 + \left(\frac{\Delta_m}{\tilde{\nu}_m}\right)^4 \ldots \right\} \quad \ldots (5.10)$$

If sufficient specimens are used for there to be a number of data points in the region of $\tilde{\nu}_m$, and if Δ_m is normally distributed with zero mean, the terms in odd powers of $\Delta_m / \tilde{\nu}_m$ will tend to zero in the summation and 5.10 reduces to

$$n_1' - n_o = \frac{n_o}{N} \sum_N \left\{ \left(\frac{\Delta_m}{\tilde{\nu}_m}\right)^2 + \left(\frac{\Delta_m}{\tilde{\nu}_m}\right)^4 + \ldots . \right\} \quad \ldots (5.11)$$

which is positive. Thus, the use of the mean method to analyse the channel spectrum data from many specimens will lead to a value for the refractive index that is systematically high, although the normalising factor $^1/N$ will, in the limit of sufficiently large number of measurements, make this error vanishingly small.

In the least-squares method, however, the difference between the two values

$$n_2' - n_o = - n_o \frac{\sum_m m}{\sum_N \delta_m + \sum_N \Delta_m} \quad \ldots (5.12)$$

goes to zero if the error set Δ_m has zero mean. Therefore, it is to be expected that the use of the least-squares method leads to the 'best' value for the refractive index as the errors in $\tilde{\nu}_m$ tend to be self-compensating.

The much smaller random errors of the least-squares method as shown in table 5.2 indicate that the expected cancellation of errors for that method has taken place. The mean result, however, is lower in both temperatures than the least-squares result, contrary to the analysis. This could have arisen from the use of an insufficiently large number of specimens to fulfil the conditions of the analysis.

5.5.4 LOCATION OF THE LOCAL MAXIMA AND MINIMA

The maxima and minima of the channel spectrum do not usually coincide with the sampling comb generating the computed spectrum and $\tilde{\nu}_m$ is often found by visual inspection of the data. This can be difficult for a specimen whose period is only just within the resolution limit as the intensity varies rapidly over the few points defining the feature. This may be relatively unimportant to the least-squares method where such errors, if random, have been shown to be self-compensating, but for the mean method it is necessary to be certain that such errors are minimised. Ideally, one would interpolate in the computed spectrum using the instrumental line shape [62] to find the true turning points, but this can be time consuming. For some of our spectral data the visually determined values of the maxima and minima were compared with the corresponding values found by fitting a parabola to the three points defining the maximum or minimum. For the 1.305 mm specimen at 293K the standard deviation of the differences between the two data sets was $0.04 cm^{-1}$ and, as refractive index values the visually determined set gave 2.5807 ± 0.0475, while the numerically determined set gave 2.5804 ± 0.0521. The lack of any real significant difference between these values illustrates the generally found result that with real data the visual method of determining the spectral positions of the maxima and minima of the channel spectrum is as good a method of estimation as the numerical method. It seems likely that this is due to the presence of intensity noise in the spectral data, especially as in recent, more precise, measurements numerical interpolation has been found to give better results than visual estimation. Thus, in the determination of the complex refractive index of water vapour [155] use of the numerical interpolation procedure gave line centres in considerably better agreement with theoretical calculations than did visual estimation.

5.6 THE POWER ABSORPTION COEFFICIENT BELOW 50cm^{-1}

The power absorption coefficient of soda lime silica glass rises monotonically from the millimetre wavelength region into the submillimetre region, increasing by over three orders of magnitude between 10mm and 100 μm wavelength [156]. In this section, power transmission measurements on this rapidly increasing absorption edge, between 3 and 50cm^{-1}, at both 4.2 and 293K are used to give the power absorption coefficient and to illustrate some of the points of chapter 4 concerning the use of approximate expressions.

5.6.1 THE MILLIMETRE WAVELENGTH SPECTRUM AT 293K

In calculating a power absorption spectrum from a transmission spectrum using the approximate expressions 4.33, 4.36 or 4.37 it is implicitly assumed that the channel spectrum due to the internally reflected rays is not resolved. Thus, the millimetre wavelength absorption spectrum of glass could not be derived from the transmission spectra of the thin specimens shown in figures 5.5 and 5.6. Instead, measurements were made on three specimens of sufficient thickness that the first interference signature due to the internally reflected rays lay outside the range of recorded path differences. These specimens had thicknesses of 3.088, 5.82 and 6.16mm, and their attenuation was sufficiently great that even had the interference signature been recorded, the intensity resolution of the spectrometer would have been too coarse to resolve it.

The power transmission spectra of these specimens were measured between 3.5 and 12cm^{-1} at 293K using an interferometer with a 190μm (750g) beamdivider and a Rollin detector. The transmission spectra of the 3.088 and the 5.82mm specimens are shown in figure 5.11. Both specimens are fairly transparent at the lowest wavenumbers, but their transmissions fall

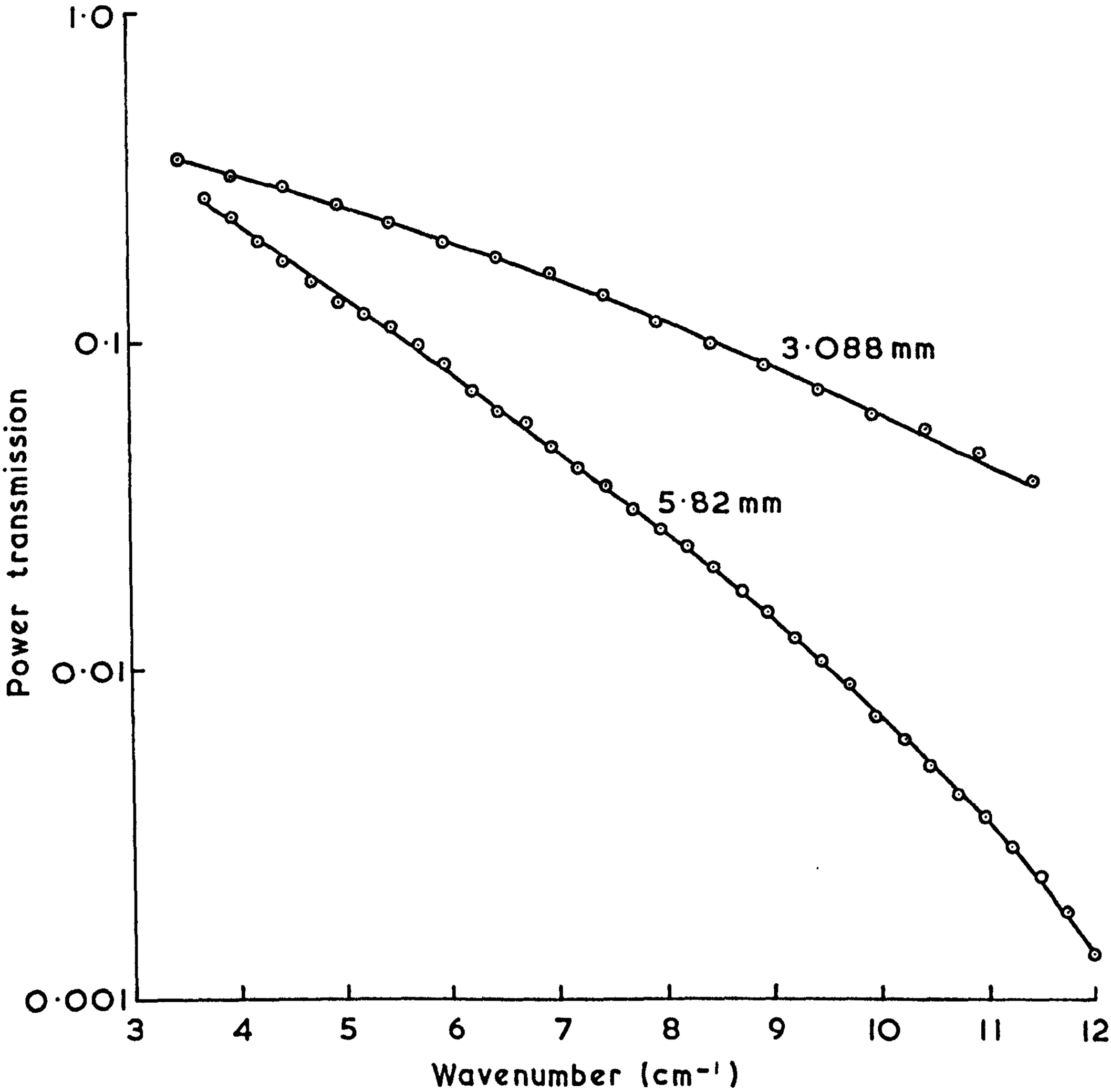

Fig.5.11. The power transmission spectra of two thicknesses of soda lime silica glass between 3 and 12cm^{-1} at 293K.

rapidly with increasing wavenumber and at $12cm^{-1}$ that of the thicker is nearly 10^{-3}. The curve for the 6.16mm specimen is not shown as it was, for all intents and purposes, indistinguishable from that of the 5.82mm one. The spectral resolution for the spectra of the two thicker specimens was $0.5cm^{-1}$, the thinnest $1.0cm^{-1}$, the difference only reflecting that the measurements were made at different times.

The power absorption coefficients corresponding to these measurements were calculated using the good approximation, equation 4.33, and the refractive index $n = 2.586$, derived in section 5.5.2. The three spectra are plotted in figure 5.12 and all show α rising from $1.5\ Np\ .cm^{-1}$ at $4cm^{-1}$ to just over $10\ Np\ .cm^{-1}$ at $12cm^{-1}$. Although very similar, the three spectra exhibit the following small differences:

(i) That of the 5.82mm specimen is systematically about $0.3\ Np\ .cm^{-1}$ greater than that of the 6.16mm specimen.

and, (ii) that of the 3.088mm specimen is greater than that of the 5.82mm specimen below $6cm^{-1}$, but identical above.

It is not possible, with such a limited set of specimens, to say whether or not these results are significant and due to compositional differences. The 6.16mm specimen, for instance, has considerably more CaO, but much less MgO and K_2O than the 5.82mm specimen, while the measurement on the 3.088mm specimen was made with a different interferometer and at a substantially different time to those of the thicker specimens. Therefore, for the purposes of the following sections of this chapter, these curves will be averaged to give the millimetre wavelength absorption spectrum.

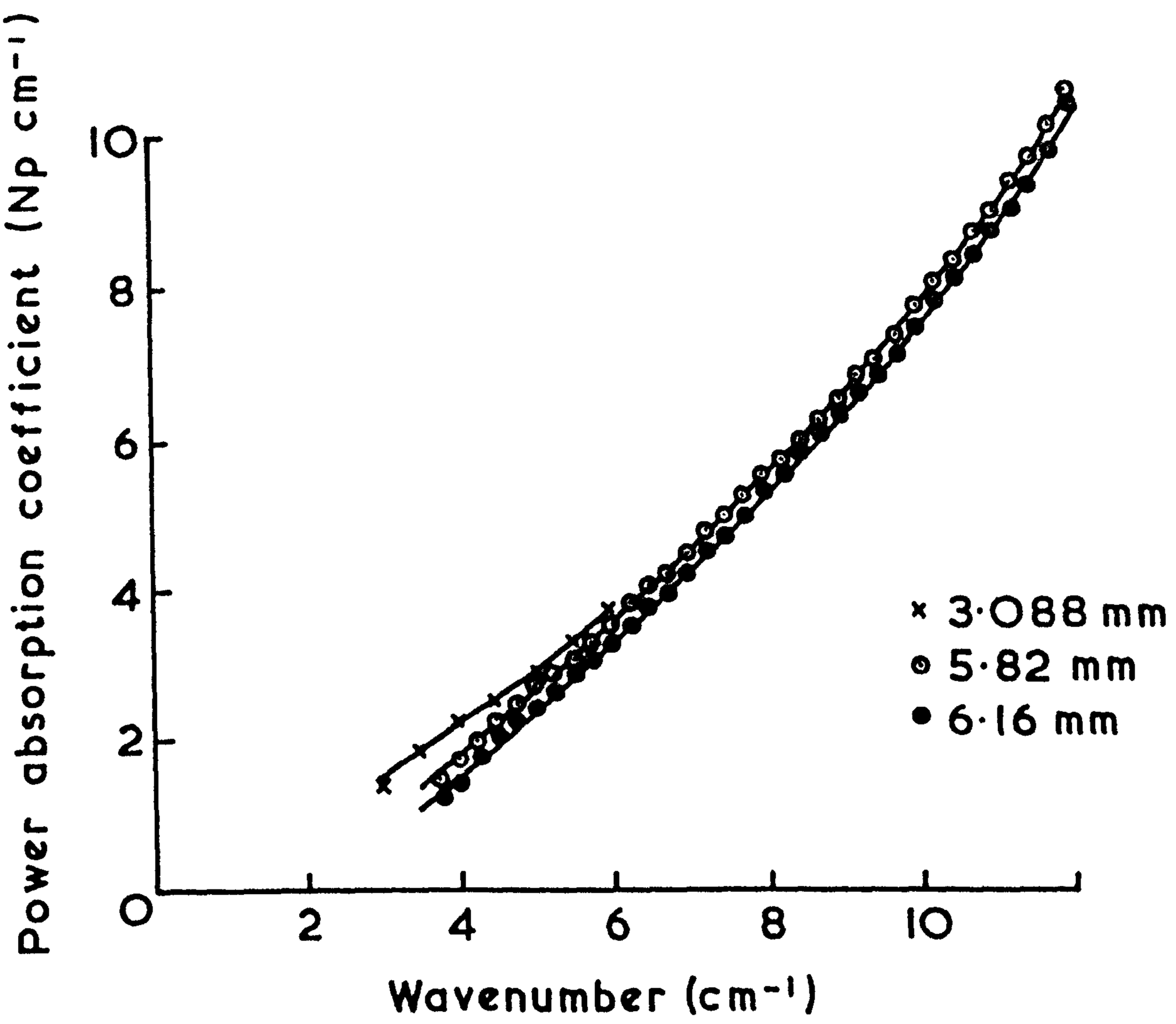

Fig.5.12. The absorption spectra of three specimens of soda lime silica glass between 3 and 12cm^{-1} at 293K.

At this stage it is possible to use the results of appendix 1 to investigate the systematic errors in the absorption spectrum arising from the use of equation 4.33, and to compare this with those that would have resulted from the use of either of the other two expressions, 4.36 or 4.37. This was done for the 5.82mm specimen with the results shown in figure 5.13. It shows the error in α plotted against the calculated α value for both expressions 4.33 and 4.36. The upper curve shows the error arising from the use of the good expression, 4.33. It is negligably small, being about 10^{-5} Np .cm^{-1} for calculated α values between 2 and 10cm^{-1}, but does increase with increasing α as the assumption, $\phi^r = \pi$, used in the derivation of 4.33 becomes less valid. As a comparison the lower curve shows the error in that would have arisen if the poor expression 4.36 had been used. In the transparent region the error is considerably greater, approaching 1% in the region of α = 2 Np .cm^{-1}, at the lowest wavenumbers. In precise dielectric measurements this could be significant and illustrates the need to avoid this expression. The error associated with this expression decreases with increasing absorption, as the approximation $1 \gg a^4 r^4$ becomes more valid. Between α = 7 and 8 Np .cm^{-1} this error curve changes sign and by 10 N .cm^{-1} is indistinguishable from that of equation 4.33. That there should be a change of sign is not obvious from the results of appendix 1 (see figure A1.2) as this only considers the errors associated with power transmissions greater than 0.1. The change of sign occurs for power transmissions less than 0.01.

The third approximate expression considered in appendix 1 used the two thickness method in which the transmission spectra of two different thickness specimens are ratioed and equation 4.37 used to give α. This form was used with the transmission spectra of the 3.088 and 5.82mm specimens and

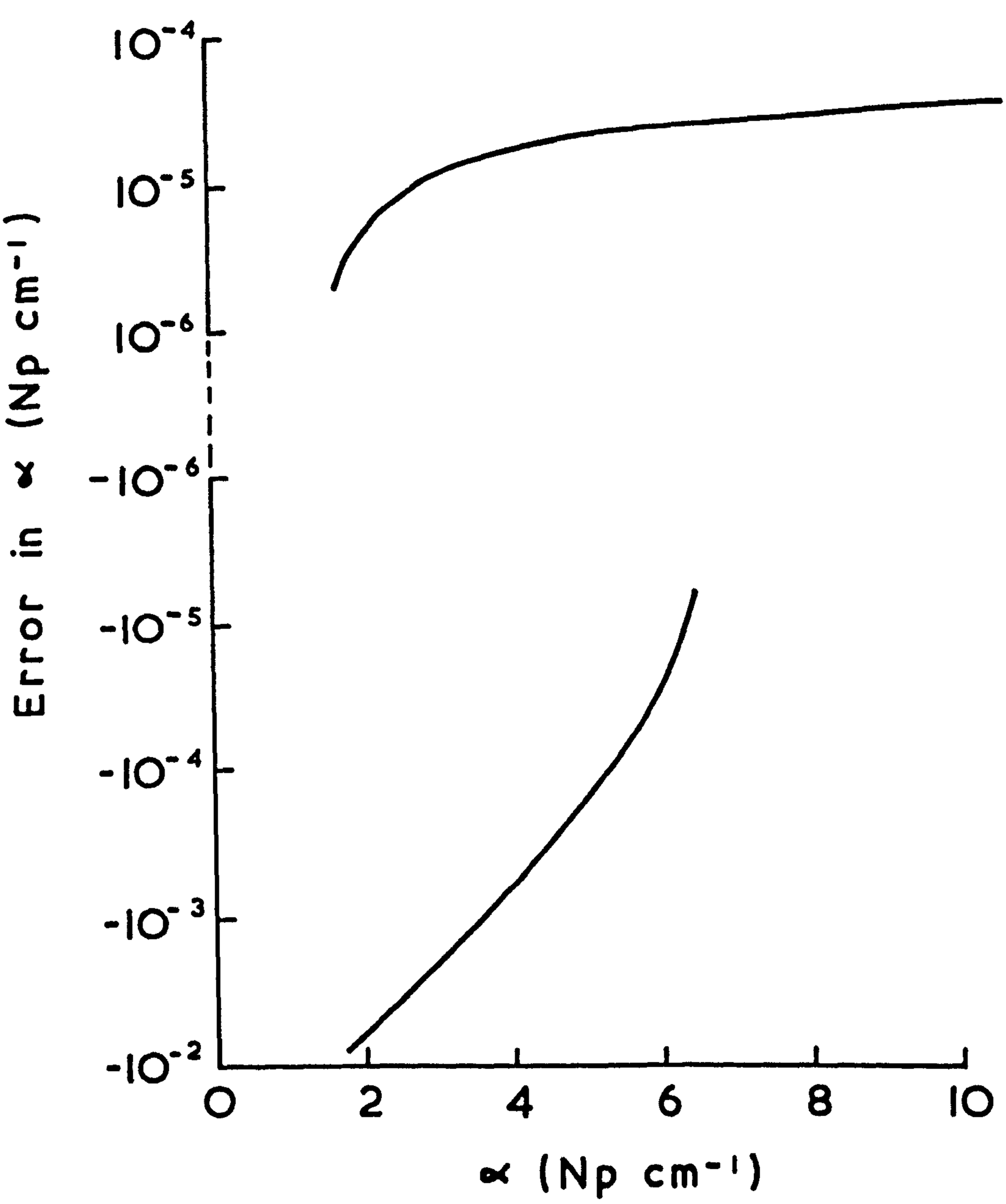

Fig.5.13. The systematic error in the calculated value of the absorption coefficient of the 5.82mm specimen arising from the use of the approximate expressions 4.33 (upper curve) and 4.36 (lower curve).

the result shown in figure 5.14. The circled points were calculated from equation 4.37, while the continuous curves are the individual absorption spectra of figure 5.12. These are somewhat smoothed but the scatter of their individual points about these curves is considerably less than the scatter on the two-thickness result. In the centre of the spectral range, where the signal-to-noise ratio is highest in the individual spectra, the two methods are in close agreement although not by as much as figure A1.4 would indicate as expected. At either end of the spectrum the two thickness result departs significantly from the other results, especially at low wavenumbers in the transparent region. The large scatter on the two-thickness results illustrates the susceptibility of this method to random error, in ratioing the two transmission spectra one introduces the random errors of both into the calculation.

5.6.2 THE SUBMILLIMETRE WAVELENGTH SPECTRUM AT 293 AND 4.2K

In the previous section the millimetre wavelength absorption spectrum of soda lime silica glass was derived from transmission measurements on specimens sufficiently thick for channel spectra not to be resolved. In this section measurements will be considered in the submillimetre wavelength region up to $50cm^{-1}$, where the rapidly increasing absorption necessitated the use of much thinner specimens ($<$ 1mm) and channel spectra were resolved. Thus, the transmission spectra of these specimens were dominated by interference effects at low wavenumbers and could only be used to calculate the absorption spectrum at higher wavenumbers where the absorption was sufficiently large to strongly attenuate the multiply reflected rays. Birch and Stone [157] have given an approximate guide to when this occurs in considering the application of the millimetre wavelength absorption in this glass to the problem of monitoring thickness changes in hot glass sheet on a production line. By

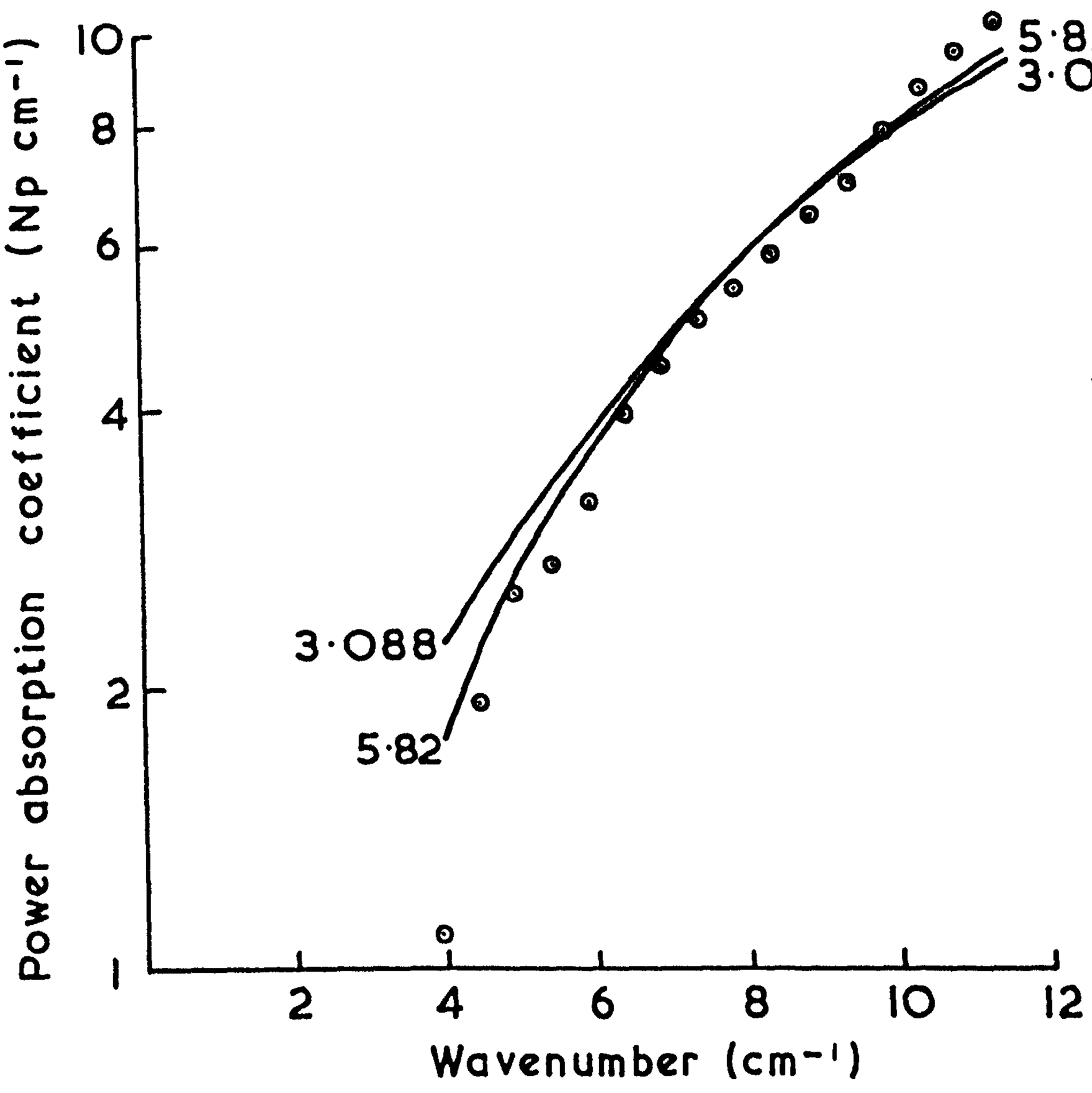

Fig.5.14. The result of using the two thickness method to determin the absorption coefficient. The plotted points represent the two thickness calculation, while the curves represent the individual absorption spectra of the two specimens used (taken from fig.5.12.).

considering the ratio of the total power transmitted through the specimen to that contributed by internal reflections they were able to show that

$$R^{-2} e^{2\alpha d} \gg 10^3 \qquad \ldots (5.13)$$

was the condition that the power in the channel spectrum be less than 0.1% of the total power transmitted. If we take this to mean that the channel spectrum is just too small to resolve we obtain the condition that for

$$\alpha d \gg 1.8 \qquad \ldots (5.14)$$

channel spectra would not be seen in glass specimens, for which n=2.586. This corresponds to a power transmission of about 0.11, and reference to figures 5.5 and 5.6 shows that this is so, below this transmission level the spectra of the four specimens illustrated are free from observable channel spectra.

With this restriction as a guide, power transmission measurements were made on seven specimens having thicknesses between 0.11 and 1.305mm at temperatures of 1.8, 4.2 and 293K. The specimens were chosen so that the small portion of the transmission spectrum of each that was free from channel spectra overlapped to give continuous spectral coverage between 10 and 50cm^{-1}. Rollin detectors were used throughout and, in common with the refractive index measurements, no difference was observed between the absorption spectra at 1.8 and 4.2K.

The power absorption spectra calculated from the transmission curves using equation 4.33 and the refractive index value appropriate to the temperature are shown for both temperatures in figure 5.15. Below 12cm^{-1} the millimetre wavelength results of the previous section have been added. Measurements were made on a few specimens thinner than 0.11mm in an attempt to

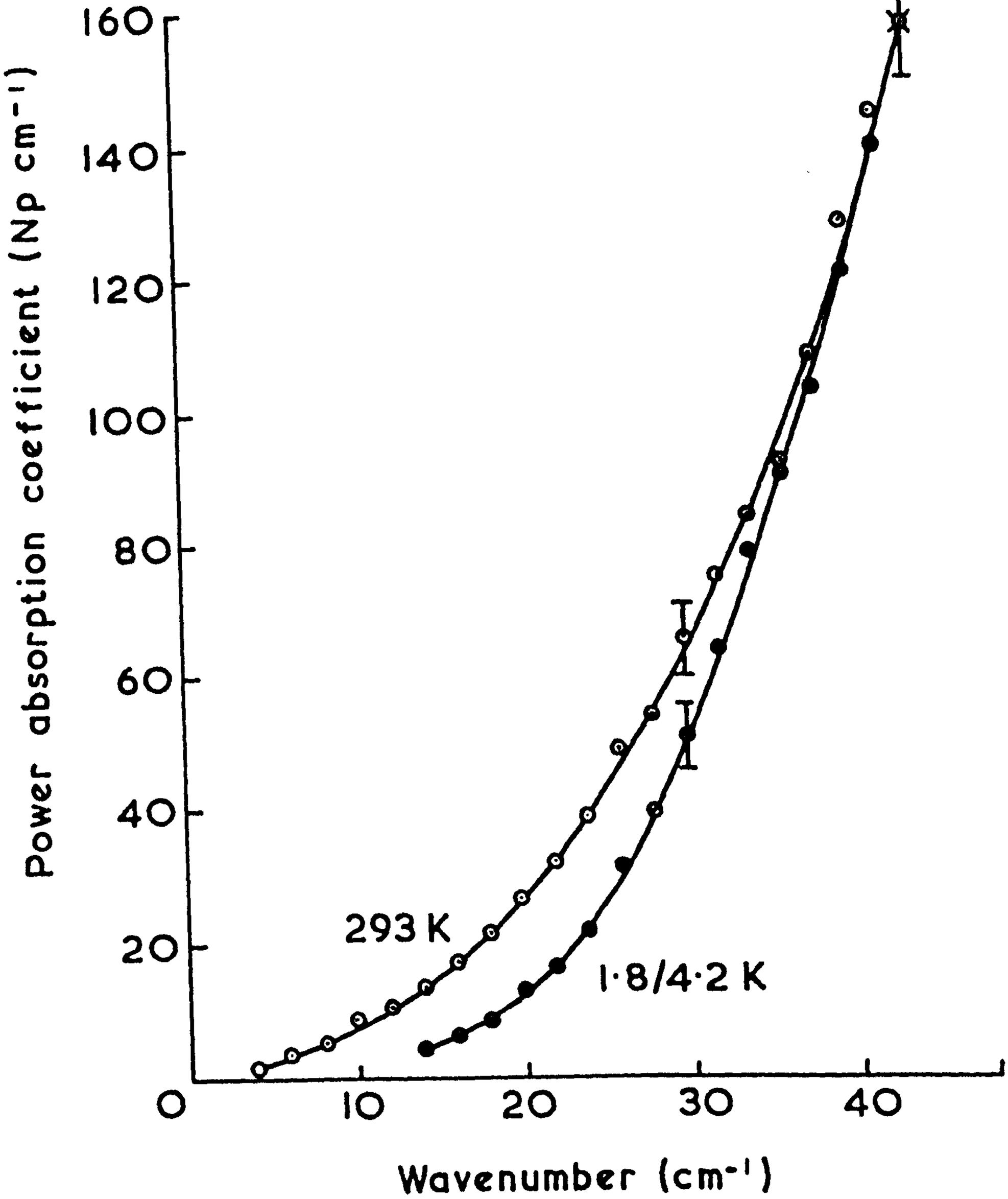

Fig.5.15. The absorption spectrum of soda lime silica glass below 45cm^{-1} at 4.2 and 293K.

extend the absorption measurements further towards the band centre, but these gave results which were inconsistent both with each other and those of the thicker specimens. In general it was found for solids that α values in excess of 150 N p .cm^{-1} could not be reliably measured by power transmission techniques. This appeared to be due to systematic effects such as an increasing uncertainty in thickness measurement, the difficulty in obtaining thin, plane parallel specimens and the increasing presence of the effects of intemally reflected rays. The level of random error may be judged from the error bars shown in figure 5.15, below 20cm^{-1} the random error is typically $\pm$ 0.5 N p .cm^{-1}, rising to $\pm$ 4 N p .cm^{-1} at 30 cm^{-1} and to $\pm$ 8N p .cm^{-1} by 45cm^{-1}.

In the region of 10cm^{-1} the absorption coefficient at liquid helium temperatures is nearly one-third of that at 293K while, by 40cm^{-1} both spectra have run together, showing the insensitivity of the peak absorption to temperature. With this strong wavenumber-dependence of α on temperature the apparent contradictions between the earlier results of Dianov et al[37], Bagdade and Stolen[38] and Hadni et al[35,36] described in section 5.3 are resolved. Thus, while the present results at 4.2K do not extend to 5cm^{-1}, it is apparent that the absorption coefficient at that wavenumber will be temperature dependent in agreement with Dianov et al[37]. At 34cm^{-1} the absorption coefficient decreases by 6 Np .cm^{-1} on cooling from 293 to 4.2K, while Bagdade and Stolen[38] found a decrease of about 3.4 N p .cm^{-1} on cooling from 293 to 107K, a reasonable agreement given the difference in temperatures. Finally, above 40cm^{-1} the absorption coefficient is insensitive to temperature, as found by Hadni et al[35,36]. The frequency dependence of this temperature variation is illustrated more clearly in figure 5.16 which shows in a qualitative manner the absorption index k as a function of temperature for various

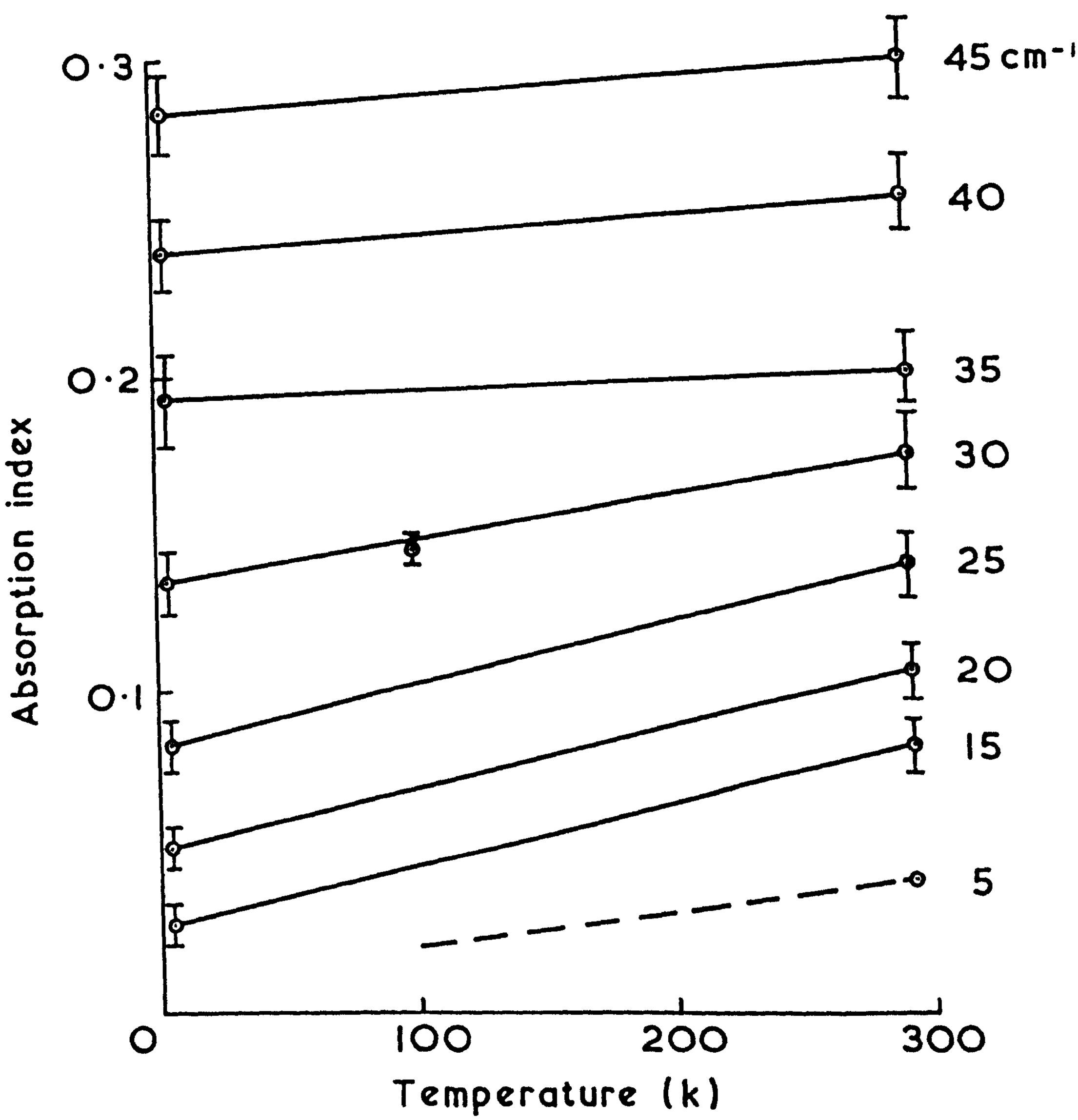

Fig.5.16. The temperature variation of the absorption index of soda lime silica glass at several wavenumbers.

wavenumbers shown on the right hand side of the figure. The straight lines merely join the two data points for each wavenumber and illustrate the strong temperature dependence at low wavenumbers. The dashed line represents the $5cm^{-1}$ measurements of Dianov et al[37] between 100 and 300K with which our single $5cm^{-1}$ point at 293K agrees well.

The slope of the straight line of Dianov et al shows good qualitative agreement with the trend of the present measurements. In order to verify further the nature of the frequency dependence of the temperature variation an independent determination of the power absorption coefficient was made at 100K using an HCN laser as a monochromatic source at $29.7cm^{-1}$*. The specimen (0.27mm) was mounted on a liquid nitrogen cooled finger in an evacuated chamber having melinex windows for the input and output laser beams. The specimen temperature was measured with a thermocouple varnished to its surface. The optical and data handling system for this measurement system have been described in relation to its use in submillimetre wavelength power measurements[80,159]. The absorption coefficient calculated from the result of this measurement is the single point at 100K plotted in figure 5.16. Within the resolution of the broad band results it can be considered to be at 30 cm^{-1} and, within experimental error, indicates that at $30cm^{-1}$ the absorption index increases linearly with temperature between 4.2 and 293K.

Recently Sievers and co-workers[160,161] have investigated in detail the temperature variation of the absorption spectrum below $10cm^{-1}$ of several amorphous dielectrics including soda-lime-silica glass. Previous microwave,

---

* This measurement was kindly performed by Mr N.R.Cross of the Division of Electrical Science, NPL, to whom the author is grateful.

thermal and ultrasonic measurements at low temperatures [162-167] had indicated that anomalous low frequency modes occur in amorphous materials. Sievers verified this, showing that with decreasing temperature the long wavelength absorption of most glasses passes through a minimum at a temperature of about 8K. In particular, for soda lime silica glass this occurred at 9.5K. [161] Sievers was able to interpret his experimental data in terms of a thermal population effect associated with a three energy level system. The difference between the absorption spectra at 1.8 and 4.2K seen by Sievers was small and only resolved because of the extreme sensitivity of his measurement system which used a He^3-cooled bolometer and specimens several centimetres or more thick. It is therefore not surprising that in this work no difference was observed between the absorption spectra at 1.8 and 4.2K. More recently Bösch [234] has made extensive low temperature measurements similar to those of Sievers and has shown that the model proposed by Sievers cannot explain the very low temperature variation of the absorption coefficient. Bösch suggests that the measurements are more correctly described by a statistical distribution of localised two-level tunnelling systems.

5.6.3 THE FUNCTIONAL FORM OF THE ABSORPTION SPECTRUM

Vinogradov [151] and Schlömann [152] have both considered the effect of a disordered charge distribution on the dielectric loss of ionic crystals, with the theory of Schlömann being more general than that of Vinogradov as the former assumes that the charge deviations at different lattice sites are correlated. Amorphous glasses may be considered as an extreme limit of a disordered ionic crystal and, if the charges are assumed to contribute independently to the dielectric loss, the two theories are equivalent and predict that the power absorption coefficient at long wavelengths should vary as the square

of the frequency, or wavenumber. Bagdade and Stolen[38] first observed this wavenumber-squared dependence in soda lime silica glass at 293K between 10 and 45cm^{-1} and in fused silica at the same temperature between 30 and 80cm^{-1}, but found that fused silica departed significantly from this behaviour below 30cm^{-1}, and attributed this to the onset of correlation between the charge deviations.

In order to investigate the functional form of the wavenumber dependence of the present absorption data a least-squares analysis was used to fit straight lines to the data expressed in the form $\log\alpha - \log\tilde{\nu}$. This led to the following functions being found as the best representation of the experimental data at the two temperatures,

$$\alpha_{293} = 0.0412\ \tilde{\nu}^{2.169} \qquad \ldots (5.15)$$

and,

$$\alpha_{4.2} = 0.000142\ \tilde{\nu}^{3.042} \qquad \ldots (5.16)$$

The room temperature data therefore appear to deviate slightly from the wavenumber-squared dependence previously found but, when allowance is made for the error bars associated with each point, it is apparent that the wavenumber-squared dependence applies within the limits of experimental error. This is illustrated in figure 5.17 which shows the absorption spectra at both temperatures plotted on a log-log scale. The dashed lines are the best fits described by equations 5.15 and 5.16, while the continuous lines represent, for 293 and 4.2K, functions having wavenumber-squared and wavenumber-cubed dependences. Both functions were normalised to pass through the 30cm^{-1} experimental point. Thus, above 14cm^{-1} a $\tilde{\nu}^2$-form describes the 293K absorption spectrum within the limits of experimental

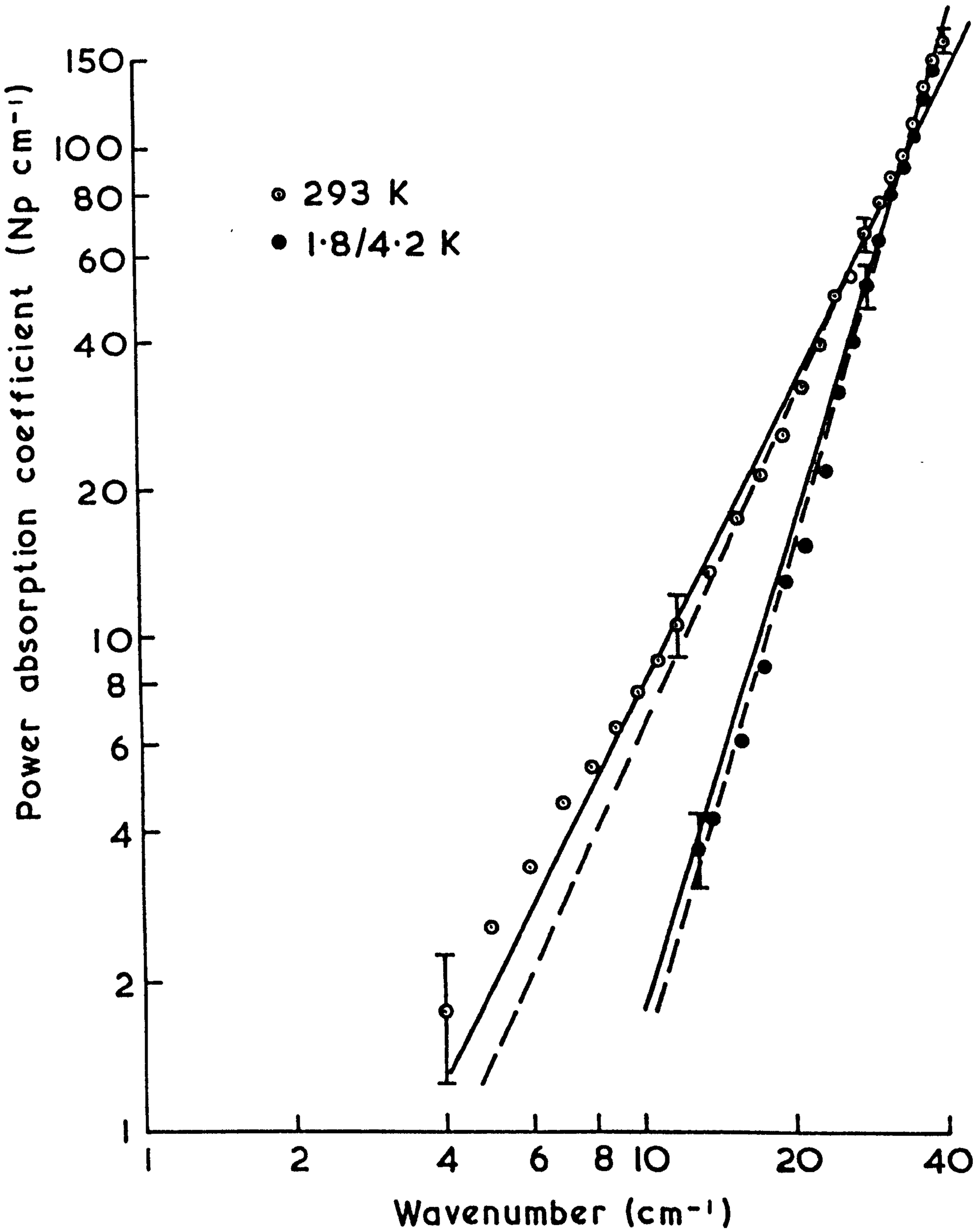

Fig.5.17. Log-log plot of the absorption spectrum of soda lime silica glass at 4.2 and 293K. The dashed lines represent the best fit to each data set found from a least-squares fit to the logarithms of the data. The continuous straight lines represent a wavenumber-squared and a wavenumber-cubed dependence of α for the 293 and the 4.2K spectra, respectively.

error, and a $\tilde{\nu}^3$-form similarly describes the 4.2K results. Below 14cm^{-1} the 293K measurements rise systematically above the $\tilde{\nu}^2$-form.

5.6.4 NUMERICAL SUPPRESSION OF THE EFFECTS OF THE CHANNEL SPECTRUM

The expressions developed for the derivation of an absorption spectrum from a transmission spectrum require the absence of a channel spectrum, and the results of section 5.6.2 showed that this limited the spectral range accessible to study with a particular specimen. In an attempt to remove this restriction an iterative method of analysis was developed to allow for the presence of the channel spectrum and thus extend the accessible spectral range.

The basic equation of the technique is 4.6 for the power transmission of a lamella specimen which, for the present purpose, is written in the form

$$\alpha = \frac{1}{d} \ln\left[\frac{a^{-2}}{T_L^m} \cdot \frac{r^{-2} + r^2 - 2\cos 2\phi^r}{(ar)^{-2} + (ar)^2 - 2\cos 2(\phi^r + \phi^a)}\right] \quad \ldots (5.17)$$

where T_L^m has been written in place of T_L appearing in equation 4.6 to emphasise that 5.17 is to be used to calculate α from measured (m) values of T_L. This equation may not be solved directly for α from the measured T_L^m spectrum as α is a parameter of every term except ϕ^a appearing on the right hand side. The following procedure may, however, be used to give an iterative solution. Firstly, the channel spectrum period is used to give a refractive index value, which allows an approximate power reflection coefficient, r^2 (equation 4.60), to be calculated. This allows an initial power absorption coefficient to be calculated.

$$\alpha_o = \frac{1}{d} \ln\left[\frac{(1 - r^2)^2}{T_L^m}\right] \quad \ldots (5.18)$$

completely ignoring internally reflected rays. A better value of r^2 can now be calculated using the Fresnel equation, 2.33, as are the phases ϕ^r and ϕ^a. All are substituted into 5.17, and a new absorption coefficient α_1, calculated. The whole process can then be repeated until the α values converge to within the desired accuracy. That the α -values should converge is apparent from the following discussion. Equation 5.17 may be rewritten as

$$\alpha = \frac{1}{d} \ln\left[a^{-2} \cdot \frac{T_L}{T_L{}^m} \right] \qquad \ldots (5.19)$$

substituting in for T_L, the calculated value of the lamella reflectivity, from equation 4.6. If α, the real part of the complex propagation factor is given its functional form, equation 2.46, then the values of α calculated on the $(n-1)^{th}$ and n^{th} iterations are related by

$$\alpha_n = \alpha_{n-1} + \frac{1}{d} \ln\left[\frac{T_L(n-1)}{T_L^m} \right] \qquad \ldots (5.20)$$

where $T_L(n-1)$ indicates that T_L has been calculated from α_{n-1}. Now, if the measured quantity T_L^m is truly described by equation 4.6, the following will hold:

(i) if α_{n-1} is smaller than the real value of α, $T_L(n-1)$ will be larger than T_L^m and $\alpha_n > \alpha_{n-1}$

(ii) if α_{n-1} is larger than the real value of α, $T_L(n-1)$ will be smaller than T_L^m and $\alpha_n < \alpha_{n-1}$

Therefore, with sufficient iterations, the calculated absorption coefficient

should converge onto the real value of α , that for which

$$T_L(n-1) = T_L^m \qquad \ldots (5.21)$$

The extent to which this analysis is successful in suppressing channel spectra can be seen from the following examples in which it has been applied to the room temperature transmission spectra of two of the glasses studied in this chapter. These were the 1.305mm specimen whose transmission spectrum is presented in figure 5.5, and the 0.215mm specimen whose 4.2 and 293K transmission spectra are shown in figure 5.6. The spectra were subjected to ten iterations of the above analysis, the results of which are summarised in figure 5.18 (a) and (b). These show, for each specimen, three separate power absorption spectra. The smooth curve rising monotonically with wavenumber represents the 'true' power absorption spectrum shown in figure 5.15. This provides the standard against which the results of this analysis will be judged. The continuous curves with periodic structure are the absorption spectra calculated after ten iterations, and the dotted curves are the absorption spectra computed from the measured transmission without any allowance for the effects of the internally reflected rays.

Where the transmission level falls below about 0.15 the iterated spectra of both specimens are in good agreement with the standard spectrum. Thus, above $25cm^{-1}$ for the 0.215mm specimen and $13cm^{-1}$ for the 1.305mm specimen the iterated and standard spectra are indistinguishable. This is expected behaviour, and not remarkable; in section 5.6.2 it was shown that for power transmissions of about 0.11 in glasses the effects of the internally reflected rays would be heavily suppressed. At lower wavenumbers, as the specimens become more transparent, the iterated solutions become

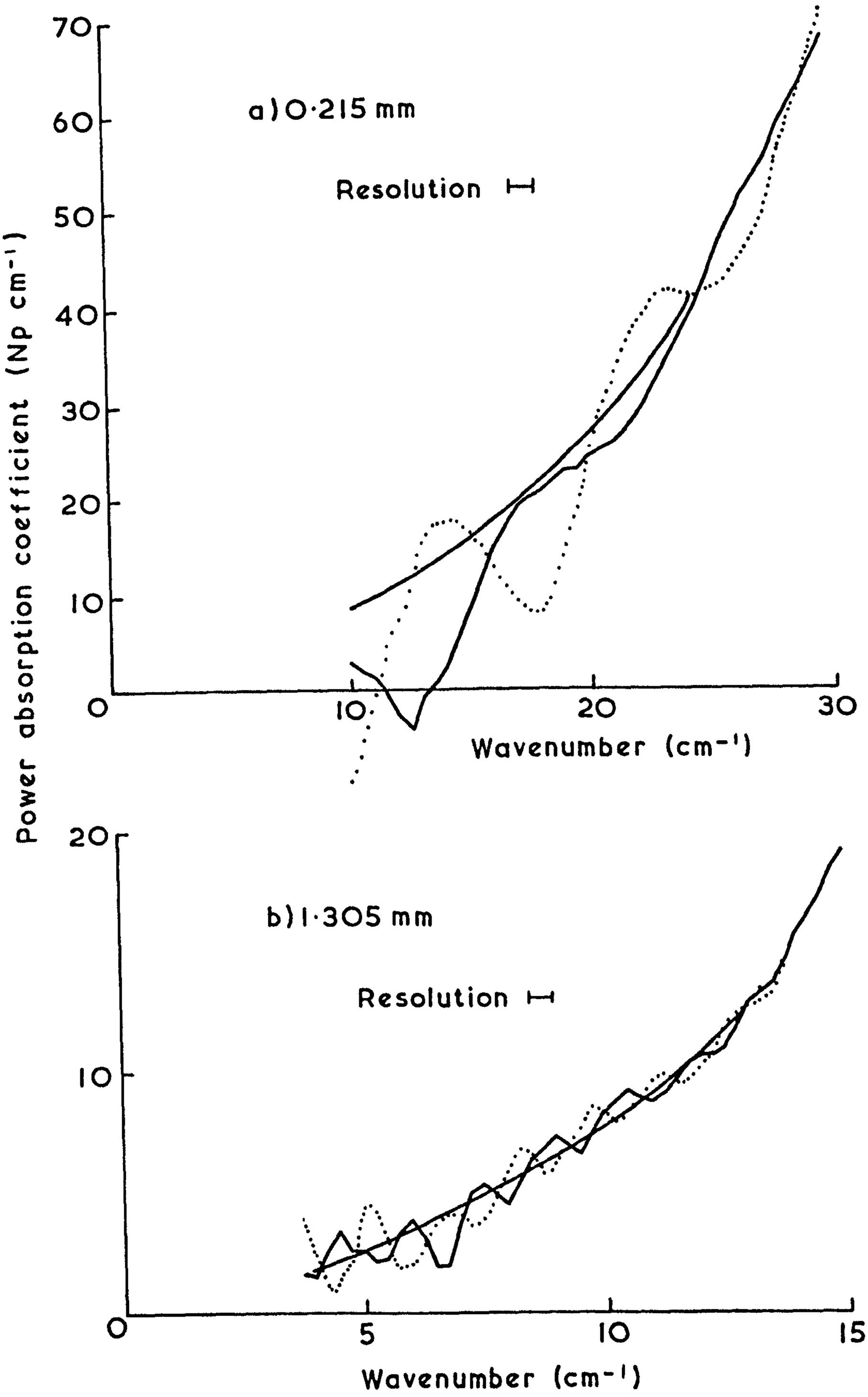

Fig.5.18. The absorption spectra of the 0.215 and 1.305mm specimens calculated with allowance made for channel spectra. The smooth curve is the 'true' spectrum from fig.5.15, the dotted curve is the spectrum calculated with no allowance made for the channel spectrum, the continuous curve is the spectrum calculated after ten iterations of the procedure described in the text.

increasingly oscillatory. In spite of this, the iterated solutions are in better agreement with the standard spectra than are the uncorrected spectra, that of the 0.215mm specimen showing fair agreement down to 17cm^{-1}. In both cases the iterated spectra are out of phase with the uncorrected spectra, having local maxima in the place of minima and vice versa.

Although ten iterations were used in the derivation of the results of figure 5.18 the iterated spectra converge more rapidly than this, as shown in figure 5.19. The two plots show the computed α value after each iteration for these specimens. Figure 5.19 (a) is for the 0.215mm specimen at 18cm^{-1} and 5.19 (b) for the 1.305mm specimen at 6.5cm^{-1}. Both wavenumbers correspond to prominent local maxima in transmission, but the results were typical of the entire spectral range. The α value for the thinner specimen converged on its final value in an oscillatory manner, whereas that of the thicker specimen converged from the same side, but both have effectively reached their final values by the fifth iteration.

The effect of an error in the refractive index or thickness was investigated and it was found that varying either by up to $\pm$ 10% did not lead to greatly improved or degraded solutions, the analysis being fairly insensitive to these parameters. In general, the solution for the thinner of the two specimens appears better than that for the thicker, and it is assumed that this is because the period of channel spectrum in the latter case was much closer to the spectral resolution than in the former. Therefore, although the measured transmission of both specimens is more correctly respresented as the convolution of T_L with the instrumental line shape of the spectrometer, the approximation of this to T_L is more valid for the thinner of the two.

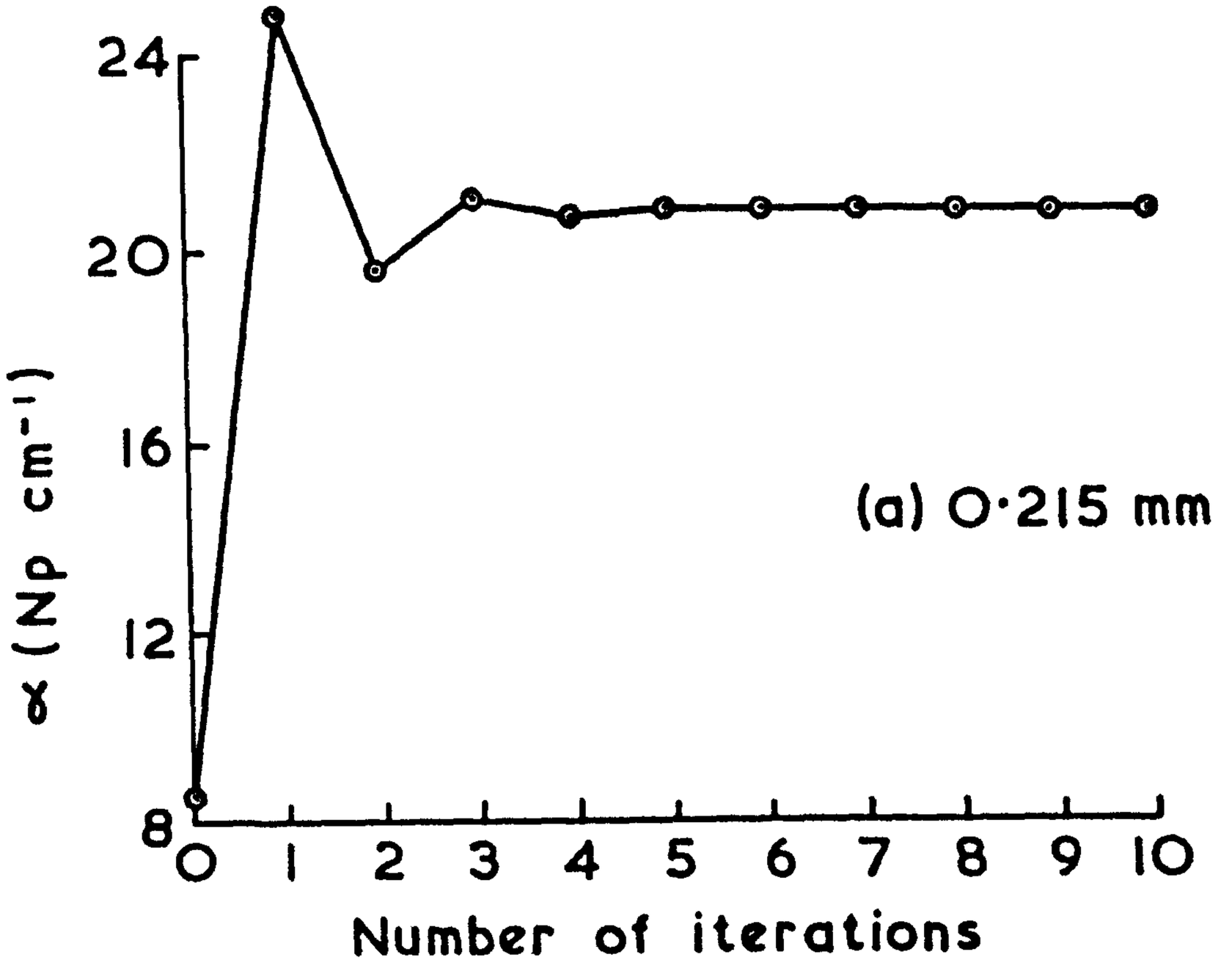

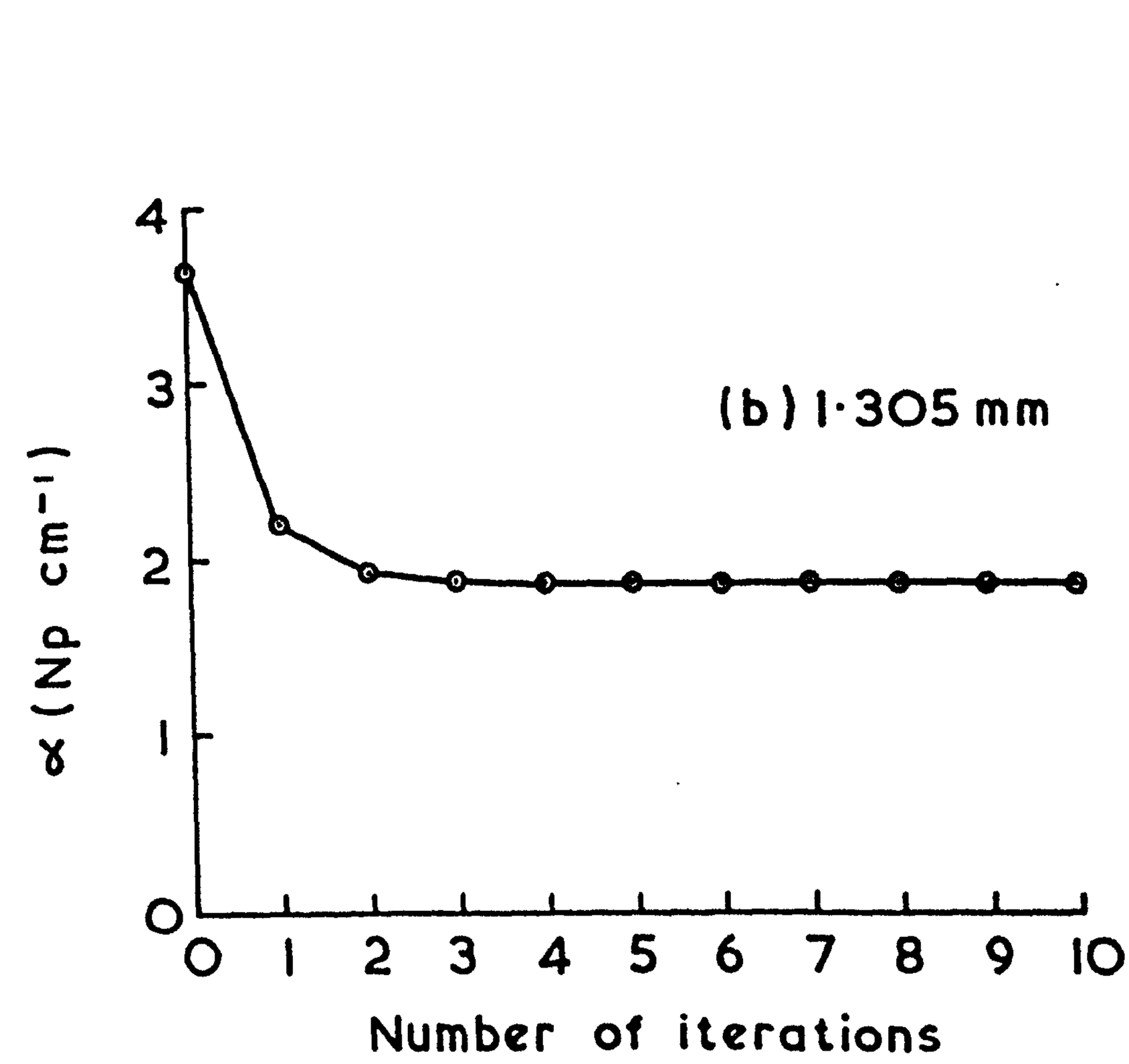

Fig.5.19. Illustrating the convergence of the iterative procedure for calculating the absorption coefficient with allowance made for the effects of channel spectra.

In conclusion one can say that although this technique does lessen the effect of the channel spectrum its general applicability will not be wide as it is not always effective. In particular, it requires the channel spectrum to be well resolved to minimise effects due to the instrumental line shape of the spectrometer, and the suppression does not appear to work well in regions of high transmission and low absorption. It is also based on the assumption that equation 4.6 for the lamella transmission truly represents the measured quantity, which is not necessarily so. However, in regions of medium to high absorption the α spectrum derived from this technique will be more nearly correct than if a correction for the channel spectrum had not been made, but in general it would not be considered sufficiently accurate for precise work.

5.7 MID-INFRARED MEASUREMENTS, 1300-4000cm^{-1}

In order to more fully characterise the extent of the region of intense absorption mid-infrared power transmission measurements were made on its short wavelength absorption edge using four thin specimens of thicknesses 0.148, 0.1991, 0.2735, and 1.310mm. The measurements were made at a resolution of 1cm^{-1} and a temperature of 290K using a Perkin Elmer model 180 double-beam spectrophotometer to cover the region from 1000 to 4000cm^{-1}*, and two of the spectra so obtained are shown in figure 5.20. The spectrum of the thicker specimen (0.1991mm) shows the general nature of the absorption in the short wavelength wing. There is a gradual edge between 1800 and 2400cm^{-1} as transparency is regained, with broad shallow absorption features apparent between 1400 and 1800cm^{-1}, and 2500 and 3500cm^{-1}. There is

---

* The transmission measurements were performed by Mr D.J.Harrison of the Division of Chemical Standards, NPL.

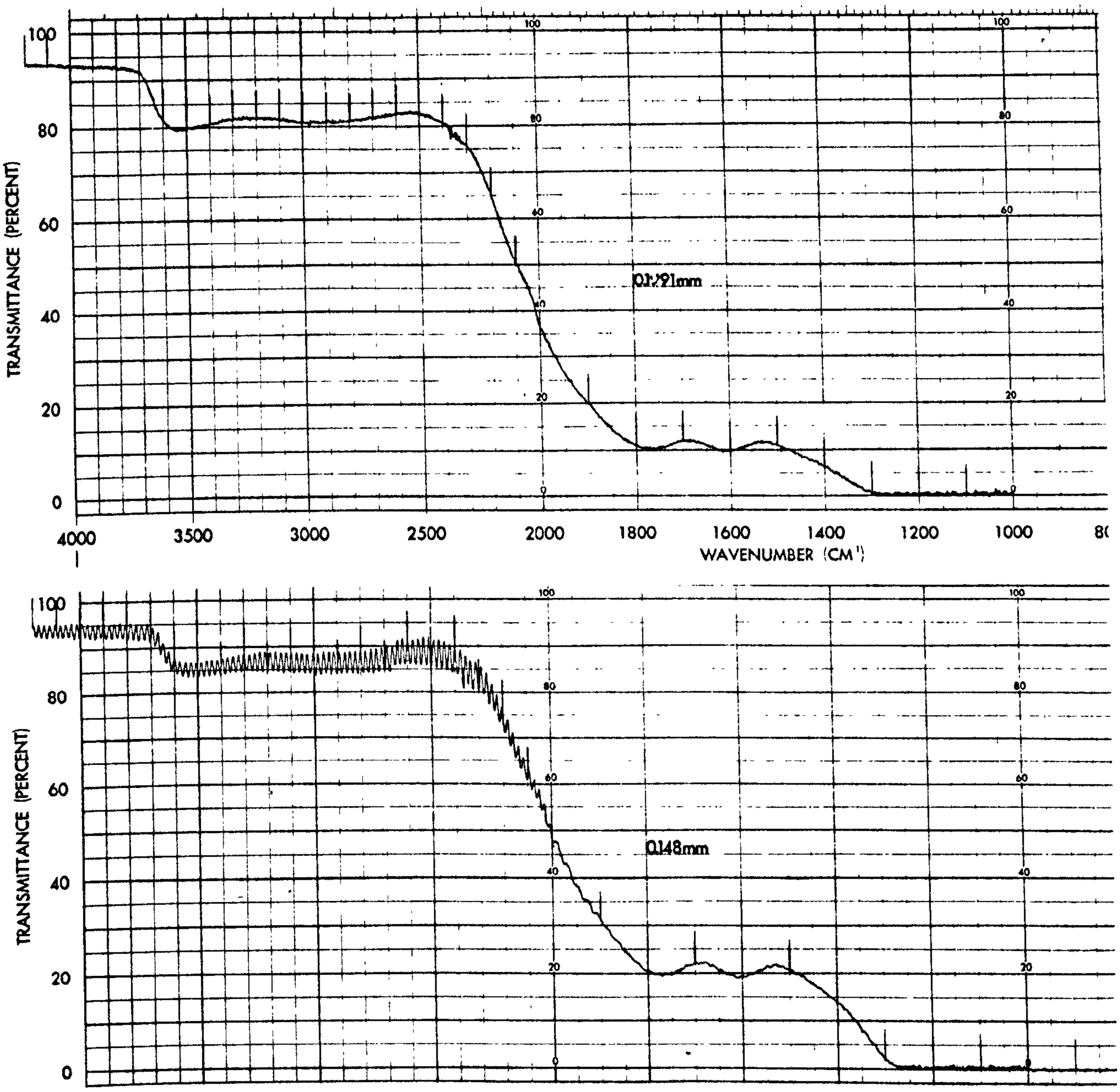

Fig.5.20. The power transmission spectra of two specimens of soda lime silica glass between 1000 and 4000cm^{-1} at 290K.

also a second, relatively sharp, edge between 3600 and 3700cm^{-1} where the glass becomes very transparent, reaching power transmission levels of about 0.93. The general features of the transmission spectrum of the thinner specimen (0.148mm) are similar to those of the thicker specimen, with the addition of a channel spectrum, due to interference between internally reflected rays, being apparent between 2000 and 4000cm^{-1}. The period of the channel spectrum varies somewhat, but is of the order of 20cm^{-1}. Both spectra show small features between 2300 and 2400cm^{-1} that are due to the presence of $C0_2$ in the spectrophotometer.

The period of channel spectrum of the thin specimen was analysed to give the refractive index spectrum shown in figure 5.21. As it was not possible to determine the order number of the local interference maxima and minima this spectrum will not contain any component of the refractive index that is linearly dependent on wavelength, as pointed out by Moss[109]. However, this is not too serious a problem as the main purpose of this spectrum in this work is to allow the power absorption coefficient to be calculated from the transmission spectra of the other specimens. Thus, unless such a linear term were particularly large, its absence will not grossly effect the calculated absorption coefficient, especially in the regions of large absorption. The results of Ellis et al[42], Blain and Douglas[168] and Crozier and Douglas[169] indicate that the overall level of these measurements is approximately correct.

The power absorption coefficients calculated from the measured transmission spectra of the three thicker specimens are shown in figure 5.22 from 1300 to 4000cm^{-1}. The spectra of the individual specimens are all slightly different from each other, mainly in terms of their overall level, but, in general terms they are very similar with the absorption coefficient falling from about

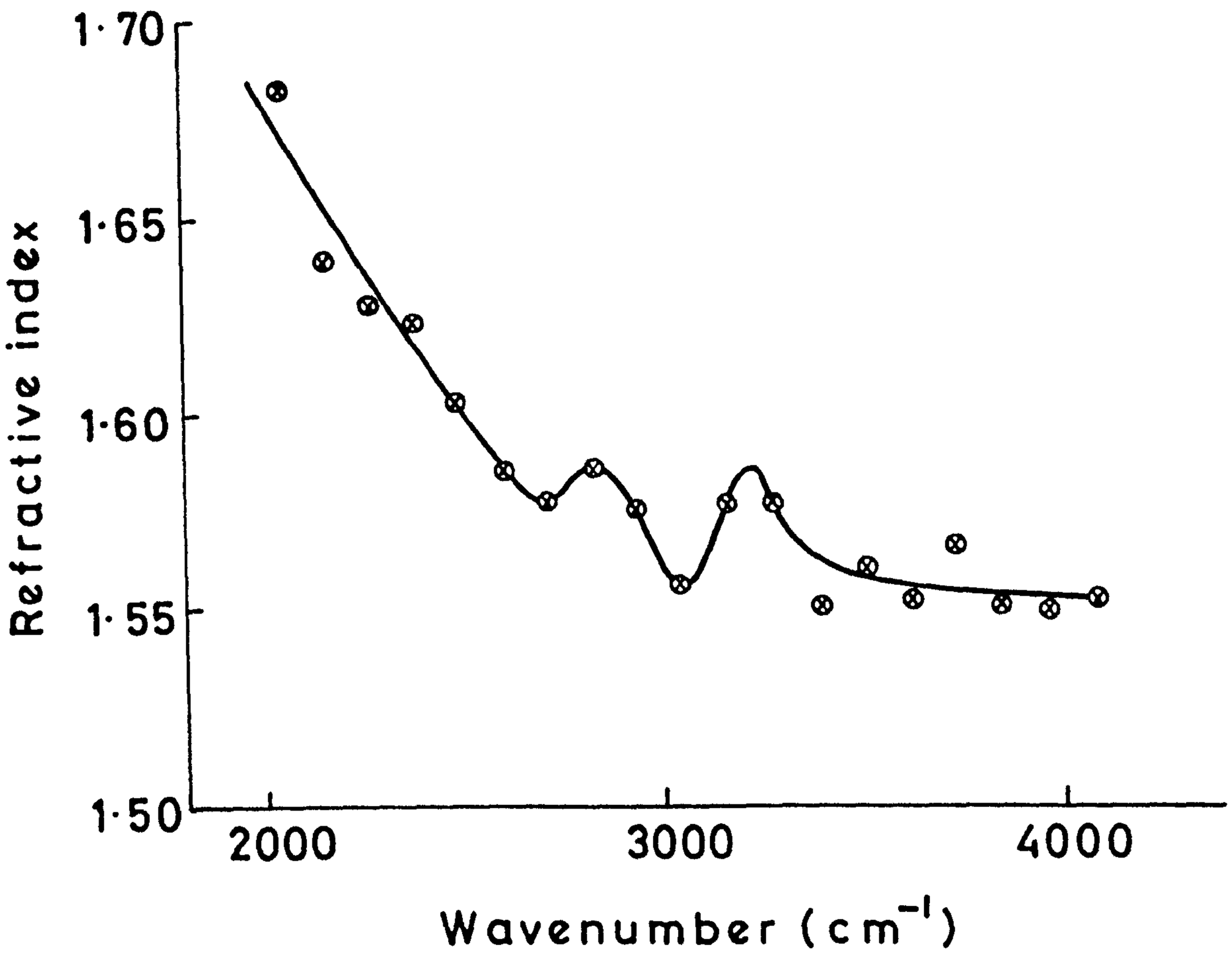

Fig.5.21. The refractive index spectrum of the 0.148mm specimen of soda lime silica glass between 2000 and 4000cm^{-1} at 290K.

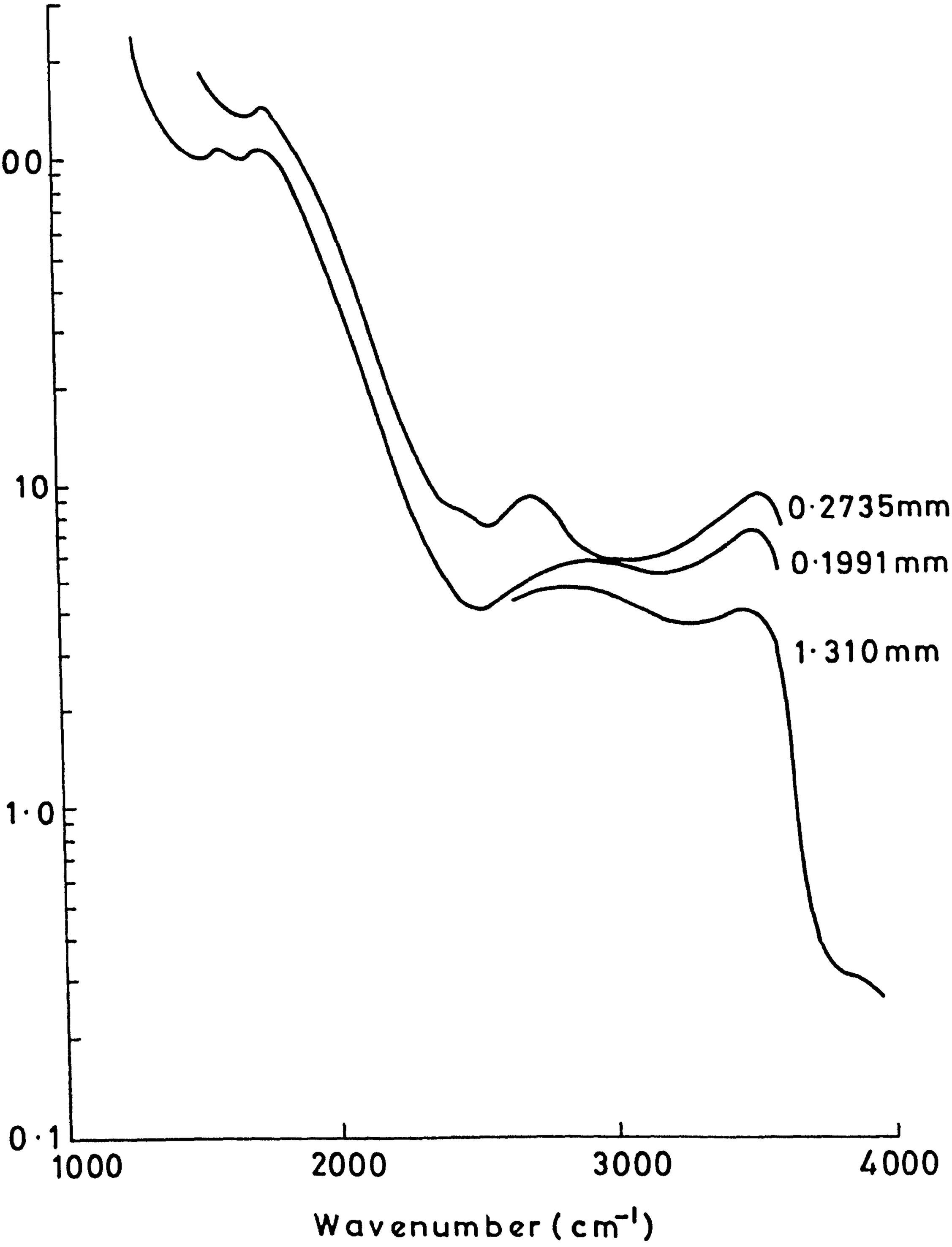

Fig.5.22. The power absorption spectra of three specimens of soda lime silica glass between 1300 and 4000cm^{-1} at 290K.

200 Np .cm^{-1} at 1300cm^{-1} to a plateau region of between 5 and 9 Np .cm^{-1} from 2500 to 3600cm^{-1}, and then decreasing rapidly to below 1 Np .cm^{-1}. Absorption maxima are apparent at 1600, 1800, ~ 2800 and 3500cm^{-1}, and the refraction spectrum of figure 5.21 shows the dispersion associated with the 2800 and 3500cm^{-1} regions. It is well known that the contamination of glasses by water during the manufacturing process leads to near-infrared absorption bands due to the hydroxyl group, OH.[32] The precise frequency and intensity of these appear to depend on the composition and history of the glass and, for compositions similar to those of the present specimens, Adams[170] has identified OH bands at 2857 and 3401cm^{-1}. Thus it appears reasonable to assign the features observed in the present spectra at ~2800 and 3500cm^{-1} to the same bands. Although the lower wavenumber features at 1600 and 1800cm^{-1} have been observed in the published spectra of similar glasses[40]. There does not appear to have been any assignments made of them.

5.8 CONCLUSIONS

The results of this chapter on the absorption and refraction spectra of soda lime silica glass from 3.5 to 50cm^{-1} at both 293 and 4.2K represent the first systematic investigation of the optical constants of this system at these wavelengths. The submillimetre wavelength absorption spectrum was found to change from having a wavenumber-squared dependence at 293K to a wavenumber-cubed one at 4.2K. Earlier measurements[35-38] on the temperature variation of the absorption had appeared somewhat contradictory, but the strong wavenumber-dependence of the temperature variation found in this work showed that the earlier measurements were, in fact, consistent with each other. The mean refractive index over the millimetre and submillimetre wave-

length regions was shown to fall from 2.586 to 2.513 on cooling from 293 to 4.2K, and comparison with an earlier measurement [37] at 77K indicated that the temperature variation was linear within experimental error.

In deriving these absorption and refraction spectra from the measured transmission spectra of the various specimens the approximate methods described in sections 4.3.2 and 4.3.3 were compared and estimates made of the errors introduced by each method. The preferred methods were the 'good' expression for the power absorption coefficient, equation 4.33, derived by assuming that the channel spectrum was not resolved, as this was shown to cause systematic errors of less than $\pm$ 1 in 10^4, and the method of least-squares fitting for the refractive index described by equation 4.28, as this was shown to lead to a low systematic error.

CHAPTER 6

DISPERSIVE TRANSMISSION MEASUREMENTS

6.1 INTRODUCTION

Dispersive Fourier Transform spectrometry is a broad band technique for the direct determination of the optical constants of a material at millimetre and submillimetre wavelengths. It uses a two beam interferometer, usually of the Michelson type, with the specimen to be studied placed in one of the beams rather than both as for conventional Fourier Transform spectrometry. This asymmetry is the important feature of the technique, leading to its sensitivity to the phase of the interaction between the electromagnetic field and the specimen. In the conventional technique the phase shift caused by the specimen is present in both beams of the interferometer and consequently does not, to first order, affect the intensity delay pattern produced at the exit aperture of the interferometer. Thus, only the power attenuation of the specimen is measured. When, however, the specimen is in one beam its refractive index causes the delay pattern to become asymmetric and shifted in path difference, and both the attenuation and the phase shift caused by the specimen may be recovered from the recorded intensity delay pattern, allowing the optical constants to be calculated. The asymmetry of the method gives rise to its alternative name, asymmetric Fourier Transform spectrometry. It is necessarily a broad band method as the uniquely bright interference fringe of broad band interferograms allows the phase shift caused by the specimen to be found unambiguously. Monochromatic measurements in this configuration have been made using a 0.337 μm wavelength HCN laser [186,187], but these were not Fourier transform measurements as the path difference variation was obtained by changing the length of the light path through the specimen, and the refractive index found by fringe counting.

The first measurements reported using these dispersive techniques were of the real refractive index of crystal quartz parallel to its optic axis between 20 and 55 cm^{-1}, published by Chamberlain, Gibbs and Gebbie[20] in 1963. Their measurements achieved a reproducibility of about $\pm$ 0.01, or one part in 10^2, although it is apparent from their results that much of this scatter is due to systematic differences between independent determinations, an error that is now understood and largely suppressed by the improved experimental technique described in section 6.3 of this chapter. These authors did not attempt to derive the absorption index from their measurements, being more interested at that time in the new information provided by the new technique*. Recent dispersive measurements on the same material[171], in which the real refractive index was determined with a precision of one part in 10^4, illustrate the improvement in measurement techniques that have occurred in the first fifteen years of dispersive Fourier Transform spectrometry.

In a dispersive transmission measurement there are two optical configurations that may be used. If the specimen is reasonably transparent it can be measured in a double pass configuration in which the radiation in the specimen arm passes through the specimen twice. The measurements of Chamberlain and co-workers on polymeric materials[21,88,172-174] used instruments of this type. If, however, the specimen is fairly absorbing it can be measured in a single pass configuration in which the radiation in the specimen arm passes through the specimen only once. The measurements of Bell and co-workers on crystal quartz[175], sapphire[176], KBr[177] and KI[188] were made with instruments of this type. Parker et al[189] have recently described a similar instrument which has been used to study specimens at temperatures down to 77K. These two configurations, single and double pass, are shown

---

* J.E.Gibbs, private communication.

schematically in figure 6.1 and, although all the measurements reported in this chapter were obtained from a double pass interferometer, we shall briefly describe in section 6.6 a single pass interferometer which is presently being developed.

6.2 THE INTERFEROMETER

The optical configuration of the dispersive interferometer used for the double pass measurements is shown in figure 6.2. The only difference between it and the basic cube interferometer of figure 3.2 described in section 3.4.1 is that the arms have been lengthened so that a specimen holder module could be inserted into the fixed mirror arm. The holder essentially consists of a rectangular plate with two 40mm diameter apertures in it and by operation of a slide mechanism it can be positioned so that either aperture is centrally located with regard to the optic axis of the arm. Specimens larger than 40mm diameter are laid over one of the apertures and held in place by a light spring clip. If smaller specimens are to be studied, circular plates with smaller apertures in them are clipped over each 40mm aperture and the specimen mounted over one of these. The unobscured aperture is used for the reference measurement and the specimen-reference change-over is performed from outside the vacuum space of the interferometer. All the main outer surfaces of the interferometer have copper cooling coils bolted to them. These are supplied with water from a constant temperature bath and, as well as stabilising the temperature of the interferometer, allow the temperature of the specimen to be varied between about 280 and 300K

6.2.1 PHASE NOISE

The extra information provided by a dispersive measurement in comparison with a non-dispersive one is the phase shift due to the specimen. Therefore,

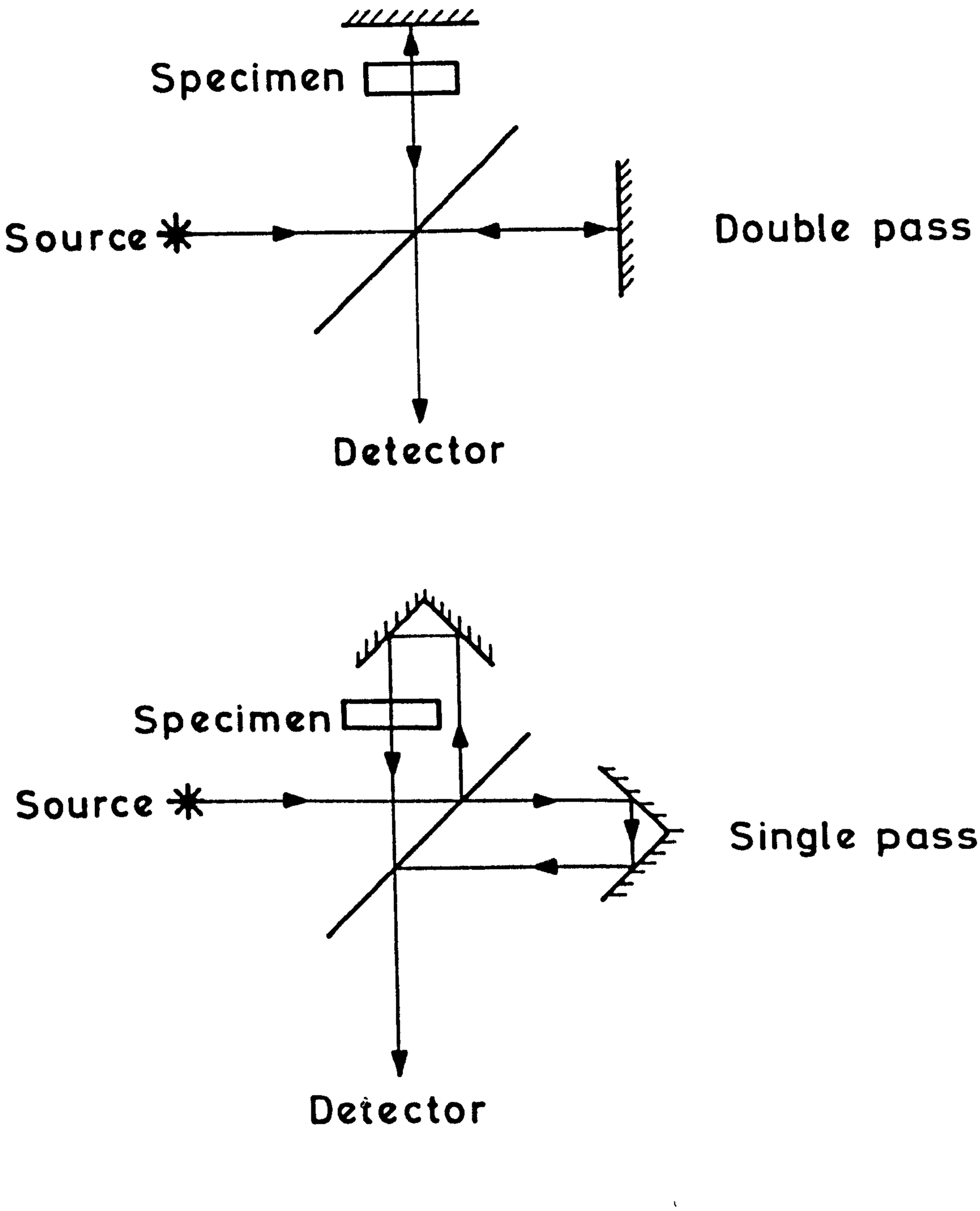

Fig.6.1. The two interferometer configurations that can be used for transmission dispersive Fourier transform spectrometry.

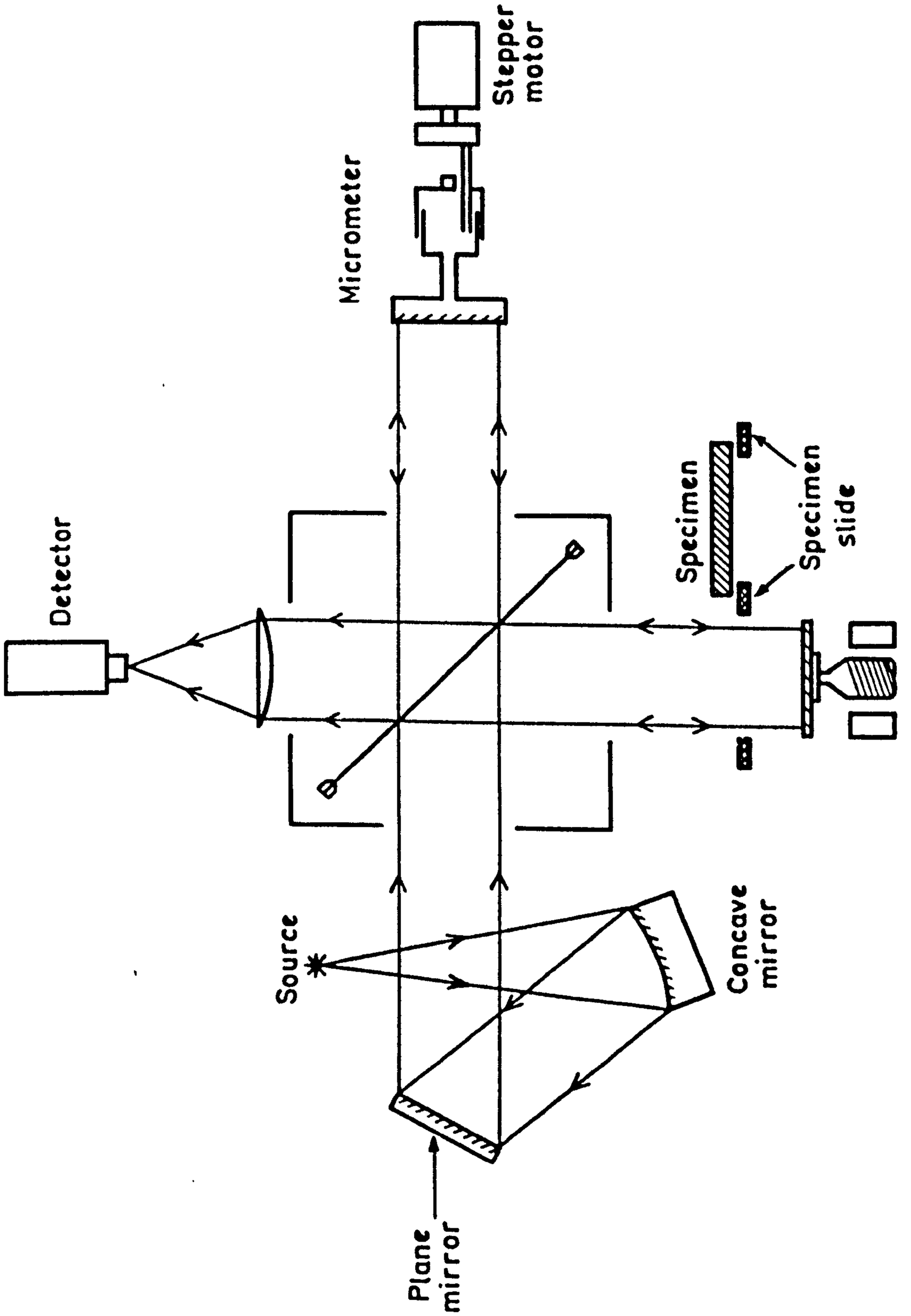

Fig.6.2. The optical configuration of the dispersive transmission interferometer.

the performance of the interferometer in providing the complex refractive index will be limited by the effects of noise, both random and systematic, in the determination of the phase shift. In this section the typical magnitude of the random noise in the phase spectrum below 40cm^{-1} is discussed and it isshown that, for most cases of practical interest, random phase noise is not the limiting factor in the determination of the refractive index.

The random noise in the modulus spectra obtained with this interferometer is similar to that described for the non-dispersive instrument in section 5.2.1, as the extra path length introduced by the specimen module has little effect on the power levels reaching the detector.

The upper graph in figure 6.3 shows a typical phase spectrum obtained from this interferometer between 10 and 40cm^{-1} using a liquid helium cooled Rollin detector. The beamdivider was 50μm thick and the spectral resolution 1.8cm^{-1}. The phase tends to $\pi/2$ radians at low wavenumbers, as one would expect for a phase modulated system but, instead of being constant, increases more-or-less linearly with wavenumber. This is because the point used for the origin of computation did not coincide with the position of zero path difference for the recorded interferogram. This is of no consequence as the effects of it disappear when the refractive index spectrum is calculated. The level of random noise in this spectrum is apparent from the lower graph which shows the difference between it and a similar spectrum obtained independently. Over most of the useful spectral range the random noise is less than $\pm$ 4 milliradians, and remains less than $\pm$ 10 milliradians between 9 and 43cm^{-1}.

In order to be able to assess whether-or-not this level of random phase noise will be significant in the calculated value of the refractive index it is necessary

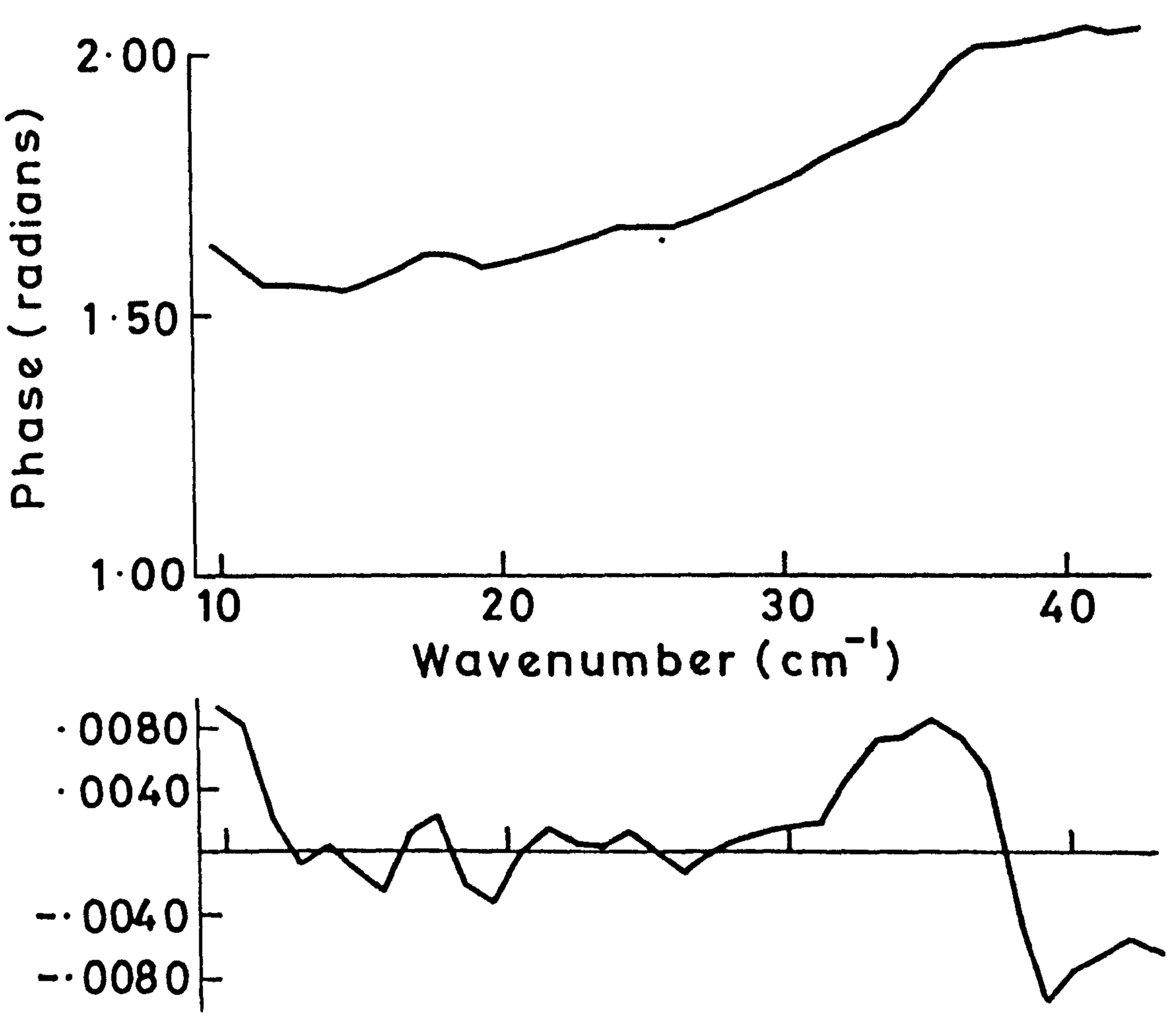

Fig.6.3. Illustrating the level of random noise present in the phase spectrum obtained from the interferometer of fig.6.2 in the spectral region below 40cm^{-1}.

to develop further equation 4.59 which was shown in section 4.4.2 to give a good approximation to the true value of the real refractive index. In practice this equation is not used in the form in which it is written. The optical thickness of the specimen is generally considerably greater than that of the vacuum which it replaces and this causes the main interference signature to be substantially shifted to positive path difference as discussed in section 4.4.1. Thus, in the Fourier transformation of the specimen interferogram it is usual to shift the origin of computation from the position of zero geometric path difference by an amount $\bar{x}$ in path difference so that it coincides with the centre of this displaced fringe. Under these circumstances the first approximation to the refractive index is calculated from

$$n_o = 1 + \frac{\Delta'_t}{4\pi\tilde{\nu}d} + \frac{\bar{x}}{2d} \qquad \ldots (6.1)$$

instead of equation 4.59. In this Δ_t now represents the difference of the phase spectra of the specimen and reference interferograms referred to the different origins. It is apparent that the term $1 + \bar{x}/2d$ in this equation represents the mean level of the refractive index over the spectral region of the measurements, while the term in Δ'_t represents the dispersion across that region. For real solids $\bar{x}/2d$ will therefore usually be greater than 0.5. If we assume a specimen thickness of 1mm the random error generated in the computed value of n_o by our typical random phase noise of $\pm$ 4 milliradians would be $\pm$ 3×10^{-4} at $10cm^{-1}$ decreasing to $\pm$ 3×10^{-5} at $100cm^{-1}$. In terms of a minimum refractive index of 1.5 these figures correspond to errors of less than 5 parts in 10^5 and are not at all significant in comparison with the systematic error that arises from the determination of the specimen thickness, d.

At numerically lower resolutions of between 0.1 and 0.2cm^{-1}, generally referred to as higher resolutions, we have shown that the level of random phase noise obtained from this type of interferometer with cooled detectors typically remains below 10 milliradians[77]. If room temperature Golay cell detectors are used then the phase noise remains below about 10 milliradians only for resolutions of about 1cm^{-1}[178]. This is discussed in the following chapter.

6.2.2 THE EFFECTS OF THE SPECIMEN HOLDER

The form of the specimen holder, in which the specimen is held over a circular aperture, has been discussed earlier in this section. In this subsection we shall consider the substantial modifying effects that the size of this aperture has on both the modulus and phase spectra obtained from this interferometer. This was investigated by recording interferograms with apertures in the fixed mirror arm whose radii varied from 5 to 20mm in steps of 2.5mm. The measurement was performed with a Rollin detector over the optical range from 10 to 40cm^{-1}.

The effect on the modulus spectra computed from these interferograms may be seen in the curves of the upper graph of figure 6.4. These show the effective power transmission of each aperture as a function of wavenumber, obtained by ratioing the modulus spectra obtained with and without the aperture in place. The radius in millimetres is shown by each ratio. This power transmission is not analogous to that which would be measured with a specimen in the same position. In that case the radiation would be attenuated on both passes through the specimen, in the present case the attenuation results from a geometric effect and only occurs on the first pass of the radiation through the aperture. The ratios are all more-or-less independent of wavenumber, and the variation

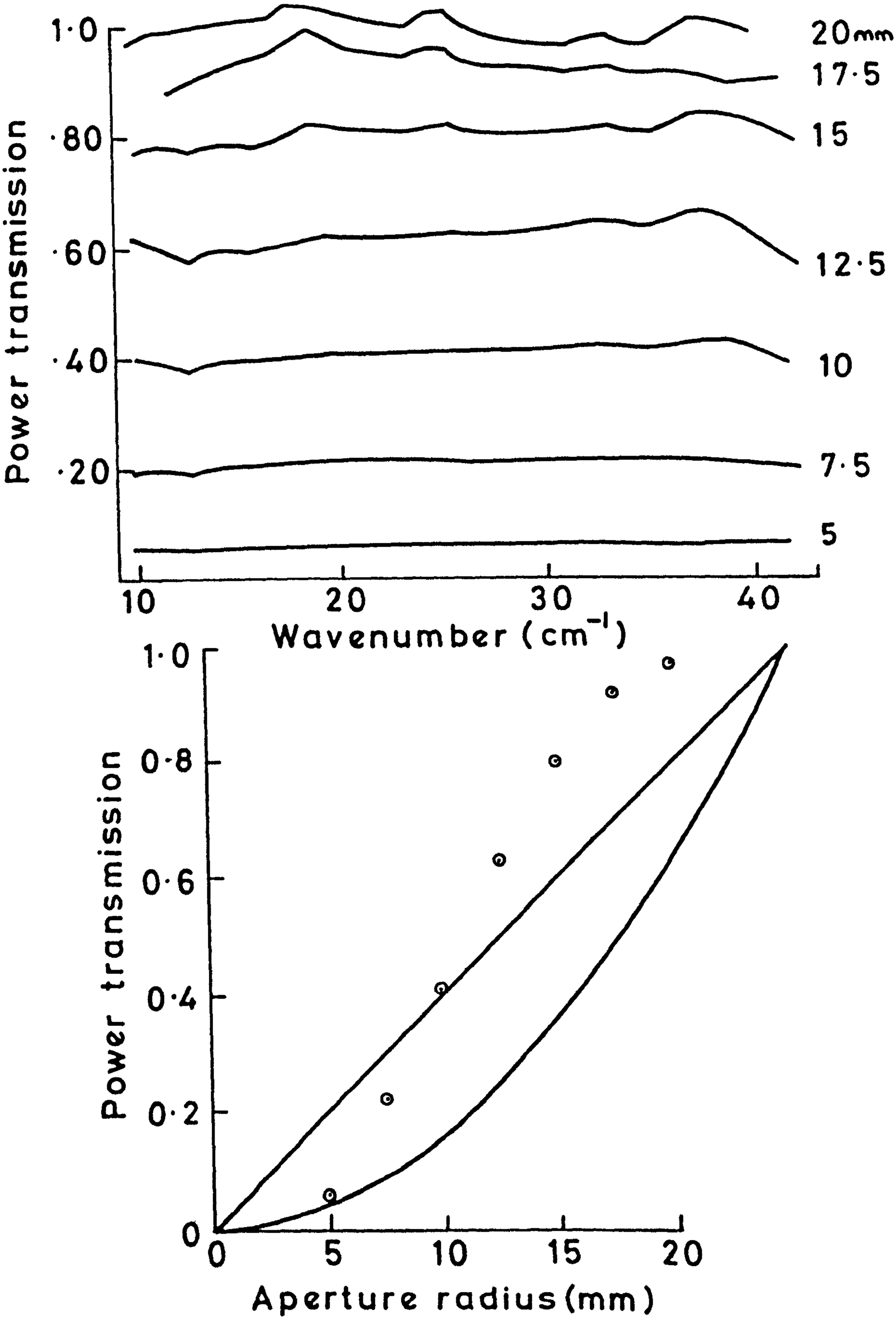

Fig.6.4. The effect of the specimen aperture size on the measured modulus spectrum, shown as the effective power transmission of the aperture. The lower graph shows the transmission of each aperture at 30cm^{-1} as a function of the aperture radius.

with aperture radius is more clearly shown by the points plotted in the lower graph of figure 6.4 which shows the effective transmission measured at $30cm^{-1}$ as a function of aperture radius. The aperture of the interferometer, as defined by the size of the moving and fixed mirrors, was 50mm diameter and as the specimen holder aperture size is reduced from this value the modulus ratio falls away from unity relatively slowly at first and is still above 0.9 for 17mm radius, but then falls rapidly to about 0.06 at 5mm radius. This represents a severe attenuation of the available signal but, in this spectral region, may still be used to give reasonable measurements due to the high signal-to-noise ratios in the interferograms obtained with the Rollin detector. In order to accommodate small specimens without this loss of signal the interferometer devised by Russell and Bell[87] used convergent radiation which was brought to a focus at the fixed mirror and the specimen placed near to the focus.

In the lower graph of figure 6.4 the continuous curve represents the variation of the transmission expected if the aperture were uniformly illuminated, and varies as the square of the radius. This is an unrealistic model as the source, in this spectral region, is the image of the linear arc of the mercury lamp produced by the collimation system, which does not fill the aperture of the interferometer. A more realistic model is provided by assuming that the image produced by the collimator is a line source of small breadth. This gives the straight line shown and provides a better fit to the observations. The finite breadth of the source image means that the aperture will be uniformly illuminated when its diameter is less than this breadth and one would expect the transmission variation to then go as the radius-squared. The results of the lower graph in figure 6.4 show this to occur at about 5mm diameter and so the source image must be about 10mm across in the region of the specimen holder.

The effect that the aperture size has on the phase spectrum is shown in figure 6.5 which shows the phase shift caused by the introduction of each aperture, i.e. the difference between the phase spectra obtained with the aperture in place and removed. The aperture radius in millimetres is again shown beside each curve. The curve for the 17.5mm radius aperture was indistinguishable from that of the 20mm aperture and is not shown. The striking feature of these is that the phase shift due to each aperture is negative, i.e. the apertures behave as if each possesses a real refractive index less than unity so that the phase velocity of the radiation propagating through them exceeds the speed of light in vacuum. An explanation for this could be that as each aperture is in 5mm thick brass they act as short lengths of circular waveguide, and it is a well known result of waveguide theory that in most cases the phase velocity of the guided wave exceeds the velocity of light in a vacuum. The effect is most apparent at the lower wavenumbers, where the wavelength begins to approach the dimension of the aperture and leads to a marked asymmetry in the recorded interferogram for the smaller apertures. As this is a common feature of specimen and reference measurements, however, it is not a problem and disappears when the phase shift due to the specimen is calculated. If it is so desired the effect can be removed by placing a similar, compensating, aperture in the moving mirror arm of the interferometer.

6.3 THE ORIGIN OF COMPUTATION

The equations relating the complex spectrum to the measured interferogram in a dispersive Fourier transform experiment were developed in chapter 4 by considering the case of a continuous interferogram of infinite extent. In practice the interferogram is discretely sampled at equal intervals of path

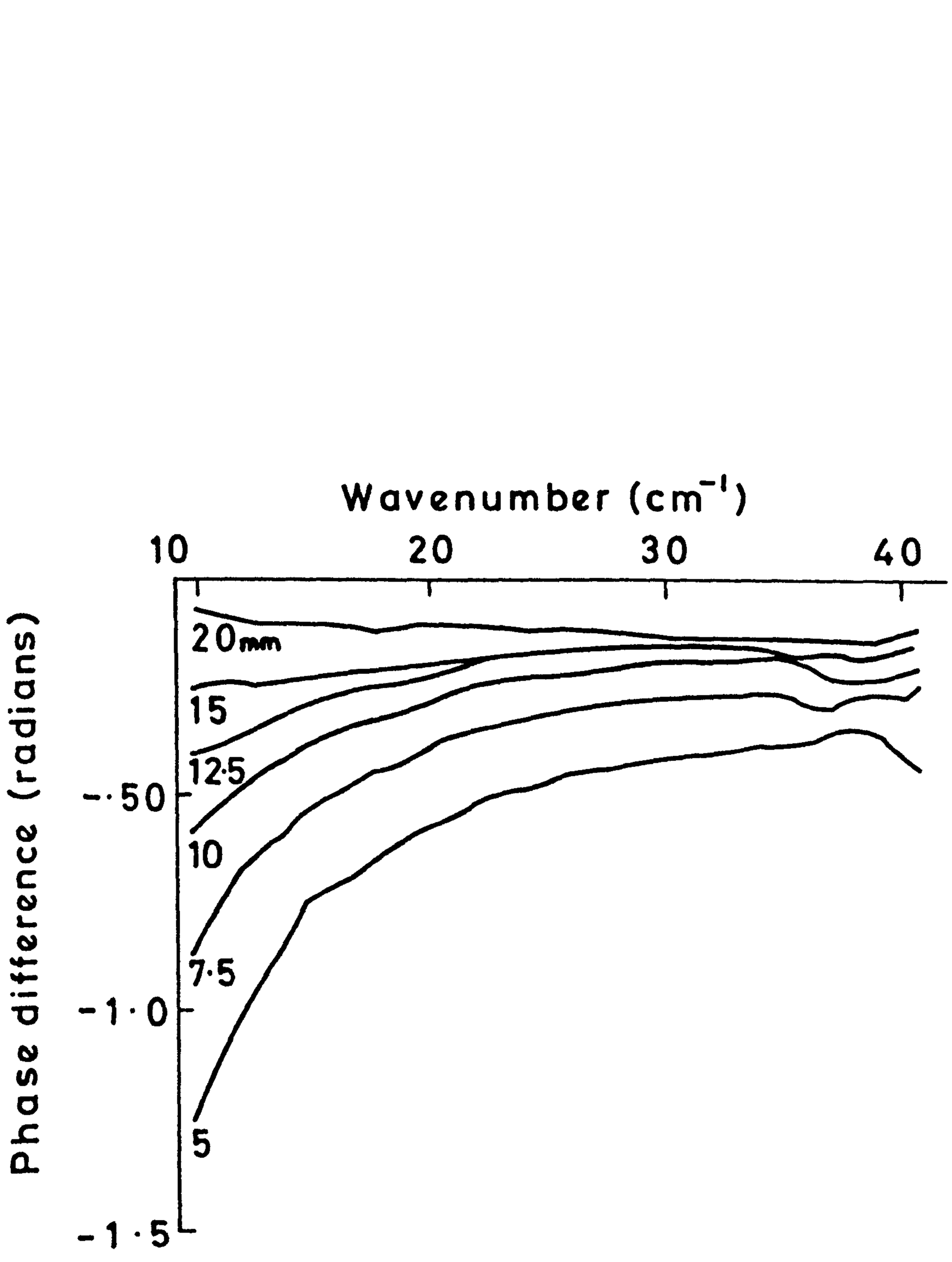

Fig.6.5. The effect of the specimen aperture size on the measured phase spectrum. The curves show the difference between the phase spectra obtained with and without the aperture in place.

difference, and is of finite extent. The limitations introduced by the application of the integral equations of chapter 4 to such real data, such as finite resolution and spectrum aliasing, are well understood and covered in the standard works on Fourier transform spectrometry [47,48]. However, the use of real data implies that, in general, the position of zero path difference in an interferogram will not coincide with a point on the sampling comb generating the recorded interferogram. Thus, the phase spectrum referred to the zero path difference position cannot be directly computed, and this is of particular relevance to dispersive Fourier transform spectrometry. There is some confusion in the literature over the consequences of this, and over the correct procedure to follow in the evaluation of the phase spectrum of a specimen in dispersive Fourier transform spectrometry. This is largely due to the unnecessary phase correction

procedure of Chamberlain et al and its description in subsequent reviews and books. In this section we shall consider the correct procedure to follow in the determination of phase spectra. This was originally outlined by Birch and Bulleid [179] and has recently been discussed in a more general manner by Birch and Parker [235].

A transparent specimen placed in the fixed mirror arm of a two beam interferometer gives rise to an interferogram having a uniquely bright interference signature at a path difference $x = \bar{x}$ displaced from that of the empty interferometer at $x = 0$. This is shown schematically in figure 6.6 where the upper interferogram represents the empty interferometer case and the lower the specimen case. We have discussed earlier in section 4.1.1 that the object of such an experiment is the determination of the complex insertion loss of the specimen. This is the ratio of the complex spectra obtained

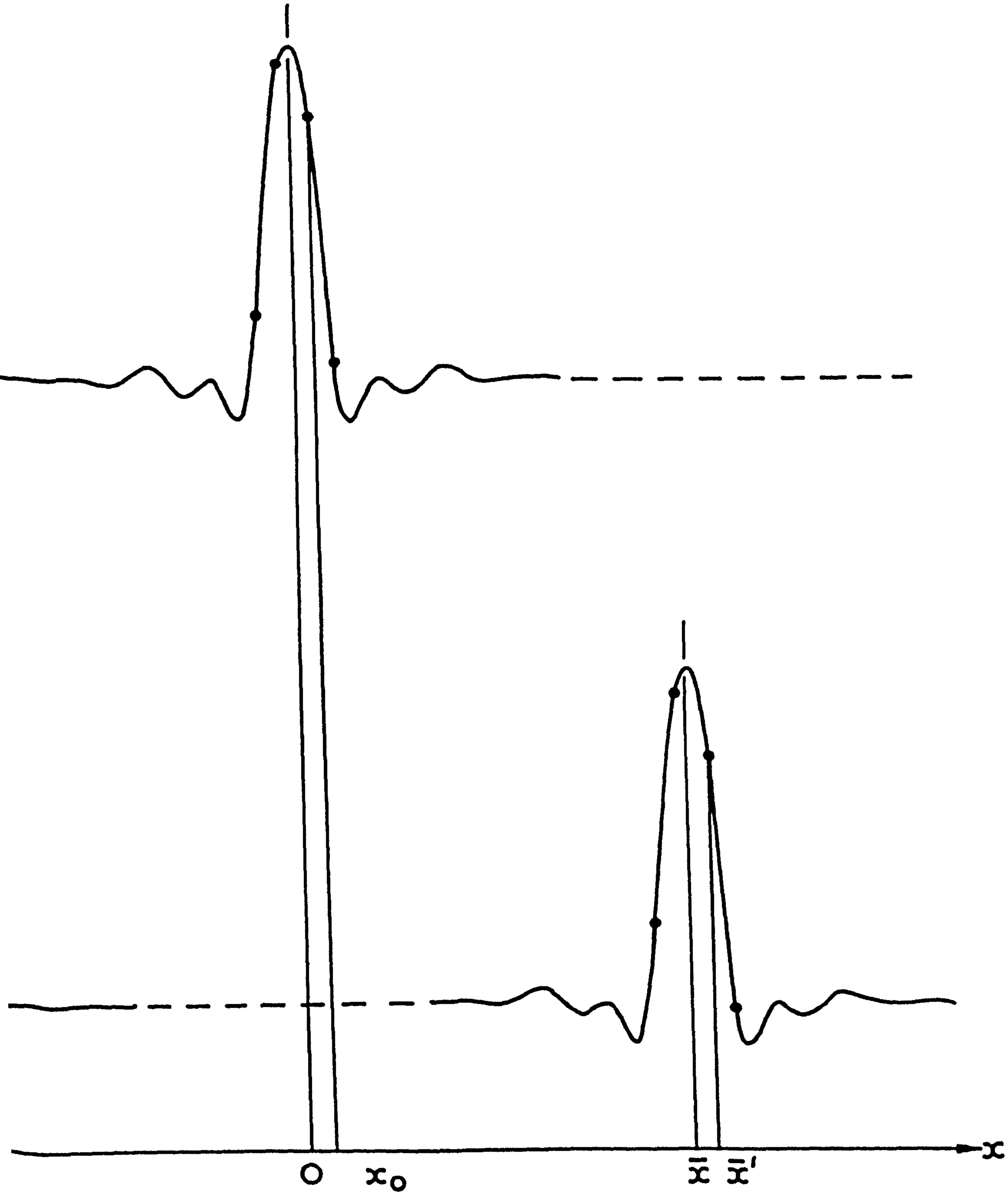

Fig.6.6. Typical interferograms obtained in a dispersive experiment. The upper is the background interferogram centred on zero path difference, the lower is the specimen interferogram centred on $\bar{x}$.

by the complex Fourier transformation of the specimen and reference interferograms using the same position of geometric path difference as the computational origin. This can be the position of zero path difference, but need not necessarily be so. Thus, the complex insertion loss, equation 4.1, would be determined from

$$\hat{L}(\tilde{\nu}) = \frac{\hat{S}_{S,o}(\tilde{\nu})}{\hat{S}_{R,o}(\tilde{\nu})} \qquad \ldots (6.2)$$

where the first subscript, S or R, to the complex spectra refers to the specimen or reference measurement, and the second subscript indicates the path difference value taken as the computational origin. The phase of the insertion loss would then be obtained from

$$\phi_L(\tilde{\nu}) = ph\left\{\hat{S}_{S,o}(\tilde{\nu})\right\} - ph\left\{\hat{S}_{R,o}(\tilde{\nu})\right\} \qquad \ldots (6.3)$$

In practice, the large displacement of the specimen interferogram from zero path difference that can occur in a transmission experiment would lead to severe phase branching if $x = 0$ were used as the computational origin for the specimen interferogram. It is generally more convenient in such circumstances to take the sampled point at $\bar{x}'$, near to the centre of the displaced fringe, as the new origin. Similarly, in practice, a sampled point may not coincide exactly with the position of zero path difference on the reference interferogram and a sample point at x_o, close to it, is used instead. Using these points, x_o and $\bar{x}'$, as the origins for the transformation of the reference and specimen interferograms, the Fourier transform shift theorem [66] shows that the phase of the complex insertion loss is given by

$$\phi_L(\tilde{\nu}) = ph\left\{\hat{S}_{S,\bar{x}'}(\tilde{\nu})\right\} - ph\left\{\hat{S}_{R,x_o}(\tilde{\nu})\right\} + 2\pi\tilde{\nu}(\bar{x}' - x_o) \qquad \ldots (6.4)$$

in addition to equation 6.3. The third term of the right hand side of equation 6.4 is called the fringe shift term and is readily determined from the recorded interferograms since the difference $(\bar{x}' - x_o)$ is a whole number of sampling intervals. (This assumes that the two interferograms were recorded in a systematic manner so that their sampling combs have a known spatial relationship. This is achieved by starting the moving mirror from known path difference values each time.) Equation 6.4 is a perfectly general result for determining the phase of the complex insertion loss of any specimen in a reflection or transmission experiment, even though it has been discussed here in the context of a transmission experiment. Although the points $\bar{x}'$ and x_o were spoken of as being close to their bright interference fringes to reduce phase branching, this is not really necessary if the spectra extend to low wavenumbers as any branching can then be corrected by inspection.

144

In the analysis of Chamberlain et al the precise separation, $\bar{x}$, of the centresof the bright interference signatures of the two interferograms is determined and used to calculate a phase spectrum

$$\phi'(\tilde{\nu}) = ph\left\{\hat{S}_{s,\bar{x}'}(\nu)\right\} + ph\left\{\hat{S}_{R,x_o}(\nu)\right\} + 2\pi\tilde{\nu}\bar{x} \quad \ldots(6.5)$$

where $\bar{x}'$ and x_o are now taken, explicitly as being the sampling points nearest to the centre of each interferogram. Unless they coincide with the centres of their respective interferograms $\phi'(\tilde{\nu})$ will not be equal to the

144

true phase of the insertion loss. Chamberlain et al then proceed to consider the case of a transmission experiment and show how the erroneous refractive index spectrum calculated from their phase spectrum, $\phi'(\tilde{\nu})$, may be corrected by the addition of a term obtained by estimating values of the small shifts of the computational origins of the two interferograms from their

respective centres. This is an unnecessary and time consuming process for the following reasons:

(i) the initial step of their procedure, the calculation of the phase spectrum $\phi'(\tilde{\nu})$, introduces the error that the remainder of the procedure removes, and

(ii) neither $\bar{x}$, nor the small shifts of the computational origins from the interferogram centres, are whole numbers of sampling intervals. Their derivation by interpolation in the interferograms will therefore introduce systematic errors. In addition, Chamberlain et al [144], suggest finding $\bar{x}$ from a second experiment using more finely sampled interferograms. Thus, additional measurements are required which, due to instrumental instabilities, will be likely to introduce additional systematic errors.

These problems are avoided if the phase spectrum is computed from equation 6.4.

As an example of the application of this equation and the use of arbitrarily chosen origins of computation we may consider dispersive transmission measurements on gaseous ammonia at 293K and 2 torr pressure that have been published separately [179]. The interferometer used for these had 900mm long arms with 5mm thick polyethylene windows in each [77]. Measurements were made between 20 and 120cm^{-1} at an apodised resolution of 1cm^{-1} using a quartz-windowed Golay cell. Figure 6.7 shows the phase spectrum

$$ph\left\{\hat{S}_{s,x'}(\tilde{\nu})\right\} - ph\left\{\hat{S}_{R,x_0}(\tilde{\nu})\right\} \qquad \ldots (6.6)$$

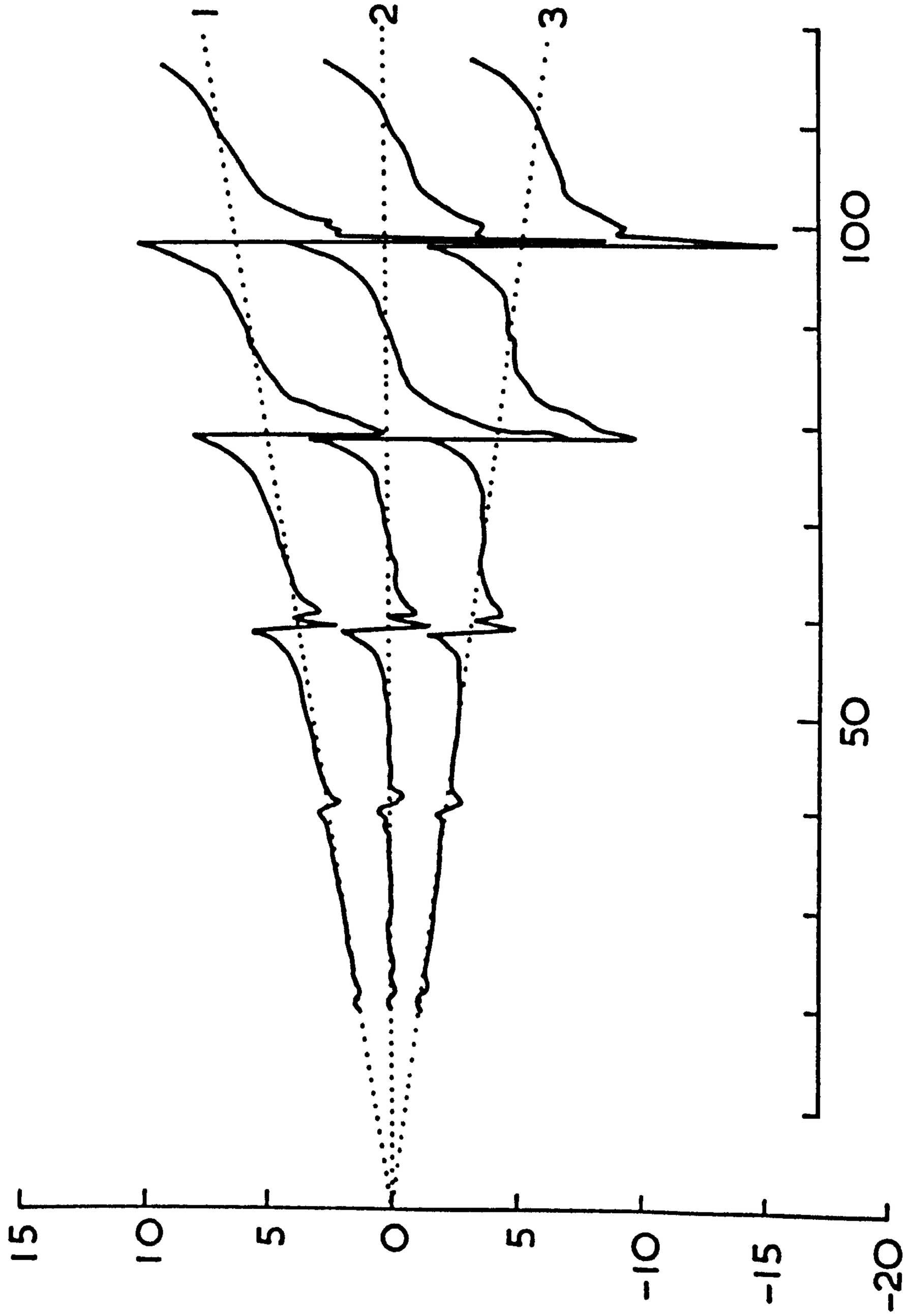

Fig.6.7. The phase spectrum of a 900mm specimen of gaseous ammonia at 2 torr and 293K computed from the same pair of specimen and background interferograms using different pairs of points as the computational origins in each case.

computed from one specimen and one reference interferogram using three different pairs of points for the computational origins, $\bar{x}'$ and x_o. The centre curve (2) used the points closest to the zero crossings of the phase modulated interferograms, the upper curve (1) used $\bar{x}' - \bar{x} = -20$ μm and $x_o = 80$ μm while the lower curve (3) used $\bar{x}' - \bar{x} = 50$ μm and $x_o = -40$ μm. The dashed lines show the linear phase offsets predicted by the shift theorem.

Each of these phase difference spectra was used to calculate $\phi_L(\tilde{\nu})$ according to equation 6.4 and then a refraction spectrum. These are shown in the form $(n-1) \times 10^3$ in figure 6.8 and it is apparent that the correct use of equation 6.4 removes the requirement of working from the zero path difference positions of the interferograms. The pure rotation spectrum of ammonia has previously been measured dispersively over this spectral range [180] at a resolution of $2cm^{-1}$ that did not resolve the inversion splitting ($\sim 1.56cm^{-1}$ [181]) which is partially resolved in the present measurements.

6.4 THE COMPLEX REFRACTIVE INDEX OF SILICON

The first dispersive transmission measurements that we shall present here are of the complex refractive index of pure silicon between 5 and $120cm^{-1}$. In themselves these have little to do with our study of the optical constants of soda lime silica glass but they are of particular value to the technique development with which we are also concerned. Thus, in the first instance, we shall use them to illustrate typical levels of random and systematic error in our dispersive transmission measurement while secondly, and most importantly, they will be used in section 7.3 to establish an absolute standard of complex reflectivity, so that it is not necessary to assume that any given metal reflector is perfectly reflecting.

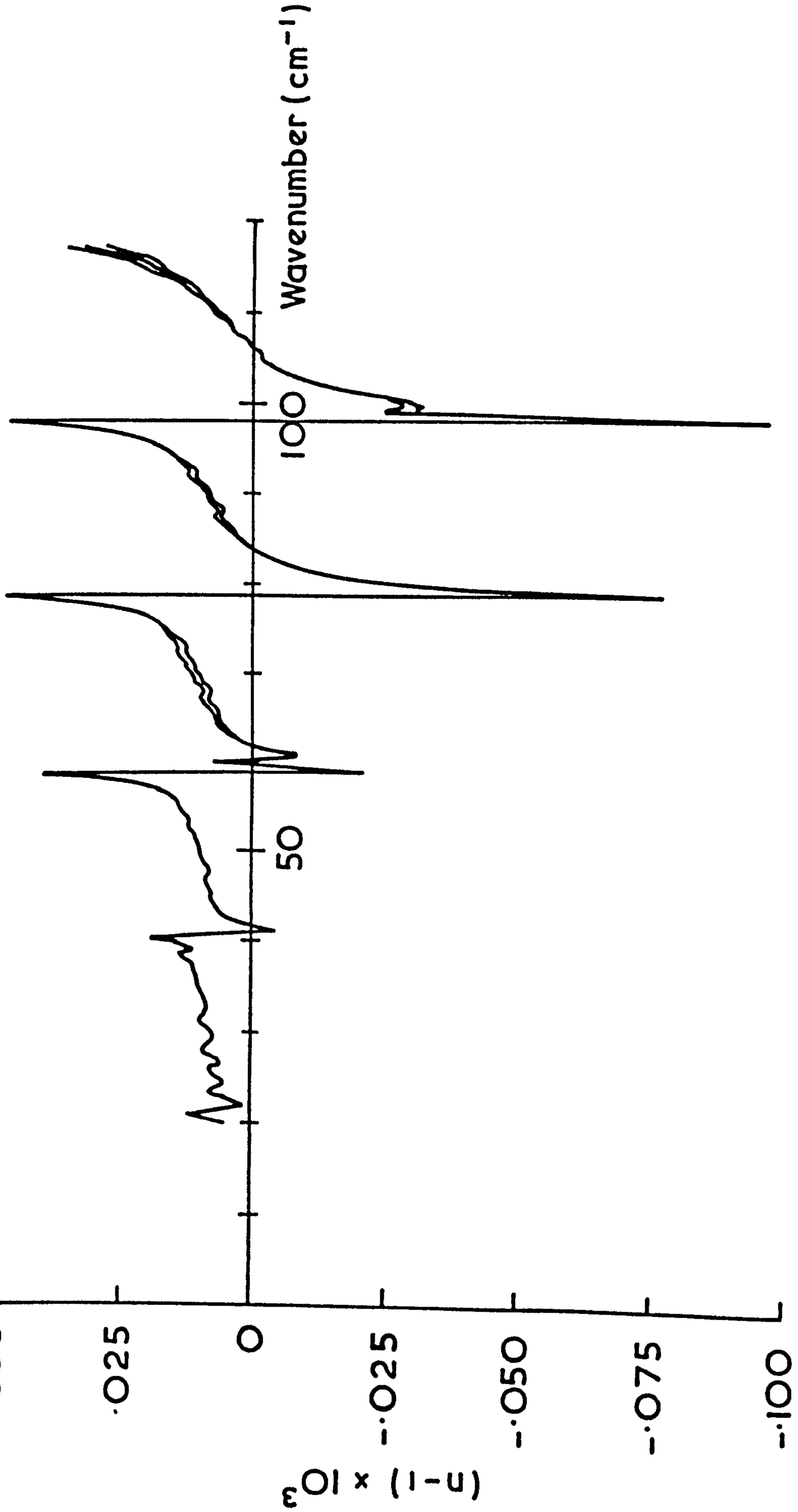

Fig.6.8. The refractive index spectrum of gaseous ammonia at 2 torr and 293K calculated from the three phase spectra of fig.6.7 with the use of equation 6.5 to remove the effects of the different computational origins.

The silicon specimen used was cut from an undoped single crystal with a nominal resistivity of 10 ohm. metre*. It was disc shaped, approximately 40mm in diameter and after optical polishing its thickness was determined to be 2.393mm by averaging micrometer readings taken at different points over its surface. The complex refractive index of this specimen was measured in the dispersive instrument described in section 6.2. Comparison of the modulus and phase spectra computed from interferograms recorded with and without the specimen in the fixed mirror arm gave the attenuation and phase shift caused by the specimen which allowed the complex refractive index to be computed via the iterative technique outlined in section 4.5.2. The measurements were performed in two parts, firstly using a liquid helium cooled Rollin detector to cover the spectral range between 5 and 30 cm^{-1}, then with a quartz-windowed Golay cell for the region from 30 to 120 cm^{-1}. The real refractive index, n, and the power absorption coefficient, α , of the specimen determined in this way are shown in figure 6.9 for a spectral resolution of $2cm^{-1}$ and a temperature of 290K.

The spectral variation of both the power absorption coefficient and the refractive index are typical of those expected from free charge carrier absorption, although calculations based on the simple classical model of this effect predict an absorption coefficient of about 0.1 $Np.cm^{-1}$ at $10cm^{-1}$, which is considerably lower than the measured value of 1.2 $Np.cm^{-1}$. This indicates that the quoted resistivity may be too high, but such a discrepancy is not relevant to the present applications. The bump on the refractive index spectrum near to $28cm^{-1}$ is not a real feature. It occurs at the high wavenumber end of the measurements made with the Rollin detector and is due to

---

* The specimen was kindly loaned by Drs W.F.Passchier and D.D. Honijk of the Gorlaeus Laboratoria, Rijksuniversiteit, Leiden, and was nominally identical to the specimens studied in their earlier dispersive measurements .

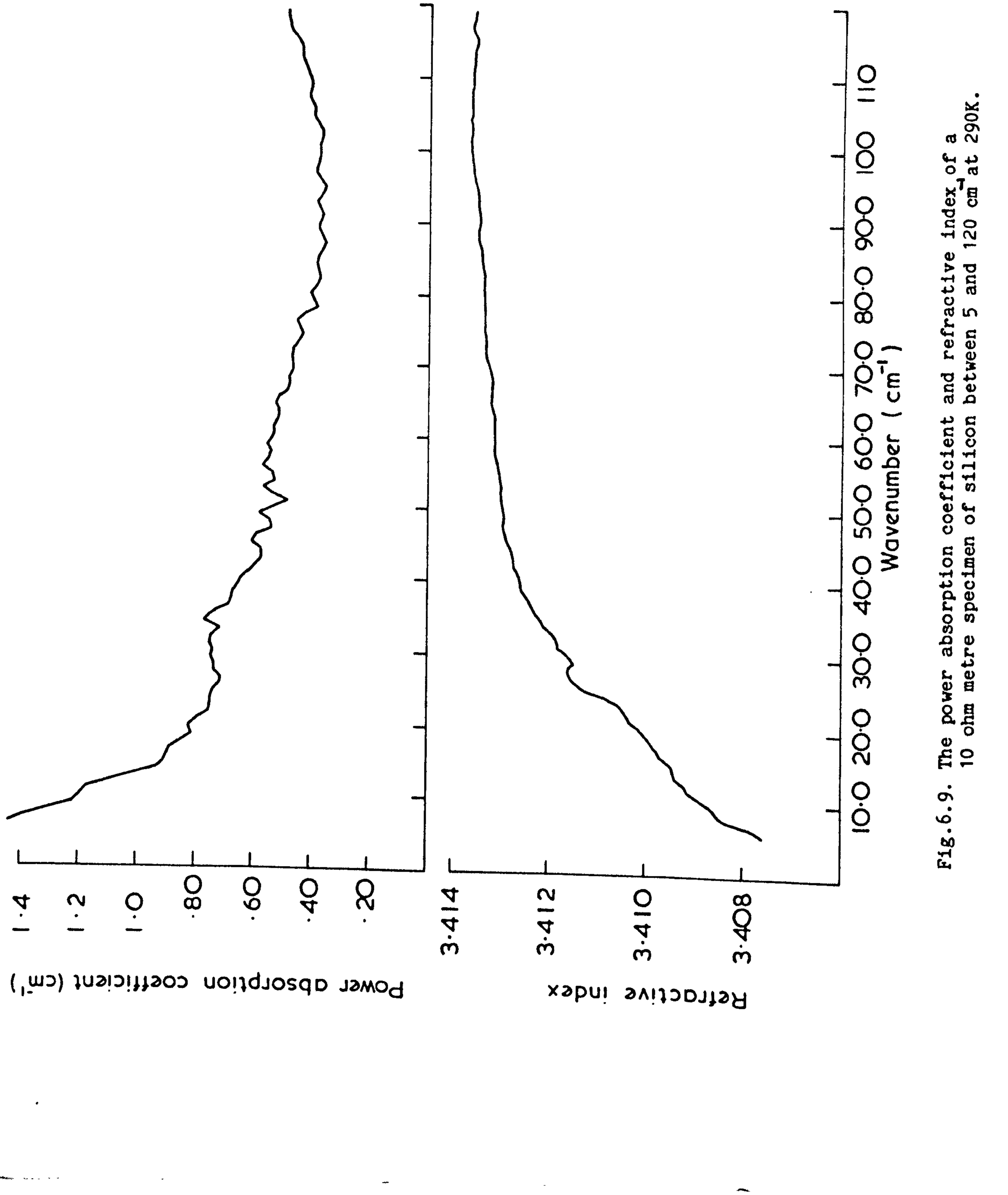

Fig.6.9. The power absorption coefficient and refractive index of a 10 ohm metre specimen of silicon between 5 and 120 cm^{-1} at 290K.

systematic effects associated with the transmission minimum of the beam-divider used in those measurements. The level of random noise in these measurements can be estimated from the standard deviation of sequential determinations, and for the refractive index this was typically between 0.0001 and 0.0002 while, for the power absorption coefficient it was about 0.05 $Np.cm^{-1}$. At these levels of precision in the refractive index determination it is important to consider possible systematic errors, and the most likely cause of such error was an incorrect measurement of the thickness of the specimen. By taking the average of many sequential measurements across the specimen surface we believe that the effective thickness for this speciment has been determined to within 0.001mm. This corresponds to a possible systematic error in the real refractive index of up to 0.001, for this specimen.

6.4.1 THE TEMPERATURE VARIATION

If this material is to be suitable in its application as a reflectivity standard to be described in section 7.3 the temperature variation of its reflectivity should, ideally, be very low, or at least known. This will be largely determined by that of the refractive index and so this was additionally measured over the restricted spectral range between 10 and 40cm^{-1} at temperatures of 291, 292.5 and 297K. It was found to increase significantly with increasing temperature in the manner summarised by the three points of figure 6.10 which show the temperature variation of the refractive index at 25cm^{-1}, and which was typical of all the measurements. A least-squares straight line fit to this admittedly sparse data yields a temperature coefficient for n of $(2.0 \pm 0.2) \times 10^{-4} K^{-1}$, and the straight line in the figure

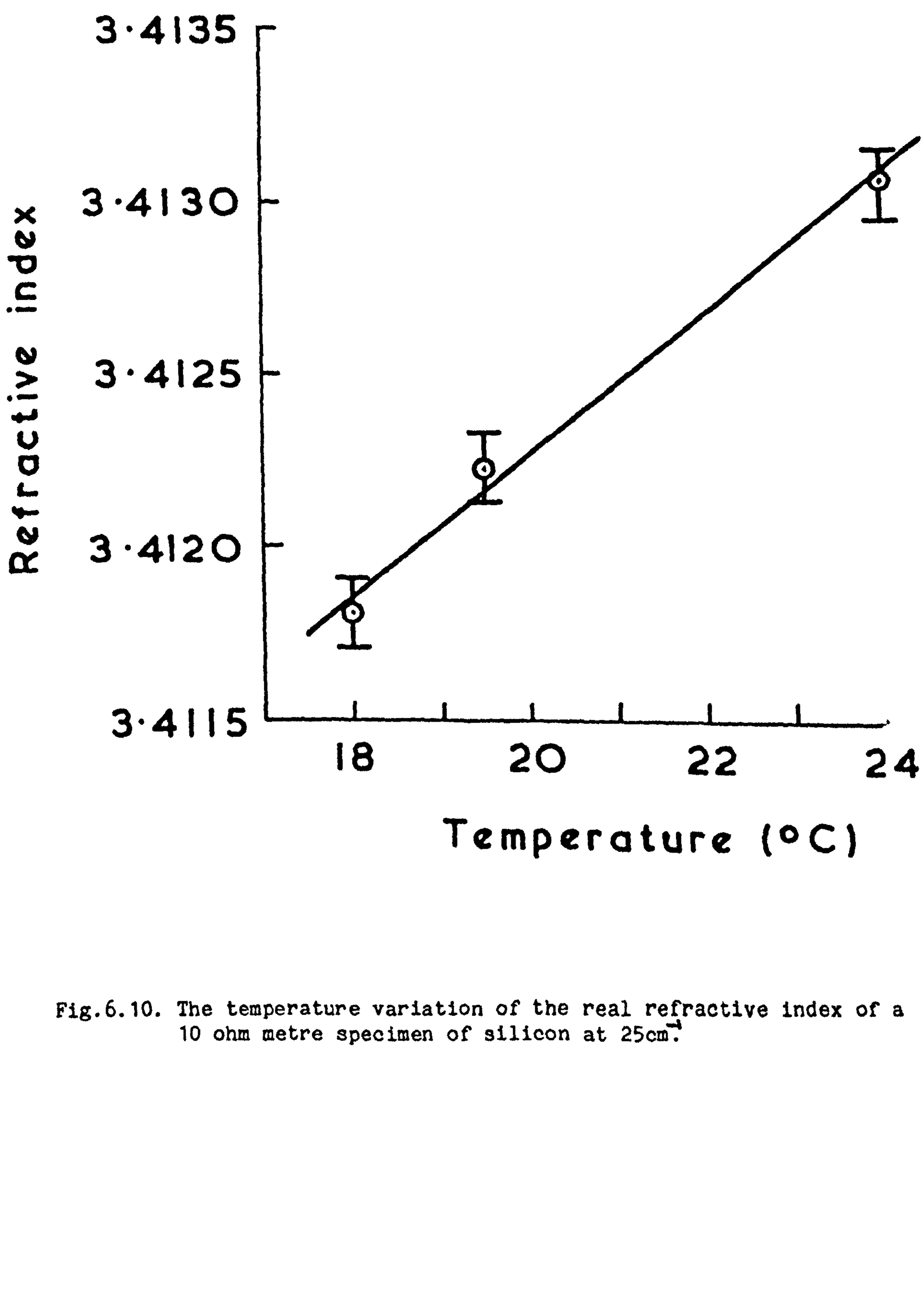

Fig.6.10. The temperature variation of the real refractive index of a 10 ohm metre specimen of silicon at 25cm^{-1}.

represents this best fit to the data. Cardona et al[182,183] have measured the temperature dependence of the refractive index for silicon at 3 μm wavelength, but their specimens were of a sufficiently high resistivity that free charge carrier effects would not have contributed significantly to their result, which cannot, therefore, be compared with the present one.

The previous submillimetre wavelength refractive index measurements on this material of Randall and Rawcliffe[184] and Loewenstein et al[111], using channel spectrum techniques, and of Passchier et al[171] using a novel reflection-transmission dispersive technique all gave values of the refractive index that are significantly higher than those found in the present study, but only in the paper of Loewenstein et al[111] is the measurement temperature given precisely. Thus, their result at $40cm^{-1}$ and 300K, 3.416 ± 0.002, becomes 3.414 ± 0.002 when normalised to 290K by our observed temperature variation, and then agrees with our measured value of 3.4125 ± 0.0002 within experimental error. This illustrates an important aspect of dispersive transmission measurements that is often overlooked by those who use these techniques. The precisions that can be achieved in the determination of the refractive index are now so high that other factors such as temperature or material variability for solids, and pressure for gases[185], can become the overall limitation on precision unless they are specified with sufficient precision.

6.5 THE COMPLEX REFRACTIVE INDEX OF SODA LIME SILICA GLASS BELOW $20cm^{-1}$

In the previous chapter the results of measurements of the power absorption coefficient and refractive index of soda lime silica glass below $50cm^{-1}$ were presented and discussed. The refractive index data were determined from the period of channel spectra exhibited by lamellar specimens in transmission

which provided a mean value averaged over the spectral region between 4 and 32cm^{-1}, thereby masking any dispersion that might have been present. In this section we shall present the results of dispersive Fourier transform measurements of the complex refractive index below 20cm^{-1} at 293K which, combined with a cavity resonator measurement at 34.86 GHz, appear to indicate the presence, in this glass, of a hitherto unexpected loss mechanism below 20cm^{-1}. The measurements were made on the 1.692 and the 3.088mm thick specimens described in table 5.1. Each specimen was approximately 50mm in diameter and the measurements were made with a liquid helium cooled indium antimonide detector used in the Rollin mode.

6.5.1 THE REFRACTIVE INDEX

The measured transmission attenuation and phase shift for each specimen were used to calculate the complex refractive index using the method described in section 4.5.2. The real refractive index spectra so determined for both specimens are shown in figure 6.11 at a spectral resolution of 1.8cm^{-1} for the thin specimen and 0.9cm^{-1} for the thick one. Due to the rapidly increasing transmission loss of the thick specimen measurements were only possible to 10cm^{-1}, whereas 20cm^{-1} was accessible with the thin specimen. Each spectrum is the average of four independent measurements and their reproducibility is indicated by the errors bars which show typical values of the standard deviation of these independent measurements across the spectrum. Thus, in the centre of the spectrum studied, where the signal-to-noise ratio would be greatest, the standard deviation was about 0.001, increasing to just over 0.002 at the low wavenumber end of the spectrum. The refractive index of the thin specimen shows a broad minimum centred about 12 to 14cm^{-1} and having a minimum value of about 2.565. As lower

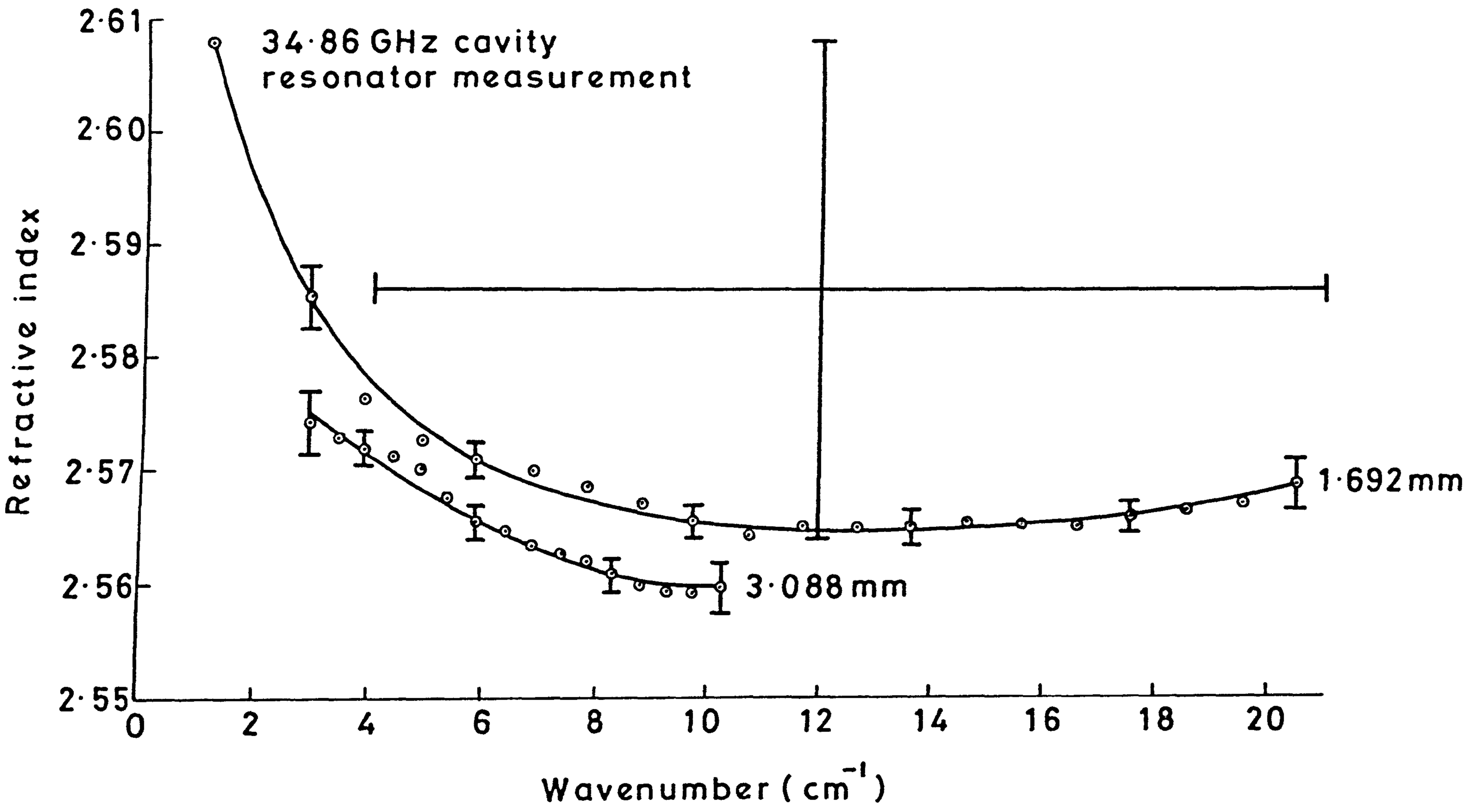

Fig.6.11. The real refractive index spectra of two specimens of soda lime silica glass between 1 and 20cm^{-1} at 293K.

wavenumbers are approached the refractive index begins to rise rapidly to reach 2.585 by $3cm^{-1}$, the lower limit of these dispersive measurements. In order to provide additional data, and as a check on possible systematic effects in the dispersive measurements, the complex permittivity of this thin specimen was measured at 34.86 GHz ($1.16cm^{-1}$) in a cylindrical cavity resonator [190]. This gave the real relative permittivity as 6.8014 and the loss angle as 1.7165×10^{-2} radians* which, when coverted to the optical constants via equations 2.19 and 2.20 gave a real refractive index of 2.608 and a power absorption coefficient of 0.327 $Np.cm^{-1}$. This refractive index point is plotted on figure 6.11 and as it lies on a reasonable extrapolation of the dispersive data to low wavenumbers one has confidence in the overall level of the measurements and that the rise to lower wavenumbers is a real effect rather than an instrumental artefact. Within its more limited spectral range the refractive index of the thicker specimen shows a similar quantitative behaviour, but at a slightly lower level. This may be significant and could result from their slightly differing compositions (table 5.1) but could equally well result from an error in the thickness measurement of either specimen, the difference being equivalent to a fractional thickness error of 3×10^{-3}. The error bars centred on $12cm^{-1}$ represent the earlier channel spectrum result of section 5.5.2 which was averaged between 4 and $32cm^{-1}$ as indicated by the horizontal bar and took the value 2.586 ± 0.022 as indicated by the vertical bar. This was derived from measurements on several specimens that were not measured dispersively, and with this in mind the agreement between the two determinations is quite good and illustrates the advantage of using dispersive Fourier transform techniques to resolve spectral variations.

---

* This measurement was kindly provided by Dr R.J.Cook of the Division of Electrical Science, N.P.L.

The most significant feature of these refraction spectra is their rapid increase to low wavenumbers. One would expect the submillimetre and millimetre wavelength refraction spectrum in these glasses to be dominated by the intense mid-infrared absorption between 200 and 500cm^{-1}. By 10 to 20cm^{-1} this band is so distant that one would anticipate that there should be little or no dispersion of the refractive index. For the refractive index to suddenly rise below 10cm^{-1} must, therefore, indicate the presence of an additional loss mechanism at low wavenumbers. This will be considered further, after the next section in which the dispersive absorption measurements are discussed.

6.5.2 THE POWER ABSORPTION COEFFICIENT

The power absorption coefficient for both these specimens as computed from the dispersive measurements are shown in figure 6.12. As for the refraction spectra of figure 6.11, each is the average of four independent determinations. The level of random error on these spectra is not easily shown by error bars as their degree of reproducibility is high. Thus, over most of the spectral range the standard deviation of the individual spectra from their mean is less than 0.1 Np.cm^{-1}, increasing to about 0.2 Np.cm^{-1} at either end of the spectral range. The spectrum of the thicker specimen is systematically lower than that of the thinner specimen, in common with their refraction spectra. We can now, however, see that this could not be due to a error in the thickness measurements as the amount of the difference, $\sim$ 0.6 Np.cm^{-1}, between the two spectra is too large to have been due to a reasonable thickness error (say $\sim$ 2–3 μm). Thus, the difference could be due to compositional variations, although, as table 5.1 shows, these two specimens

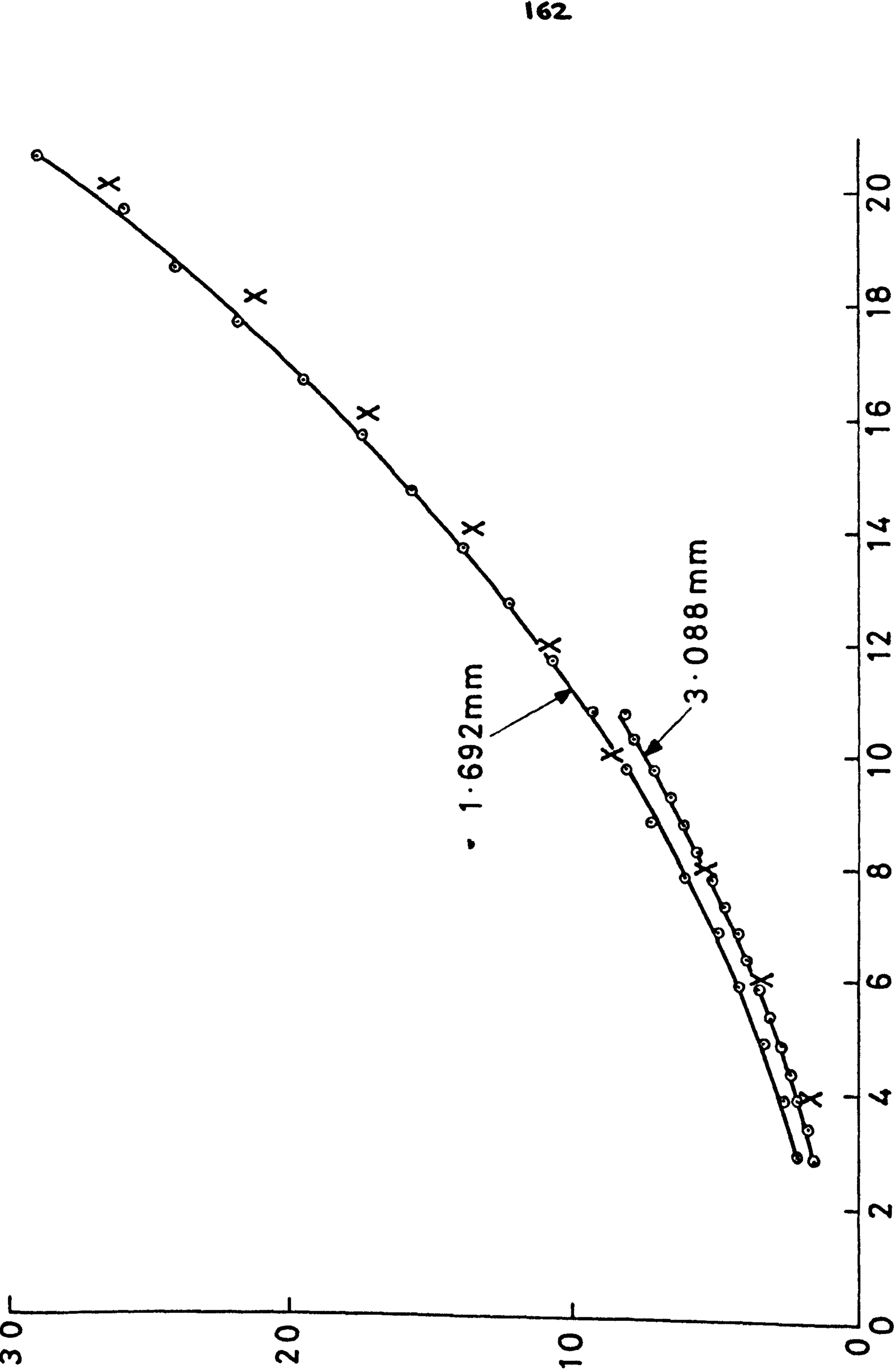

Fig.6.12. The power absorption spectra of two specimens of soda lime silica glass between 3 and 20cm^{-1} at 293K. The measurements were made by transmission DFTS, and the large crosses represent the results of the non-dispersive determination of the previous chapter for comparison.

are very similar, or to an unconsidered systematic effect such as different focussing-defocussing effects due to the different thicknesses of the specimens as each is introduced into the nominally collimated radiation within the interferometer. Compositional effects will not be considered further here, but it is hoped that they will be the subject of a subsequent investigation.

It is obviously of interest to compare these dispersive measurements with the non-dispersive ones of the previous chapter. This is even more so than for the refractive index measurements as in that case the non-dispersive measurements only gave a mean value masking any spectral variation. For the absorption coefficient, however, both dispersive and non-dispersive methods are capable of giving the full spectral variation of the absorption and so can provide a more useful comparison of the two methods. This can be seen initially from figure 6.12 where the large crosses plotted at $2cm^{-1}$ intervals represent the results of the power absorption measurements by non-dispersive methods described in the previous chapter and summarised in figure 5.15. Below $10cm^{-1}$ these are in fairly good agreement with the dispersive measurements on the 3.088mm specimen, but tend to be systematically lower than those of the 1.692mm specimen, by about 1 $Np.cm^{-1}$. As with the non-dispersive refractive index value this non-dispersive absorption spectrum is an average composed of measurements on several different specimens. Therefore, its comparison with these specific dispersive spectra cannot be considered quantitatively and one can only say that there is fairly good agreement between the determinations of the two methods. A more valid comparison may be had from the 3.088mm specimen as this has been measured both dispersively

and non-dispersively. This is shown in figure 6.13 which shows both determinations of its absorption spectrum between 3 and 10.5cm^{-1} at 293K. The measurements were unfortunately made at different times and different spectral resolutions so that the spectral sampling combs are not coincident. Thus, they cannot be directly subtracted one from the other to reveal the difference between them. However, it is apparent from figure 6.13 that the non-dispersive measurement is systematically higher than the dispersive measurement by between 0.1 and 0.2 Np.cm^{-1}, except at the ends of the spectral range where random noise begins to dominate. Small as this is it represents about a 3% error in the measurement of one or both of the transmission spectra and this is a significant amount, especially in precise measurements. Without performing more extensive investigations it is not possible to identify the source of this difference, but it seems likely that it could be due to the different measurement geometries used. Both measurements were made in nominally collimated radiation, but if the radiation were not well-collimated then each specimen would give rise to different focussing-defocussing effects[145] which could be significant and account for the difference between the two methods. The difference between the two spectra is not, however, too large and for most practical purposes would not be considered significant.

In considering these dispersive measurements we have not so far discussed the possibility of an additional low wavenumber absorption indicated by the refractive index spectra of figure 6.11. If such a feature exists one might expect to see evidence for it in the low wavenumber absorption spectrum. That this is so can be seen with reference to figure 6.14 in which the dispersive absorption spectra of figure 6.12 have been plotted on a log-log

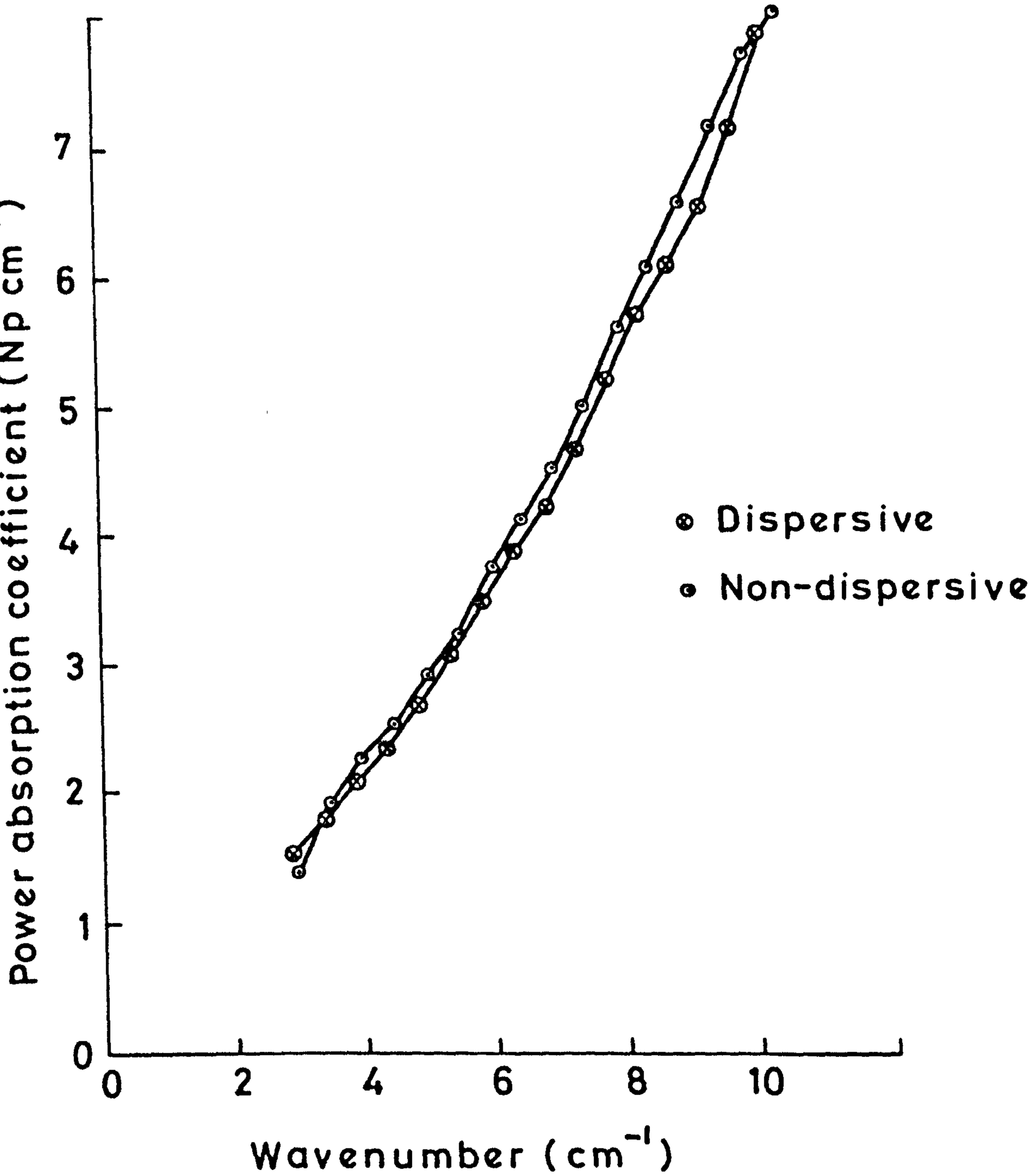

Fig.6.13. A comparison of dispersive and non-dispersive determinations of the power absorption spectrum of a 3.088mm specimen of soda lime silica glass.

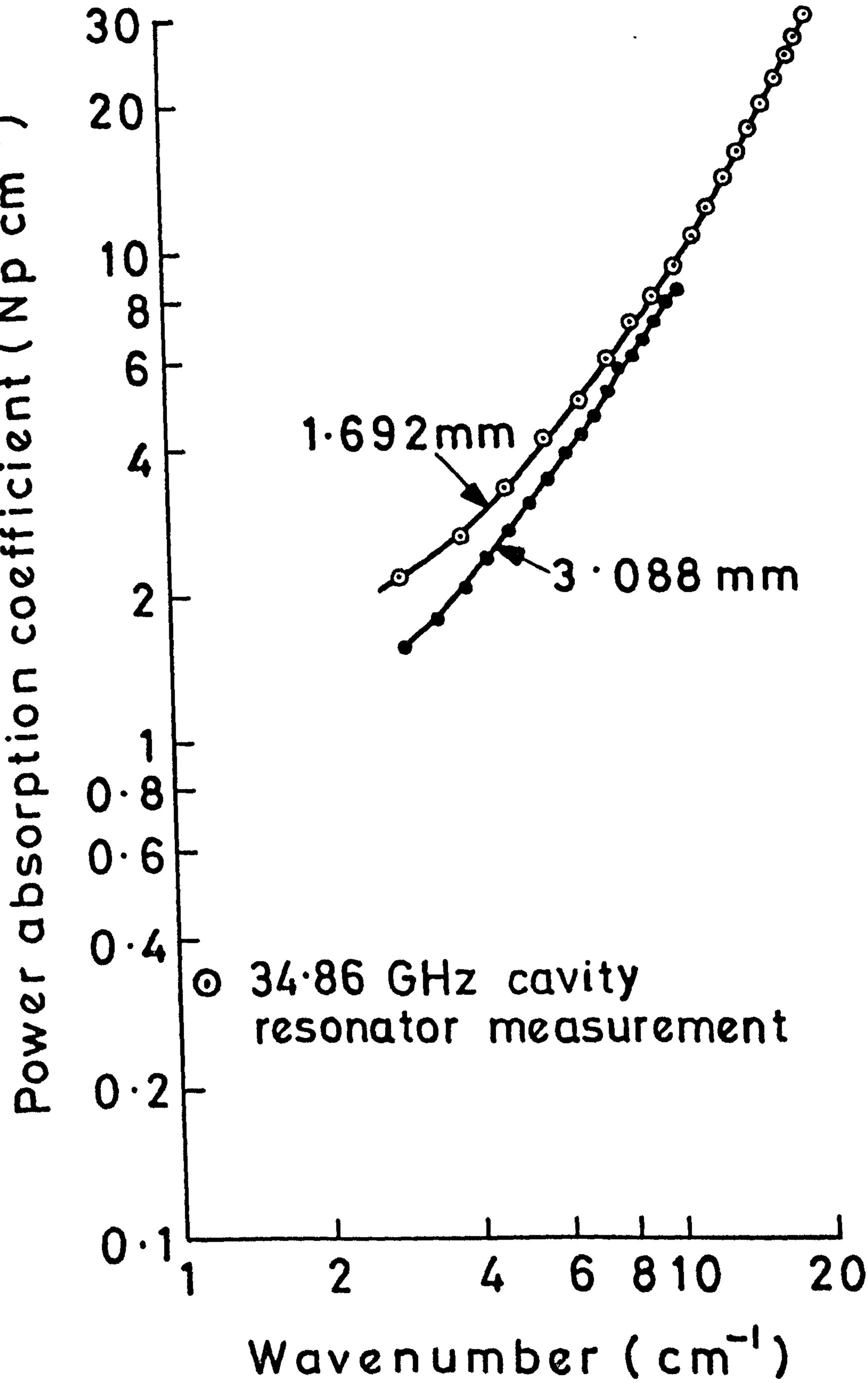

Fig.6.14. A log-log plot of the power absorption spectra of two specimens of soda lime silica glass showing the low wavenumber anomaly.

scale to emphasize the low wavenumber, low absorption part of the spectrum. Above $10cm^{-1}$ the absorption spectrum of the 1.692mm specimen tends to the wavenumber-squared dependence discussed in chapter 5, while below $10cm^{-1}$ the absorption tends to flatten off and does not extrapolate smoothly to the 34.86 GHz result. This indicates the presence of an absorption feature somewhere between 1 and $20cm^{-1}$, superimposed on the rapidly falling wing of the mid-infrared absorption. Strom et al [193] have recently shown that a quadratic dependence of the absorption coefficient on wavenumber is a common feature of many amorphous materials, although it usually extends to much lower wavenumbers than in soda lime silica glass. It seems plausible, therefore, to suggest that it also applies to this glass, but that the full, low wavenumber extent of the quadratic dependence is obscured by this unexpected absorption feature. To investigate this further we have subtracted the almost-wavenumber-squared dependence of the absorption coefficient described by equation 5.15 from the measured absorption coefficient of the 1.692mm specimen shown in figures 6.12 and 6.14 and have plotted this excess absorption spectrum in figure 6.15. It takes the form of a broad feature centred on $9cm^{-1}$ having a full width at half peak height of $15cm^{-1}$. One can, of course, argue that the difference of these two spectra, which run together at $20cm^{-1}$ and which both tend to zero absorption at zero wavenumber, is bound to give a bell-shaped spectrum of the type shown in the figure without necessarily indicating the presence of a discrete absorption feature. This is so, and without the refractive index spectrum it would be unwise to place too much significance on the result. However, the spectral variation of the refraction spectrum, reproduced as the dashed line in the figure, clearly shows that the absorption and refraction spectra, taken

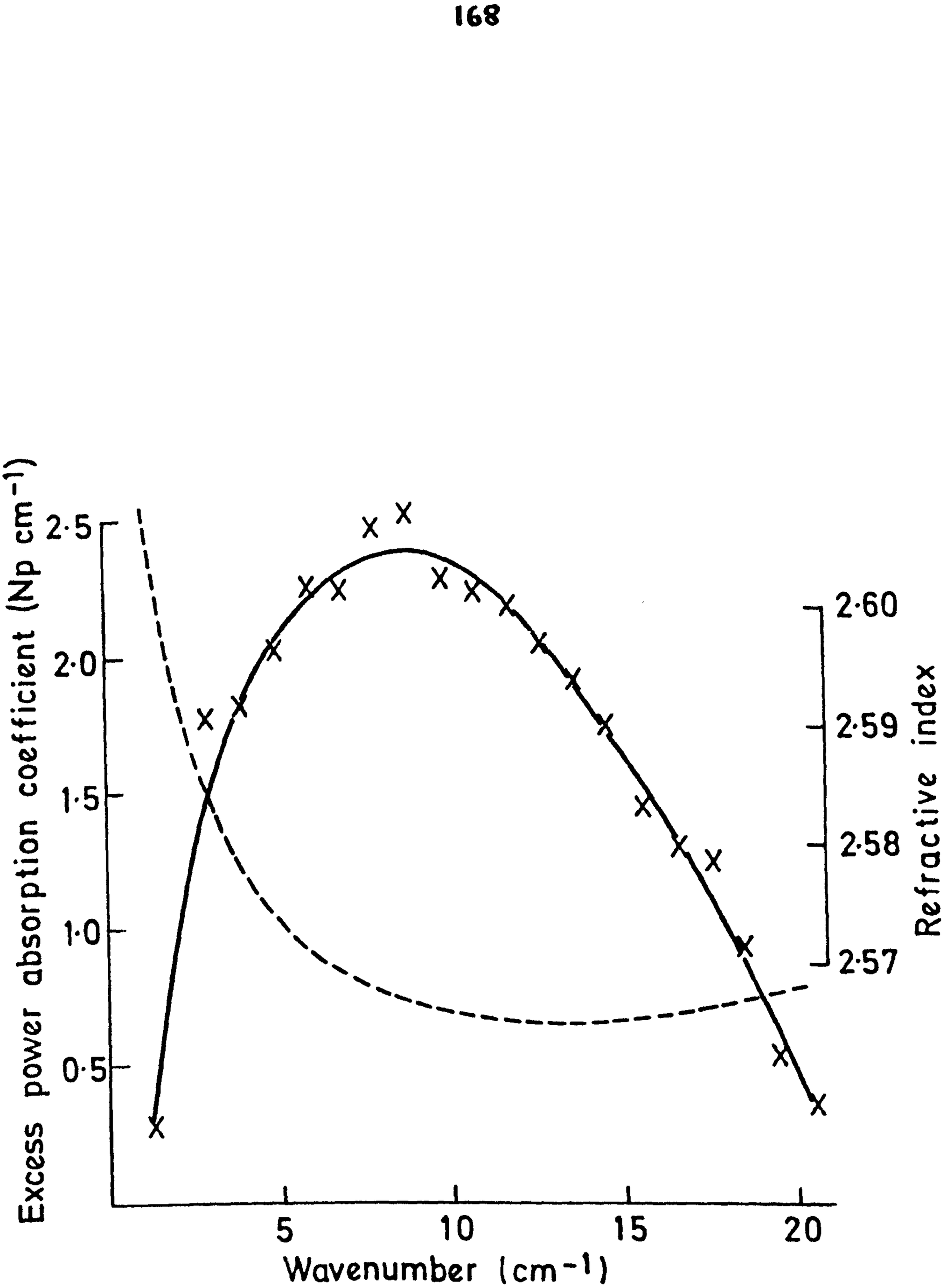

Fig.6.15. The power absorption spectrum of soda lime silica glass remaining after the wavenumber-squared absorption seen at higher wavenumbers has been subtracted. The dashed line shows the refractive index spectrum for comparison.

together, are typical of the variation of the optical constants expected across an absorption feature. This can be characterised in a more quantitative manner by a consideration of a modified Kramers-Krönig analysis applied to these measurements. Chamberlain [191,192] has derived expressions which relate the integrated absorption of an isolated feature to the dispersion across it but, as these only apply to wavenumbers more distant than twice the half width from line centre, they cannot be applied to the present case. However, one can proceed by considering the Kramers-Krönig integral relating the refractive index at a particular wavenumber, $\tilde{\nu}_o$, to the power absorption coefficient measured over the entire spectrum

$$n(\tilde{\nu}_o) - n(\infty) = \frac{1}{2\pi^2} \cdot \int_0^\infty \frac{\alpha(\tilde{\nu})}{\tilde{\nu}^2 - \tilde{\nu}_o^2} \cdot d\tilde{\nu} \qquad \ldots (6.7)$$

For an isolated feature, the total dispersion across the entire spectrum due to it alone is thus found by putting $\tilde{\nu}_o$ to zero in the above equation, giving

$$n(0) - n(\infty) = \frac{1}{2\pi^2} \cdot \int_0^\infty \frac{\alpha(\tilde{\nu})}{\tilde{\nu}^2} \cdot d\tilde{\nu} \qquad \ldots (6.8)$$

but, as the feature is isolated, the limits of the integral may be restricted to those wavenumbers, $\tilde{\nu}_1$ and $\tilde{\nu}_2$, where the absorption associated with it is significantly different from zero. Thus, equation 6.8 becomes

$$n(\tilde{\nu}_1) - n(\tilde{\nu}_2) = \frac{1}{2\pi^2} \int_{\tilde{\nu}_1}^{\tilde{\nu}_2} \frac{\alpha(\tilde{\nu})}{\tilde{\nu}^2} \cdot d\tilde{\nu} \qquad \ldots (6.9)$$

It is reasonable to say that this should apply to the excess absorption of the glass, as the intense mid infrared bands are sufficiently distant for their effects to be considered constant over the width of the excess. Thus,

equation 6.9 evaluated for the absorption data of figure 6.15 leads to a refractive index dispersion of 0.045 if the feature is a real absorption. This is almost exactly the observed value of 0.044, and one concludes that there is, in fact, a discrete absorption feature in soda-lime-silica glass at 9cm^{-1} whose presence is obscured in the directly observed absorption spectrum by the rapidly falling absorption associated with the mid infrared bands.

Wood[236] has observed a similar feature to this excess absorption in the spectrum of fused silica and, as this is the major constituent of the present glass, it is tempting to suggest that they have a common origin. Wood made conventional power transmission measurements on a specimen of spectrosil at temperatures of 120, 200, 290, 490 and 630K. At the four lowest temperatures a discrete absorption feature is clearly visible in his results. Its intensity decreases with increasing temperature, and at 290K the peak absorption coefficient is $\sim$ 0.1 Np.cm^{-1} and it is centred on 12cm^{-1}. Wood proposed that this arose from localised modes of a structural defect used by Clark and Strakna[237] to explain the low temperature excess specific heat of fused silica. The defect is an elongated Si - O - Si bond having two equilibrium positions for the bridging oxygen atom, and the absorption arises from relaxational loss due to motion of the bridging oxygen atom in the elongated bond. The spectral variation of the refractive index shown in figure 6.15, decreasing across the absorption feature without turning points, is characteristic of a relaxational rather than a resonance loss and, therefore, further supports Wood's assignment of this absorption to the localised modes of a structural defect.

6.6 A SINGLE PASS INTERFEROMETER

All of the measurements reported in this chapter were made using the double pass interferometer shown schematically in figure 6.2. This is not the most convenient instrumental configuration for measurements on heavily absorbing materials. If the complex transmission factor of the specimen is $\hat{t}(\tilde{\nu})$ then, for such a double pass system, the ratio of the specimen and reference modulus spectra gives $|\hat{t}^2(\tilde{\nu})|$ whereas in a system which only allows the radiation to pass through the specimen once $|\hat{t}(\tilde{\nu})|$ would be determined. As $|\hat{t}(\tilde{\nu})| \gg |\hat{t}^2(\tilde{\nu})|$ for heavily absorbing materials, often by more than one order of magnitude, the single pass determination is an easier and more precise measurement. Such instruments have been described by Russell and Bell[87] and by Parker et al[189] and are of the type shown schematically in figure 6.1 which used roof-top reflectors to spatially separate the incident and return beam in each arm so that the specimen may be placed in only one of them. The modular hardware of the interferometers used in this work suggested an alternative configuration for a single pass interferometer that would not return any interferometrically modulated radiation to the source so that both output beams could be used, leading to improved signal levels in the detected interferograms. It is a Mach-Zehnder used with broad band radiation as opposed to its more common monochromatic usage. This is presently being developed and in this section we shall briefly outline its construction and the particular advantages of its use.

The basic optical configuration of the interferometer is shown in figure 6.16. The collimated radiation from a mercury vapour arc source is split into two beams by the first melinex beamdivider, M1, with each then reflected from

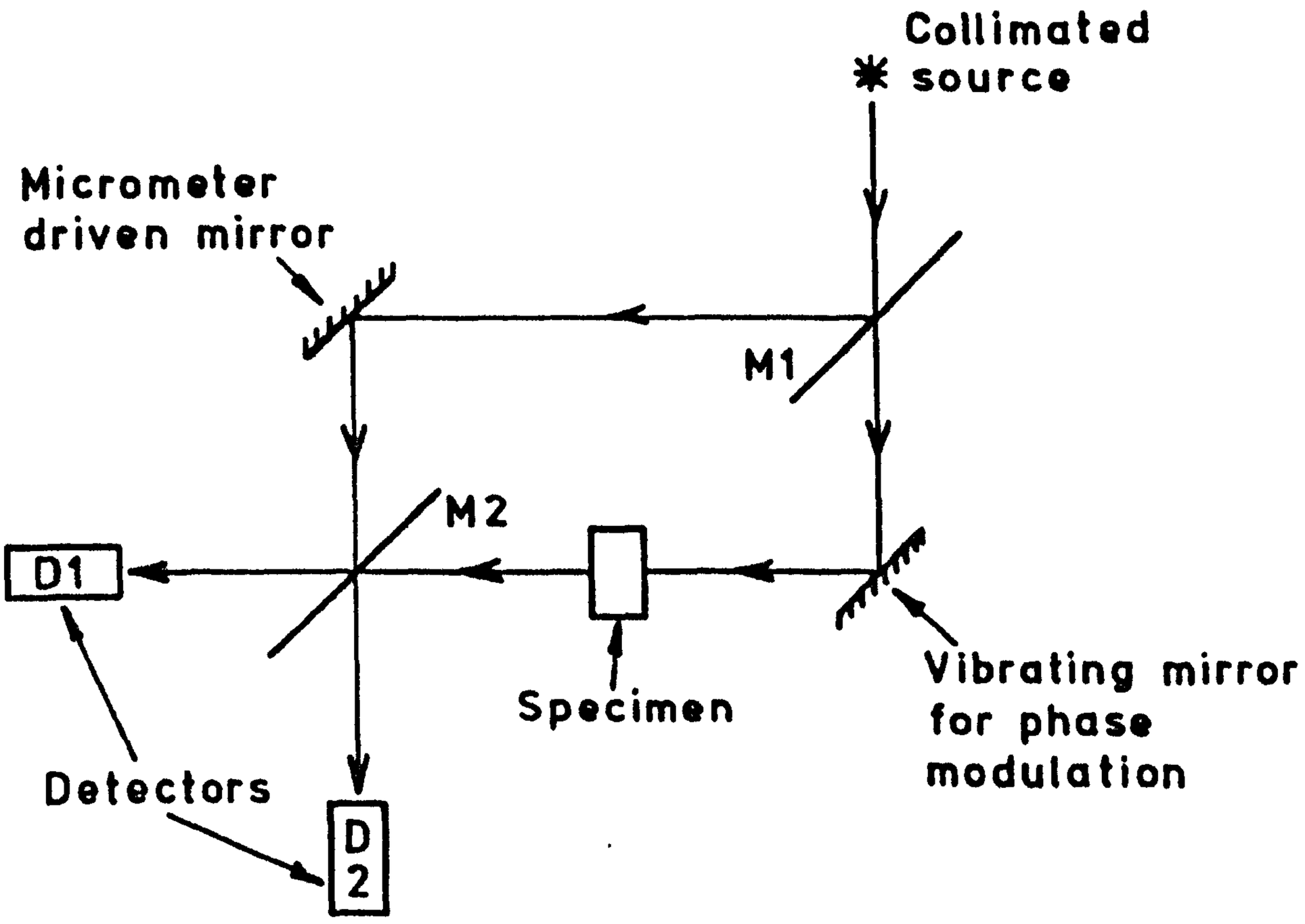

Fig.6.16. Schematic representation of a Mach-Zehnder interferometer used for single pass dispersive transmission measurements.

separate plane mirrors to recombine at the second beamdivider, M2. One of the plane mirrors is mounted on the spindle of a motor-driven micrometer to provide the path difference variation, while the other is connected to a vibration generator so that phase modulation can be used. The second beamdivider reflects and transmits different fractions of each of the two incident beams so that two interfering beams travel to each detector, D1 and D2, one from each arm of the interferometer. If the beamdividers are similar and have complex reflection and transmission factors $\hat{r}$ and $\hat{t}$ respectively then,without the specimen present,the beams leaving M2 for D1 have unequal relative complex amplitudes $\hat{r}^2$ and $\hat{t}^2$, while those going towards D2 have equal relative amplitudes, $\hat{r}\hat{t}$. It is easily shown, however, that the detected interference signals at both detectors are proportional to $|\hat{r}^2\ \hat{t}^2|$ but of opposite sign so that the recorded interferograms ideally correspond to identical modulus spectra and to phase spectra that differ by π radians. Similarly, introduction of the specimen into one of the interferometer arms causes both interferograms to be attenuated and shifted in path difference by the same amounts. As both interferograms contain the same information we have chosen to operate the instrument in a mode of operation where the two interferograms are subtracted which, remembering that they are of opposite sign, gives a single interferogram having a $\sqrt{2}$ improvement in its signal-to-noise ratio over each individual interferogram, in a detector-noise-limited system.

A potential limitation of the instrument derives from the non-normal incidence of the radiation on the micrometer driven mirror. This causes the image of the source from the moving mirror arm at M2 to be displaced transversely across that from the other arm. This could decrease the intensity of the interferometrically modulated radiation away from zero path difference in two ways. First, if either or both of the condensing lens or the collimator

is not perfect the two images of the source on each detector will not coincide at large path differences. Secondly, the image of the source from the moving mirror arm will begin to be obscured by the physical aperture of the interferometer at sufficiently large path differences. Both of these would lead to an optical weighting of the interferogram and a decrease in the spectral resolving power available for a particular path difference variation. However, for the resolutions required for studies on most highly absorbing solids ($> 0.5 cm^{-1}$) these should not prove to be severe limitiations.

Another problem, consequent upon the optical weighting discussed above, is present for dispersive measurements and arises from the shift of the bright fringe of the interference pattern to positive path difference when the specimen is in the interferometer. This will not affect the optical weighting function, which will remain centred on zero geometric path difference. Thus, the recorded interferogram would be weighted asymmetrically leading to a distortion of the computed values of the optical constants, However, in the study of highly absorbing materials we shall be working with specimens whose thickness is considerably less than 1mm, which should minimise the effect.

CHAPTER 7

DISPERSIVE REFLECTION MEASUREMENTS

7.1 INTRODUCTION

In chapter 5 on power transmission measureremements the effective opacity of soda lime silica glass in the spectral region between about 50 and 1000cm^{-1} was demonstrated. The single pass dispersive technique discussed in the previous chapter should allow the extension of transmission measurements further into this region of opacity but, unless extremely thin specimens are to be used, the centre of the absorption will remain inaccessible to transmission techniques. In such a situation the optical constants can only be determined from a reflection measurement.

7.1.1 REFLECTION METHODS

There are three reflection methods that have traditionally been used to determine the optical constants of a solid. First, methods such as those of Simon [118], Avery [119] and Linquist and Ewald [120] which rely upon measurements at two angles of incidence or two polarisations and the use of pre-computed charts or graphical constructions based on Fresnel's equations to give the optical constants. These suffer the disadvantages of requiring two sets of measurements and the extreme sensitivity of the graphical analyses to small changes in the measured reflectivity under some conditions. Secondly, there is the use of the Kramers-Krönig integral relation to compute the phase, ϕ^r, from measurements of the normal incidence power reflectivity. This was first used by Robinson [121] and Robinson and Price [122] and is widely applied in all parts of the electromagnetic spectrum even though errors which arise from the necessary truncation of the infinite integral can be significant, and although there are situations in which

the use of the relation may be erroneous or fail [123-127]. Finally, internal reflection spectrometry may be used. This was originally developed by Fahrenfort [128,129] and Harrick [130] and overcomes the lack of sensitivity of the normal reflection spectrum to the absorption index by using an angle of incidence greater than the critical angle of an interface. There are several advantages to the method, weak features may be studied through multiple reflections, the measured spectrum can be made to resemble the transmission spectrum by careful choice of the angle of incidence, and there are no interface effects arising from the finite size of the specimen as the interaction occurs via a non-propagating wave. However, practical restrictions on the range of angles of incidence that may be used due to dispersion, and on the materials available for use as the internal reflection element have limited the application of the method to the near infrared and visible spectral regions.

These traditional methods are unsuitable for application to the precise determination of optical constants at submillimetre and millimetre wavelengths and, in these spectral regions, it is necessary to use dispersive Fourier transform spectrometry to directly measure the full complex reflectivity of a plane surface of the material under study. The measurement is made by comparing the complex spectrum obtained from a symmetric interferometer with that obtained when the fixed mirror of the interferometer is replaced by the specimen. In this chapter we shall discuss the construction and performance of an interferometer that has been developed for such measurements at ambient temperatures, and illustrate its performance with measurements on soda lime glass between 20 and 360cm^{-1}.

7.1.2 DISPERSIVE METHODS

The dispersive Fourier transform spectrometry of highly absorbing and opaque solids was originally developed by Bell [25,26] using the replacement method described in the previous section wherein the specimen physically replaces a reference reflector. Genzel and his co-workers [196-200] have, more recently, described the development of another instrument of the replacement type which, in its final form, is capable of measurements at temperatures down to 6K. Happ et al [201-203] have used an instrument similar to that of Genzel to study the millimetre wavelength behaviour of some ferroelectrics. A major problem with the replacement method is ensuring the exact replacement of the specimen surface with the reference surface. If this is not done a phase error proportional to the product of the displacement between the two surfaces and wavenumber is introduced into the phase spectrum. This possibility is avoided in the method of Parker et al [74, 204-207] in which partial aluminising of the specimen and appropriate division of the field of view of the interferometer by a system of screens allows the measurement to be made without changing the specimen. The most recent form of this instrument [207] has been used at temperatures down to 4K. With such a system the limiting systematic error in the phase spectrum derives from backlash in the drive of the moving mirror which introduces an unknown displacement between the sampling combs of the specimen and reference interferograms. Staal and Eldridge [208] have completely overcome this backlash problem with an elaboration of the technique of Parker in which their circular specimen surface is divided into sixteen alternately aluminised and clear segments of equal area. An eight-segmented shutter obscures either the specimen or aluminised sectors and by switching it from one position to the other both specimen and reference interferograms can be recorded during one scan of the moving mirror. The interferometer that is described in the next section has been used for ambient temperature measurements on intrinsic indium

antimonide[209], KDP and ADP[73] and was developed from an earlier version used in measurements on KBr[210]. It is an interferometer of the replacement type and is operated in a mode which allows the backlash error to be measured and, hence, corrected for.

7.2 THE INTERFEROMETER

Reflectivity measurements are ideally made at normal incidence to enable the simplified form of Fresnel's equations to be used. This requires a directional coupler to spatially separate the reflected beam from the incident beam and is usually sufficiently lossy for most power reflection measurements to be made at slightly non-normal incidence, although normal incidence configurations have been described[30]. In dispersive measurements, however, the specimen forms part of the interferometer and normal incidence is achieved with high throughput without such problems. The interferometer used in these measurements is shown schematically in figure 7.1. The main difference between it and the non-dispersive interferometer described in chapter 3 is the specimen chamber which forms the end of the static mirror arm as shown. Reflecting optics collimated the radiation from a dc stabilised 120W mercury vapour[81] arc and various thin film dielectric beamdividers gave spectral coverage between 5 and 450cm^{-1}. The interferometer was mounted so that the fixed mirror arm was vertically upwards and terminated inside the specimen chamber by the tops of three rigidly mounted, equilaterally spaced steel balls of 0.75mm radius. During a measurement the specimen and reference would rest on these in turn. The possibility that soft specimens might indent onto these balls under the action of their own weight was avoided by additionally supporting the reflector in use on three other balls set between the rigid ones to form the points of a regular hexagon. The extra supports were each fixed to a counter-balanced arm that was free to move in a vertical arc with the counterbalances

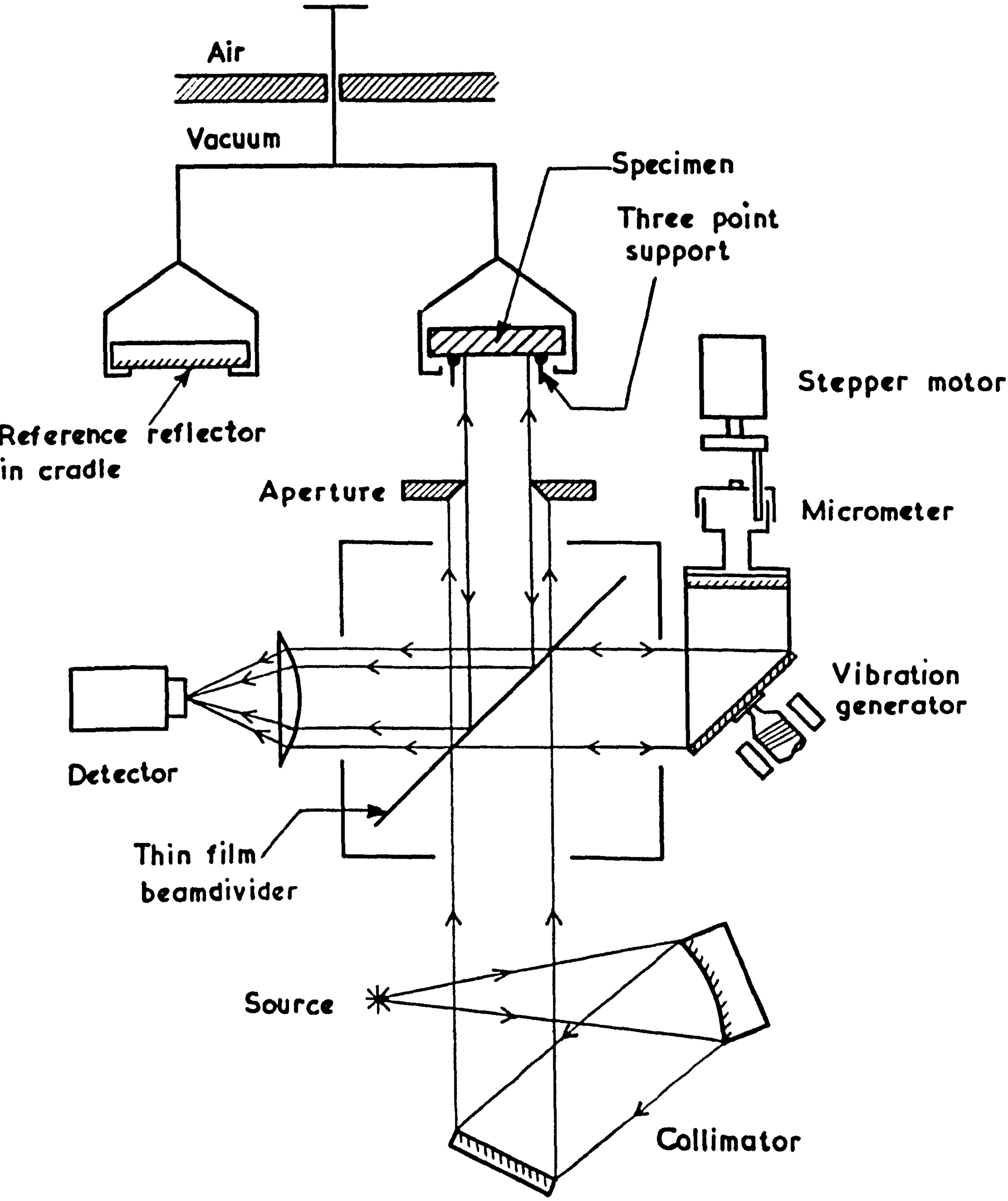

Fig.7.1. Schematic representation of the dispersive reflection interferometer.

adjusted to take almost all of the specimen weight so that the net downward force on the fixed supports was small. A small vee-block in each arm located on a knife edge to form the pivot of the system. The three fixed supports were mounted on an adjustable gimball so that the reflecting plane could be set perpendicular to the incident radiation. This support-alignment assembly is shown in a partially cut-away form in figure 7.2. The specimen and reference were lifted on-and-off of the supports by cradles that were not in contact during a measurement. These were manually operated from outside the vacuum space. In order to accommodate specimens of irregular shape, and to avoid the necessity of machining specimen and reference into similar shapes, a circular aperture 25mm below the supporting balls was used to define the reflecting area on the specimen and the reference. Reflections from the lower surface of this aperture were unimportant as they would only contribute significantly to the recorded interferogram in the region of -50mm path difference, which was not accessible with the micrometer drive used. The moving mirror arm was bent through a right angle by a plane mirror mounted on a vibration generator so that phase modulation could be used.

7.2.1 PHASE NOISE

The performance of an interferometer is limited by the effects of random noise and systematic error in either or both of the modulus and phase spectra. In the previous chapter it was shown that phase noise is generally the limiting factor in dispersive spectrometry and that for transmission measurements the accuracy with which the specimen thickness may be determined usually provides the overall limitation on the determination of the refractive index. Dispersive reflection measurements, of the type which we shall consider, do not usually require a knowledge of the specimen thickness and in this section we shall examine the magnitudes of the phase noise from various sources in

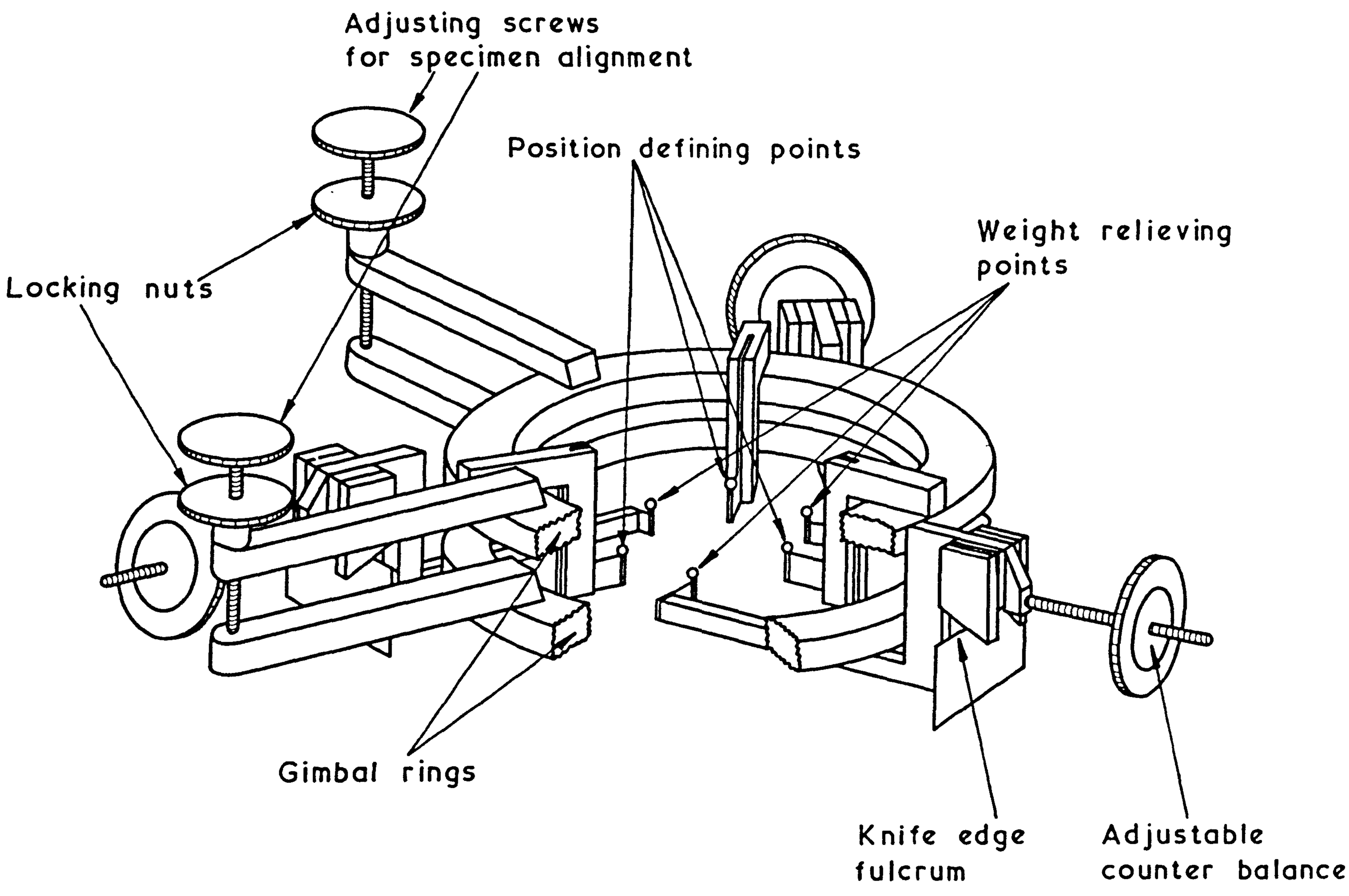

Fig.7.2. The specimen support and alignment system. The gimbal rings are shown partly cut-away for clarity.

this interferometer:

(a) Systematic phase error.

Systematic phase error in this instrument has three main sources and is, potentially, of far greater magnitude than random phase noise:

(i) Backlash in the moving mirror drive, or differential thermal expansion between the two arms of the interferometer, will cause an unknown displacement of the sampling combs of the specimen and reference interferograms.

(ii) Non-exact replacement of the specimen surface by that of the reference, and vice versa.

(iii) Non-flat specimen and reference surfaces.

All three of these have the same effect of introducing an additional term into the phase spectrum that is linearly dependent on the product of wavenumber and a distance that is characteristic of the particular error. The first of these, backlash, may be eliminated by the use of the mode of operation described in the following section and is not discussed here. The typical size of the second source of systematic error, non-exact replacement of the reflecting surfaces, may be seen with reference to figure 7.3. The left hand side of this, (a), shows the central portion of a phase modulated interferogram in the vicinity of zero path difference. Over a few micrometres on either side of zero path difference the interferogram intensity is a fairly good linear function of path difference and can be used to monitor changes in the position of the supported reflector. Thus, in (b), the points show the intensity (left hand ordinate scale) recorded near to zero path difference for sequential removals and replacements of a

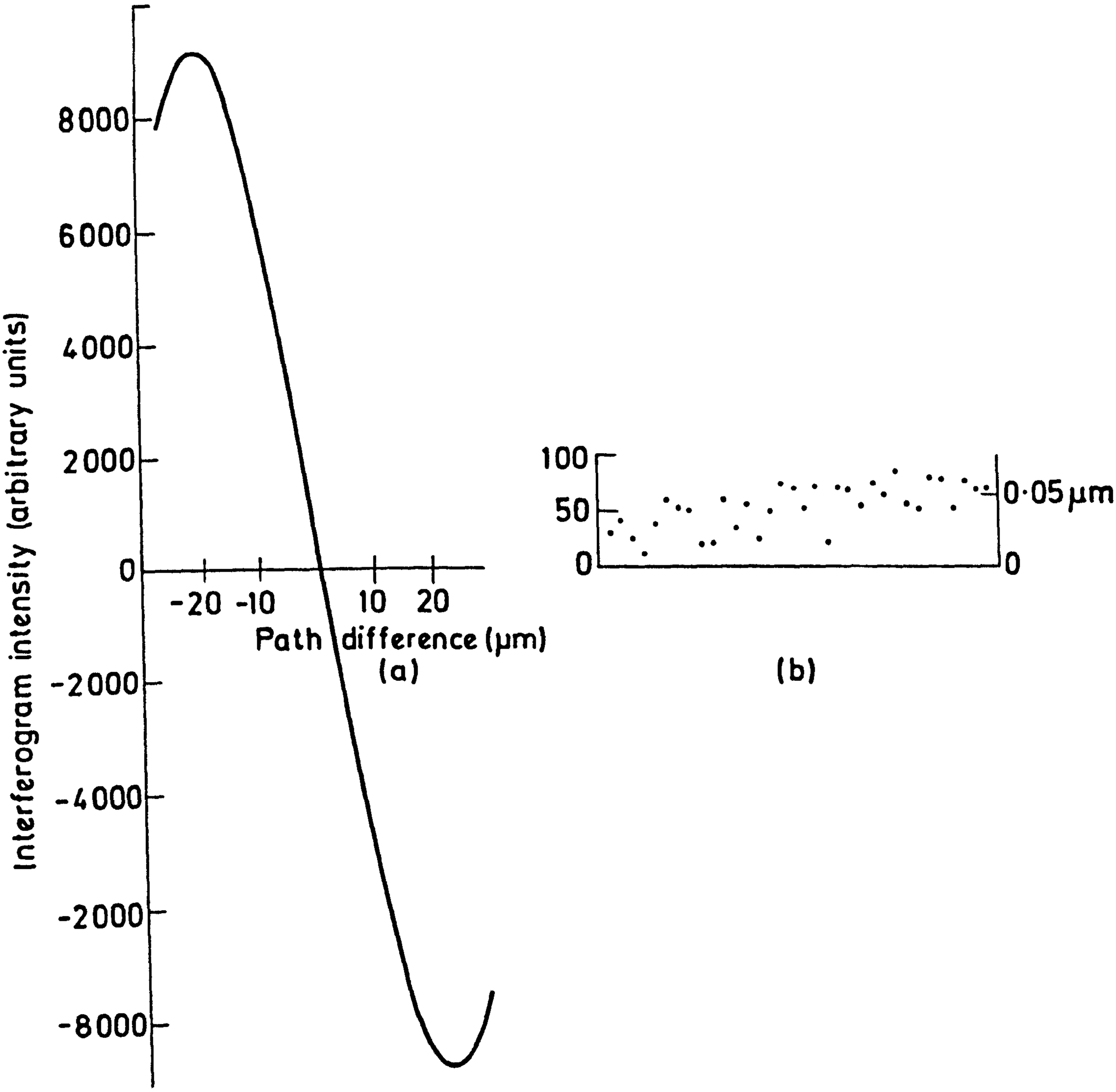

Fig.7.3. The first part,(a), shows the variation of interferogram intensity near to zero path difference for a typical phase modulated interferogram. In (b) the path difference of the interferometer has been set close to zero and each point represents (on the LHS ordinate scale) an independent recording of the interferogram intensity after the mirror was lifted off and replaced on the support system. The point-to-point variation provides a measure of the reproducibility of the positioning of the specimen. The RHS ordinate scale shows the corresponding displacement scale derived from the intensity-path difference information of (a).

mirror on the six point support. The right hand ordinate scale is the corresponding mirror position derived from (a), and the standard deviation of these points from their mean value corresponds to a displacement of 0.016μm in path difference. The displacement-equivalent of the random intensity noise at zero path difference was 0.008μm and therfore, over a series of measurements, we conclude that the specimen support system would give an average value of the displacement of the specimen and reference surfaces that was less than 0.01μm , in path difference terms. At a wavenumber of $100cm^{-1}$ this would be equivalent to a systematic phase error of about 0.6 milliradians. The steady increase with time of the ordinates of the points plotted in (b) was due to differential thermal expansion between the arms of the interferometer.

The effect that a non-flat surface has on the measured phase and modulus spectra may be discussed with reference to figure 7.4 which shows an interferometer in which one of the reflectors has a concave surface, a situation that can often arise with thin specimens. If we consider that this surface can be divided up into a large number of small plane elements all of which are, to first order, parallel then the electric field vector reflected from the n^{th} element will interfere at the exit aperture with that reflected from the corresponding element on the moving mirror surface to give the intensity interferogram

$$I_n(x_n) = \int_{-\infty}^{\infty} W_n \cdot \hat{S}_o(\tilde{\nu}) \exp(-i2\pi\tilde{\nu} x_n) \cdot d\tilde{\nu} \qquad \ldots (7.1)$$

In this W_n is the fraction of the spectrum, $\hat{S}_o(\tilde{\nu})$, incident on the entire specimen that reaches the n^{th} element, and x_n is the path difference between that element and the corresponding one on the moving mirror. This will occur for each element forming the surface so that elements displaced from each other by δ in path difference give rise to interferograms whose bright fringes are

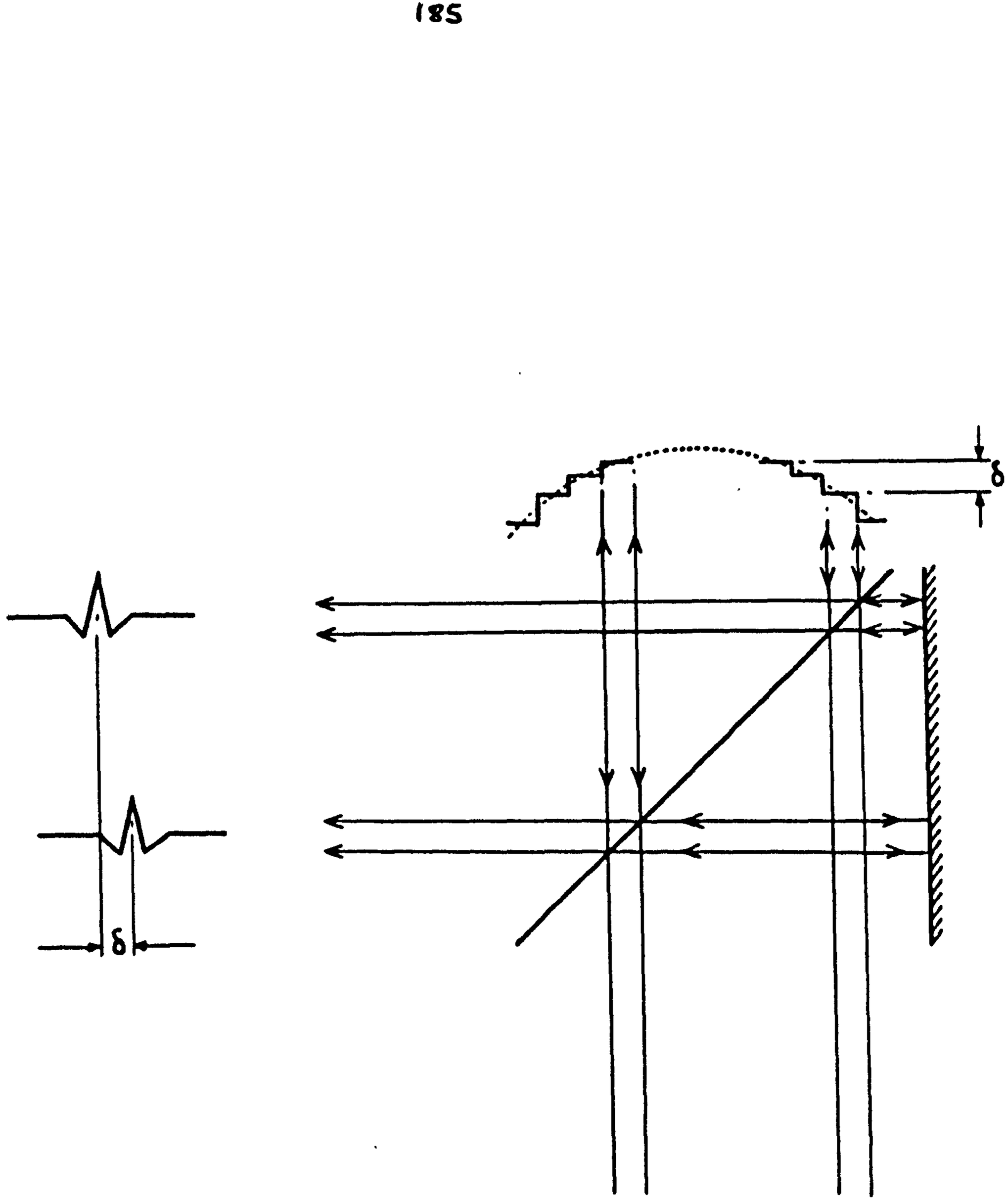

Fig.7.4. Illustrating the effect that a non-flat specimen has on the measured interferogram.

similarly displaced as shown in the figure. When, therefore, the output beam is condensed onto a detector the interferogram recorded from the entire specimen would be thesum of these elemental interferograms and after transformation gives the complex spectrum

$$\sum W_n . \hat{S}_o (\tilde{\nu}) . \exp i2\pi\tilde{\nu}\Delta_n \qquad \ldots (7.2)$$

where Δ_n is the displacement of the zero path difference position of the n^{th} interferogram from the position taken as the computation origin of the composite interferogram. As the summation of W_n over the entire surface is unity the computed modulus spectrum will be independent of the surface profile, within the limitation of the model of that profile. The phase spectrum will, however, be affected by the surface profile and will include the term

$$2\pi\tilde{\nu}\sum\Delta_n \qquad \ldots (7.3)$$

due to the deviation of the surface from a plane profile. In this the sum, $\sum\Delta_n$, represents the displacement of the 'equivalent' flat surface of the specimen from the plane that a perfectly flat surface would have occupied in its place. This simple analysis breaks down when the surface at the n^{th} element is not normal to the incident radiation so that the reflected radiation does not meet that from the moving mirror at the exit aperture.

The linear phase errors introduced by these two systematic effects are best dealt with by having a well designed instrument and a flat specimen so that neither occur. This may not always be possible andunder certain conditions the error can be removed from the phase spectrum by a separate determination of the optical constants over a limited spectral range in, or adjacent to, that of the reflection measurements. This allows the true value of the phase to be calculated and the measured spectrum adjusted to pass through this value. The subsidiary measurement would normally be performed in a transmission

dispersive experiment and would be in the single pass mode described in section 6.6 as the specimen would usually be heavily absorbing.

(b) Random phase noise

Random phase noise arises from the effects of random intensity noise in the recorded interferogram. Its magnitude and character reflect the quality of the experimental procedure and are both wavenumber and resolution dependent. Typical levels of random phase noise obtained with this instrument may be seen from the curves plotted in figure 7.5. The upper curves refer to the main ordinate scale and represent two independent determinations of the phase spectrum using a plane aluminised glass blank as the reflector. They were obtained with a 25mm aperture, a 6μm thick melinex beamdivider and a diamond-windowed Golay cell at a resolution of $1.2cm^{-1}$. The two are very similar and show a small linear increase with wavenumber due to non-coincidence of the zero path difference position with the sampling comb. The significant deviations from this which occur above $300cm^{-1}$ result from interferogram asymmetry but are not important as they disappear when the phase difference is formed. The level of random noise in these spectra may be judged by the insert which shows their difference. Over most of the spectral range the level of random noise is less than $\pm$ 5 milliradians, increasing significantly towards the low and high wavenumber beamdivider cutoffs where the signal levels become low. Although this is a typical result it must be remembered that it was obtained with the use of mirror reflectors. In a real measurement the specimen reflectivity may be significantly less than unity and the specimen interferogram will have a correspondingly lower signal-to-noise ratio than the reference interferogram, which will give rise to a noisier phase spectrum.

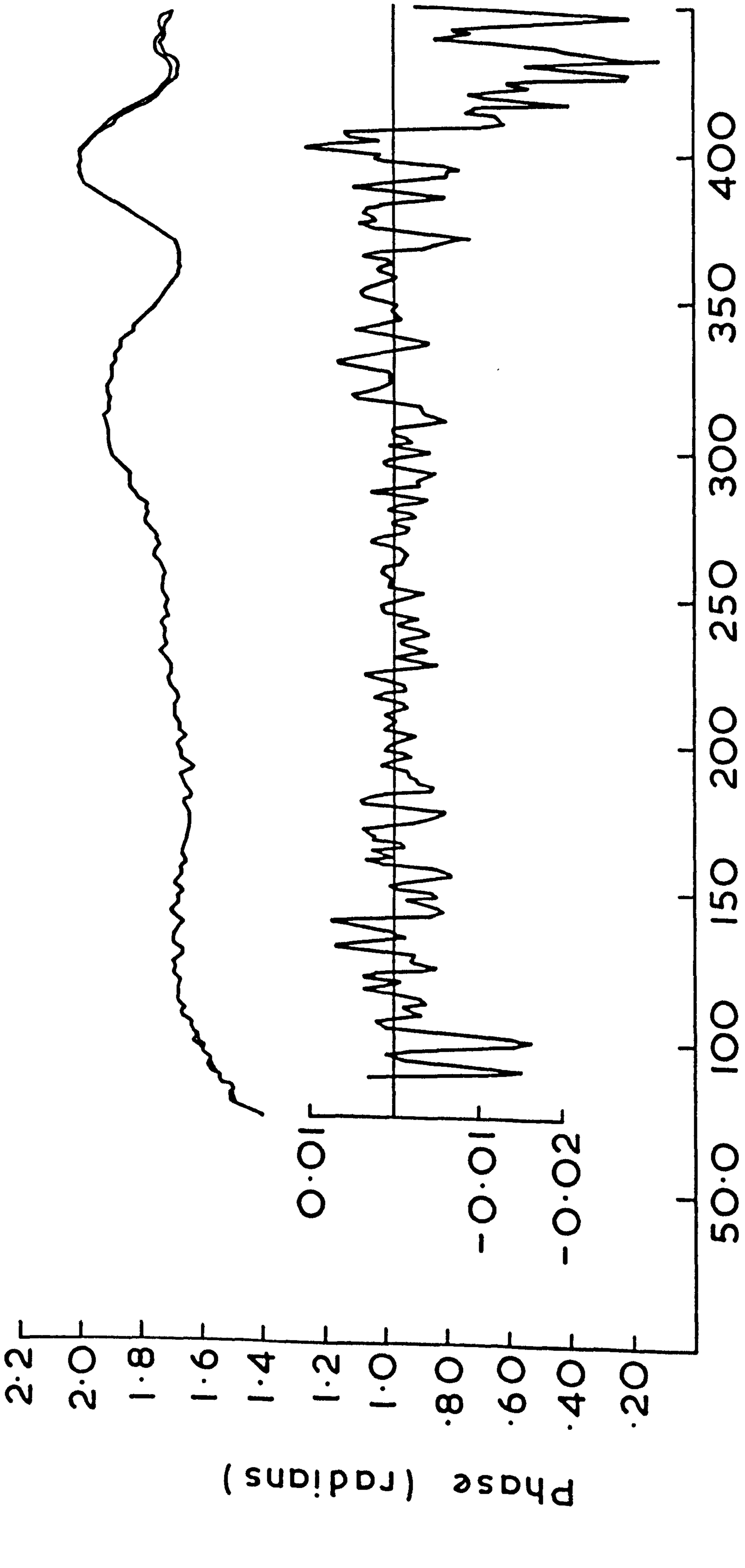

Fig.7.5. The upper curves, which refer to the main ordinate scale, show two typical phase spectra obtained independently from the dispersive reflection interferometer. The insert shows the difference of the two spectra and illustrates the level of random noise present in the measurement.

7.2.2 BACKLASH

If the sampling combs of the specimen and reference interferograms do not have a known spatial relationship a systematic phase error similar to those discussed in the previous section will result. This is usually avoided by starting the moving mirror drive at the same path difference position for each interferogram. If, however, there is backlash in the drive system, or if the starting point is carelessly set, or if there is differential expansion between the two arms of the interferometer the sampling combs will be displaced by an unknown amount. It is necessary to suppress or avoid this effect as it can easily distort the small phase shift that one is attempting to measure. The following procedure eliminates this effect and removes the necessity for starting the mirror drive at the same position for each interferogram.

Firstly, the interferogram for the reference reflector is recorded in the usual manner and the moving mirror then set to a position near to zero path difference. For a phase modulated system this should lie between the positions of minimum and maximum detected intensity on either side of zero path difference. The interferogram intensity at this point is recorded, several times if necessary to provide a noise-free average and, without displacing the moving mirror, the reference reflector is replaced by the specimen and the new interferogram intensity recorded. Finally, the specimen interferogram is recorded. As the two reference intensities were recorded at the same position of path difference the identification of the same values in the appropriate interferograms allows the correct spatial relationship of the two sampling combs to be discovered, removing the effects of backlash.

In general the intensity values to be found in the interferograms will not occur at sample points so that it is not convenient to align them prior to transformation

and the adjustment is made in the phase spectra, the modulus spectra being unaffected by the displacements of the sampling combs. The nature of the correction procedure may be seen with reference to figure 7.6 which shows a reference and a specimen interferogram recorded in the manner set out in the previous paragraph. The reference intensities i_1 and i_2 have been identified in their respective interferograms at apparent path differences of x_1 and x_2 as shown, although the backlash procedure has determined that they occur at the same path difference value. The sample points at apparent path differences x_R and x_S are used as the computational origins and the phase difference spectrum

$$\Phi = ph\{\hat{S}_{x_S}\} - ph\{\hat{R}_{x_R}\} \qquad \ldots (7.4)$$

is computed, whereas that required for the computation of the optical constants is

$$\Phi' = ph\{\hat{S}_{x_2}\} - ph\{\hat{R}_{x_1}\} \qquad \ldots (7.5)$$

in these $\hat{S}$ and $\hat{R}$ represent the specimen and reference spectra respectively and the subscript gives the path difference position used as the computational origin. The Fourier transform shift theorem shows that the phases of the spectra computed from the various origins are related by

$$ph\{\hat{S}_{x_S}\} = ph\{\hat{S}_{x_2}\} + 2\pi\tilde{\nu}(x_2 - x_S) \qquad \ldots (7.6)$$

and,

$$ph\{\hat{R}_{x_R}\} = ph\{\hat{R}_{x_1}\} + 2\pi\tilde{\nu}(x_1 - x_R) \qquad \ldots (7.7)$$

Thus, the required phase spectrum, Φ', may be obtained from the computed phase difference, Φ, by use of the expression

$$\Phi' = \Phi - 2\pi\tilde{\nu}\{(x_2 - x_S) - (x_1 - x_R)\} \qquad \ldots (7.8)$$

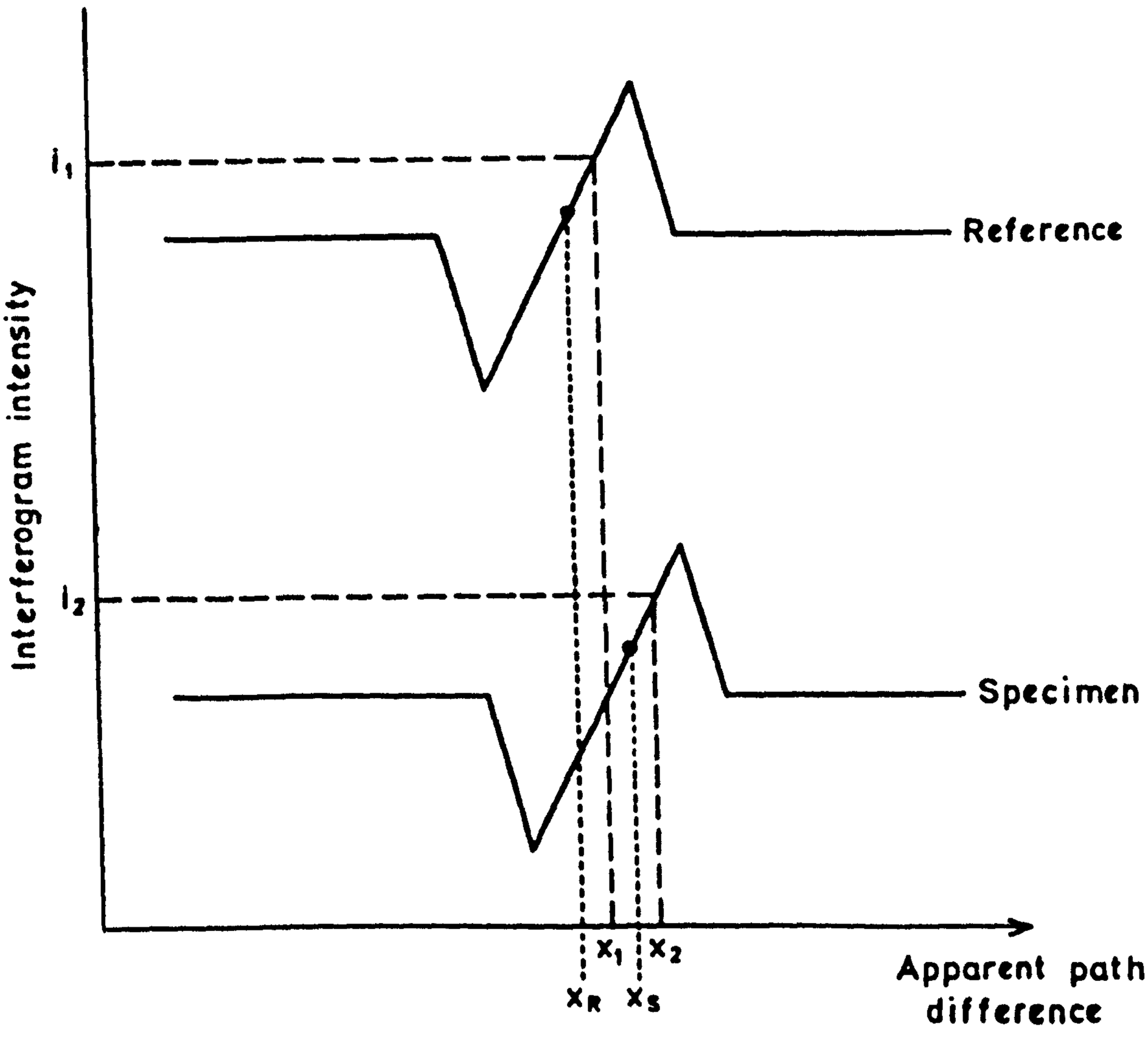

Fig.7.6. Illustrating the backlash procedure. The reference intensities i_1 and i_2 have been identified in their respective interferograms at apparent path differences of x_1 and x_2 as shown. The sample points at apparent path differences of x_R and x_S are used as the computational origins.

as both $(x_2 - x_S)$ and $(x_1 - x_R)$ are known quantities determined by the backlash procedure. Thus, the effects of backlash-like errors have been suppressed by the use of the reference intensities to effectively align the sampling combs of the two interferometers.

As these reference intensities will not in general occur at sampled interferogram ordinates it is necessary to interpolate in each interferogram to find the apparent path differences at which they occur. This was achieved by the use of the following inverse interpolation procedure based upon Stirling's formula for central differences [211]. The sampled intensity value, i_o, in the interferogram that is closest to the reference value, i, is located and the following difference table computed

Path Difference	Intensity				
x_{-2}	i_{-2}				
		Δ_{-2}			
x_{-1}	i_{-1}		Δ^2_{-2}		
		Δ^1_{-1}		Δ^3_{-2}	
x_o	i_o		Δ^2_{-1}		Δ^4_{-2}
		Δ^1_o		Δ^3_{-1}	
x_1	i_1		Δ^2_o		
		Δ^1_1			
x_2	i_2				

where the difference Δ^n_m is given by

$$\Delta^n_m = \Delta^{n-1}_{m+1} - \Delta^{n-1}_m \qquad \ldots (7.9)$$

Scarborough [211] shows how Stirling's formula for central differences may be inverted and used with this difference table to give the path difference x_1 at which the reference intensity i is located as

$$x_i = x_o + h.\left[\left\{\frac{i-a_o}{a_1}\right\} - \frac{a_2}{a_1}\cdot\left\{\frac{i-a_o}{a_1}\right\}^2 + \left\{\frac{-a_3}{a_1} + 2\left\{\frac{a_2}{a_1}\right\}^2\right\}\cdot\left\{\frac{i-a_o}{a_1}\right\}^3\right.$$

$$\left. + \left\{\frac{-a_4}{a_1} + 5.\frac{a_2 a_3}{a_1^2} - 5.\left\{\frac{a_2}{a_1}\right\}^3\right\}\cdot\left\{\frac{i-a_o}{a_1}\right\}^4 + \ldots\ldots\right] \quad \ldots (7.10)$$

where h is the path difference interval between adjacent sample points, and

$$a_o = i_o$$

$$a_1 = \frac{\Delta^1_{-1} + \Delta^1_o}{2} - \frac{\Delta^3_{-2} + \Delta^3_{-1}}{12}$$

$$a_2 = \frac{\Delta^2_{-1}}{2} + \frac{\Delta^4_{-2}}{24} \quad \ldots (7.11)$$

$$a_3 = \frac{\Delta^3_{-2} + \Delta^3_{-1}}{12}$$

$$a_4 = \frac{\Delta^4_{-2}}{24}$$

All of these steps, the location of i_o, setting up the difference table and the solution of equation (7.10) were executed by a single, short Algol programme. The backlash procedure could be used for amplitude modulated interferograms but it would be necessary to define which side of the bright fringe the reference intensity was on in order to avoid ambiguity.

7.2.3 THERMAL STABILITY

In principle the backlash procedure should remove the effects of the differential thermal expansion between the two arms of an interferometer from the phase difference spectrum. In practise gross expansions which fluctuate on the time scale of a single measurement will not be taken out. In order to guard against

this two precautionary measures were taken in the construction of the interferometer.

Firstly, the bulk of the interferometer was made from duraluminium with some mild and stainless steel in the specimen support system and moving mirror drive. Therefore, in the original form of the interferometer the two arms were designed to be thermally equivalent at zero path difference. This meant that the sum

$$\sum \alpha . \ell \qquad \ldots (7.12)$$

of the product of the coefficient of linear expansion, α, and the length, ℓ, taken over all of the components of each arm was the same for each arm.

Secondly, the large outside areas of the interferometer had copper cooling plates bolted to them. These had loops of copper tubing soldered to them which were connected in a circuit through which water from a temperature controlled bath was pumped to stabilise the interferometer temperature in order to minimise thermal fluctuations.

The extent to which these measures were successful in stabilising the thermal behaviour of the interferometer can be seen from the curves of figure 7.7. These show the variation of interferometer temperature with time for two typical sets of operating conditions, each with the corresponding time variation of the path difference between the two arms. The path difference variation was determined from the intensity changes observed near to zero path difference in the manner described in section 7.2.1. In part (a) of the figure the water of the temperature-stabilising circuit had not been flowing for long and the temperature of the interferometer was still falling. In a period of 45 minutes it fell by $1.5^{o}C$ while at the same time the path difference between the two arms

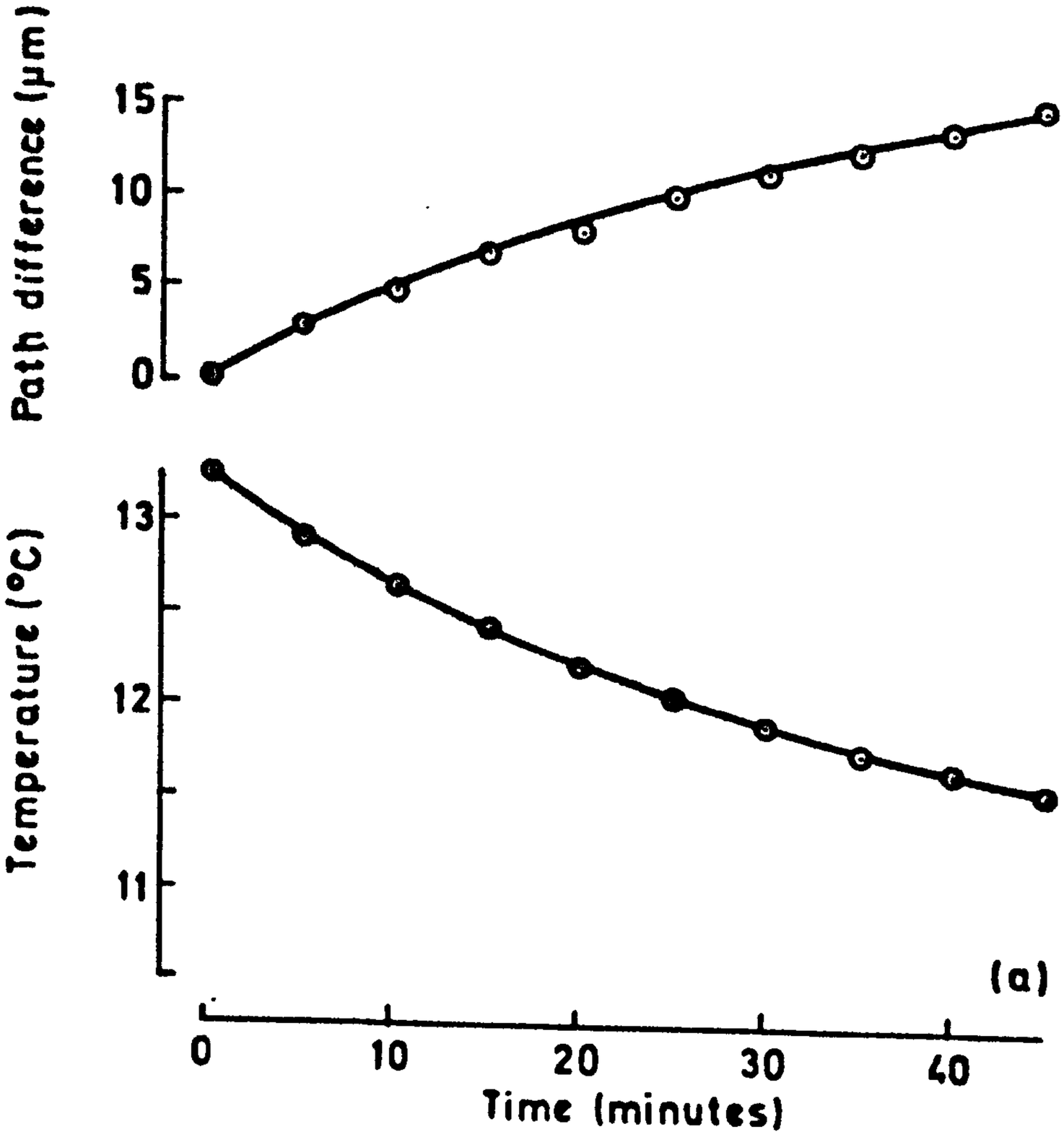

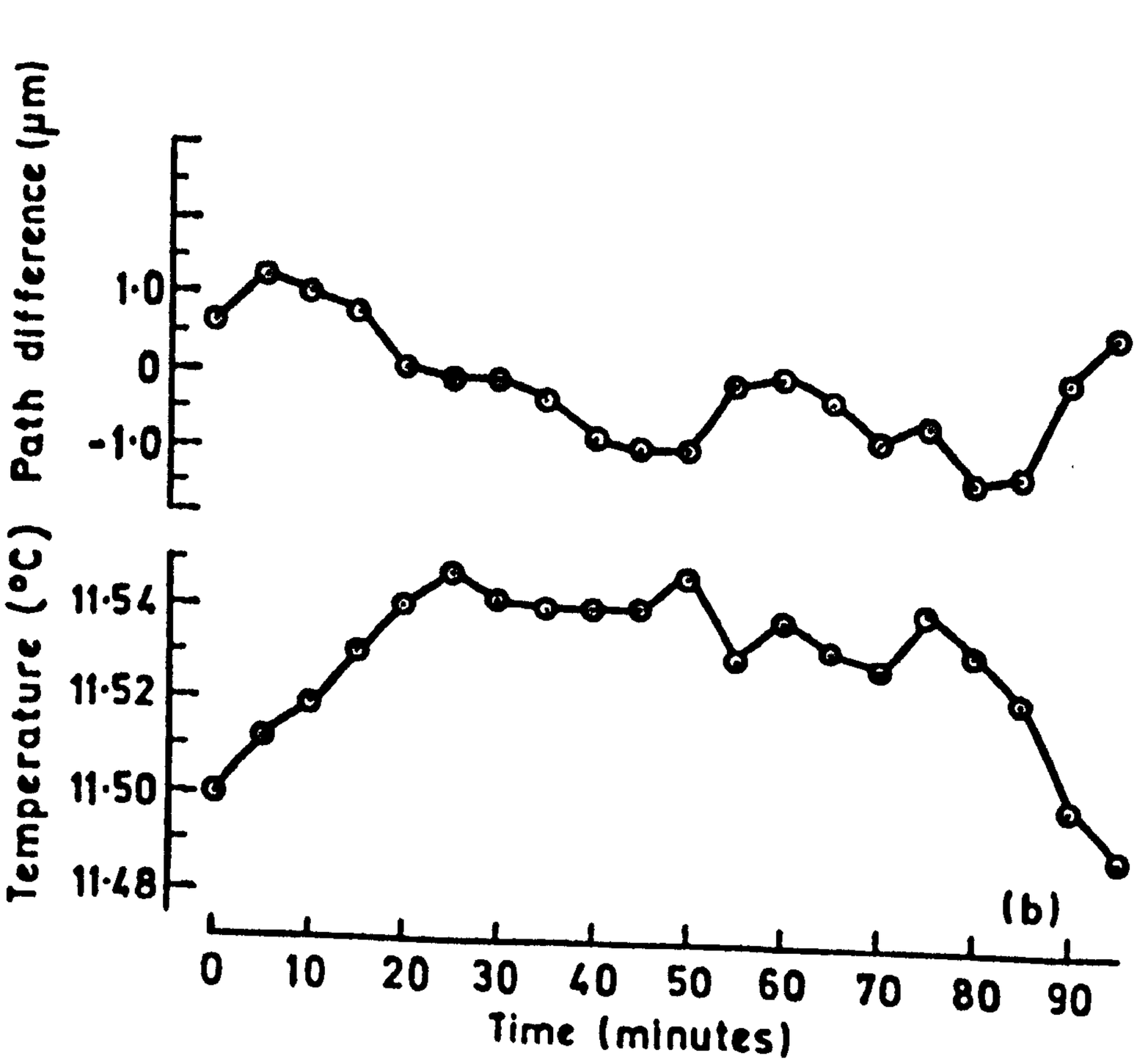

Fig.7.7. Both curves, (a) and (b), show the variation of interferometer path difference with time caused by a variation in the temperature of the interferometer. (a) shows the variation just after the cooling circuit had been turned on and its temperature was still falling. (b) shows the variation an hour later when the temperature was more stable.

increased by 15μm , indicating that either the moving mirror arm had lengthened by 7.5μm , or the fixed mirror arm had shortened by the same amount, or an appropriate combination of both had occurred. The relatively large change in path difference that happened showed that the two arms were no longer thermally equivalent. The measurements shown in part (b) of the figure were taken an hour or so later when the interferometer had stabilised in temperature just above 11.5°C. Over the first 45 minutes the temperature rises to about 11.54°C, stabilises and then falls with superimposed shorter term variations. During this time the temperature varied by less than 0.05°C. Although this is a relatively small change the path difference varied in direct relation with the temperature, falling when it rose, and vice-versa, with excursions between $\pm$ 1μm. This would be a significant amount in an experiment which relied upon the stability of the interferometer to maintain the alignment of the sampling combs but the time scale of these fluctutations is large compared to the time taken to record the reference intensities for the backlash procedure (less than one minute) and, therefore, this level of thermal instability can be accommodated within the experimental procedure.

7.2.4 MODULUS NOISE

The ultimate limitation on the performance of this instrument is the level of noise in the phase spectrum although the noise level in the modulus spectrum also affects the quality of a measurement and is related to the phase noise as both spectra are parametric functions of the sine and cosine transforms of the interferogram. Typical levels of the modulus noise are shown by the curves of figure 7.8. The lower curve, (a), shows a modulus spectrum obtained under the same conditions as the phase spectra of figure 7.5, using a 25mm diameter portion of

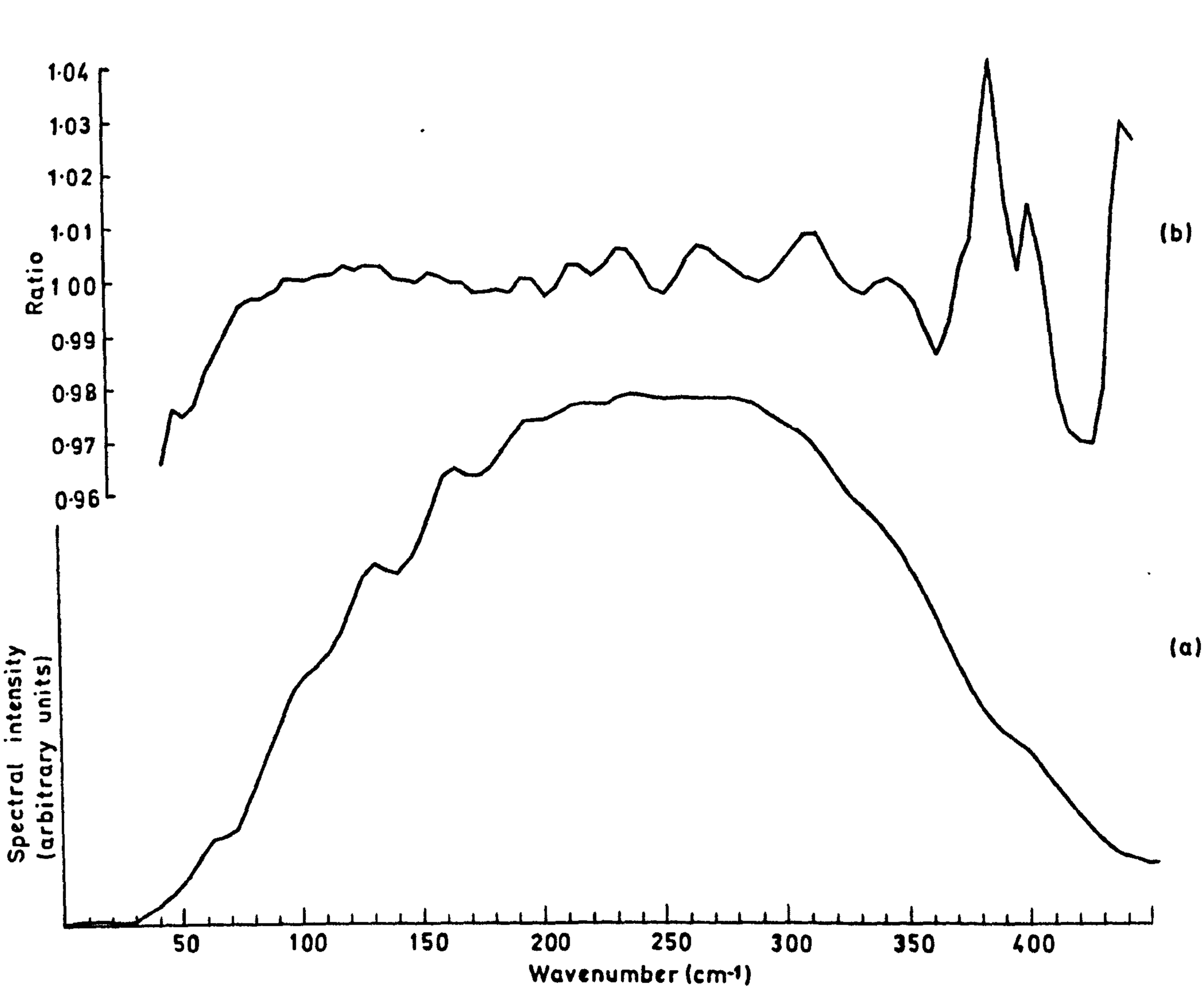

Fig.7.8. The lower curve, (a), shows a typical modulus spectrum obtained with the dispersive reflection interferometer. The upper curve, (b),shows the ratio of this with a similar spectrum recorded independently and illustrates the level of random noise present in these spectra.

an aluminised glass blank as the reflector, a 6μm thick beamdivider and a diamond-windowed Golay cell. The apodised spectral resolution was $2cm^{-1}$. The upper curve, (b), is the ratio of this modulus spectrum with a similar one taken under the same conditions. Over most of the spectral range the ratio is very close to unity, having an rms deviation of about 0.003. Towards the ends of the spectral range, where the signal levels are low, large departures from unity occur and it is usual to restrict the spectral range used for the measurements to avoid these.

7.3 THE ABSOLUTE DETERMINATION OF COMPLEX REFLECTIVITY

The measurement of specular reflectivity at millimetre and submillimetre wavelengths is properly thought of as a relative measurement whose accuracy ultimately rests upon assumptions concerning the reflective properties of a reference surface. In the most usually applied form of the technique the power reflected from a specimen is compared to that reflected from a metal surface which is assumed to be perfectly reflecting so that the ratio of the two detected powers gives the power reflectivity of the specimen. Similarly, the comparison of specimen and reference modulus and phase spectra in a dispersive experiment assumes that the reference surface has a complex amplitude reflectivity

$$\hat{r} = 1.0 \exp i\pi \qquad \ldots (7.13)$$

In either measurement the reference reflector is usually an aluminium, silver or gold thin film vacuum-evaporated onto a glass substrate. Unless the surface is fresh and unscratched, and sufficiently thick to avoid size and skin depth effects, its reflectivity may depart significantly from the ideal behaviour described by equation 7.13 and the above measurement procedures become invalid.

These problems do not occur in the near infrared, visible and ultraviolet regions of the spectrum where techniques that do not assume perfect reflectivity exist (see, for example [212–214]). These depend upon sampling both the incident and reflected beams so that the reflectivity can be calculated independently of a reference surface. The sampling is usually accomplished by switching the position of the detector or by beam deflection techniques with care taken to maintain the equivalence of the switched optical paths and beam geometries. Such methods are not ideally suited to millimetre and submillimetre wavelengths where beams are often poorly defined and have larger cross sections than at shorter wavelengths.

In order to avoid these difficulties of relative measurements a technique was developed for the determination of the complex reflectivity of a fairly transparent specimen in which the reflectivity is related to the optical constants of vacuum to provide an absolutely determined standard of complex reflectivity against which unknown specimens may be compared with confidence. The method is based upon the fact that if the optical constants of a specimen are known with sufficient precision the specular reflectivity of its surface can be calculated more accurately than it can be measured. It relies upon the use of dispersive Fourier transform spectrometry and simply consists of measuring the complex refractive index of a plane parallel, transparent but fairly reflecting solid specimen in a dispersive transmission experiment. This can be done with high precision as demonstrated in the previous chapter and the complex reflectivity of a plane surface of the solid may then be calculated from the measured complex refractive index using Fresnel's equations. As the refractive index measurement only required knowledge of the defined refractive index of vacuum

$$\hat{n} = 1.0 + i\,0.0 \qquad \ldots (7.14)$$

and the length standard, this can be taken as providing an absolute determination of complex reflectivity at submillimetre and millimetre wavelengths. Having thus established a calculated reference material for complex reflectivity it is now possible to perform comparison or calibration experiments in which the complex reflectivity of an unknown specimen is compared to that of the reference in a dispersive reflection measurement. The use of a dispersive measurement at this stage is essential as its phase sensitivity ensures that the complex reflectivity that is transferred is that of the surface of the reference specimen, and not that of it as a whole, as would result from a comparison using power reflection techniques.

7.3.1 THE REFLECTIVITY STANDARD

The material chosen for these studies of reflectivity standards must satisfy several requirements. It should be sufficiently transparent in the spectral region of interest that its complex refractive index can be measured in a transmission experiment with high accuracy but, it must also be sufficiently reflecting for its calculated reflectivity to be accurately transferable to an unknown specimen in a reflection comparison. Additionally, it must be capable of being optically worked to a plane parallel form with its thickness unambiguously determined to better than 1 part in 10^3, and must be optically and mechanically stable. These requirements are easily met by pure, elemental semiconductors and silicon was adopted for this work. Its optical constants have been studied by several workers at submillimetre wavelengths [111,171,184] and was chosen in preference to germanium as the presence of phonon bands in germanium at wavenumbers as low as $100cm^{-1}$ leads to structure in the optical constants which is best avoided for the present application. The corresponding bands in

silicon occur above 600cm^{-1} and are consequently not a problem. The particular specimen of silicon used was that whose optical constants were presented and discussed in section 6.4. Using these measured values of the complex refractive index spectrum, the complex amplitude reflectivity of a surface of the specimen was calculated from equations 2.33 and 2.34 for normal incidence from a vacuum and is shown in figure 7.9. Over the spectral range covered by these measurements the amplitude reflectivity changes by about 1 part in 10^3 as it increases from 0.5462 at 5cm^{-1} to a virtually constant value just below 0.5469 at 120cm^{-1}. The imaginary part of the complex refractive index was sufficiently small (< 0.023) that the amplitude reflectivity was primarily determined by the real refractive index and closely followed its spectral variation. The phase on the other hand was primarily determined by the absorption index and was, for the low values of k in this material, very close to π radians, increasing above this by only 4 milliradians close to 5cm^{-1} where k was greatest.

These curves represent the calculated values of the complex reflectivity of an interface between vacuum and the silicon specimen, for normal incidence from the vacuum. As these spectra are going to form the basis of an absolute complex reflectivity it is appropriate to estimate the level of random and systematic error present in them arising from errors in the measurement of the complex refractive index. This is summarised in table 7.1. The major uncertainty arises from the

Source		Δr	$\Delta\phi^r$ (rad)
Random	Systematic		
n, 10^{-4}-2×10^{-4}	-	10^{-5}-2×10^{-5}	-
α, 0.05 Np.cm^{-1}	-	-	7.4×10^{-5} *
-	thickness, 10^{-3}mm	10^{-4}	-
-	temperature change of 1-10K	10^{-5} - 10^{-4}	-

Table 7.1 The estimated errors, Δr and $\Delta\phi^r$, in the complex reflectivity of the silicon specimen calculated from its measured complex refractive index. *Calculated for $\tilde{\nu}$ = 10cm^{-1}.

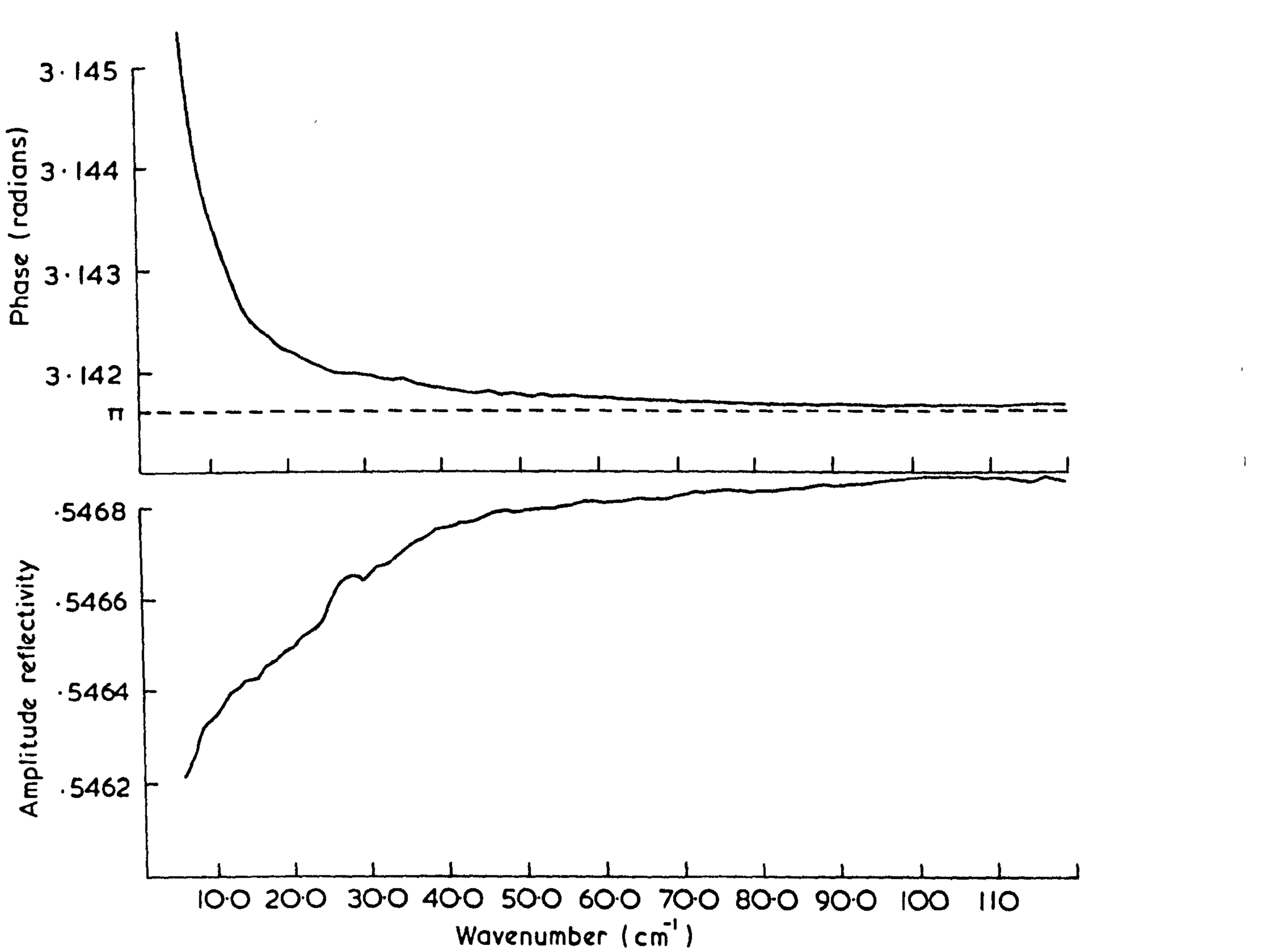

Fig.7.9. The complex reflection spectrum of a 10 ohm metre specimen of silicon. The spectrum was calculated from the measured complex refractive index spectrum of the specimen described in section 6.4.

possible systematic error of up to 10^{-3}mm in the thickness measurement which, through the real refractive index, leads to a possible systematic error in the amplitude reflectivity of 10^{-4}. All other errors in the reflectivity are nearly an order of magnitude below this. The major error in the calculated phase arises from the random error in the determination of the power absorption coefficient which leads to a phase uncertainty of 7.4×10^{-5} radian which, as will be demonstrated in the following sections, is insignificant compared to the random error generated in the dispersive measurement of ϕ^r.

7.3.2 THE APPLICATION TO THIN METAL FILMS

The technique for the absolute determination of complex reflectivity outlined in the previous section is most suitable for use with fairly transparent specimens. If the specimen whose reflectivity is to be determined is not sufficiently transparent for its complex refractive index to be measured in transmission its complex reflectivity can be compared to that of a transparent specimen that has previously been calculated by the above procedure. In order to illustrate the precision with which the calculated complex reflectivity scale of the front surface of the silicon specimen may be transferred to specimens of unknown reflectivity, measurements were made of the complex reflectivity of four thin aluminium films vacuum evaporated onto glass substrates. This is a particularly important measurement as it will also establish the extent to which these films depart from ideal reflecting behaviour. The film thicknesses were 0.017, 0.040, 0.095, and 0.20 μm* and each was deposited onto a 50mm diameter by 5mm thick disc of soda lime silica glass. The blanks were optically polished to be flat to better than 0.2 μm on their aluminised surfaces. The complex

---

* The films were produced, and their thicknesses measured, by Mr M.J.Downs and Miss D.J.Croxford of the Division of Mechanical and Optical Metrology, NPL.

reflectivity of each was measured using the silicon specimen as the reference reflector in the dispersive reflection interferometer. The measurements were made between 10 and 40cm^{-1} at a spectral resolution of 2cm^{-1} and a temperature of 290K using a liquid helium cooled Rollin detector.

The results of these measurements are shown in figure 7.10 which shows the amplitude of the complex Fresnel reflectivity for each film-substrate structure. The skin depth at 10cm^{-1} for bulk aluminium of resistivity 2.76×10^{-8} ohm.m is about 0.15 μm so that the observed decrease in reflectivity with decreasing wavenumber for the thinner films is not surprising. Each curve is the average of four independent determinations and over most of the spectral range these were reproducible to within $\pm$ 0.001. Below 14cm^{-1} beamdivider cut off caused the reproducibility to become somewhat worse than this as is shown by the measured reflectivity of the 0.20 μm specimen rising above unity. The small periodic structure on all of these spectra, with a period of between 3 and 4cm^{-1}, is not real, but arises from imperfect ratioing out of a channel spectrum present in the background spectrum of the interferometer. The amplitude of this is about 0.001. Thus, the amplitude reflectivity scale of the silicon specimen front surface, which had been calculated with a precision of about 10^{-4}, has been transferred to the thin films with a precision of about 10^{-3} that was largely determined by the random and systematic errors in the reflectivity comparison. In a similar manner the phase of the complex reflectivity of all three films was found to be π radians within a random scatter of 10 milliradians arising from the phase comparison. The most important aspect of these results is that they show that significant departures from the perfect reflecting behaviour or equation 7.13 are found in aluminium films of less than 0.1 μm thickness. However, most aluminised mirrors used at these wavelengths would be much thicker than this. For example, in reflectivity measurements in this laboratory film thick-

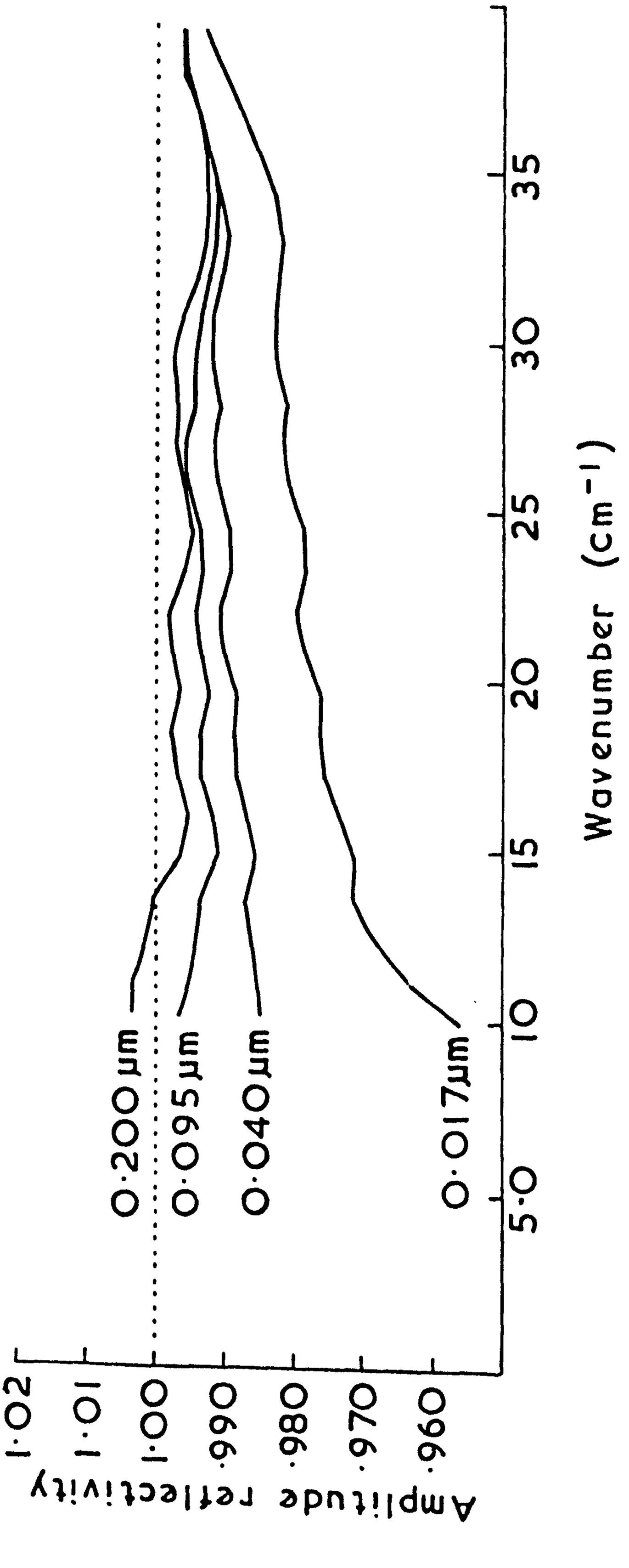

Fig.7.10. The amplitude reflection spectra of four thin films of aluminium vacuum evapourated onto silicate glass substrates. The spectra were determined by comparison with the calculated reflectivity of the silicon specimen shown in fig.7.9 using the absolute method of determining complex reflectivity described in this section.

nesses of about 0.5 μm are normally used, so that the approximation of their reflectivity to 1.0 $\exp i\pi$ would be a more valid assumption than for the thinner films. The most precise dispersive reflectivity measurements, though, ought to be performed with a calculated reflector such as the silicon specimen as the reference reflector.

It is of interest to compare these measurements with calculations based upon simple theory. Carli[215] has developed expressions for the reflectivity of a thin metal film sandwiched between two semi-infinite media using the bulk conductivity model in the limit that the film thickness is very much less than the skin depth. As the thinnest of our films is only just approaching this condition we have made exact calculations for both the bulk conductivity assumption and a simple size effect model, in both cases treating the reflecting structure as possessing three interfaces, vacuum-metal, metal-glass and glass-vacuum. The infinite summation of all the internally reflected rays of such a structure can be dealt with in a variety of ways that have been summarised by Heavens[216]. For a non-absorbing three interface structure Crook[217] has derived an explicit expression for the amplitude reflectivity that is easily generalised into the following expression for the complex reflectivity

$$\hat{r}_{0123} = \frac{\hat{r}_{01} + \hat{r}_{12}\hat{a}_1^2 + \hat{r}_{23}\hat{a}_1^2\hat{a}_2^2 + \hat{r}_{01}\hat{r}_{12}\hat{r}_{23}\hat{a}_2^2}{1 + \hat{r}_{01}\hat{r}_{12}\hat{a}_1^2 + \hat{r}_{01}\hat{r}_{23}\hat{a}_1^2\hat{a}_2^2 + \hat{r}_{12}\hat{r}_{23}\hat{a}_2^2} \quad \ldots (7.15)$$

of layers 1 and 2 immersed between media 0 and 3 to form the structure 0 1 2 3, for incidence from medium 0. This is cumbersome to use, however, as it does not explicitly separate the modulus and phase terms. We have found it more convenient to deal with the problem in a manner similar to that of Rouard[218], but using complex arithmetical procedures written into an Algol 60 programme to extend the total complex reflectivity at each interface. The values for the

optical constants of glass used in these computations were taken from the dispersive measurements of the previous chapter, and the results of the computations are presented in figure 7.11 for the 0.017 and the 0.095 μm films. The crosses are the experimentally determined points replotted from figure 7.10. The lines marked (a) were derived from the bulk conductivity model using 2.76×10^{-8} ohm.m for resistivity. The measured values are systematically lower than the calculated ones with the discrepancy being particularly pronounced for the 0.017 μm film. The calculated spectra show periodic structure due to multiple beam interference within the layered films, but this occurs below the level of 1 part in 10^5 for the amplitude reflectivity due to the intense absorption in the metal layer and is not apparent on the scale of the figure. In order to improve upon these calculations Fuchs' size effect model for free electrons [219], as outlined by Chopra [220], was applied to the calculation of the reflectivity of the 0.017 μm film. This describes the geometrical limitations imposed by the film boundaries in terms of an effective conductivity σ_{eff} related to the bulk conductivity σ_B by

$$\frac{\sigma_B}{\sigma_{eff}} = \frac{4}{3\delta\left[\ln(1/\delta) + 0.4228\right]} \qquad \ldots (7.16)$$

in the limit that δ, the ratio of film thickness to mean free path, is $\ll 1$. This result is derived by assuming diffuse scattering of the electrons at the film boundaries. For the 0.017 μm film, which most nearly satisfied the condition $\delta \ll 1$, application of equation 7.16 leads to an effective film resistivity of 6.7×10^{-8} ohm.m. Using this value in the calculation of the film reflectivity gives curve (b) of figure 7.11. Between 20 and 35cm^{-1} the calculations are in good agreement with the measurements, but as the model gives a frequency independent resistivity it is unable to describe the spectral

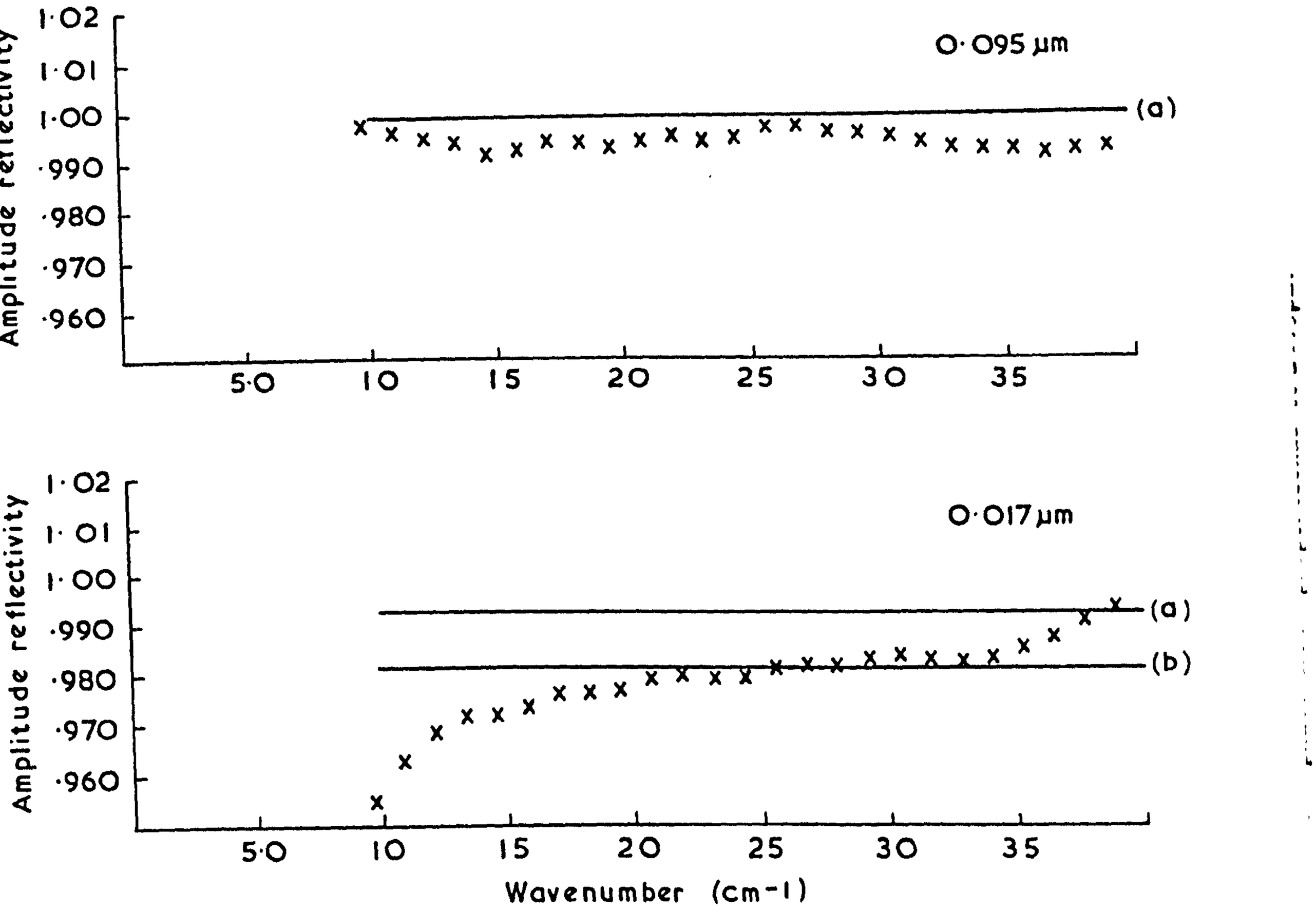

Fig.7.11. A comparison of measurement and theory for the reflection spectra of the 0.017 and 0.095μm films. The crosses show the measured spectra from fig.7.10. The continuous curves labelled (a) represent spectra calculated from the bulk conductivity model, while curve (b) represents the spectrum of the 0.017μm specimen calculated with allowance made for the finite thickness of the film using Fuchs' size effect model for free electrons.

variation of the reflectivity. A more realistic model would need to allow for the nature of the substrate surface, the continuity of the metal film and the parameters of the vacuum deposition as these are all factors which are known to affect the resistivity and, hence, the reflectivity of thin metal films.

7.3.3 POOR QUALITY MIRRORS

In the previous section it was demonstrated that aluminium films with thicknesses of about 0.5 μm on glass substrates show near perfect complex reflectivity behaviour. This was done with measurements on good quality, freshly evaporated films. In practice, laboratory mirrors often become scratched through long usage and it seems reasonable to expect this to degrade the reflectivity for at least two reasons. Firstly, the film is no longer continuous and would have a larger effective resistivity than when freshly formed and, secondly, the total reflecting area has been reduced by the removal of the scratched material.

In order to demonstrate the reduced performance of poor quality mirrors and to underline the need for high quality mirrors for precise reflectivity measurements, the reflectivity of a scratched aluminium-on-glass mirror was determined using the silicon standard as a reference reflector. The mirror was 0.48 μm layer on a 50mm diameter glass blank and had been in use in the laboratory for about six months. Its amplitude reflectivity was determined between 30 and 120cm^{-1} using a quartz-windowed Golay cell at 2cm^{-1} apodised resolution. Figure 7.12 shows the measured amplitude reflectivity of this mirror. The spectrum shown is the average of eleven independent measurements and the standard deviation of this set is also shown, below the main graph. Below 60cm^{-1} the amplitude reflectivity lies within plus-or-minus one standard deviation of unity ($\sim \pm 0.005$). Above 60cm^{-1} the reflectivity falls systematically below unity, showing the degrading effect of the poor quality surface, and reaching values below 0.99 by 120cm^{-1}. This is only 0.01 below unity and may not seem an excessively large

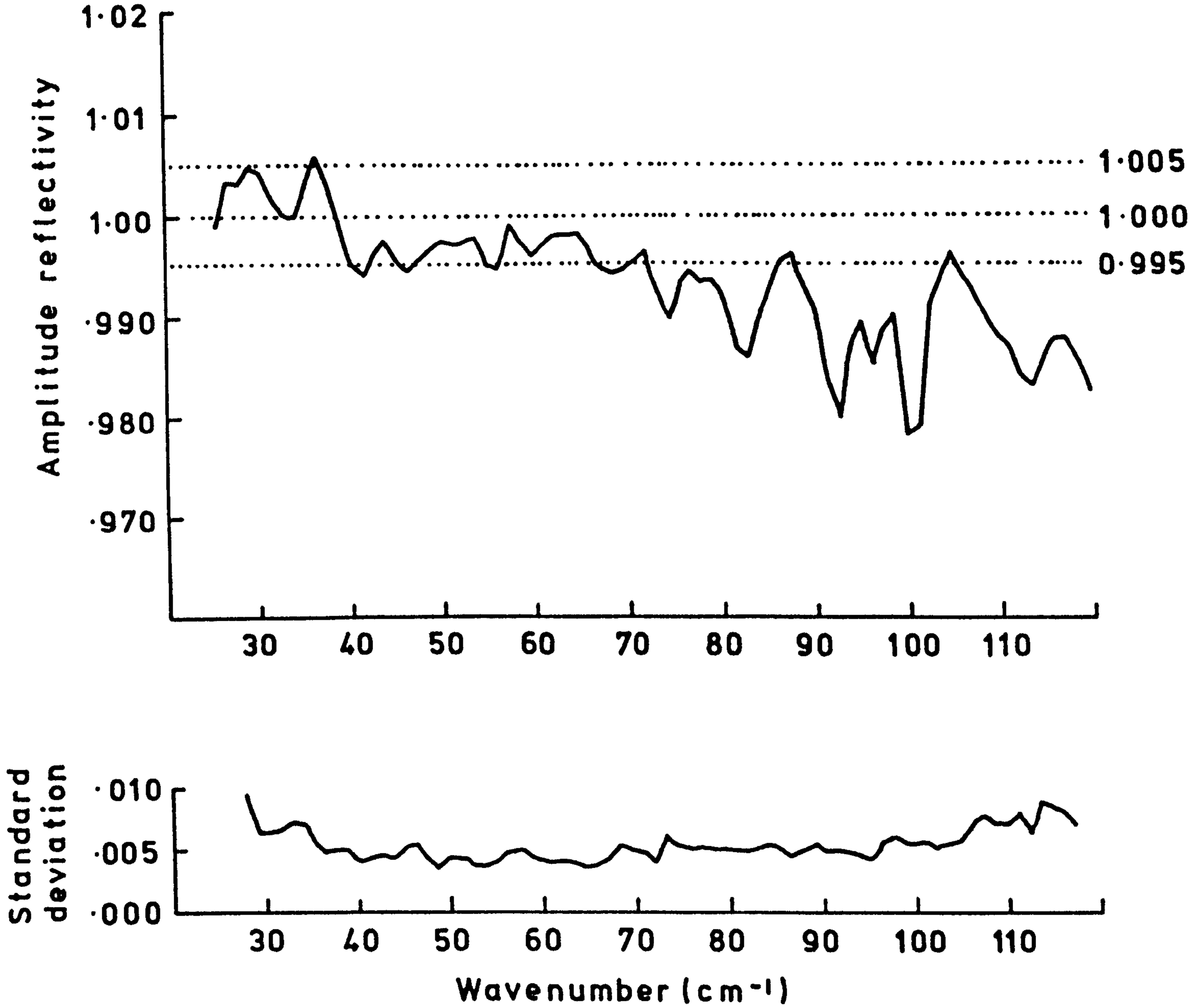

Fig.7.12. The mean and standard deviation of eleven independent determinations of the amplitude reflectivity of a scratched mirror determined between 30 and 120cm^{-1} by comparison with the calculated reflectivity of the silicon specimen using the absolute method of determining complex refectivity.

amount, but the corresponding power reflectivity spectrum of figure 7.13 falls to values close to 0.96 and this would introduce significant errors if the mirror were used in an application where perfect reflecting behaviour had been assumed.

In the spectra of figure 7.12 and 7.13 the sharp features just above 80, 90 and $100cm^{-1}$ are not real but appear to result from the imperfect ratioing out of features present in both mirror and silicon spectra.

7.4 THE EFFECTS OF PHASE AND MODULUS NOISE

Although the performance of this interferometer has been considered in section 7.2 this was with reference to the phase and modulus noise inherent to the measurement process and did not consider how these translated over into noise in the calculated complex reflectivity and refractive index spectra. In this section we shall therefore present the results of measurements on the reststrahlen band of single crystal cadmium telluride in the region of its transverse optic (TO) phonon at $141cm^{-1}$, and will investigate the reproducibility of successive measurements in order to obtain figures for the effects of noise in the computed values of the optical constants. Cadmium telluride was chosen for this investigation for two reasons. Firstly, both r and ϕ^r change by large amounts over the reststrahlen band, allowing the effects of noise to be studied over a wide range of values of the optical constants. Secondly, as distinct from glasses, the dispersive mechanism is fairly well understood so that at least qualitatively, if not quantitatively, the more gross effects of phase and modulus noise become apparent.

7.4.1 THE COMPLEX REFLECTIVITY OF Cd Te

For this investigation of the effects of measurement error the complex reflectivity of a cadmium telluride single crystal in the form of a lamella specimen

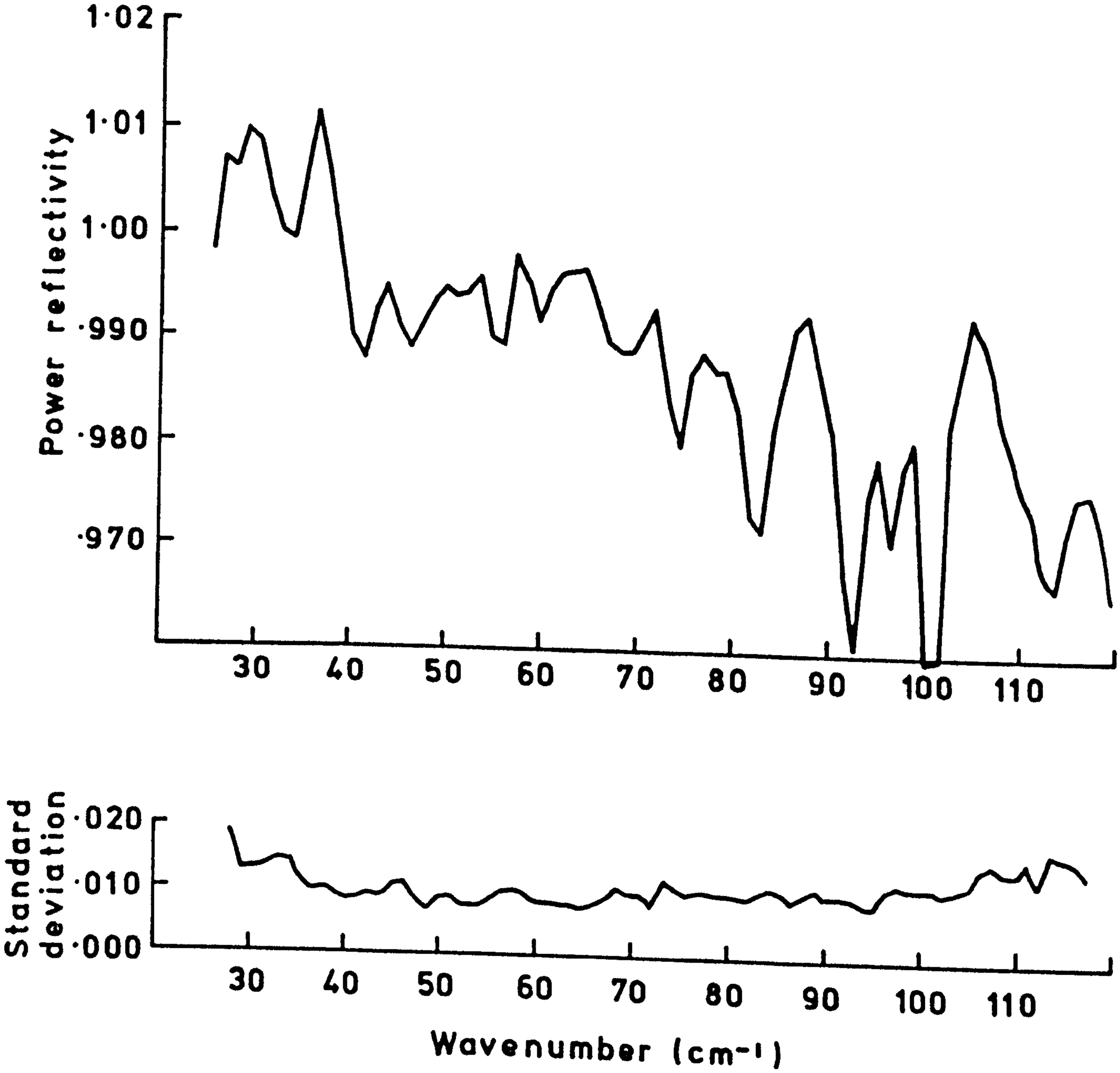

Fig.7.13. The power reflectivity and standard deviation spectra of the scratched mirror calculated from the spectra of fig.7.12.

38mm diameter by 3mm thick was measured between 40 and 240cm^{-1} at 290K. The measurements were made at a resolution of 1cm^{-1} using a 12 μm thick melinex beamdivider and a quartz-windowed Golay cell. The amplitude reflectivity, power reflectivity and phase difference, $\phi^r - \pi$, computed from the specimen and reference phase spectra are shown in figure 7.14. They each represent the average of the same six independent measurements and the standard deviation of both the amplitude reflectivity and the phase difference are also shown.

The reflectivity spectrum is dominated by the reststrahlen band with the amplitude reflectivity increasing from a virtually constant value of 0.54 at the low wavenumber end of this measurement to a maximum of 0.95 at 159cm^{-1}, before falling sharply away to a minimum of 0.14 at 176cm^{-1} to give the characteristic reflectivity profile associated with the lattice resonance. This spectrum also illustrates a very significant advantage of dispersive, rather than power, reflection techniques. With the former r is measured and this is always greater than r^2, which is determined by the latter. Thus, in regions of low reflectivity where $r \gg r^2$ a dispersive measurement is always much easier than a power measurement. Hence, if the present spectrum had been measured non-dispersively, it would have been necessary to determine a reflectivity of 0.02 at the reststrahlen minimum, which could not have been achieved with the same accuracy as the dispersive determination of a reflectivity of 0.14. The phase difference changes rapidly over the reststrahlen band, indicating the large dispersion of the optical constants that is occurring, and reaches a sharp peak of 1.78 radian at 167cm^{-1}, near to the centre of the falling amplitude reflectivity edge.

The standard deviation of the amplitude reflectivity between 50 and 200cm^{-1}, where the signal-to-noise ratio in the modulus spectrum was greatest, is typically about 0.007. This is about twice that studied in section 7.2.4 but, as the

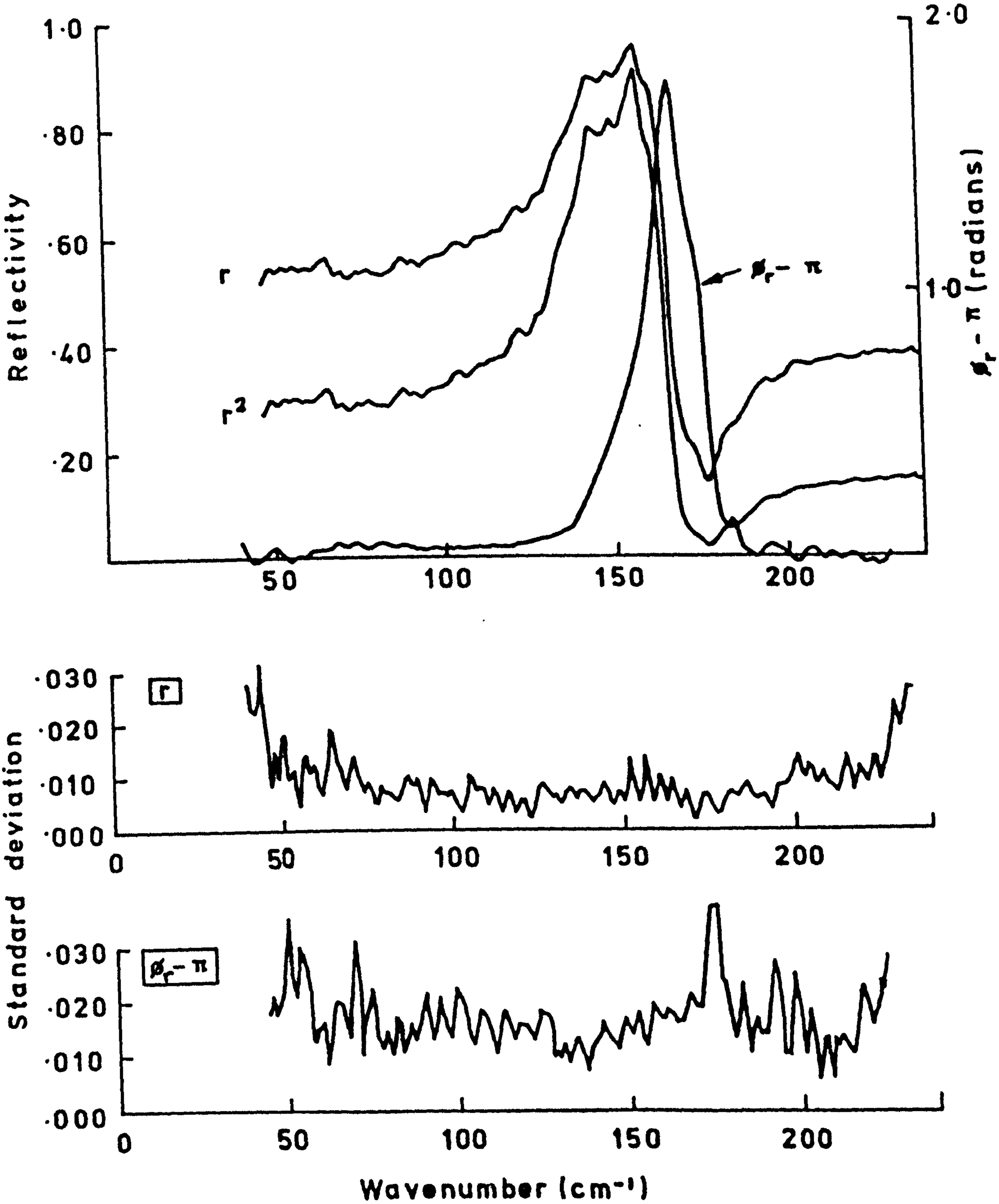

Fig.7.14. The amplitude r, power r^2, and phase difference $\phi_r - \pi$, spectra of a single surface of a specimen of cadmium telluride between 40 and 240cm^{-1} at 290K. The measurements were made using the dispersive reflection interferometer. Each spectrum is the mean of six independent determinations and the standard deviations of the amplitude and phase spectra are also shown.

present results were obtained with twice the resolving power of those earlier studies and were also in a spectral region giving lower signal-to-noise ratios in the recorded interferograms, it is not surprising the standard deviation of the reflectivity does not change significantly in the region of the reflectivity minimum although the signal-to-noise ratio in the reflectivity spectrum does. The standard deviation of the phase difference spectrum, however, more than doubles at the reflectivity minimum. This is expected as the phase difference spectrum contains the arc tangent of the quotient of the sine and cosine transforms of the specimen interferogram. Therefore in regions of low reflectivity both transforms will tend to zero, exaggerating the effects of noise in their quotient. Away from the reflectivity minimum the phase noise is fairly constant at about 0.015 radian.

7.4.2 THE COMPLEX REFRACTIVE INDEX OF Cd Te

In order to investigate the manner in which the phase and modulus noise of the complex reflectivity spectrum manifest themselves in the complex refraction spectrum it is convenient to separate the effects of random and systematic error.

(i) Random effects

The effects of the random phase and modulus noise of the complex reflectivity may be seen from the curves of figure 7.15. The upper graph shows the refractive and absorption indices calculated from the measured averaged complex reflectivity of figure 7.14, while the lower two show the standard deviations of each. Both indices show the strong dispersion expected of this type of resonance and, from the marked similarities between the form of the variation of the n- and r- spectra and of the k- and ($\phi^r - \pi$)- spectra, it is apparent that the former of each pair is largely determined by the latter, as would be expected from the form of Fresnel's equations.

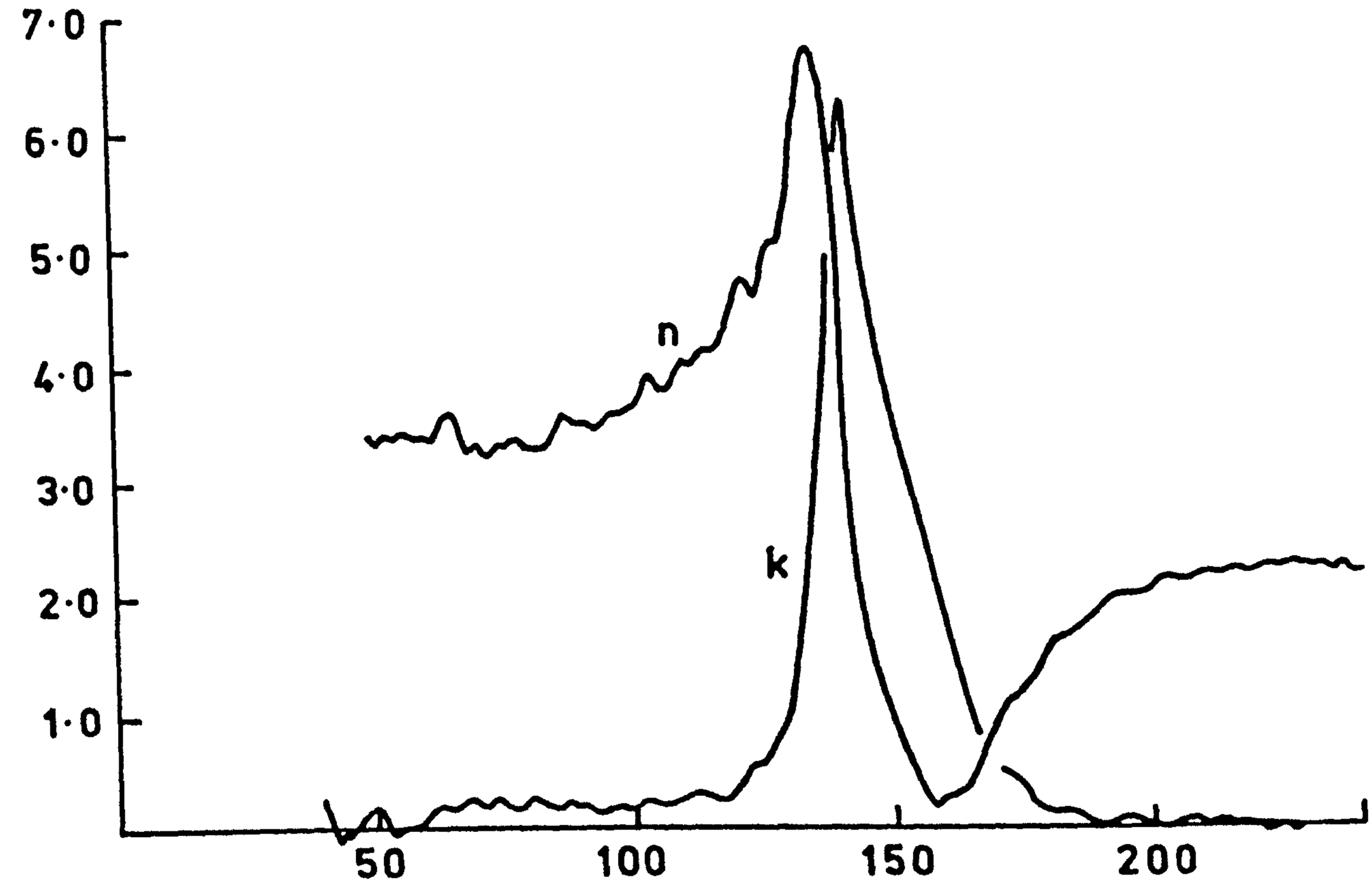

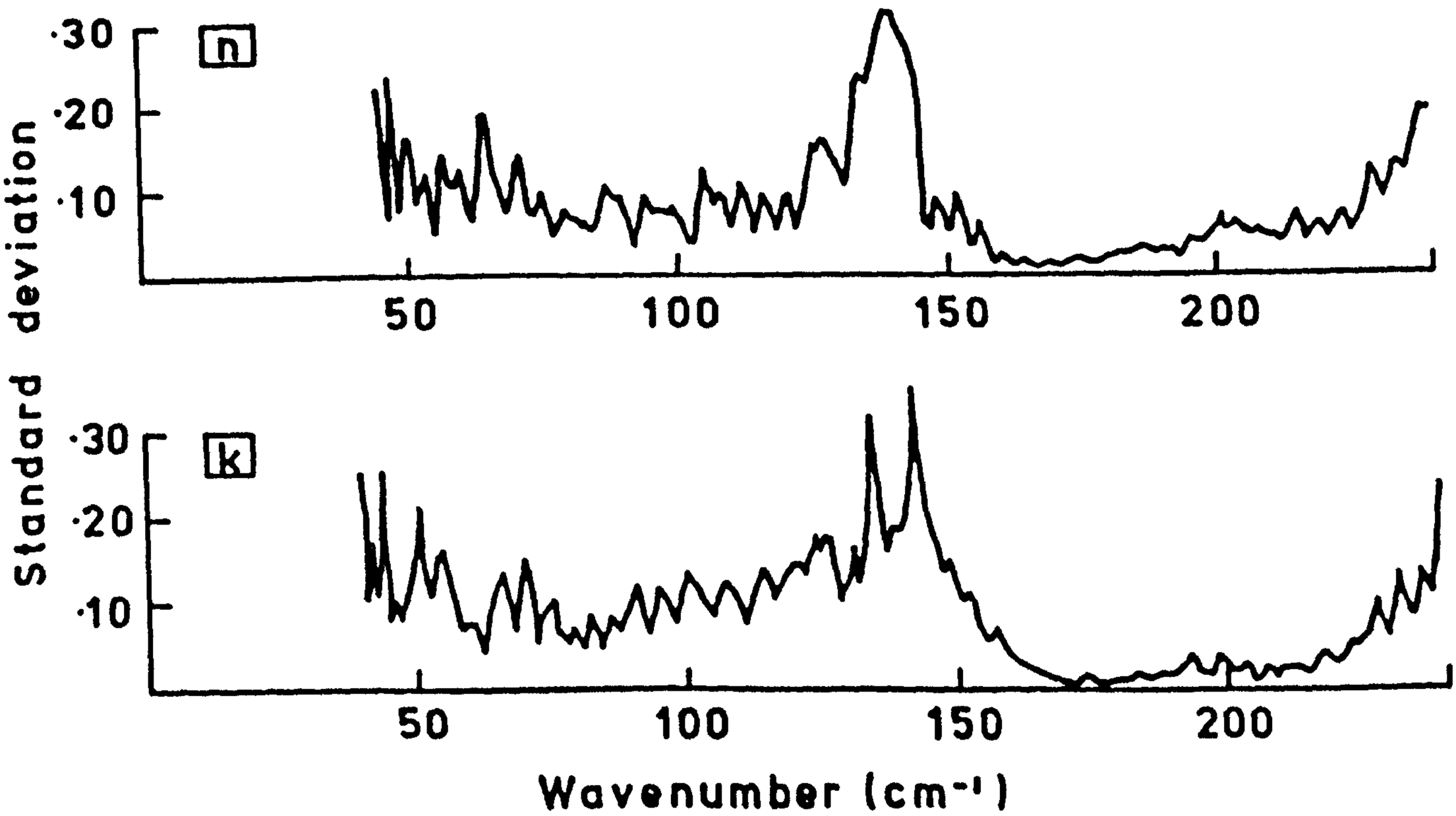

Fig.7.15. The real and imaginary parts of the complex refractive index, $\hat{n}=n+ik$, of cadmium telluride at 290K calculated from the complex reflectivity shown in fig.7.14. The corresponding standard deviation spectra are also shown.

The standard deviations of n and k are qualitatively very similar. Both fall from about 0.15 at 40cm^{-1} to a broad minimum between 80 and 90cm^{-1} and then rise to maxima of about 0.3 between 140 and 150cm^{-1}. After this both fall to very low values around 180cm^{-1} and then increase again with increasing wavenumber, reflecting the poor signal-to-noise ratio near the beamdivider cut off. This can be qualitatively understood by considering equations 4.75 and 4.76 which give $\hat{n}$ in terms of $\hat{r}$. Partial differentiation of each leads to the following expressions for the errors Δn and Δk in the calculated value of $\hat{n}$ caused by the measurement errors Δr and $\Delta\phi^r$ in $\hat{r}$, provided that the former are small. Thus,

$$\Delta n = - nk \Delta\phi^r \qquad \ldots (7.17)$$

$$\Delta n = \frac{k}{\sin\phi^r} \left\{ 1 + \frac{n}{r} (r + \cos\phi^r) \right\} \Delta r \qquad \ldots (7.18)$$

$$\Delta k = k (\cot\phi^r - k) \Delta\phi^r \qquad \ldots (7.19)$$

and,
$$\Delta k = \frac{k}{r} \left\{ 1 + \frac{k(r + \cos\phi^r)}{\sin\phi^r} \right\} \Delta r \qquad \ldots (7.20)$$

the most relevant aspect of these equations to the present discussion is that the absorption index, k, appears as a multiplicative factor in all four. Therefore, when k is small the absolute magnitude of the errors in $\hat{n}$ will be small, and vice versa. Thus, one anticipates that the standard deviation spectra of figure 7.15 will, superficially, resemble the spectrum of the absorption index, which they do. In particular, the difference in the levels of the standard deviation below and above 140cm^{-1} reflects the difference in the levels of k on either side of the resonance.

(ii) Systematic effects

The predominant systematic error in complex reflectivity measurements is found in the phase spectrum and takes the linear dependence on wavenumber that

has been previously discussed. It can arise from the effects of backlash, from non-exact replacement of specimen by reference or from a non-flat reflecting surface. The effect of such an error in the complex refractive index spectrum can be studied by introducing a linear wavenumber-dependent term into a phase difference spectrum and recomputing the optical constants. This was performed for the present CdTe results by the addition of terms proportional to $\pm$ 0.5 μm which is typical of an uncorrected backlash error and represents $\pm$ 0.078 radian at 250cm^{-1}. The effect that this has on the computed complex refractive index spectrum is illustrated in figures 7.16 and 7.17. In both of these the centre spectrum of the three plotted is the experimentally determined one from figure 7.15. In the real refractive index spectrum the effect of the error is to decrease n when the error is positive and to increase it when negative so that the upper curve is for the -0.5 μm term and the lower for the 0.5 μm term. In the wings of the refraction spectrum where $k \rightarrow 0$ the effect is small as indicated by equation 7.17, while at the maximum of the spectrum n varies by as much as $\pm$ 10%, a significant amount. The effect on the absorption index is more complex than this. In the wings of the absorption feature the positive error gives increased k-values, but towards the centre of the feature this reverses and the positive error decreases the k-spectrum.

Overall then it is clear that the effects of typical systematic phase errors are likely to be far more significant than the effects of typical random phase or modulus errors, and as one would rather be limited by random errors the values of the backlash procedure, the six point specimen support and the use of flat specimens become apparent.

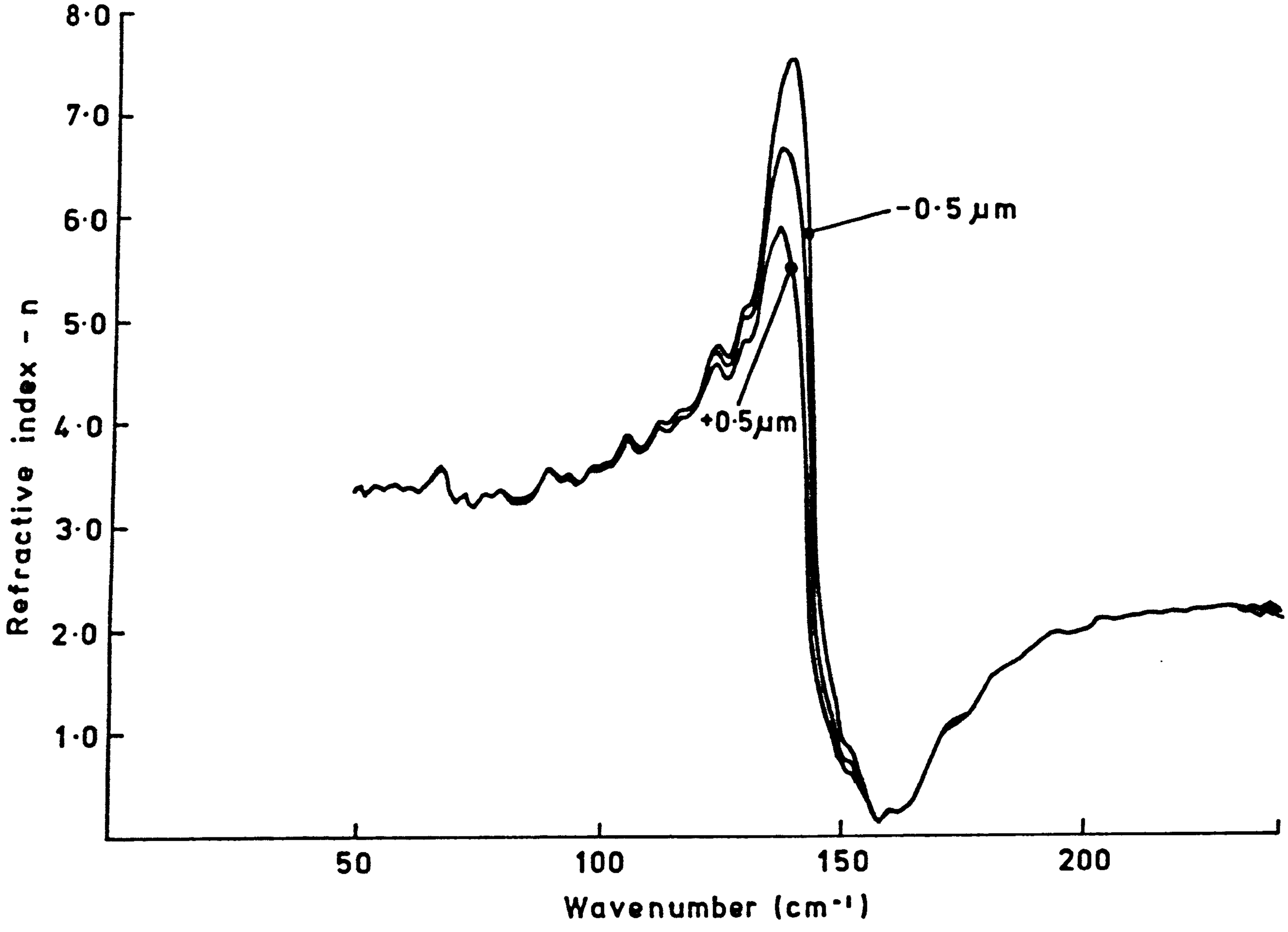

Fig.7.16. The effect on the calculated refractive index spectrum of a linear phase error proportional to ±0.5µm.

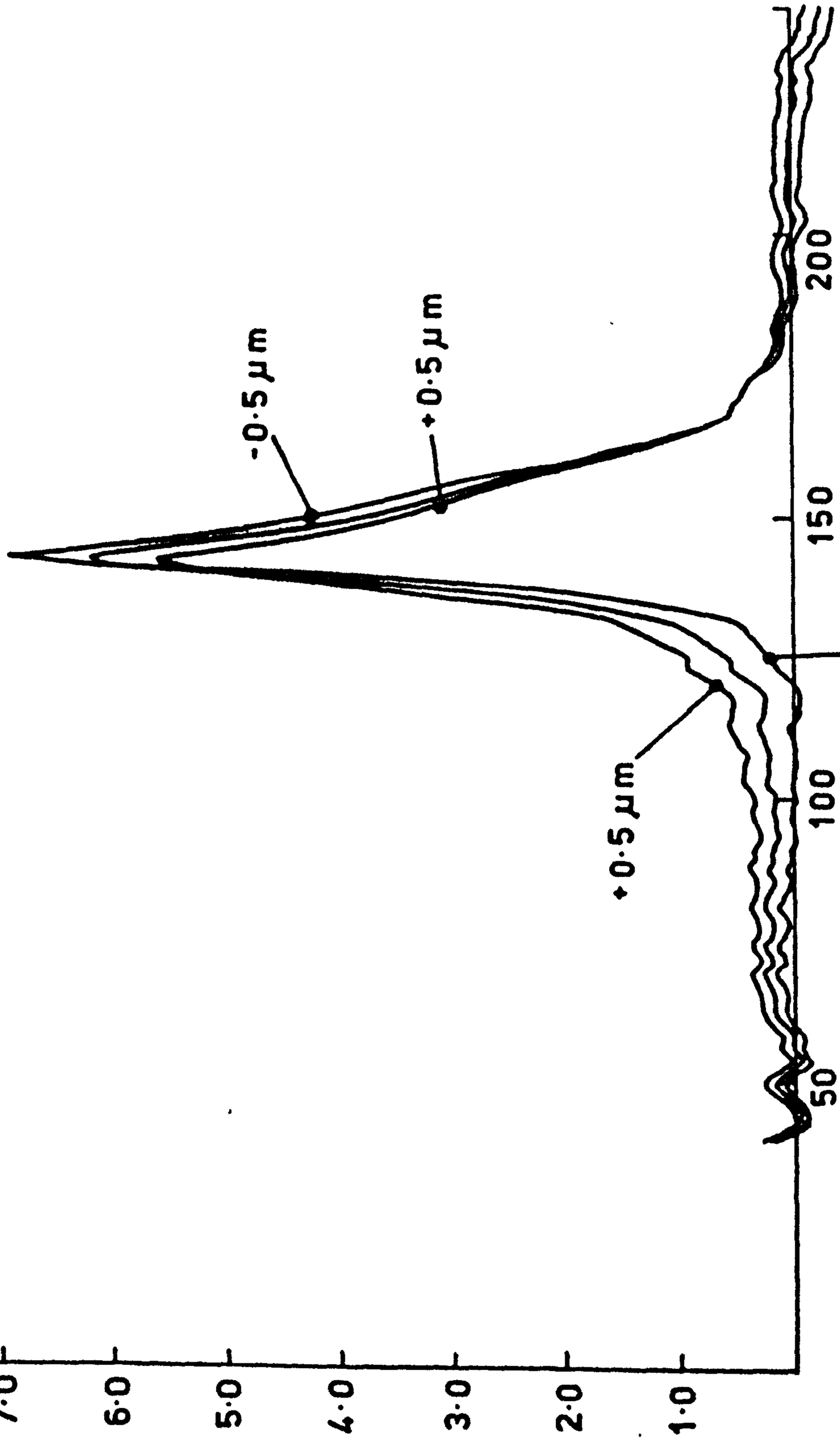

Fig.7.17. The effect on the calculated absorption index spectrum of a linear phase error proportional to ±0.5μm.

7.4.3 THE COMPLEX RELATIVE PERMITTIVITY OF CdTe

An alternative method of checking on the precision of these measurements may be made by comparing the complex relative permittivity calculated from these measurements with model calculations based on the classical damped harmonic oscillator representation of the phonon mode. One would not expect this model to describe the permittivity precisely but, as earlier workers [221,222] have discussed their results in terms of the parameters of this model, it can be used to compare their results with the present measurements. The model describes the complex relative permittivity by the form

$$\hat{\varepsilon}(\tilde{\nu}) = \varepsilon(\infty) + \frac{S_T \tilde{\nu}_T^2}{\tilde{\nu}_T^2 - \tilde{\nu}^2 - i\tilde{\nu}\gamma_T} \qquad \ldots (7.21)$$

where $\varepsilon(\infty)$ is the high frequency contribution to the permittivity, S_T the dimensionless mode strength, $\tilde{\nu}_T$ the mode wavenumber and γ_T the mode damping. A more rigorous description would include a complex damping term to allow for weakly anharmonic effects and a term for a free charge carrier contribution, but as there is no evidence for plasma effects in these measurements, the exclusion of the latter is justified.

For either part of the permittivity, real or imaginary, it was possible to obtain a fairly good fit to the measured data but, however, the parameters giving the best fit to, say ε', gave a poor fit to ε'' and vice versa. This situation is illustrated in figure 7.18. In either part the continuous curve represents the best fit to that particular spectrum while the dashed curve was calculated from the parameters of the best fit to the other experimental spectrum. The best fit curves were judged by eye rather than by the use of an automatic procedure to minimise the difference between measurements and model, and, in arriving at them, the sum $\varepsilon(\infty) + S_T$, which equals the static permittivity, was kept

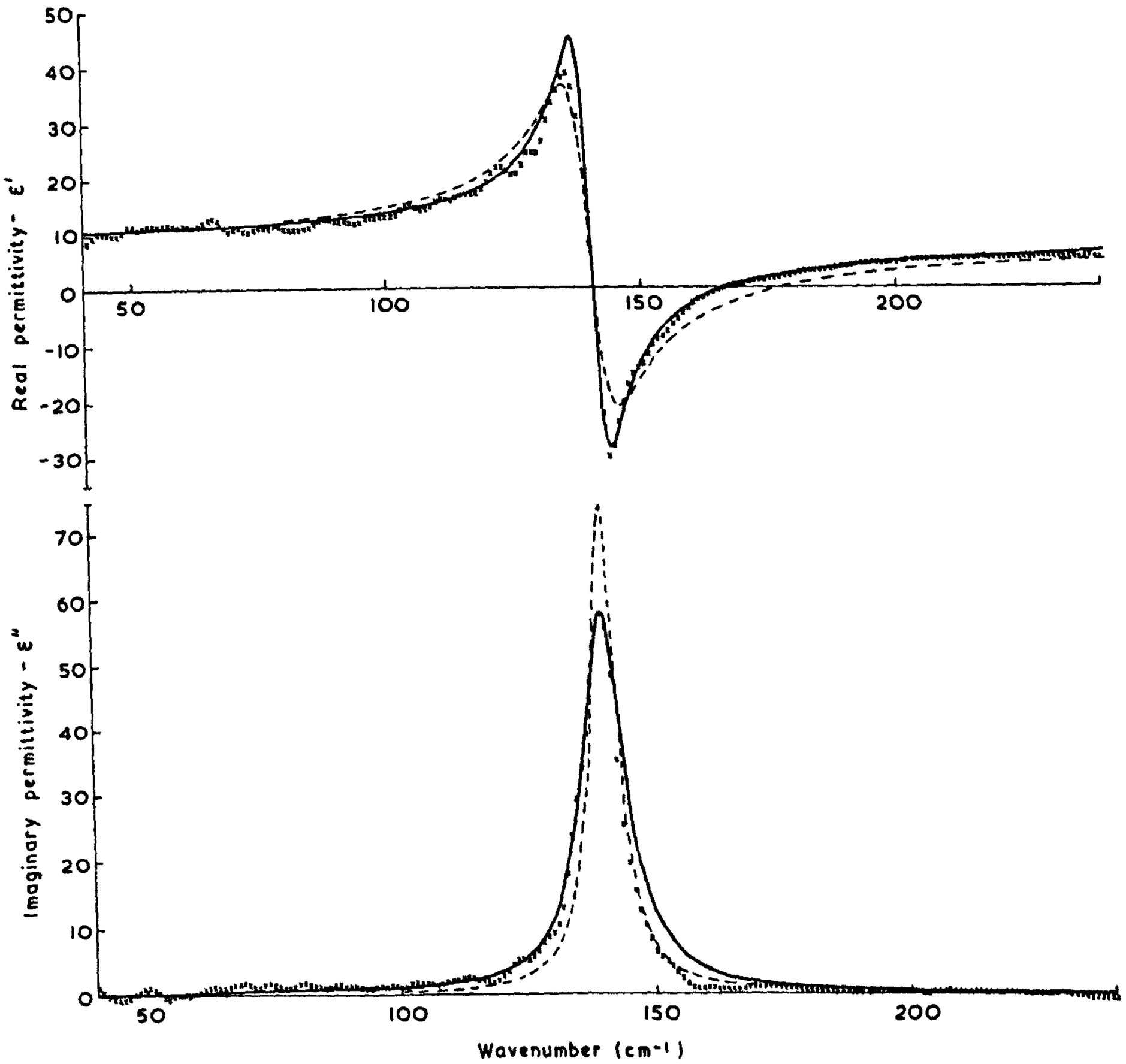

Fig.7.18. The real and imaginary parts of the complex relative permittivity of cadmium telluride at 290K. The crosses were computed from the complex reflectivity shown in fig.7.14. In each part the continuous curve is the best fit of the classical damped harmonic oscillator model to that particular data set, it not being possible to find a unique set of parameters capable of adequately describing both ε' and ε''. In the ε' plot the dotted curve was calculated from the best fit to the ε'' data and vice versa.

constant at 10.2 to give the best agreement with the low wavenumber ε' -data. The values of these best fit parameters and those derived from the earlier works are given in table 7.2. Both earlier sets of results were derived from power

Sources	$\tilde{\nu}_T(cm^{-1})$	$\gamma_T(cm^{-1})$	S_T	$\varepsilon(\infty)$	$\varepsilon(o)$
Present work, ε'	140.5	6.1	3.2	7.0	10.2
Present work, ε''	140.5	10.0	4.1	6.1	10.2
Ref. 221	141	6.67	3.194	7.13	10.324 ± 0.008
Ref. 222	141.0	6.67	3.100	7.194	10.294

Table 7.2 The values of the best-fit parameters for the classical damped harmonic oscillator representation of the TO phonon in Cd Te at 293K.

transmission measurements, those of Randall and Rawcliffe[221] from 10 to 45cm^{-1} and those of Danielewicz and Coleman[222] from 10 to 100cm^{-1}, with both using the channel spectrum due to multiple internal reflections in thin specimens to give the real refractive index data. Danielewicz and Coleman additionally combined their data with earlier mid-infrared measurements cn the short wavelength side of the reststrahlen band. The parameters derived from the present ε'-spectrum are in quite good agreement with those of the earlier studies, although the damping coefficient is somewhat lower, while those from the ε''-spectrum are substantially different. This is not at all surprising as the present data have shown that the complex permittivity cannot be represented in a satisfactory manner by a single set of parameters for the simple classical model. In addition, the agreement between the ε'-derived parameters, which are largely dominated by the refractive index, and the earlier ones could almost have been expected as the latter appear to have been determined mainly from fits to the refraction and reflection spectra and, in particular, the parameters of Randall and Rawcliffe, which gave a good fit to their measured refraction spectrum,

gave a poor fit to their absorption spectrum.

Finally, it is of interest to derive values for the wavenumber of the longitudinal optical phonon associated with this transverse mode. This may be calculated from the Lydanne-Sachs-Teller relation [223]

$$\left\{\frac{\tilde{\nu}_L}{\tilde{\nu}_T}\right\}^2 = \frac{\varepsilon(0)}{\varepsilon(\infty)} \qquad \ldots (7.22)$$

which relates the wavenumber of the LO phonon, $\tilde{\nu}_L$, to that of the TO phonon and the static and high frequency real relative permittivities. This interpretation is only truly valid in the limit of small damping and the equation can be extended to a generalised lattice possessing more than one normal mode of oscillation by replacing the left hand side of equation 7.22 with a product of terms like $(\tilde{\nu}_L/\tilde{\nu}_T)^2$, one for each mode [224,225]. This is not necessary in the present situation and application of equation 7.22 to the data of table 7.2 gives the values for the wavenumber of the LO phonon in CdTe listed in table 7.3. The values determined from the present ε' -spectrum and the earlier

Source	$\tilde{\nu}_L$ (cm^{-1})
Present work, ε'	169.58
Present work, ε''	181.63
Ref. 221	169.62
Ref. 222	168.62

Table 7.3 The wavenumber of the LO phonon in CdTe at 293K calculated from the Lyddane-Sachs-Teller relation using the parameters listed in table 7.2.

measurements are in good agreement with each other, all lying within limits of $\pm$ 0.5cm^{-1} which reflects the similarities between the harmonic oscillator parameters describing these three sets of measurements. The value determined from the ε'' -spectrum, however, is nearly 12cm^{-1} higher than these other values and this illustrates the difficulties that can arise in the characterisation of such a lattice resonance in terms of this simple model.

7.5 SODA LIME SILICA GLASS

In the previous sections of this chapter we have outlined the construction and performance of the dispersive reflection interferometer, studying the typical levels of random and systematic error obtained in the complex spectrum and seeing how these transform into errors in the calculated values of the optical constants. In this section we shall present and discuss the results of the first determination of the optical constants of normal soda lime silica glass* up to 360cm^{-1}. Previously, the opacity of this glass had prevented its study between 50 and 360cm^{-1}, although Sweet and White[40] and Aronsen and Strong[41] have made power reflectivity measurements above 330cm^{-1}, and Exarhos and Risen[39] have made transmission measurements on a mechanically ground specimen of the binary silicate glass $Na_2O \cdot SiO_2$ dispersed in a polyethylene matrix. In this section we shall firstly present the computed values of the optical constants and combine them with the dispersive and non-dispersive measurements of the previous two chapters to provide a description of the optical constants of this glass from 0.29 to 360cm^{-1} and from 1200 to 4000cm^{-1}. We shall then identify in a quantitative manner the total contribution of the glass additives to the complex permittivity and this will lead on to the following chapter

---

*Normal is taken to imply a composition by weight of approximately 70% SiO_2, 12% Na_2O and 10% CaO. Measurements on other compositions are considered in the following chapter.

in which measurements on silicate glasses of different compositions are used to identify the resonant absorption due to each additive.

7.5.1 THE COMPLEX REFLECTIVITY

The complex reflectivity measurements were made on a 5.94mm specimen, 50mm in diameter, that had a slight greenish hue to it. The major constituents of this specimen are listed in table 7.4. The interferometer described earlier in this chapter was used for the measurements with various thickness beamdividers and quartz- or diamond-windowed Golay cells used as appropriate to cover the

SiO_2	Na_2O	CaO	MgO	Al_2O_3	K_2O	TOTAL
72.15	12.50	8.40	4.20	1.65	0.65	99.55

Table 7.4 Compositional analysis of the major constituents of the 5.94mm specimen used in the dispersive reflection measurements. The figures are percentages by weight.

spectral region between 18 and 360cm^{-1} at 4cm^{-1} resolution and a temperature of 293K. The reflection and phase spectra determined in this way are shown in figures 7.19 and 7.20 respectively. The amplitude reflectivity falls from around 0.45 at 20cm^{-1} to a broad minimum of about 0.35 between 250 and 270cm^{-1}, while the phase difference, $\phi^r - \pi$, rises to a broad maximum of about 0.23 radian between 200 and 250cm^{-1}. The random noise levels present in these spectra are two-to-three times greater than those which one might expect from the discussions of section 7.2. This is a result of these measurements being among the earliest with this interferometer which, at that time, incorporated amplitude, rather than phase, modulation. The subsequent use of the latter form of modulation gave the improved instrumental performance of section 7.2.

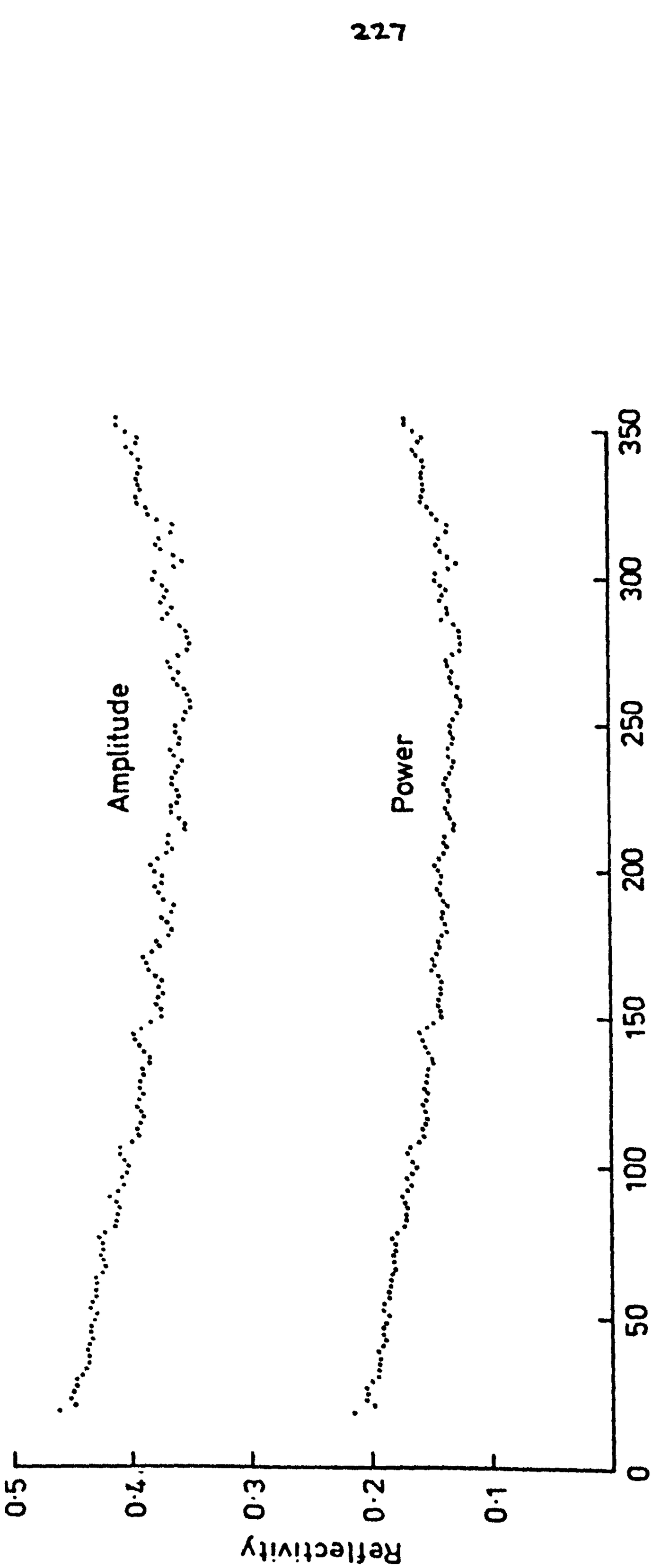

Fig.7.19. The amplitude and power reflection spectra of soda lime silica glass between 18 and 360cm^{-1} at 293K.

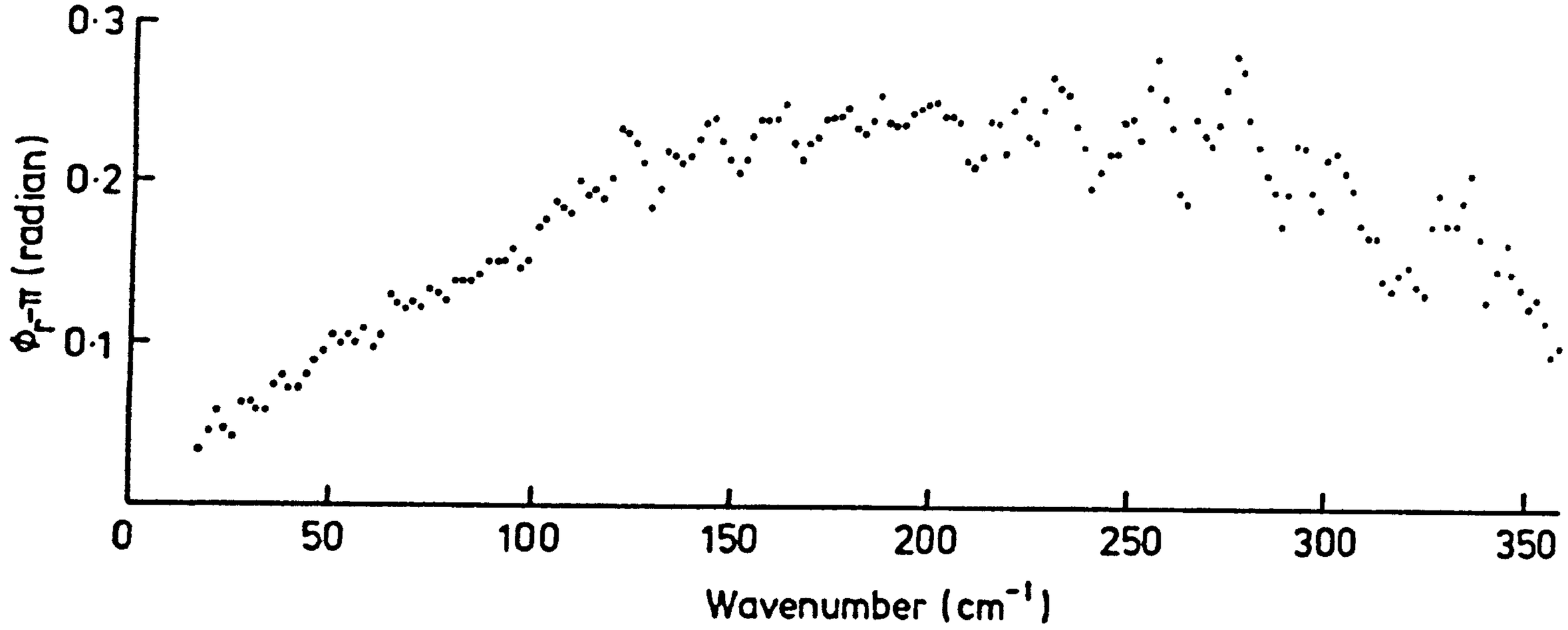

Fig.7.20. The phase difference spectrum of soda lime silica glass between 18 and 360cm^{-1} at 293K.

This may be seen from the more recent measurements on other silicate glasses discussed in the following chapter.

7.5.2 THE COMPLEX REFRACTIVE INDEX

The real and imaginary parts of the complex refractive index were calculated from the measured complex reflectivity via equations 4.75 and 4.76 and are shown in figure 7.21. The real refractive index exhibits a broad minimum, falling from about 2.6 at 20cm^{-1} to about 2.0 around 250cm^{-1} and then rising rapidly to 2.4 at 360cm^{-1}. As the near infrared measurements of chapter 5 showed n to be about 1.6 at 2000cm^{-1} it is apparent that there must be at least one additional dispersive process between 360 and 2000cm^{-1}. This is borne out by the thin film transmission measurements of Blair and Douglas[168] and Crozier and Douglas[169] which show the refractive index taking a value of about 2.5 at 1000cm^{-1}. The absorption index also reflects the strong dispersion in this region, rising from 0.1 at 20cm^{-1} to a broad peak of about 0.4 between 100 and 200cm^{-1}, then decreasing slowly towards 360cm^{-1}. Above 250cm^{-1} the large amplitude of the random fluctuations in k derive from the corresponding fluctuations in the phase spectrum.

By combining these dispersive reflection determinations of n with the near infrared transmission determinations of chapter 5 and the dispersive transmission determinations of chapter 6 it is possible to present a fairly comprehensive description of the spectral variation of the optical constants of soda lime silica glass between much of the interval 1 to 4000cm^{-1} and this is shown in figure 7.22. The dispersive reflection measurements are shown as dots between 20 and 360cm^{-1}, the dispersive transmission measurements as circled dots, ⊙ , between 3 and 25cm^{-1}, and it is an indication of the precision of the two methods that, in the spectral region of overlap, they lead to the same values for the

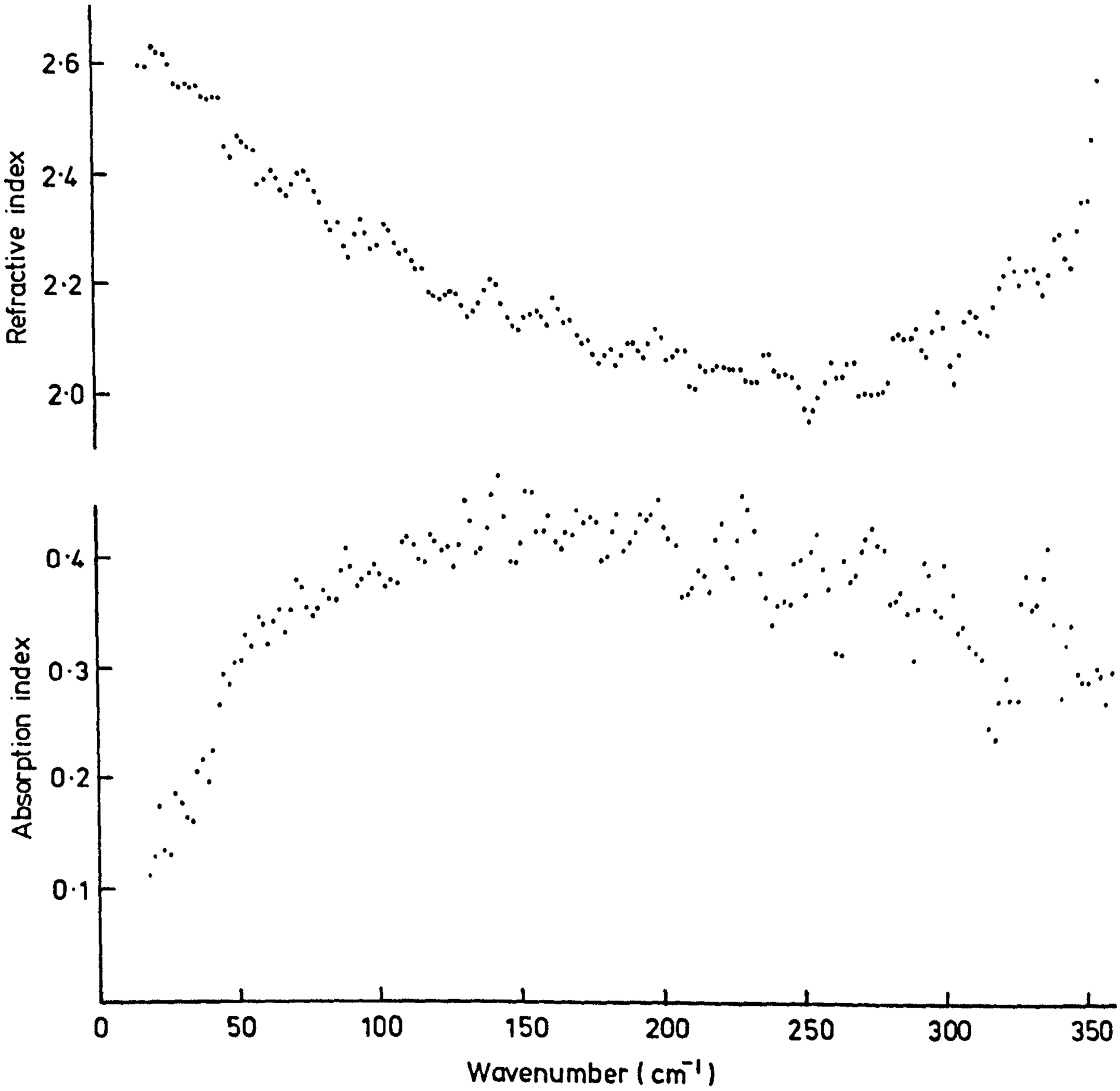

Fig.7.21. The refractive and absorption indices of soda lime silica glass between 18 and 360cm^{-1} calculated from the complex reflection spectrum of figures 7.19 and 7.20

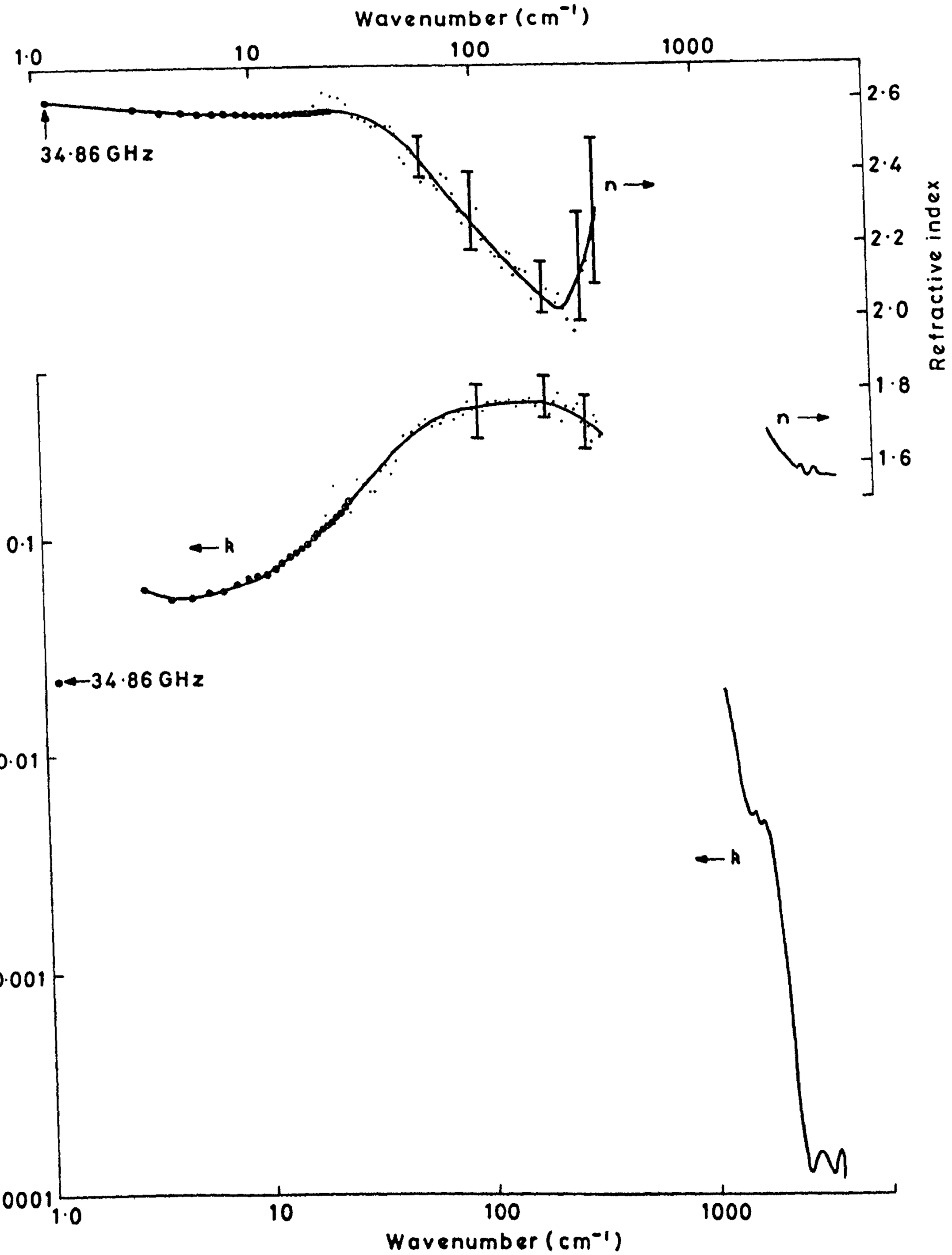

Fig.7.22. The refractive and absorption indices of soda lime silica glass between 1 and 4000cm^{-1} at 293K. The spectra are compiled from the near infrared power transmission measurements of chapter 5, the dispersive transmission measurements of chapter 6 and the dispersive reflection measurements of this chapter.

optical constants. Although it may appear reasonable to join the mid- and near-infrared absorption spectrum to the far infrared measurements by a monotonically rising extrapolation, the refractive index dispersion between 360 and 2000 cm^{-1} clearly indicates that this would be incorrect. The dispersion below $20cm^{-1}$ discussed in section 6.5 in conjunction with the absorption band at $10cm^{-1}$ is now seen to be relatively small in terms of the dispersion above $30cm^{-1}$. Because of the wavenumber factor involved in going from power absorption coefficient to absorption index, a local maximum is shown to exist between 1 and $10cm^{-1}$ in the latter spectrum.

In many ways the power absorption coefficient is a more useful parameter than the absorption index as it enables one to directly appreciate the attentuation characteristics of a material. Therefore, in figure 7.23, the absorption index spectrum of figure 7.22 has been replotted as the power absorption coefficient. The dispersive transmission data is again shown as circled dots, while the crosses represent the liquid helium temperature data of chapter 5, included here for comparison. The arrows labelled $\tilde{\nu}^2$ define that portion of the data between 15 and $50cm^{-1}$ where the power absorption coefficient varies as the square of the wavenumber, as discussed in chapter 5. The data of figures 7.22 and 7.23, together with the corresponding values of the real and imaginary parts of the complex relative permittivity, are tabulated in appendix 2.

7.5.3 THE COMPLEX RELATIVE PERMITTIVITY

The transmission measurements of Exarhos and Risen[39,40,226] on specimens of simple binary oxide glasses, $M_2O.A_xO_y$, have shown that each glass has a broad, intense absorption band somewhere between 50 and $500cm^{-1}$ that is characteristic of the vibration of the metal cation, M^+, about its equilibrium

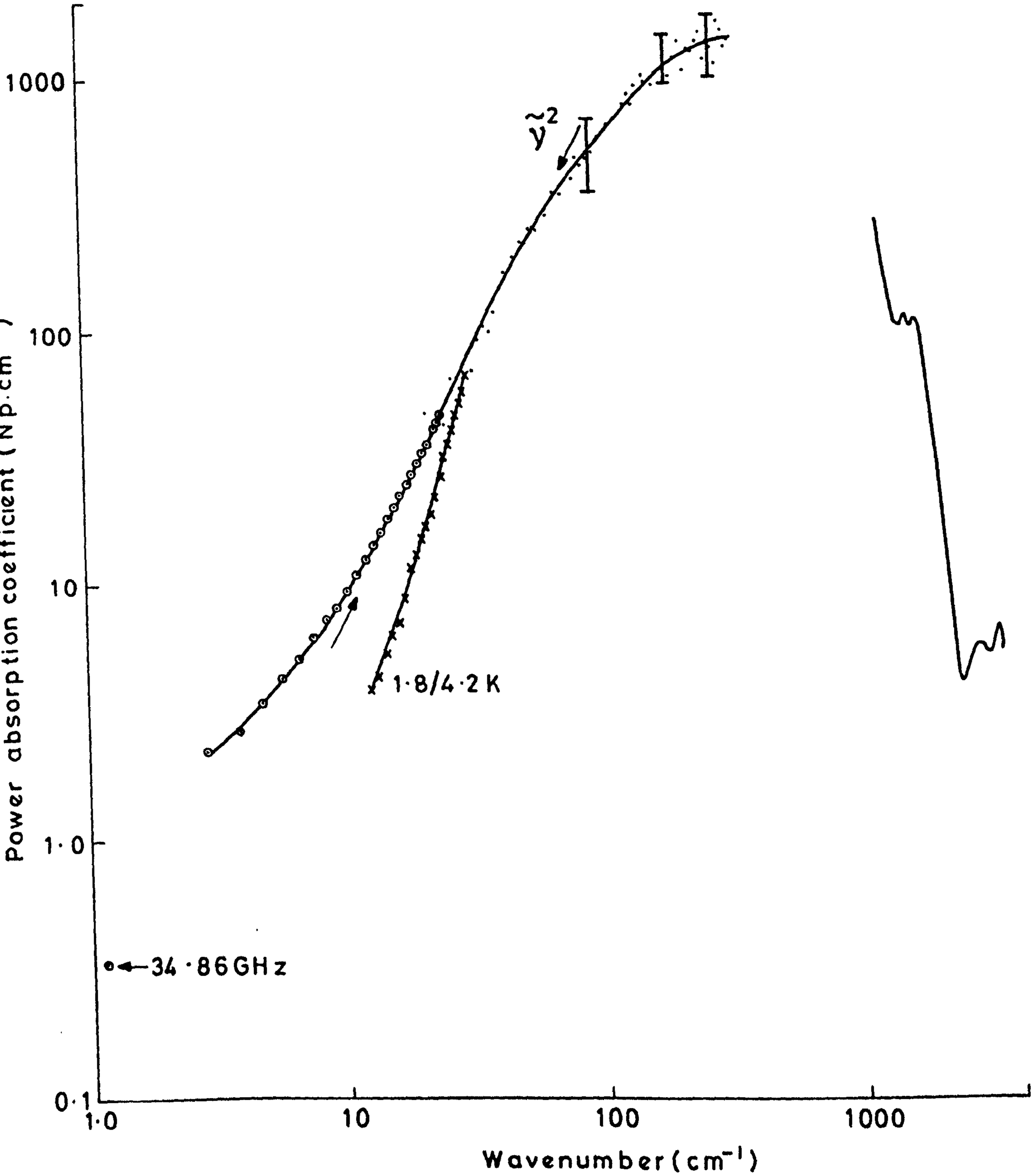

Fig.7.23. The power absorption spectrum of soda lime silica glass between 1 and 4000cm^{-1} at 293K computed from the absorption index spectrum of the previous figure. The liquid helium temperature results of chapter 5 for the spectral region below 50cm^{-1} are included.

position in the basic glass network of the oxide A_xO_y. It seems reasonable, therefore, to expect that much of the intense absorption which we have observed below 360cm^{-1} in the present, multi-component, soda lime silica glass can be ascribed to the additive effects of its Na, Ca, Mg and Al metal ions. In this section we shall demonstrate, from our results, that there is an intense broad absorption band superimposed upon the background absorption of the SiO_2 network. Then, in the following chapter, measurements on three binary and three ternary silicate glasses of different compositions are presented that allow the individual contributions of the Na, Ca, Mg and Al ions to this broad absorption to be resolved.

In order to demonstrate the existance of this absorption band it is necessary to subtract, in some way, the contribution of the SiO_2 network to the complex permittivity from the present measurements. To do this we have drawn on the work of Aronson and Strong[41] who measured the power reflectivity at 30° incidence of a commercial plate glass between 330 and 1450cm^{-1}, and obtained excellent agreement between their measurements and calculations based upon a model for the complex permittivity which assumed four Lorentzian oscillators at 444.6, 672, 750 and 975cm^{-1}. As discussed in Wong and Angell[156] these absorptions have all been assigned to various vibrational modes of the SiO_2 network on the basis of similar features in the spectrum of fused silica (see, for example [227,228]) and the density-of-states calculations of Bell et al[229]. There are no strong, discrete absorption features in fused silica at lower wavenumbers so it is reasonable to assume that the complex permittivity of the SiO_2 network of the glass below 400cm^{-1} is largely determined by these four bands. Thus, we have calculated the complex permittivity of the SiO_2 network of the glass using equation 7.21 and the parameters of Aronson and Strong shown in table 7.5.

Aronson and Strong[41]	$\tilde{\nu}_T$ (cm^{-1})	444.6	672.0	750.0	975.0
	γ_T (cm^{-1})	86.16	78.62	62.17	140.30
	S_T	1.431	0.085	0.063	0.798
Ellis et al[42]	$\tilde{\nu}_T$ (cm^{-1})	458	-	788	1013
	Width (cm^{-1})	85	-	120	134
	$\Delta\varepsilon$	0.74	-	0.09	0.51

Table 7.5 The line parameters assigned by Aronson and Strong[41] and by Ellis et al[42] to the spectral region between 400 and 1400cm^{-1} in soda lime silica glass.

The table also includes the parameters presented by Ellis et al[42] below 1100cm^{-1}.

The parameters of Ellis et al are the line centre, the full width at half height of the ε''-spectrum and the oscillator strength

$$\Delta\varepsilon = \frac{2}{\pi}\int \frac{\varepsilon''}{\tilde{\nu}} \cdot d\tilde{\nu} \qquad \ldots (7.23)$$

Aronson and Strong additionally used a value for the high frequency permittivity, $\varepsilon'(\infty)$ of 2.262. The major difference between these two schemes is the absence of the 672cm^{-1} line from that of Ellis et al, but, as it is the weakest of the four lines and, hence, the one having the least effect in the spectral region of interest, its inclusion, whether-or-not correct, is unlikely to significantly affect the conclusions of the present analysis. There is, however, other experimental evidence for the presence of such a feature; Wong and Angell[156], for example show the transmission spectrum of a fused silica specimen having a weak absorption at 695cm^{-1}, while Gaskell and Johnson[228] have identified a feature at 620cm^{-1} in neutron irradiated silica. The remaining three features are common to both schemes, although at somewhat higher wavenumbers in that of Ellis et al[40,230], but their positions are known to be composition-dependent

and, again, small differences in line position are unlikely to affect the conclusions of the present analysis.

The complex relative permittivity of the SiO_2 network of the glass computed from these parameters of Aronson and Strong is shown in figure 7.24 between 0 and 1500cm^{-1}. The effects of the four oscillators are clearly visible in both real and imaginary parts and one sees the relatively small contribution of the 672cm^{-1} band in comparison to those of the strong 444.6 and 975 cm^{-1} bands. The contributions of these bands to the complex permittivity in the region of interest, below 360cm^{-1}, is shown more explicitly in figure 7.25. Here both real and imaginary parts fall monotonically with decreasing wavenumber, ε' towards the limiting value 4.639 imposed by the sum of the high frequency permittivity and the oscillator strengths of the four bands, and ε'' towards zero. The corresponding real and imaginary parts of the complex relative permittivity of the soda lime silica glass specimen are presented in figure 7.26. These were calculated from the complex refractive index spectrum of figure 7.21 using equations 2.17 and 2.18 and, as $k \ll n$ and also changes proportionally more than n, we find, as one would expect, that both n and ε', and k and ε'', have qualitatively similar spectral variations. The difference between the measured complex permittivity of this glass and the calculated one of the SiO_2 network was formed and is shown in figure 7.27. As the glass of Aronson and Strong had a different SiO_2 content (70% by weight) to that of the present specimen (72.15% by weight) the contributions of the four oscillators of Aronson and Strong to the calculated spectrum were increased by the factor 1.03 ($\cong$ 72.15/70) to allow for this. The imaginary part of the difference spectrum reveals quite clearly the presence of a broad loss feature having a maximum around 150cm^{-1} and biased somewhat asymmetrically towards low wavenumbers.

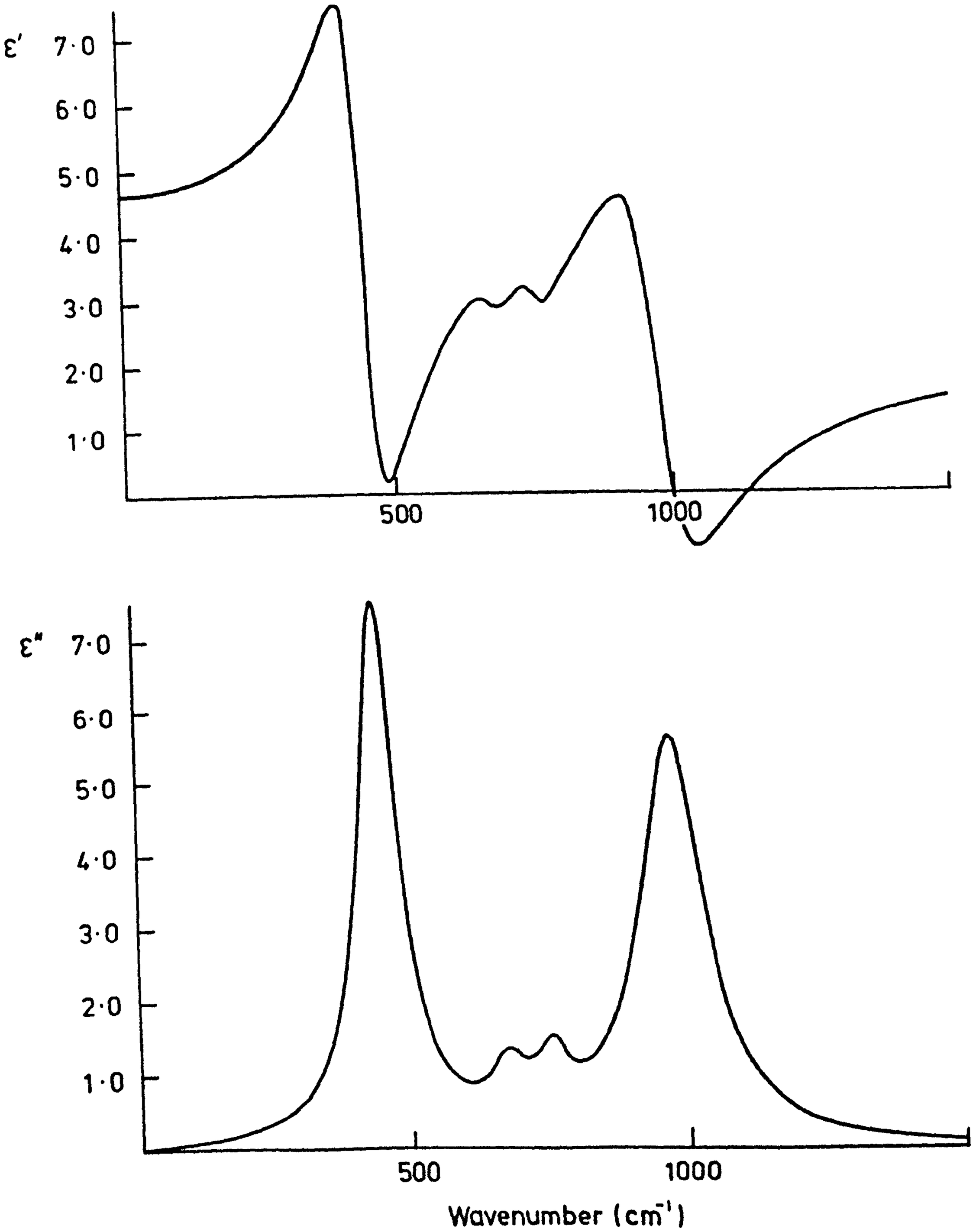

Fig.7.24. The complex relative permittivity of the SiO_4 network of soda lime silica glass below 1500cm^{-1} calculated from the parameters given by Aronson and Strong.

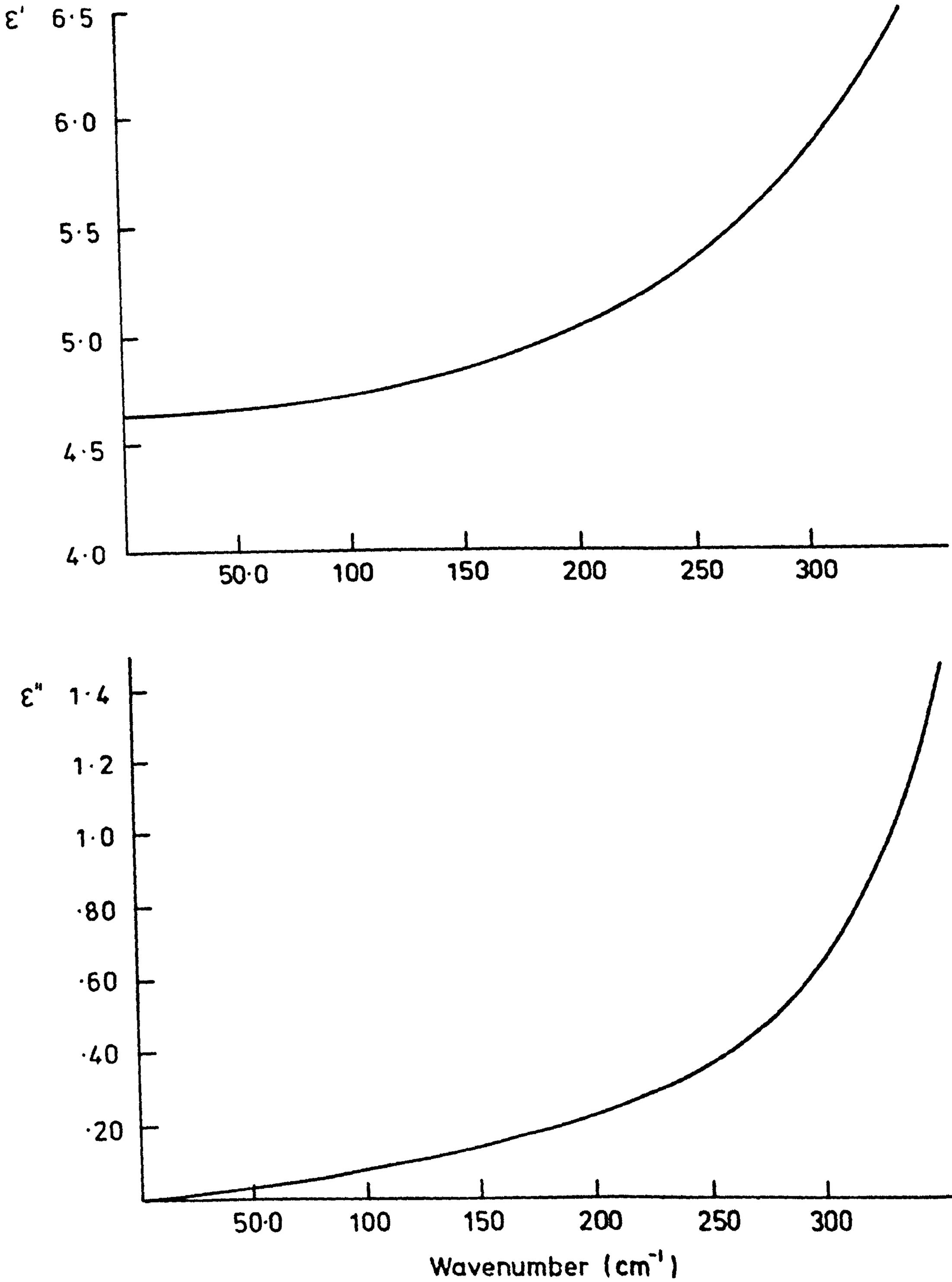

Fig.7.25. The low wavenumber region of the complex relative permittivity of soda lime silica glass shown in the previous figure.

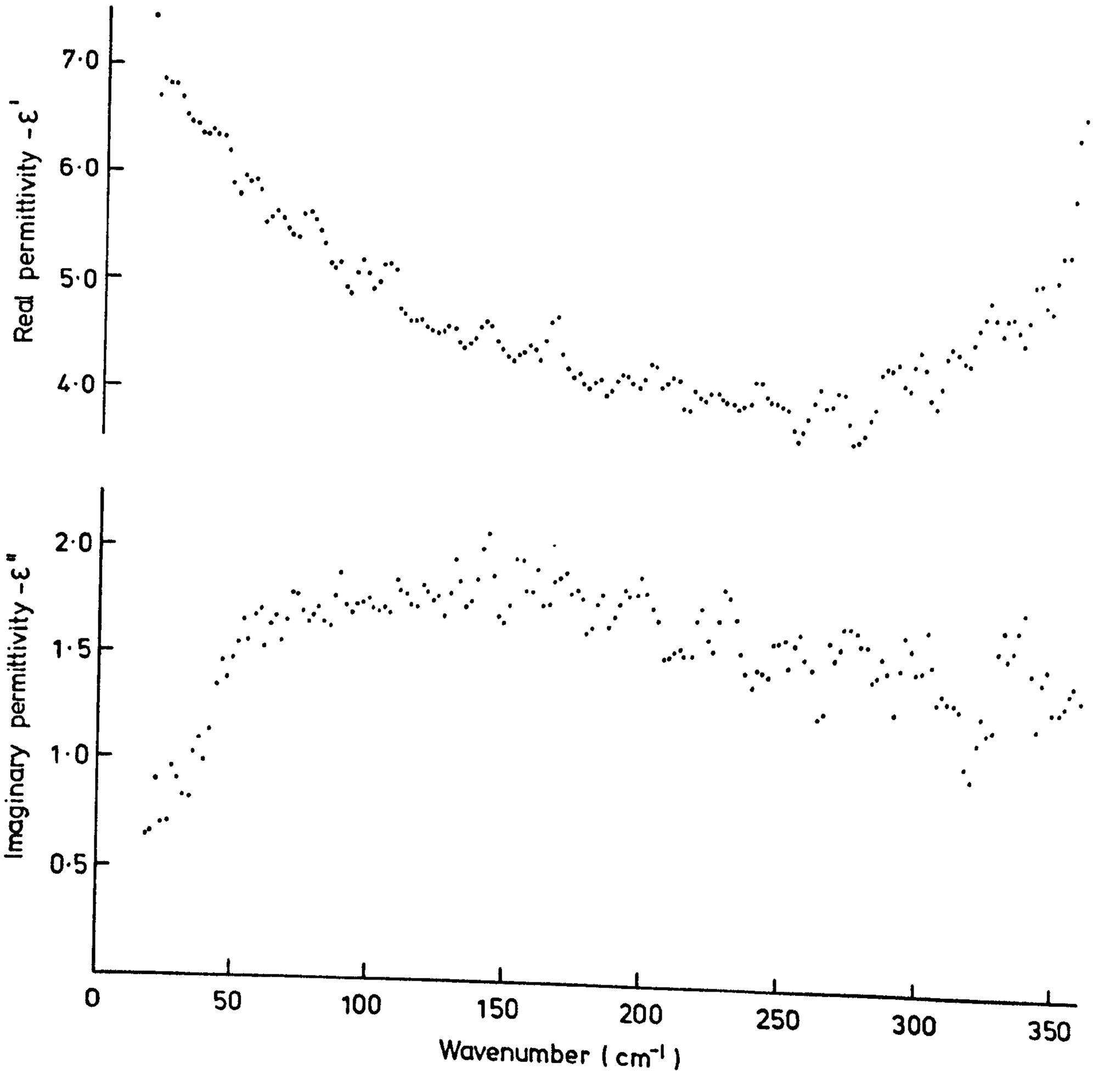

Fig.7.26. The experimentally determined complex relative permittivity of soda lime silica glass between 18 and 360cm^{-1} at 293K.

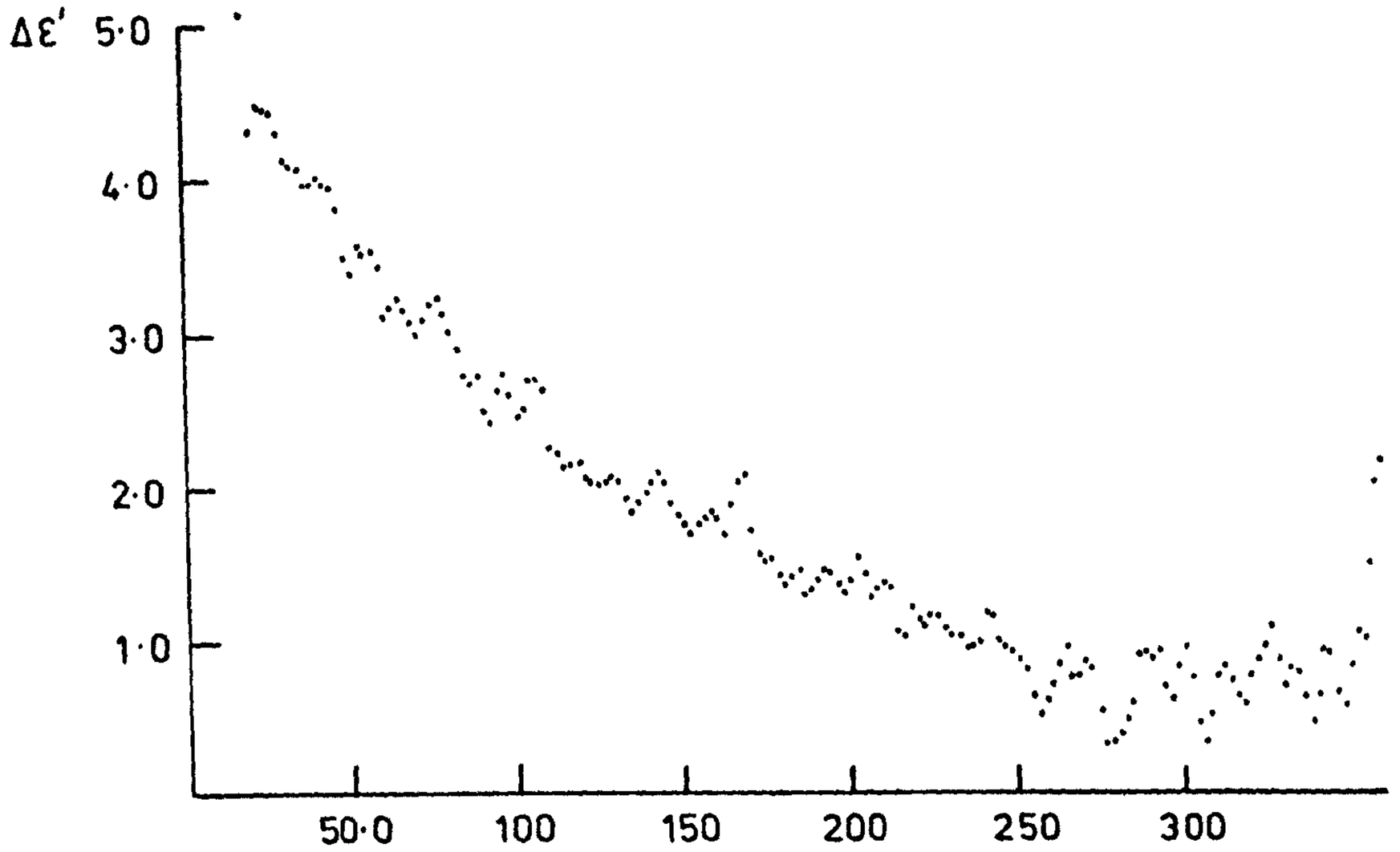

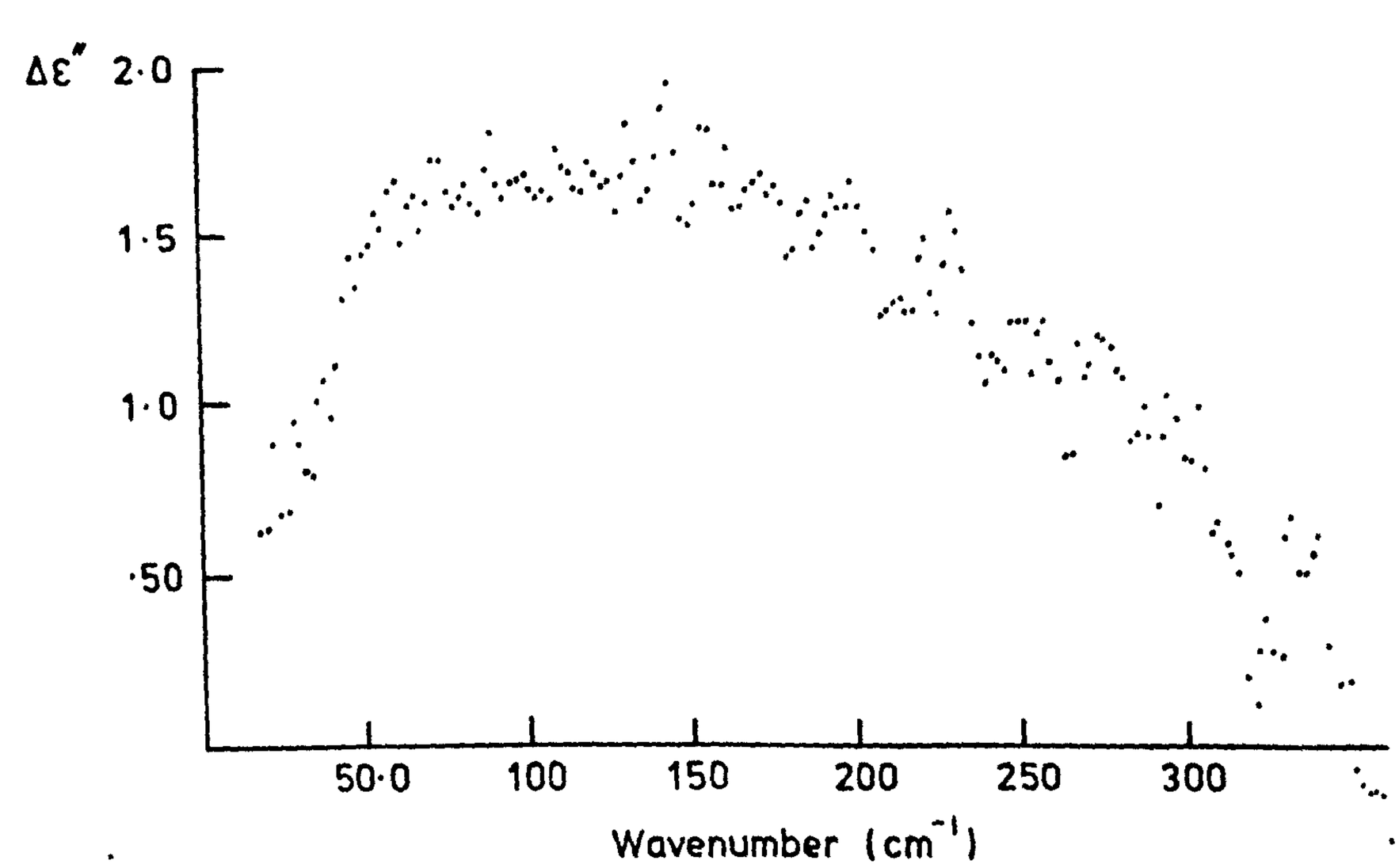

Fig.7.27. The difference between the measured complex relative permittivity of soda lime silica glass and that calculated for the SiO_2 network of the same glass.

It has a width at half peak height of $260 \pm 20 cm^{-1}$ which agrees well with the value of $270 \pm 5 cm^{-1}$ found by Exarhos and Risen[39] for a mechanically ground specimen of $Na_2O \cdot SiO_2$ dispersed in a polyethylene matrix, although their band centre was at $230 \pm 5 cm^{-1}$. As the present glass is a multicomponent glass we attribute this difference in band centres to the effects of the Ca, Mg and Al additives not present in the binary glass of Exarhos and Risen. In the following chapter we shall present data on other silicate glasses of different compositions which will allow the quantitative resolution of the contributions of the individual metal ions to this loss feature.

Before moving on to this though, it is of some interest to evaluate the oscillator strengths associated both with all the loss processes contributing to the absorption below $360 cm^{-1}$ and then with the contribution of the SiO_2 network subtracted. This has been done by the numerical evaluation of equation 7.23 for both sets of data and leads to the values of 2.69 for the full permittivity spectrum and 2.38 after the contribution of the SiO_2 network has been subtracted. From their Kramers-Krönig analysis of the reflection spectrum of soda lime silica glass between 10 and $3 \times 10^5 cm^{-1}$ Ellis et al[42] obtained a value of 5.30 for the total oscillator strength associated with the submillimetre, infrared, visible and ultraviolet regions of the electromagnetic spectrum. Thus, one finds that, not only are the submillimetre wavelength loss processes responsible for over half the oscillator strength observed in this glass, but also that the majority of this submillimetre wavelength contribution is associated with the glass additives which modify the basic SiO_2 network.

CHAPTER 8

THE ABSORPTION DUE TO THE METAL IONS

8.1 DISCUSSION

In the previous chapter we discussed how the measurements of Exarhos and [39,40,226] Risen on simple binary oxide glasses led to the conclusion that each glass has a broad mid infrared absorption that is characteristic of the vibration of the metal ion about its equilibrium position in the basic glass network provided by the oxide material. By subtracting the calculated contribution of the SiO_2 network from the measured complex permittivity of soda lime silica glass we were able to identify the presence of a broad and very intense absorption band below $350cm^{-1}$ in that glass, which, by an extension of the arguments of Exarhos and Risen, was assigned to the sum effect of the vibrational modes of the individual metal ions present. In order to provide a more quantitative demonstration of this and to associate, if possible, characteristic vibrational parameters with the absorption due to each metal ion, further dispersive reflectivity measurements were made on six additional silicate glasses* having the chemical compositions given in table 8.1. The composition

Specimen	SiO_2	Al_2O_3	Na_2O	CaO	K_2O	MgO	TOTAL
94A	80	-	20	-	-	-	100
95A	80	-	-	-	20	-	100
96A	90	-	-	-	10	-	100
174	63.38	17.96	18.66	-	-	-	100
176	63.29	14.35	22.36	-	-	-	100
177	55.0	5.0	-	40.0	-	-	100
SLS	72.15	1.65	12.50	8.4	0.65	4.2	99.55

Table 8.1 The chemical compositions of all the silicate glasses studied by dispersive reflection spectrometry, including the soda lime silica (SLS) glass of the previous section. The figures are percentage by weight.

* Supplied by Dr G.W.F. Pardoe of Pilkington Brothers Ltd.

of the soda lime silica glass of the previous section has been included in this for comparison. Three of these specimens, 94A, 95A and 96A, were binary silicate glasses having either Na_2O or K_2O as the additive, while the remaining three, 174, 176 and 177, were ternary silicate glasses having various combinations of Al_2O_3, Na_2O and CaO as their additives. The measured complex reflectivities of these six specimens, and the complex refractive indices, the power absorption coefficients and the complex relative permittivities computed from them, are presented in figures 8.1 to 8.8 between 40 and 360cm^{-1}.

We consider first the measurements on specimens 94A, 95A and 96A shown in figures 8.1 to 8.4. These can only be considered as having qualitative value, as measurements with a Fizeau interferometer have shown that the reflecting surface of each was either concave or convex with the centre being up to 5 μm out of the plane of the circumference. This results in the measured phase difference, $\phi^r - \pi$, for each specimen containing a systematic error that is linearly dependent on wavenumber as discussed in section 7.2.1. This was particularly apparent for the measured phase difference of 95A which went negative at wavenumbers above 200cm^{-1}. Therefore, the phase, ϕ^r, of this specimen shown in figure 8.1 is the result of correcting the measured spectrum by the addition of the term $2\pi\tilde{\nu}x$ ($x = 0.51$ μm) to ensure that ϕ^r was $\geqslant \pi$ radians at all wavenumbers, the minimum value that it can take in accordance with physical reality (i.e. α and $k \geqslant 0$). If these systematic phase errors are small then, to a first approximation, the conclusions of section 7.4 indicate that the corresponding k, α and ε'' spectra will contain systematic errors that are also linearly dependent on wavenumber. Thus, the overall shape of these spectra will not be too distorted and the spectral positions of absorption features should be reproduced reasonably well, although absolute intensities will not be reliable. Referring,then,to the derived power absorption

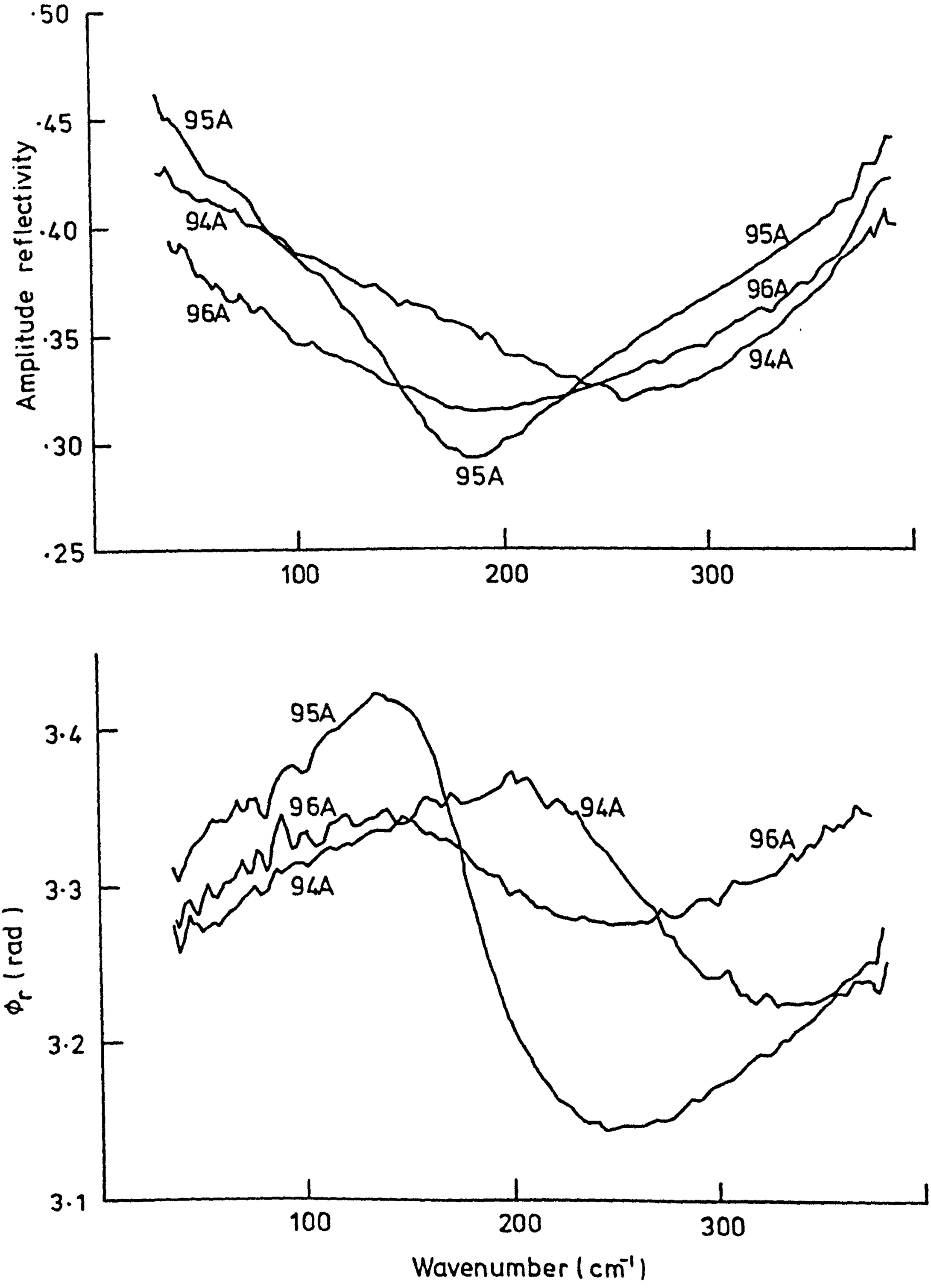

Fig.8.1. The measured amplitude, r, and phase, ϕ_r, of the complex Fresnel reflectivity of specimens 94A, 95A, and 96A below 400cm^{-1} at 290K.

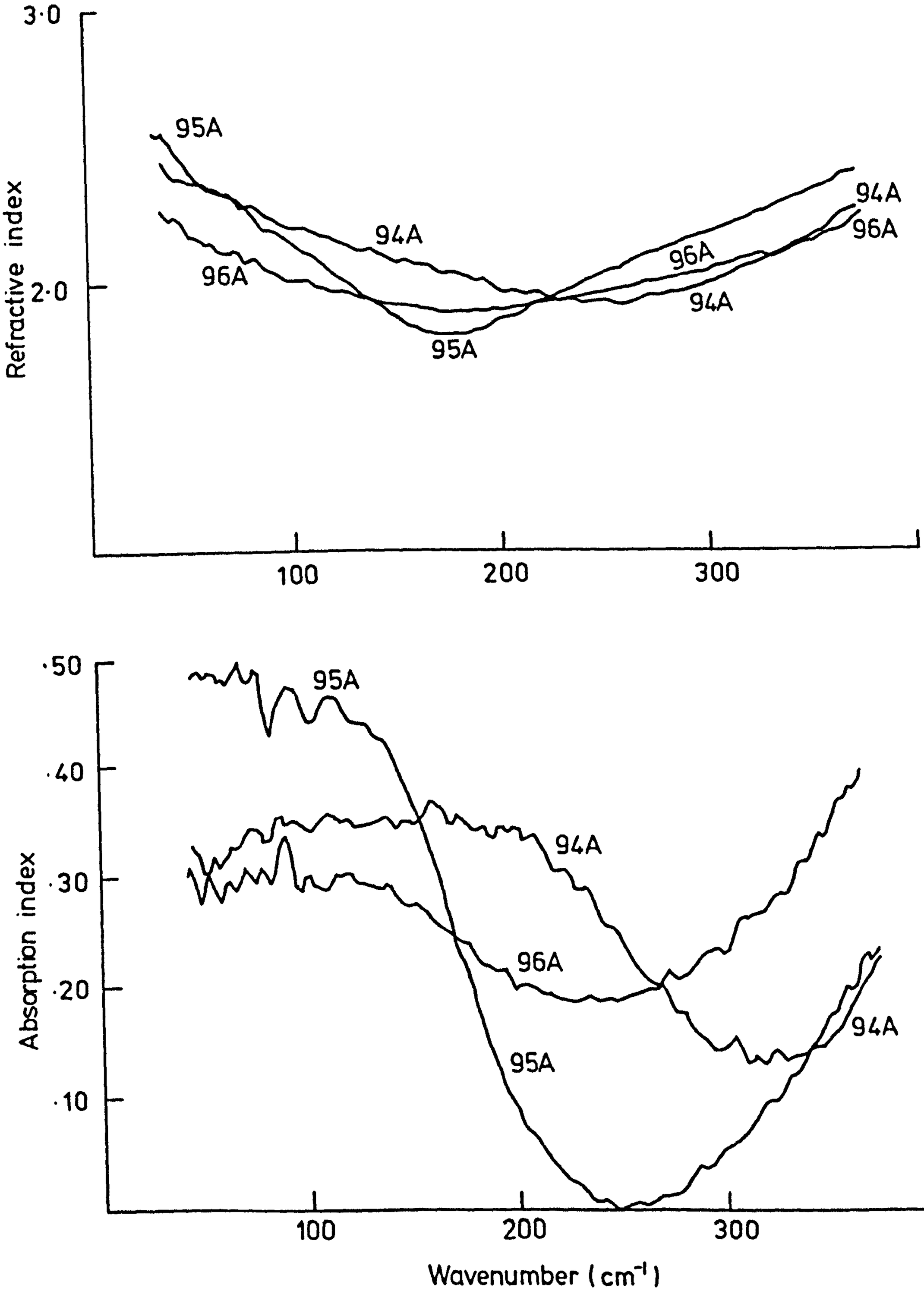

Fig.8.2. The refractive and absorption indices of specimens 94A, 95A and 96A calculated from the complex reflectivity shown in fig.8.1.

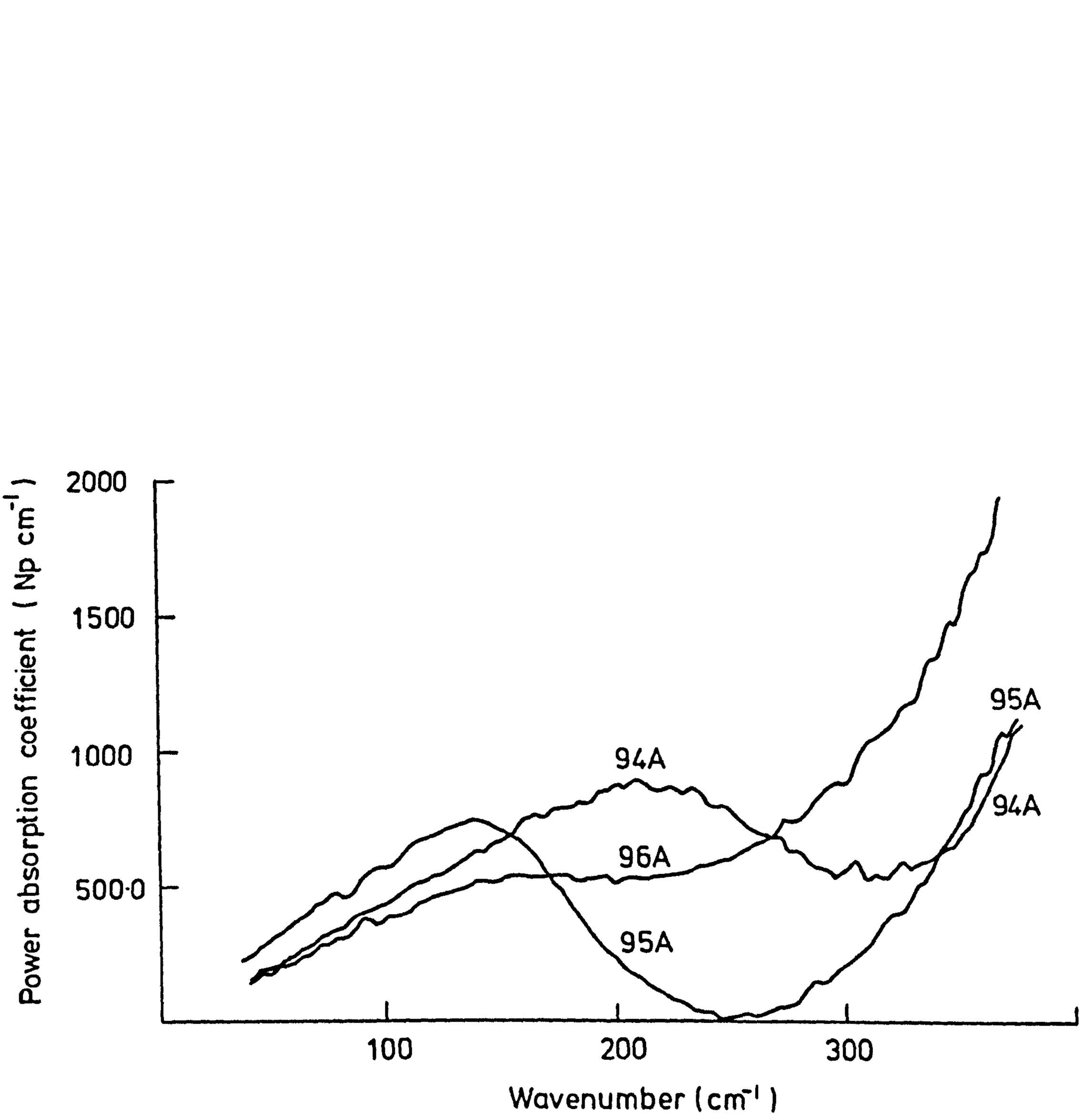

Fig.8.3. The power absorption spectrum of specimens 94A, 95A and 96A calculated from the complex reflectivity shown in fig.8.1.

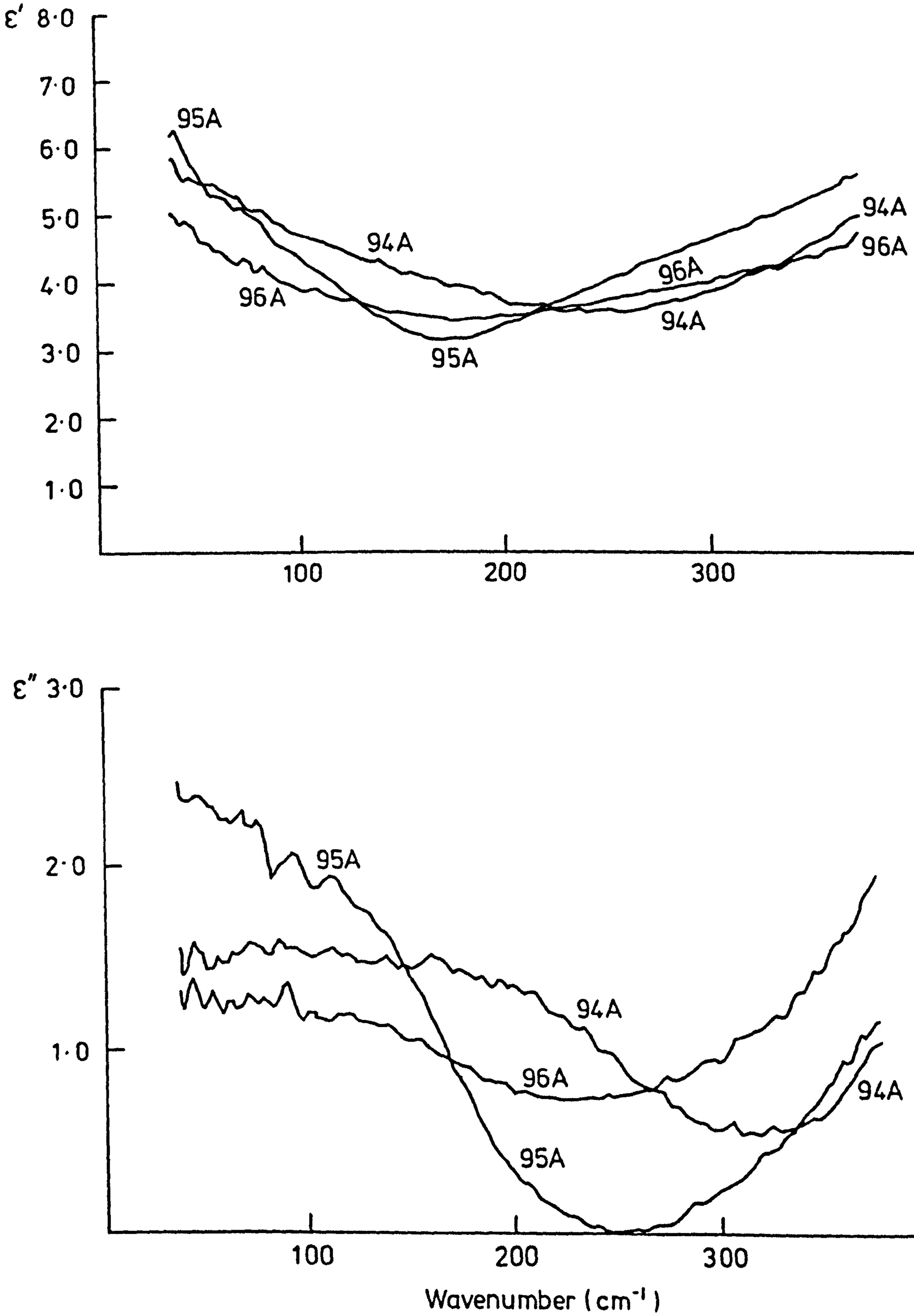

Fig.8.4. The real and imaginary parts of the complex relative permittivity $\hat{\varepsilon} = \varepsilon' + i\varepsilon''$, of specimens 94A, 95A and 96A calculated from the complex reflectivity shown in fig.8.1.

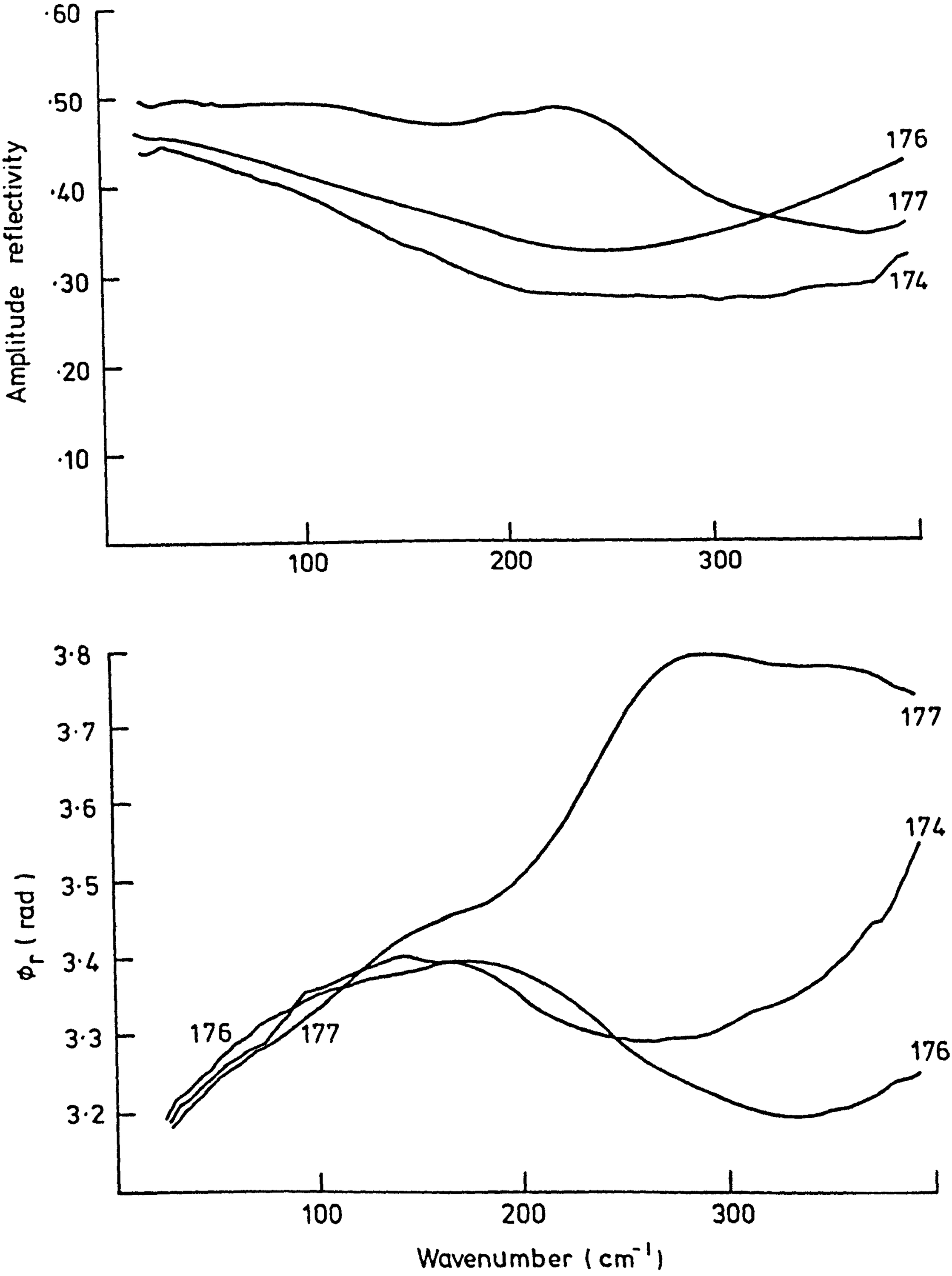

Fig.8.5. The measured amplitude, r , and phase, ϕ_r, of the complex Fresnel reflectivity of specimens 174, 176 and 177 below 400cm^{-1} at 290K.

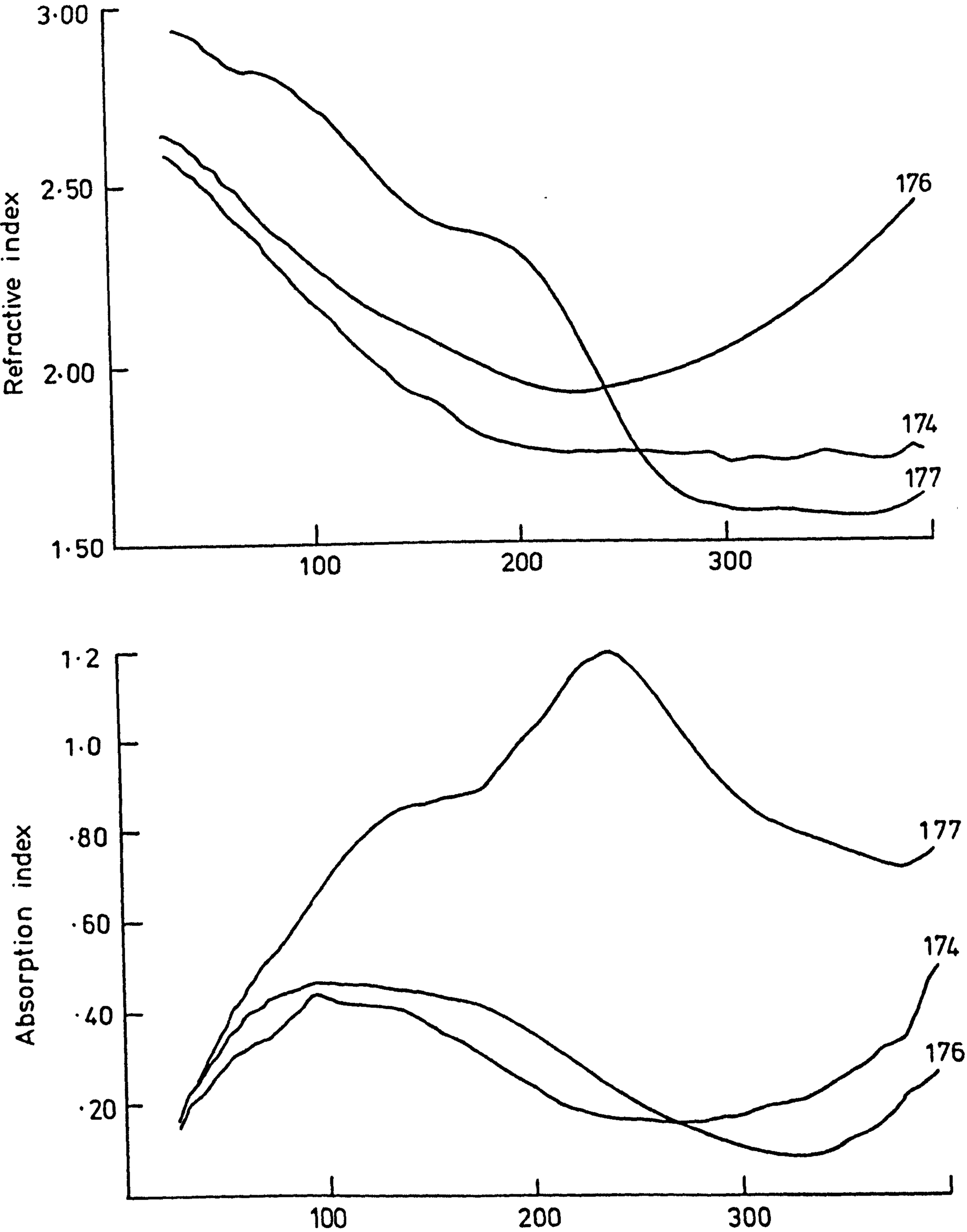

Fig.8.6. The refractive and absorption indices of specimens 174, 176 and 177 calculated from the complex reflectivity of fig.8.5.

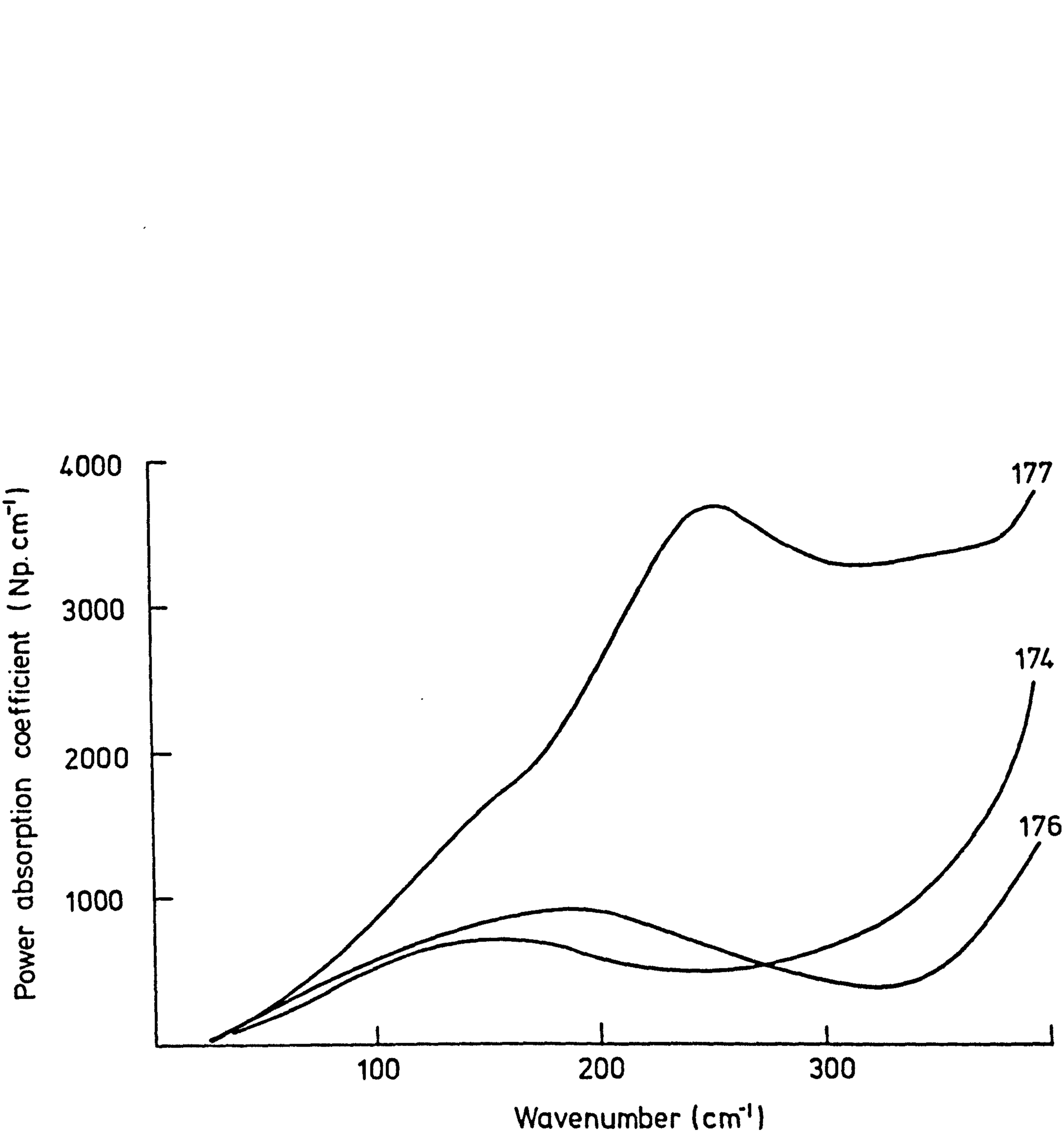

Fig.8.7. The power absorption spectrum of specimens 174, 176 and 177 calculated from the complex reflectivity spectrum of fig.8.5.

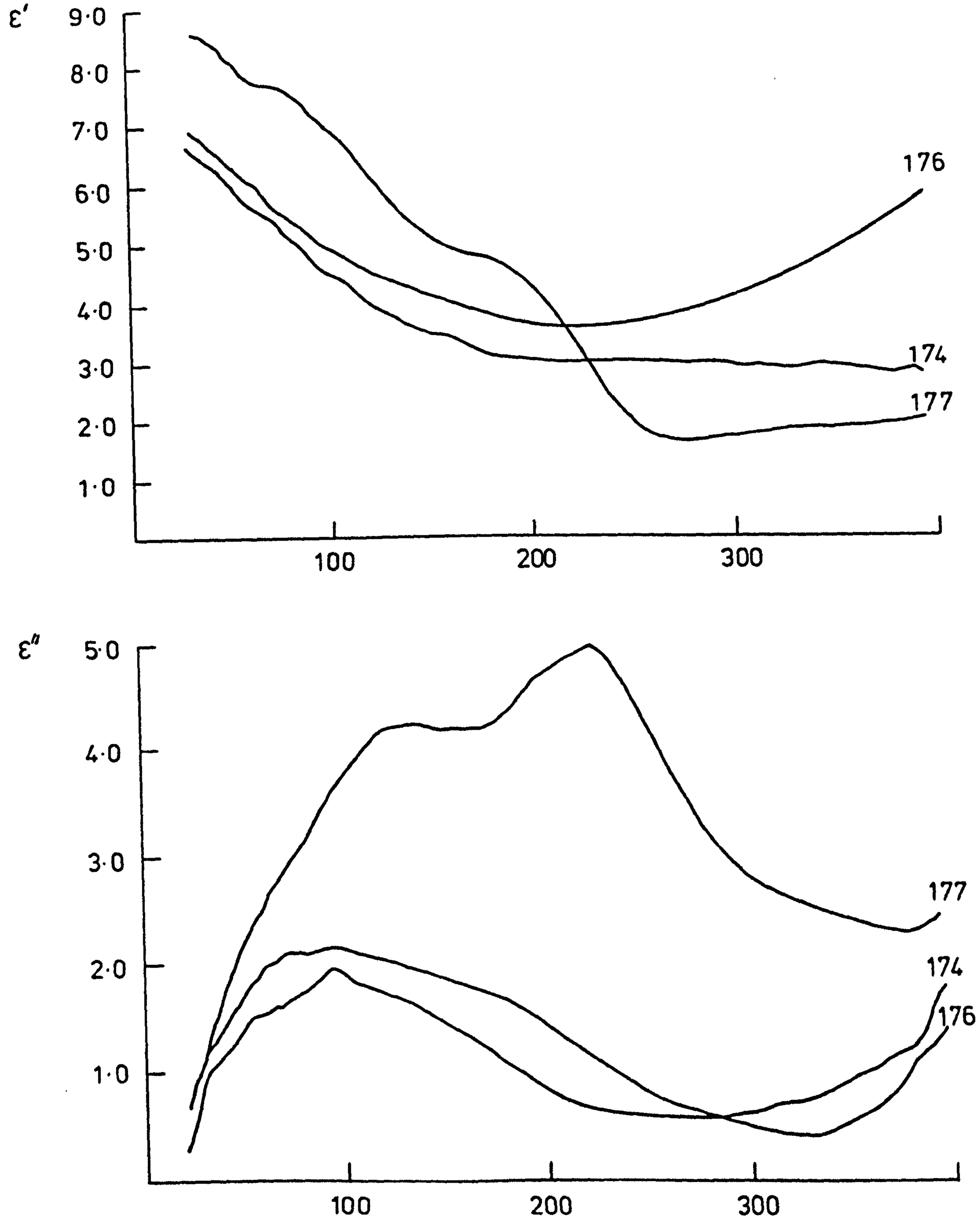

Fig.8.8. The real and imaginary parts of the complex relative permittivity $\hat{\varepsilon} = \varepsilon' + i\varepsilon''$, of specimens 174, 176 and 177 calculated from the complex reflectivity shown in fig.8.5.

coefficient spectra of these three binary silicate glasses shown in figure 8.3 it is immediately apparent that each has a broad absorption band superimposed on the monotonically falling absorption of the near infrared SiO_2 bands. The maxima of the bands of 95A and 96A both occur at $140cm^{-1}$ and that of 94A at $210cm^{-1}$. These glasses are binary systems having only one component in addition to SiO_2. It is therefore reasonable to assign the origins of these absorption bands to the additives, and,in particular,to vibrational modes of the metal ions following Exarhos and Risen[39]. Thus, the spectra of 95A and 96A, which share the same additive, K_2O, indicate that the charactersitic vibrational wavenumber of the K ion in SiO_2 is at $140cm^{-1}$. Similarly, the spectrum of 94A, which has the additive Na_2O, indicates that the characteristic vibrational wavenumber of the Na ion in SiO_2 is at $210cm^{-1}$.

Moving on to the measurements on the remaining specimens, 174, 176 and 177, we first note that measurements with the Fizeau interferometer indicated that the surfaces of these specimens were flat to about 0.2 μm. One therefore expects that this, combined with the use of the backlash operating procedure and the reproducibility of the specimen-reference support, would reduce any systematic phase errors to within the level of the random phase noise. It was, therefore, possible to have confidence in the absolute level of the n, k, α, ε' and ε'' spectra of figures 8.6 to 8.8, and then to follow an analysis along the more quantitative lines of that applied to the measurements on soda lime silica glass in section 7.5.3. The contribution of the SiO_2 network of each glass to its ε'' spectrum was calculated from the parameters of Aronson and Strong[41] and subtracted from the measured spectra to leave the difference spectra, $\Delta\varepsilon''$, of figure 8.9. These glasses are all ternary systems in which two metal oxides have been added to the SiO_2. Thus, one expects each difference spectrum to be the sum of two distinct components, one for each metal ion. That this appears

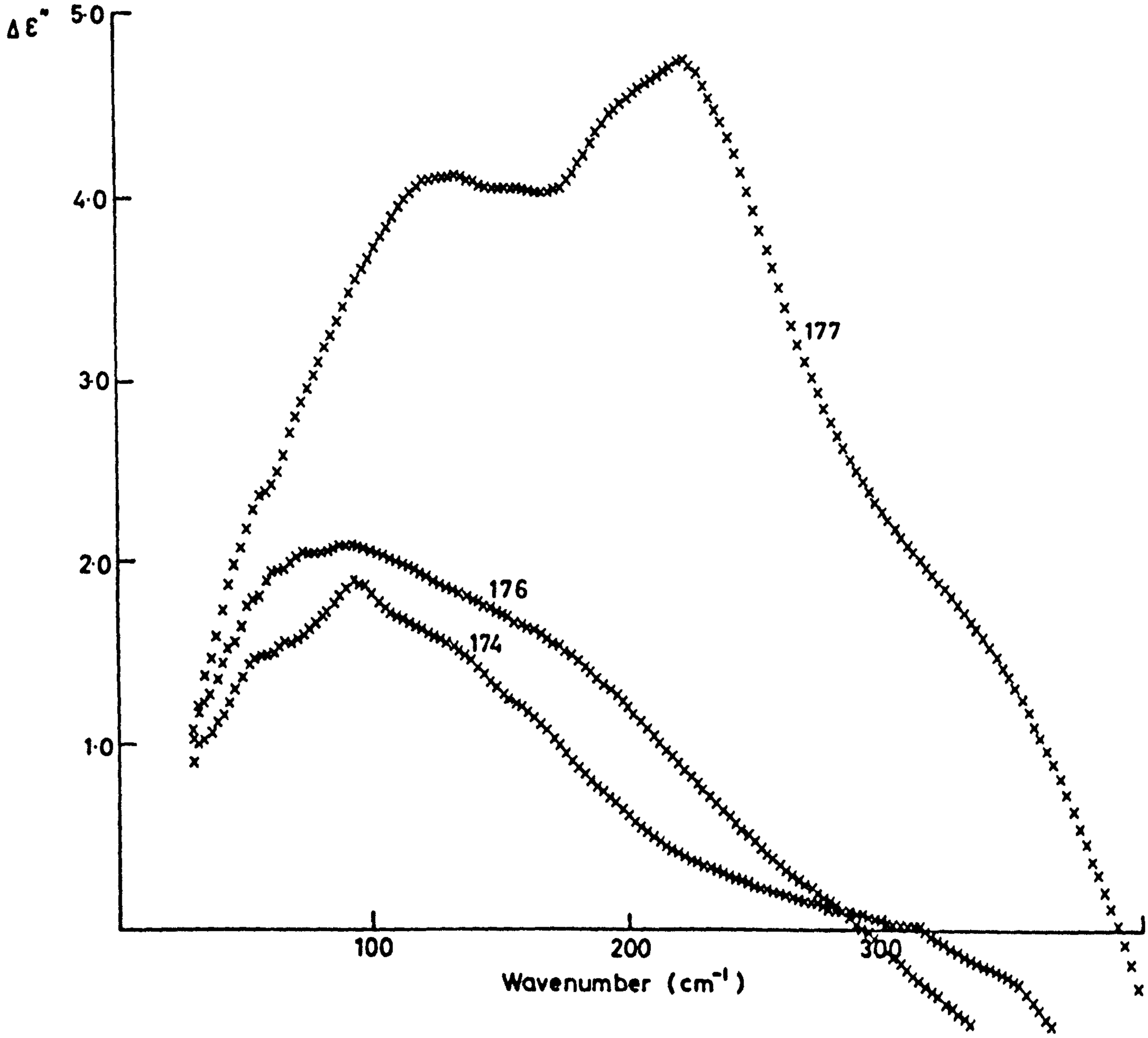

Fig.8.9. The difference between the imaginary part of the complex relative permittivities of specimens 174, 176 and 177 and that calculated for the SiO_2 network of each glass from the parameters of Aronson and Strong.

to be so is indicated by the two maxima of the 177 spectrum and the shoulder on the high wavenumber side of the peak of the 176 spectrum. All three difference spectra go negative above $300cm^{-1}$ indicating that either the glass measurements were lowered by unexpected systematic errors or that the SiO_2 ε'' -spectrum calculated from the concentration-scaled parameters of Aronson and Strong is not representative of the SiO_2 network in these glasses. In view of the surface quality of these specimens, and the present operating procedures, the latter seems the most likely explanation. This is particularly so when one examines the calculated ε'' -spectrum for the SiO_2 network shown in figure 7.25. Above $300cm^{-1}$ it rises very rapidly with increasing wavenumber so that small errors, or inapplicabilities, in the parameters of Aronson and Strong would be most likely to affect the difference spectra of figure 8.9 above $300cm^{-1}$ in the manner shown. As the ε'' spectrum of the SiO_2 network falls to zero at zero wavenumber and is much less rapidly varying below $300cm^{-1}$ than above, such errors in its calculation are not expected to have a gross affect on the conclusions of the present analysis which will concern wavenumbers about and below $200cm^{-1}$.

Although the ε'' spectrum of 177 indicates the presence of two contributions to the absorption spectrum, those of 176 and 174 are not so explicit, and it is necessary to proceed to some form of model calculation in order to obtain meaningful parameters with which to characterise these individual contributions, or, indeed, to see whether-or-not it is reasonable to represent these spectra as the sum of two components. Exarhos et al [43] have described the absorption associated with cation vibrations in simple metaphosphate glasses in terms of a broad damped harmonic oscillator model in which the broadening results from the different anharmonic potentials at each cation site. It seems reasonable, therefore, to extend this model to the present measurements and we have

generalised the single damped harmonic oscillator description of the complex relative permittivity given by equation 7.21 to include the contributions from N such oscillators. Hence

$$\hat{\varepsilon}(\tilde{\nu}) = \varepsilon(\infty) + \sum_{j=1}^{N} \frac{S_j \tilde{\nu}_j^2}{\tilde{\nu}_j^2 - \tilde{\nu}^2 - i\tilde{\nu}\gamma_j} \qquad \ldots (8.1)$$

from which the real and imaginary parts are obtained as

$$\varepsilon'(\tilde{\nu}) = \varepsilon(\infty) + \sum_{j=1}^{N} \frac{S_j \tilde{\nu}_j^2(\tilde{\nu}_j^2 - \tilde{\nu}^2)}{(\tilde{\nu}_j^2 - \tilde{\nu}^2)^2 + \tilde{\nu}^2\gamma_j^2} \qquad \ldots (8.2)$$

and,

$$\varepsilon''(\tilde{\nu}) = \sum_{j=1}^{N} \frac{S_j \tilde{\nu}_j^2 \gamma_j \tilde{\nu}}{(\tilde{\nu}_j^2 - \tilde{\nu}^2)^2 + \tilde{\nu}^2\gamma_j^2} \qquad \ldots (8.3)$$

We have made calculations of $\varepsilon''(\tilde{\nu})$ from equation 8.3 with N=2 using $\tilde{\nu}_j$, S_j and γ_j as adjustable parameters to obtain good (by-eye) fits to the $\Delta\varepsilon''$ spectra of figure 8.9. Initial values for some of the $\tilde{\nu}_j$'s were obtained from the following arguments.

(i) 177 has maxima in its $\Delta\varepsilon''$ spectrum at 130 and 225cm^{-1}. Therefore the initial values were taken as $\tilde{\nu}_1 = 130\text{cm}^{-1}$ and $\tilde{\nu}_2 = 225\text{cm}^{-1}$.

(ii) 174 and 176 both peak in the region of 100cm^{-1}. Therefore $\tilde{\nu}_1$ was initially taken as 100cm^{-1} for both.

(iii) 174 and 176 both have long shoulders to the high wavenumber side of their peaks. Therefore, $\tilde{\nu}_2$ will be greater than 100cm^{-1} for both.

Additionally, we note that all of the $\Delta\varepsilon''$ spectra of figure 8.9 have widths of about 200cm^{-1}, or greater. It therefore seems reasonable to assume that the damping coefficients, γ_j, which determine the width, will be greater than, say 50cm^{-1}.

The results of these model fits to the experimental data are presented in figure 8.10. Each graph shows the experimental $\Delta\varepsilon''$ -spectrum plotted as crosses, together with three continuous curves. The one with the largest ordinates is the best fit of equation 8.3 to the experimental data, while the two smaller curves show the contribution of the individual oscillators to the best fit result. It is immediately clear that the experimental $\Delta\varepsilon''$ -spectrum of each glass is reasonably well described by this simple two oscillator model. The agreement between measurement and theory is best below $200cm^{-1}$ in all three cases as the two spectra diverge at higher wavenumbers where the measured spectra go negative, a situation that cannot be described by this model and one that probably results from the incorrect subtraction of the SiO_2 contribution, as discussed earlier in this section. The centre wavenumbers of the six component oscillators used in these calculations fall in three distinct groups (100, 105 and $130cm^{-1}$; 155 and $180cm^{-1}$; $232cm^{-1}$;)and, although there is a spread of wavenumbers within the first two groups, this suggests that the oscillators within each group are characterstic of the same vibrational mode. These modes have been labelled 1, 2 and 3 in figure 8.10 and the best fit oscillator parameters for each are listed in table 8.2. Thus, all three glasses have an oscillator that can be assigned to mode 1, 174 and 176 have oscillators that can be assigned to mode 2,

MODE / SPECIMEN	1. $\tilde{\nu}_1$	γ_1	S_1	2. $\tilde{\nu}_2$	γ_2	S_2	3. $\tilde{\nu}_3$	γ_3	S_3
174	100	130	1.6	155	150	0.67	-	-	-
176	105	160	2.3	180	140	0.7	-	-	-
177	130	120	2.4	-	-	-	232	140	2.4

Table 8.2 The classical damped harmonic oscillator parameters giving the best fit to the $\Delta\varepsilon''$ spectra of the three glasses. The mode wavenumber, $\tilde{\nu}$, and mode damping, γ, are in cm^{-1}, the mode strength, S, is dimensionless.

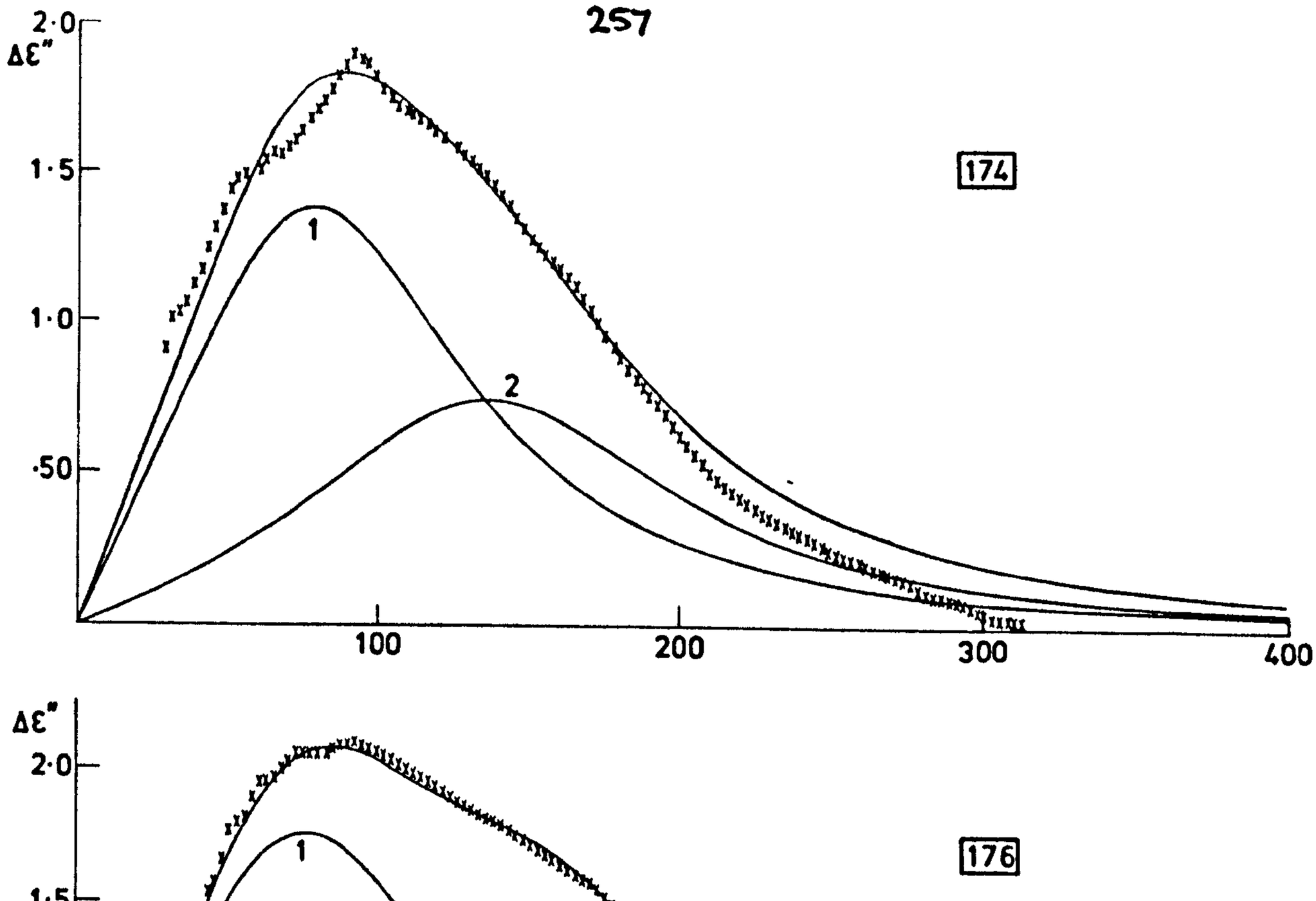

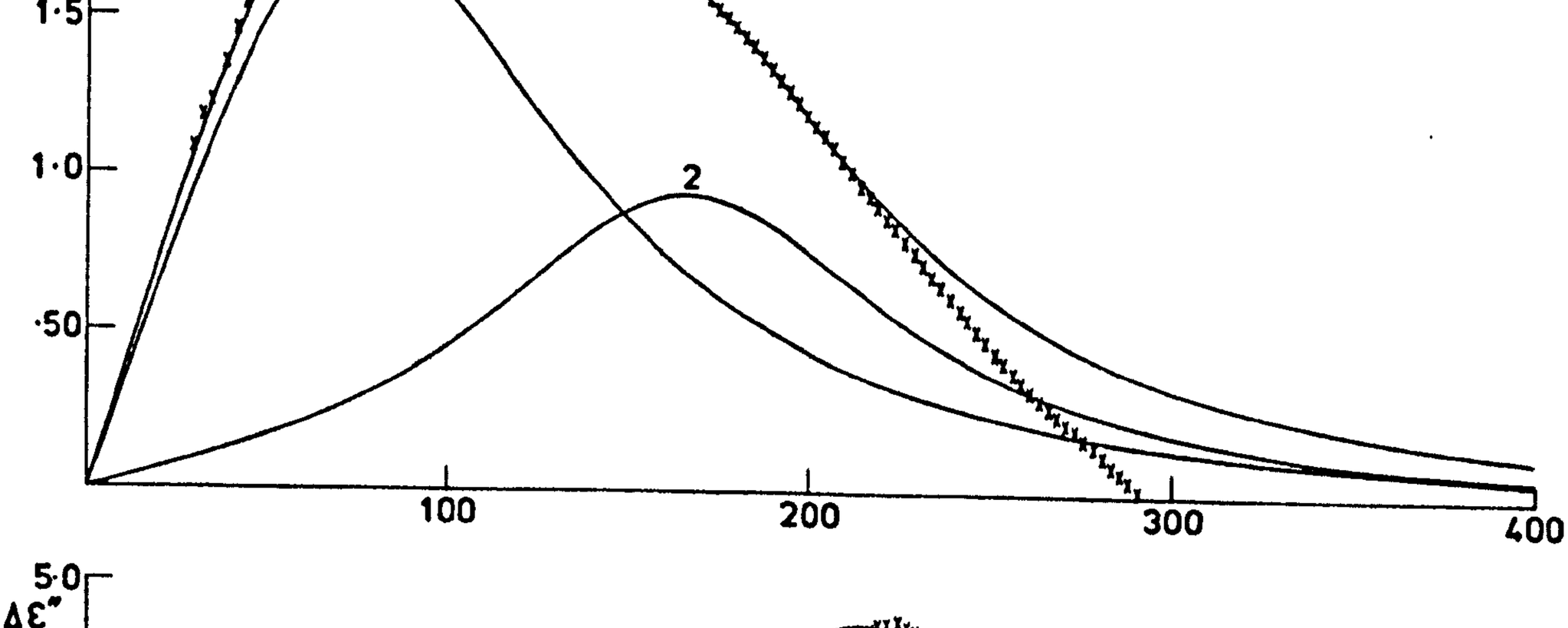

WAVENUMBER (cm^{-1})

Fig.8.10. Damped harmonic oscillator fits to the $\Delta\varepsilon''$-spectra of specimens 174, 176 and 177. The crosses are the experimentally determined points of fig.8.9. The continuous curve with the largest ordinates represents the sum of the contributions from the individual oscillators 1, 2 or 3.

and only 177 has a mode 3 oscillator. When this distribution is compared to that of the metal oxides of each glass - Al_2O_3 common to all three, Na_2O in 174 and 176, and CaO in only 177 - it seems that mode 1 is associated with the vibrational motion of the Al ion, mode 2 with the vibrational motion of the Na ion and mode 3 with the vibrational motion of the Ca ion.

Having obtained such reasonable agreement between this simple model and the $\Delta\varepsilon''$ spectra it is appropriate to examine the corresponding behaviour of the measured and calculated $\Delta\varepsilon'$ spectra. These are shown in figure 8.11 with the crosses representing the experimental data and the continuous curves the calculations using the appropriate parameters from table 8.2 with $\varepsilon(\infty)$ as 2.262 (from Aronson and Strong) in equation 8.2. For 176 and 177 the calculated curves reproduce the spectral variation of the experimental data quite well, although, in both cases, the calculated result is systematically above the experimental data by an amount that varies between 0.2 and 1.5. This is unlikely to be due to an error in $\varepsilon(\infty)$ as the visible refractive indices of silicate glasses ($\sim$ 1.5) indicates that $\varepsilon(\infty)$ must be taken as being about 2.25 for the present model which would not otherwise explicitly include the effects of the ultra violet absorption bands. It is more probable that this comparison is showing similar behaviour to that of experiment and theory for the CdTe measurements of section 7.4.3, i.e. that it is not reasonable to expect a single set of parameters for the classical damped harmonic oscillator model to represent both ε' and ε'' of a real system, especially a glass for which the observed absorption bands would be expected to be envelopes encompassing the bands of individual ions or groups of ions broadened and shifted by local disorder. Experiment and theory diverge most of all for 174, with the two being most separate at higher wavenumbers. However, in general, the dispersion across these ionic absorption bands is not too inconsistent with the present,

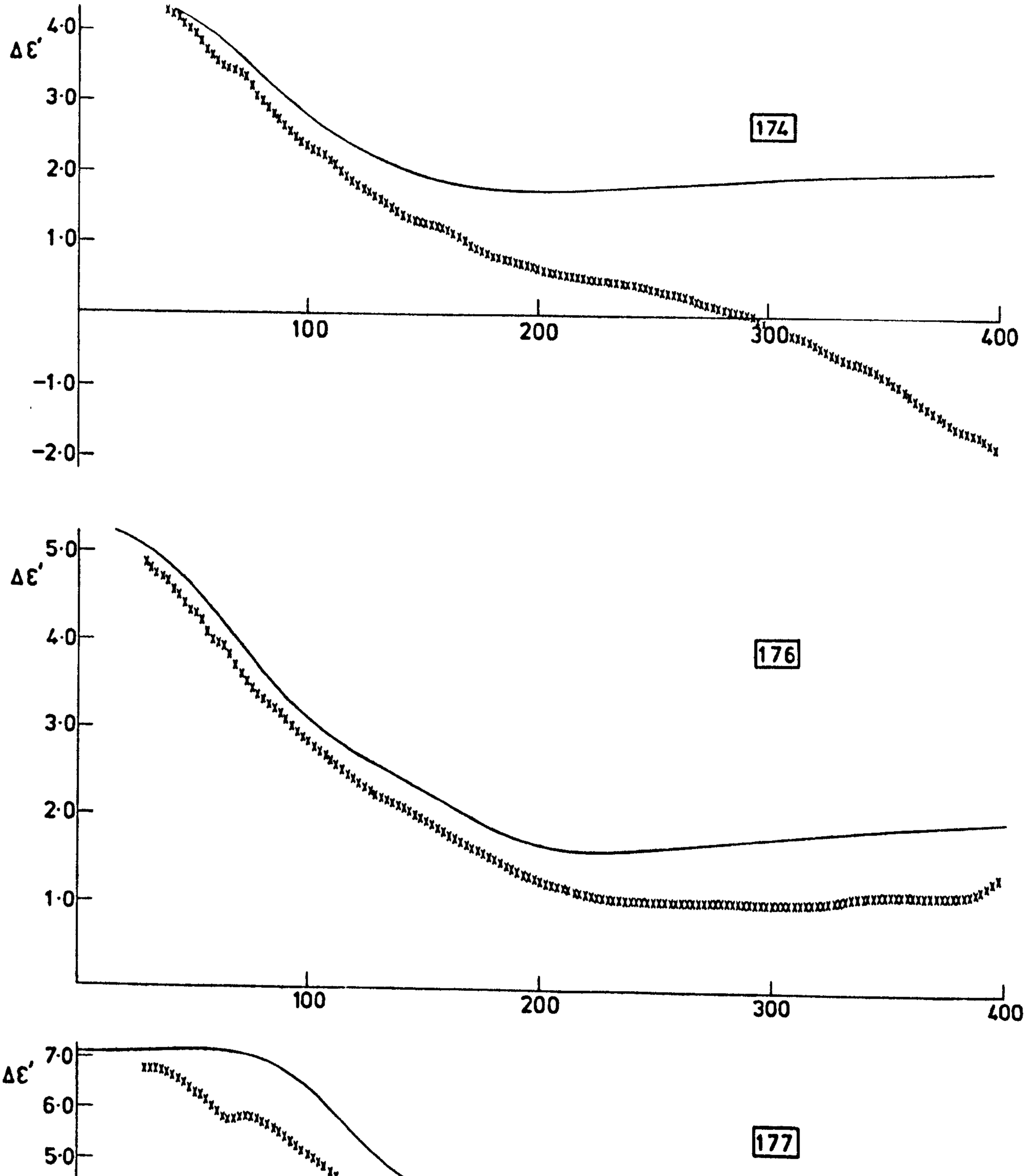

Fig.8.11. Damped harmonic oscillator fits to the $\Delta\varepsilon'$-spectra of specimens 174, 176 and 177. The crosses are the experimentally determined points, while the continuous curves are calculated from the parameters of the best fit $\Delta\varepsilon''$-spectra of fig.8.10.

simple calculations.

In order to estimate reasonable error limits to put on the best fit parameters the model $\Delta\varepsilon''$-spectrum of 176 was recalculated for six sets of new parameters in which those of the first mode ($\tilde{\nu} = 105cm^{-1}$, $\gamma = 160cm^{-1}$, $S = 2.3$) were singly varied by the following amounts, $\Delta\tilde{\nu} = \pm 5cm^{-1}$, $\Delta\gamma = \pm 10cm^{-1}$ and $\Delta S = \pm 0.1$. The results of these calculations are shown in figure 8.12. Each part summarises the effects of varying one particular variable, (a) for $\tilde{\nu}$, (b) for γ and (c) for S. In each, the crosses are again the experimental points from figure 8.9, and the centre curve of each of the sets of continuous curves is that of figure 8.10 obtained from the best fit parameters of table 8.2. The other two curves represent the spectrum recalculated using the new values of the parameter being varied. The displacement of these recalculated spectra from the experimental points, especially in the region of the overall band centre, allows estimates to be made of reasonable limits for the best fit parameters. Thus, for the parameters listed in table 8.2, the mode wavenumber, $\tilde{\nu}$, is determined to $\pm 2cm^{-1}$, the mode damping, γ, to $\pm 5cm^{-1}$ and the mode strength, S, to ± 0.1.

It is interesting to note, from figure 8.10 and table 8.2, that the maximum of the $\Delta\varepsilon''$ spectrum of any of the individual oscillators does not coincide with its wavenumber, but is always displaced to lower wavenumbers by as much as $30cm^{-1}$ in some cases. This is because of the heavy damping of these oscillators for which $\gamma_j \sim \tilde{\nu}_j$. The effect of this may be seen by solving equation 8.3 for the wavenumber, $\tilde{\nu}_{max}$, of the ε'' maximum. This gives

$$\tilde{\nu}^2_{max} = \frac{(2\tilde{\nu}_j^2 - \gamma_j^2) + \sqrt{(2\tilde{\nu}_j^2 - \gamma_j^2)^2 + 12\tilde{\nu}_j^4}}{6} \quad \ldots (8.4)$$

and it is apparent that $\tilde{\nu}_{max} < \tilde{\nu}_j$ unless $\gamma_j = 0$.

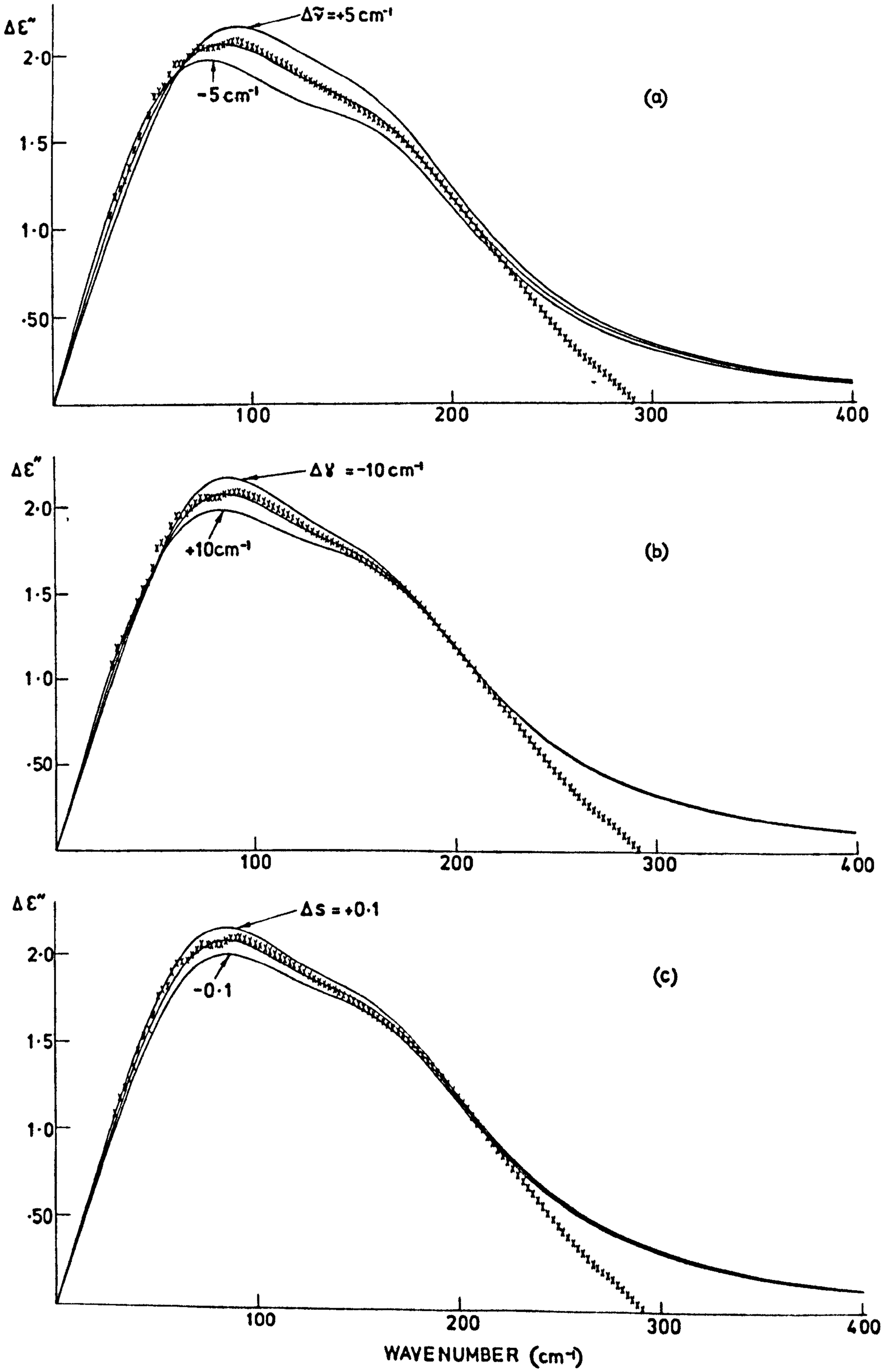

Fig.8.12. Model calculations of the $\Delta\varepsilon''$-spectrum for specimen 176. In (a) $\tilde{\nu}_j$, in (b) γ_j and in (c) s_j, are varied by the amounts indicated in order to establish reasonable error limits for these parameters.

In their study of ionic absorption bands in metaphosphate glasses by transmission techniques Exarhos et al [43] found linear relationships between the band width and the band frequency and between integrated absorption intensity and band frequency squared which they were able to predict by an extension of the work of Whalley and Bertie [231] on the infrared absorption of one dimensional disordered crystals. It is not possible to pursue a similar analysis of the present measurements for two reasons. Firstly, Exarhos et al considered a larger number of ions than the present work and, secondly, their measurements were on single oxide glasses. Thus, from their measurements they were able to unambiguously associate a band centre, width and intensity with a particular ion. In the present measurements quantitative experimental data is only available for the three ternary silicate glasses and it is not possible to resolve the experimentally observed bands into their two components, other than by model calculation. However, given the reasonable agreement found between the experimental $\Delta\varepsilon''$ spectra of these ternary glasses and the simple two oscillator calculations the parameters of the calculations were investigated to see whether-or-not any systematic trends, such as smooth dependences on composition, could be discerned. The results of this are summarised in figure 8.13, the various parts of which show $\tilde{\nu}_j$ and S_j against precentage composition, γ_j against $\tilde{\nu}_j$ and $\tilde{\nu}_j$ against the atomic mass of the particular ion associated with the mode. The only firm conclusion that one can arrive at from this figure is that this is insufficient data to detect any significant trends. Ideally, more measurements would now be made on a wider range of compositions for particular metal oxides, and also on more metal oxides. There are, however, some tentative conclusions that can be put forward on the basis of the present data:

(i) The limited data for the variation of the centre wavenumber of the Al band with composition show a smooth variation, with

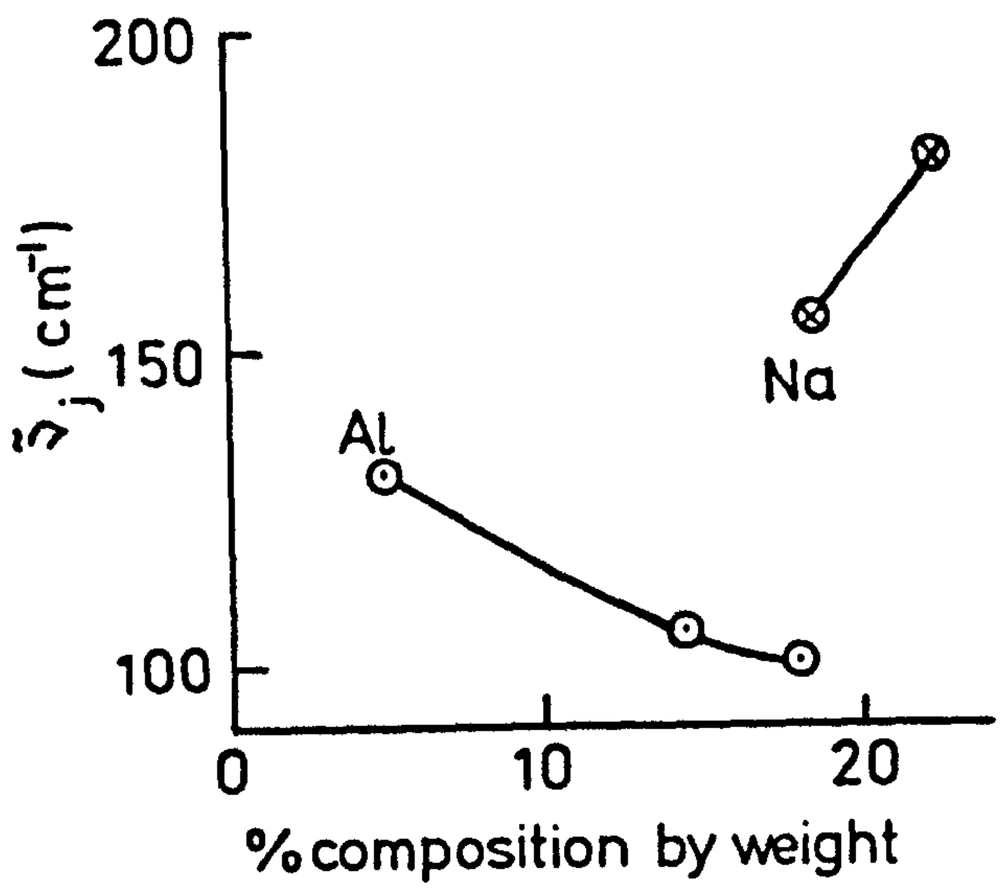

(a)

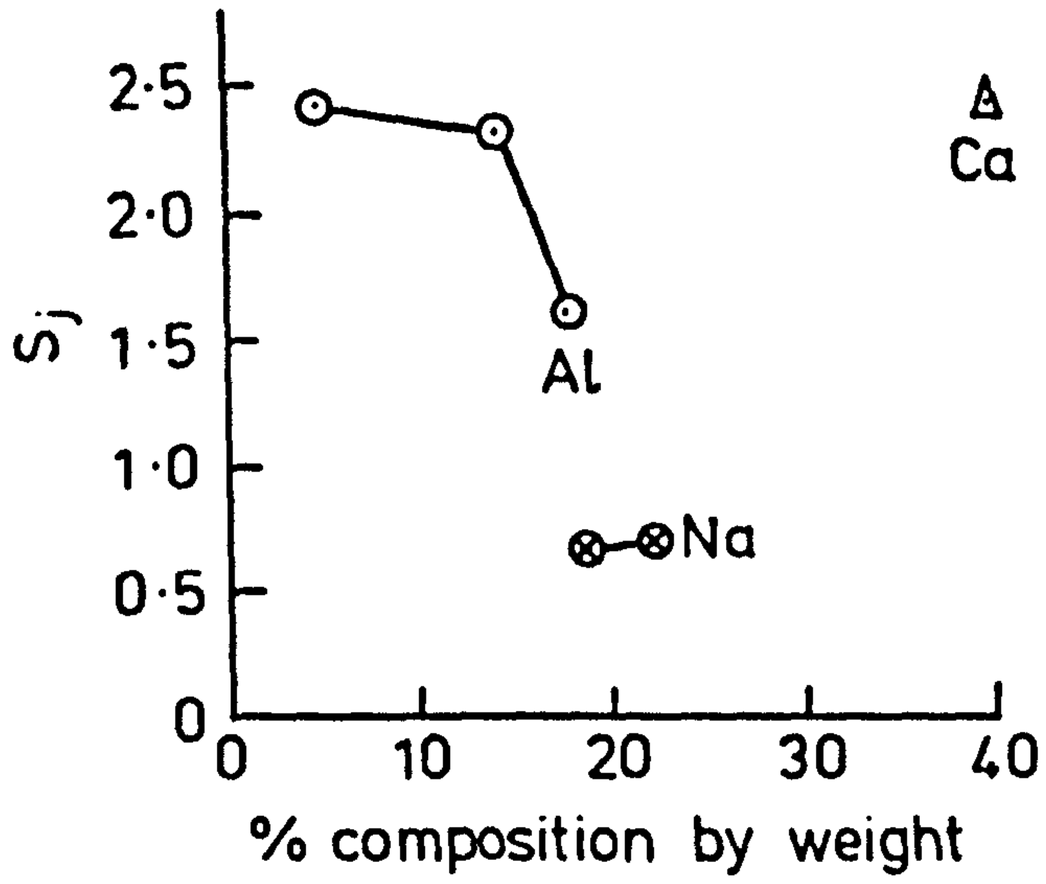

(b)

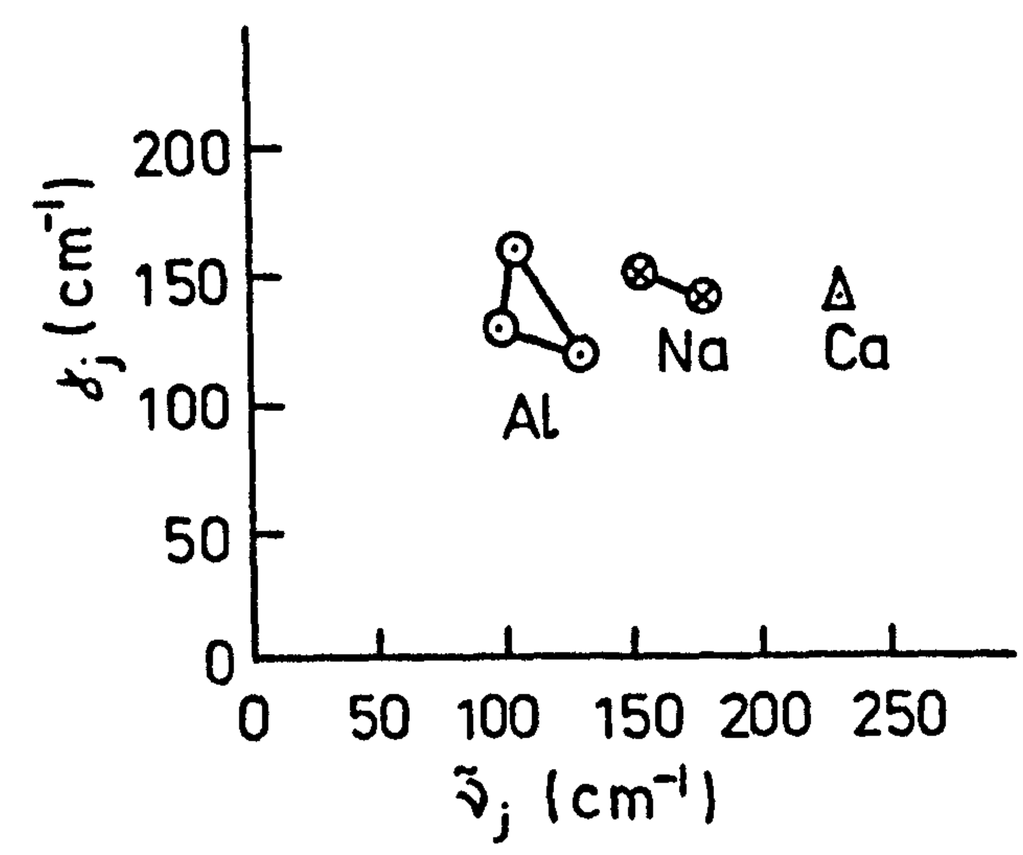

(c)

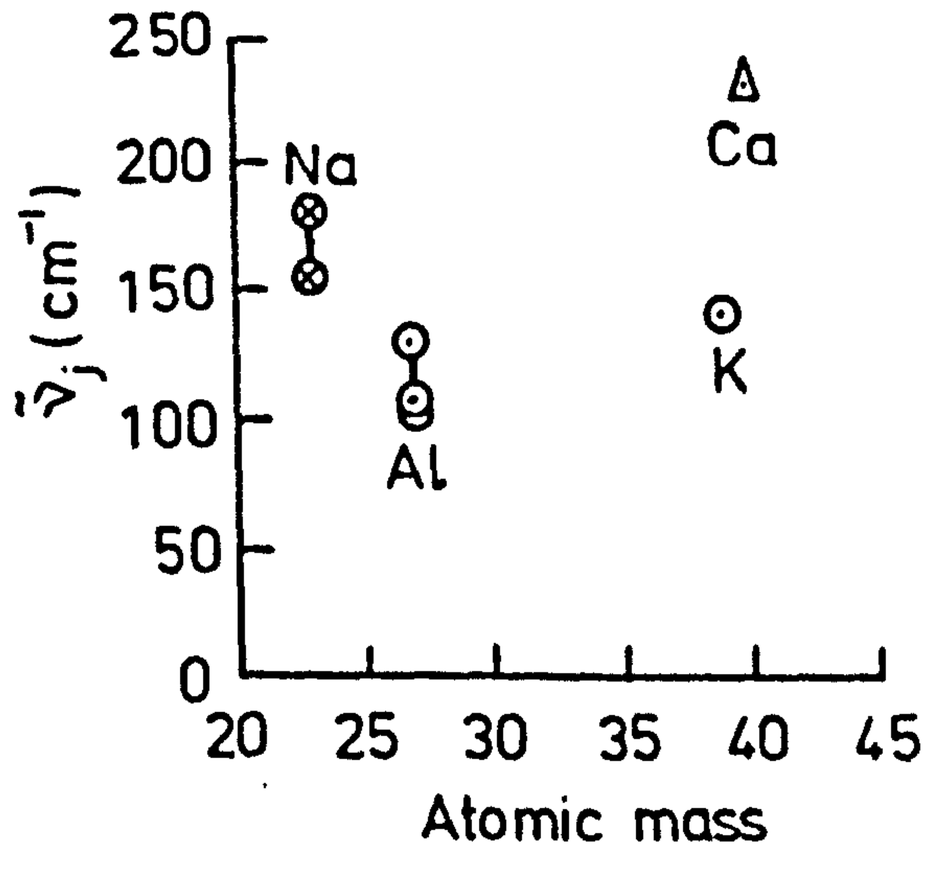

(d)

Fig.8.13. The relationships between the best fit parameters of the $\Delta\varepsilon''$-spectra and the composition of the glasses.

the band centre moving to lower wavenumbers as the Al_2O_3 component decreases. The two points representing the Na band indicate the opposite behaviour, a movement of the band to higher wavenumbers with increasing Na_2O component. This is consistent with the behaviour of the corresponding band in $(Na_2O)_x \cdot P_2O_5$ found by Exarhos et al[43]

(ii) In their measurements of the vibrational absorption bands of alkali metal cations in some inorganic oxide glasses Exarhos and Risen[39] found that the frequency of the band centre varied approximately as $(m_c)^{-\frac{1}{2}}$, where m_c is the mass of the cation, in accordance with the theoretical treatment of Charles[232]. In part d of figure 8.13 the centre wavenumber of the various bands is therefore plotted against the atomic mass of the assigned ion (this includes the $140cm^{-1}$ potassium band of the binary glasses 95A and 96A). Again there is insufficient data from which conclusions can be drawn. Such a variation just falls with the error limits of the two groups of points (Al and Na.) As the compositions of 177 (Ca band) and 95A and 96A (K band) are very different from those of 174 and 176 it is not surprising that those points do not fall close to that particular trend.

Having used these measurements on the three ternary silicate glasses to assign characteristic oscillator parameters to the absorption bands associated with the Al, Ca and Na metal oxide additives it was obvious that the next step to take was to calculate a $\Delta\varepsilon''$ spectrum from these parameters that might be representative of soda lime silica glass. The calculation was performed using the set of parameters listed in table 8.3. These were derived from the parameters

Mode	Oxide	$\tilde{\nu}_j$	γ_j	S_j
1	Al_2O_3	150	145	0.6
2	Na_2O	130	145	0.6
3	CaO	232	140	0.5

Table 8.3 The classical damped harmonic oscillator parameters for the first calculation of the $\Delta\varepsilon''$ spectrum of soda lime silica glass. These were derived by scaling by composition from the parameters of table 8.2. The mode wavenumber, $\tilde{\nu}$, and damping, γ, are in cm^{-1}, the mode strength, S, is dimensionless.

of table 8.2 by scaling to the composition of the oxides in soda lime silica glass (Al_2O_3 1.65%, Na_2O 12.5%, CaO 8.4%). Thus, for 1.65% of Al_2O_3 figure 8.13a indicates that the mode frequency should shift to $150cm^{-1}$ and that the strength on a straight line extrapolation between 0 and 5% composition on figure 8.13b, should be 0.6. The mode damping was taken to be the average of that for 174 and 176 as these are the most similar glasses to soda lime silica glass. Similar extrapolations gave the parameters for the Na_2O mode, while, for the CaO mode, for which there is only one data point, the mode wavenumber and damping were held constant and the strength reduced in proportion to concentration. Using these parameters the contribution of the three modes to the imaginary permittivity between 0 and $400cm^{-1}$ was calculated and is shown in figure 8.14a. In this figure the crosses are the experimentally determined $\Delta\varepsilon''$ spectrum of figure 7.27, the continuous curve with the largest ordinates is the calculated contribution of all three modes, while the three smaller curves represent the individual mode contributions. The agreement between the experimentally derived spectrum and the calculated one is fairly

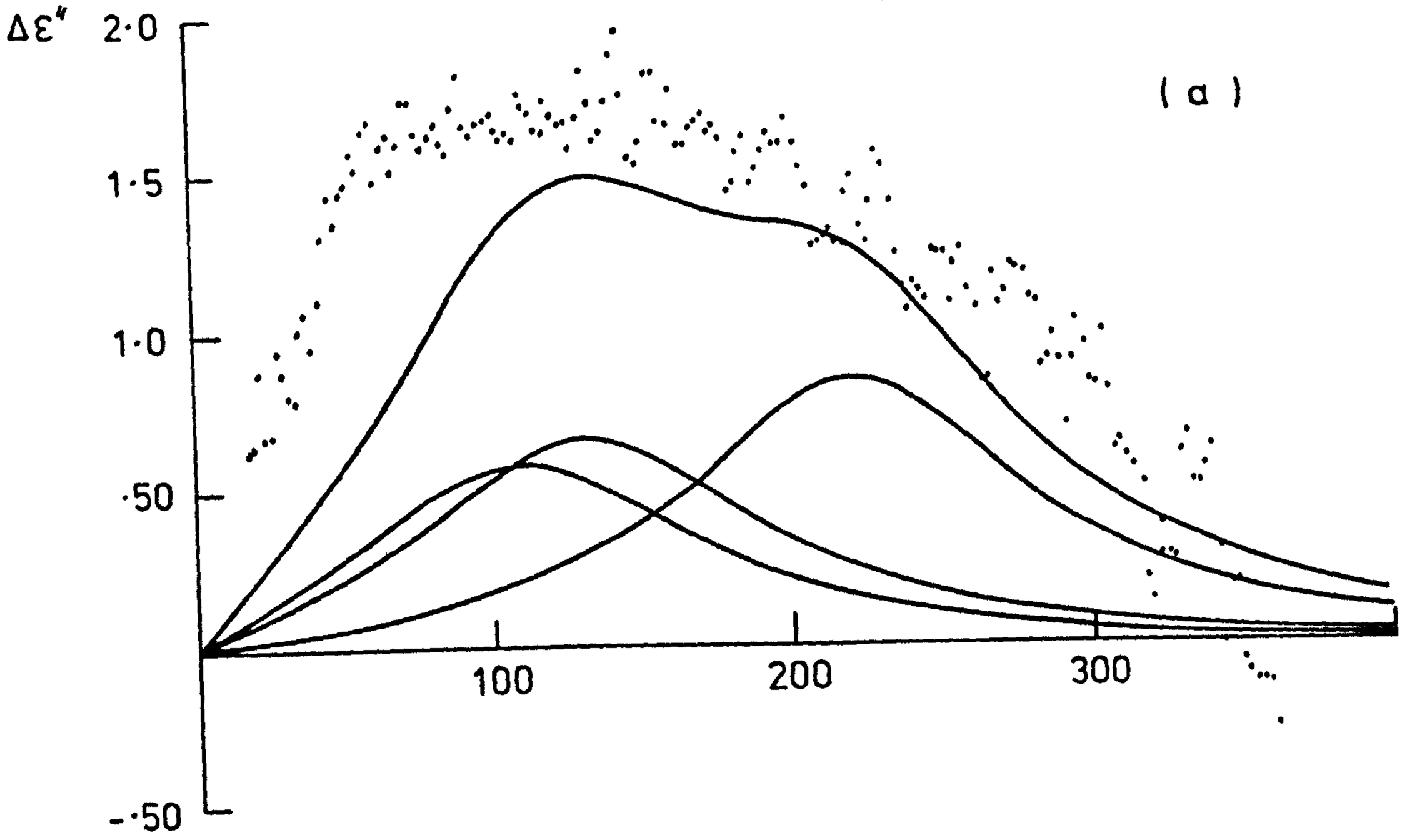

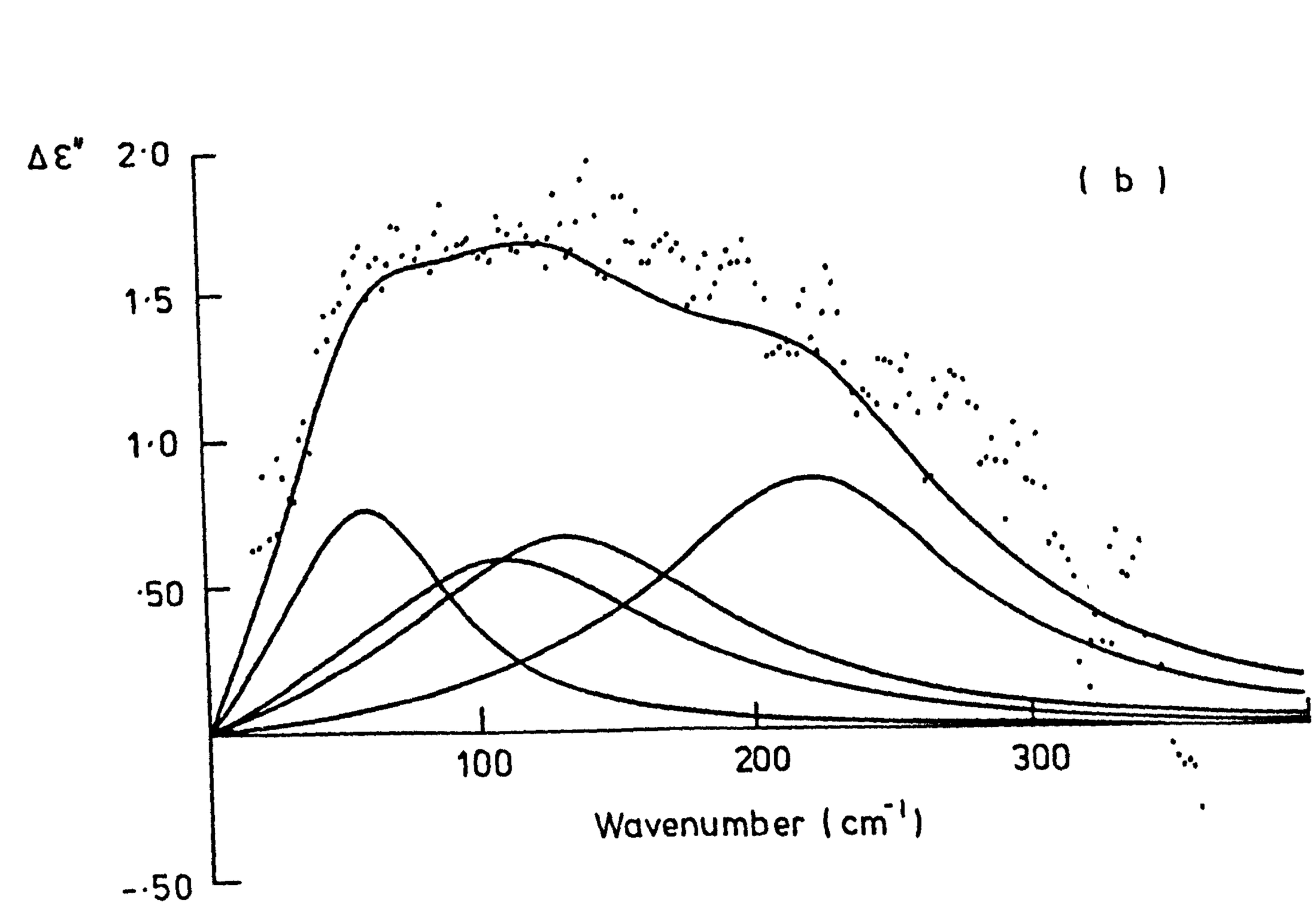

Fig.8.14. Damped harmonic oscillator fits to the $\Delta\varepsilon''$-spectrum of soda lime silica glass shown in fig.7.27. The experimental data are shown as crosses. (a) was calculated for a 3-oscillator model of the ionic contribution, (b) for a 4. In both parts the curve with the largest ordinates represents the sum of the individual ionic contributions shown below it.

good, particularly above 130cm^{-1}, but at the lower wavenumbers where the two differ by significant amounts the three mode model is obviously incapable of describing the experimentally observed spectrum. However, in applying a three mode description of the complex permittivity to soda lime silica glass we have ignored the fact that this glass has four metal oxide additives, containing 4.2% by weight of MgO in addition to the Al_2O_3, Na_2O and CaO used in the calculations of figure 8.14a. Thus, it seemed reasonable to extend the calculated spectrum of this figure to include a fourth mode which would occur somewhere below 100cm^{-1} and which would be characteristic of the MgO additive. The $\Delta\varepsilon''$ spectrum was therefore recalculated with the parameters of the first three modes kept the same as those used for figure 8.14a and those of the fourth mode adjusted to give the best fit 'by eye' to the experimental spectrum. The results of this are shown in figure 8.14b. The best fit occurred for $\tilde{\nu}_4 = 70\text{cm}^{-1}$, $\gamma_4 = 80\text{cm}^{-1}$ and $S_4 = 0.8$, and is represented by the larger of the five curves, the four smaller ones representing the individual mode contributions, as before. The agreement obtained between measurement and calculation is very good over the entire spectrum and leads one to conclude that the four mode description of the excess complex permittivity of soda lime silica glass below 400cm^{-1} provides a good description of the absorptive loss arising from the ions associated with the metal oxide additives of the glass. This conclusion can be criticised on the grounds that an absorption envelope can generally be represented as the sum of a sufficient number of classical oscillators, without there necessarily being any physical significance to the oscillators. This is of course so, but the oscillator parameters for three of the soda lime silica glass modes were not adjustable parameters chosen from a fit to the experimental spectrum, but were derived from fits to the measurements on the simple two oxide, ternary glasses. This, and the one-to-one correspondence between the number of modes necessary

to fit the experimental spectra and the number of metal oxide additives of each glass (95A - 1:1; 174, 176 and 177 - 2:2; soda-lime-silica glass - 4:4;) lead one to believe that the original conclusion was correct.

Figure 8.15 provides further evidence for the general validity of this simple description of the excess loss in soda lime silica glass. It presents the experimentally determined $\Delta\varepsilon'$ - spectrum of figure 7.27, representing all contributions to the relative permittivity except that of the SiO_2 network, together with those calculated from the three- and four-mode parameters discussed above for the $\Delta\varepsilon''$ -spectrum. Above $100cm^{-1}$ the two calculated spectra are quite similar and have virtually run together by $400cm^{-1}$. Below $100cm^{-1}$, however, the three mode spectrum clearly does not represent the measurements, in common with its behaviour in the $\Delta\varepsilon''$ -spectrum. The four mode calculation does, however, provide a good representation of the overall shape of the spectrum, although it is at a higher level, in common with the calculations for the ternary glasses shown in figure 8.11.

8.2 CONCLUSIONS

The measurements presented in this chapter of the complex reflectivity of some binary and ternary silicate glasses, and of soda lime silica glass, represent the first direct determinations of the optical constants of silicate glasses in their region of mid-infrared opacity. Using the measurements on the binary and ternary glasses it was possible to assign characteristic oscillator parameters to the vibrational loss processes of the ions associated with the metal oxide additives of the glasses. These parameters were then used to account for all of the loss between 20 and $360cm^{-1}$ in soda lime silica glass in terms of a summation of the contribution from the four ions of that system, together with the background loss due to the SiO_2 network.

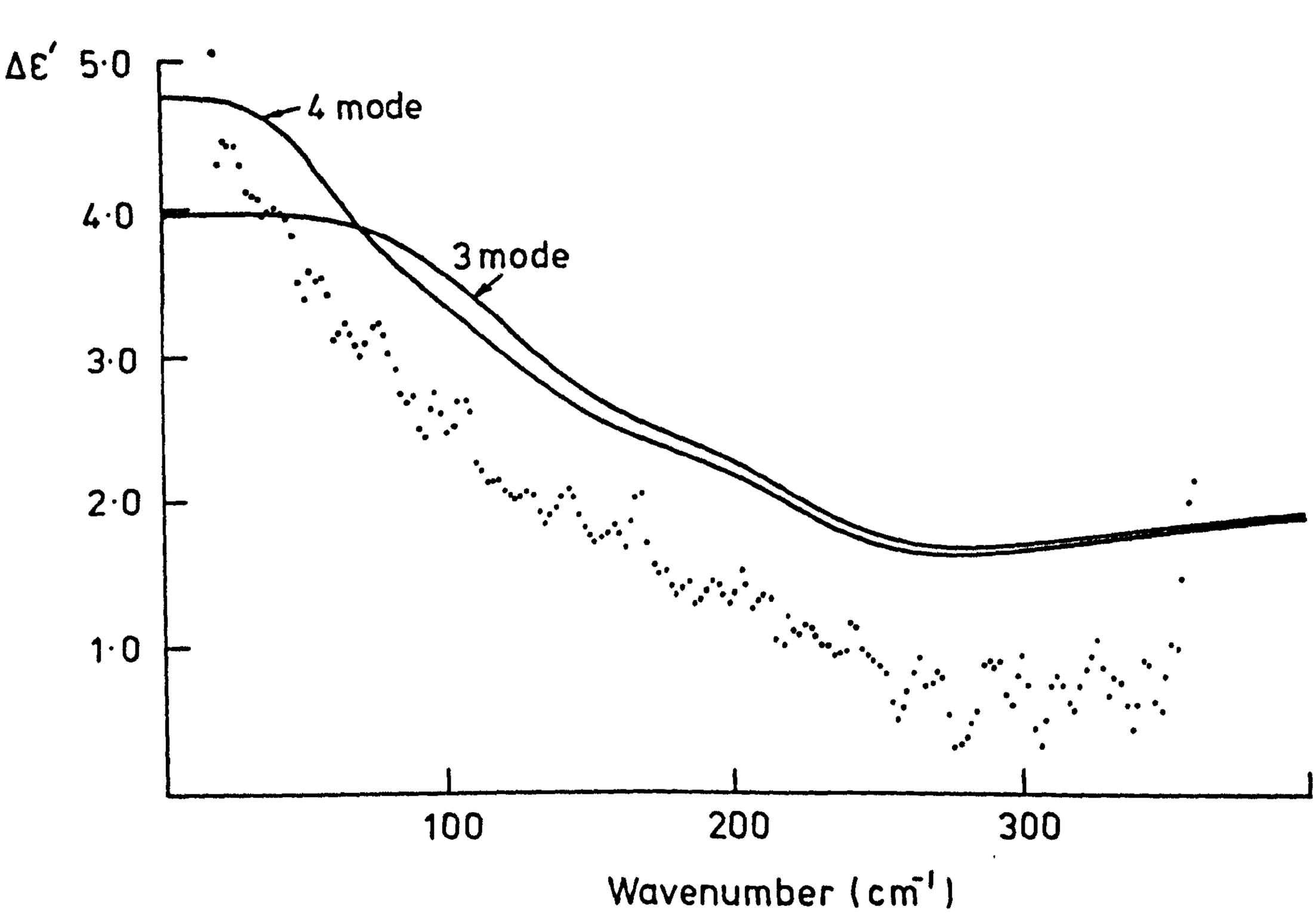

Fig.8.15. The 3- and 4-mode damped harmonic oscillator fits to the $\Delta\varepsilon'$-spectrum of soda lime silica glass corresponding to the calculations of fig.8.14.

CHAPTER 9

CONCLUSIONS

This work has been mainly concerned with the development and use of broad band Fourier transform spectrometric methods for the study of the optical constants of solid materials at millimetre and submillimetre wavelengths. Power transmission, dispersive transmission and dispersive reflection methods have been considered, and it has been shown that, within the limits of experimental error and the applicability of each method, all three give equivalent results. The particular experimental difficulties of each method have been considered and the techniques developed to the extent that the optical constants of a solid can be determined with the accuracies outlined in table 9.1. These are largely determined by the

α ($Np.cm^{-1}$)	Accuracy in	Power transmission	Dispersive transmission	Dispersive reflection
<20	α	0.05 - 0.1	0.05 - 0.1	-
	n	0.02	0.0001	-
20-150	α	0.1 - 10	0.1	-
	n	-	0.001	-
>150	k	-	-	0.01
	n	-	-	0.01

Table 9.1 Typical accuracies that can be achieved in the determination of the optical constants of a solid by Fourier transform spectrometry. The dispersive transmission figures refer to a double pass measurement. Note that for the reflection measurements the accuracy in k, not α, is considered.

magnitude of the power absorption coefficient, but the spectral range and resolution are also factors that influence the accuracy that can be achieved. Thus,

for measurements on fairly transparent solids ($\alpha < 20$ Np.cm^{-1}) both power and dispersive transmission measurements allowed the power absorption coefficient to be determined with an accuracy of between 0.05 and 0.1 Np.cm^{-1}. The refractive index, however, could only be found to about 0.02 from an analysis of channel spectra, whereas the use of dispersive transmission measurements enabled it to be found to about 0.0001, provided that the specimen thickness was adequately well-defined. For more absorbing, but still transmitting, materials the accuracy achieved in α from power transmission measurements was found to vary between 0.1 and 10 Np.cm^{-1} as α increased to $\sim$ 150 Np.cm^{-1}. Dispersive transmission measurements gave a similar uncertainty of about 0.1 Np.cm^{-1} in α at the lower end of this absorbing range, and should give somewhat smaller uncertainties at the higher α-values than power transmission measurements, as the phase sensitivity of the former measurements will remove some of the ambiguities associated with the effects of partially resolved, internally reflected rays found to be a limiting factor in power transmission measurements. Also, as discussed in chapter 6, single pass dispersive transmission measurements will allow very much higher α-values to be measured directly in transmission. Preliminary measurements with the Mach-Zehnder interferometer described in that chapter have shown α-values in excess of 600 Np.cm^{-1} to be accessible to measurement. In this more absorbing range of α-values the large absorption generally prevented the observation of channel spectra so that it was not possible to determine the refractive index from power transmission measurements, but dispersive transmission methods still worked and the refractive index could be determined to about 0.001 by their use. At even higher absorptions, where practical specimens became effectively opaque, dispersive reflection measurements were necessary and these generally allowed both the refractive index and the absorption index to be determined with an uncertainty of about 0.01.

This study of measurement methods, their ranges of applicability, experimental difficulties and susceptibility to random and systematic error, has been facilitated by the study of optical constants of some silicate glasses, particularly soda lime silica glass, between 3 and 400cm^{-1}. This has resulted in the following. The first quantitative description of the optical constants of soda lime silica glass in this spectral region, from millimetre wavelength transparency to submillimetre wavelength opacity; the identification of a previously unsuspected loss mechanism at 9cm^{-1}; the isolation of the total contribution of the metal ion additives to the mid infrared absorption, and the assignment of characteristic oscillator parameters to the absorption associated with the individual metal ions. None of these achievements would have been practical without the use of dispersive Fourier transform spectrometry, both in transmission and reflection, and, therefore, this work may also be considered to have had a third, implicit theme, the demonstration of the experimental potential of dispersive Fourier transform spectrometry.

APPENDIX 1

APPROXIMATE EXPRESSIONS FOR THE POWER ABSORPTION COEFFICIENT

A1.1 INTRODUCTION

In this appendix detailed consideration is give to the errors that can arise from the use of the approximate expressions (4.33, 4.36) and (4.37) for the power absorption coefficient. The first section deals with systematic errors arising from the fact that the expressions are only approximate while the second and third sections consider the effects that random noise on the measured transmission and refractive index have on α.

A1.2 SYSTEMATIC EFFECTS

The systematic effects of the approximations used to derive equations (4.33), (4.36) and (4.37) for the power absorption coefficient α are more conveniently considered in terms of the absorption index

$$k = \alpha / 4\pi\tilde{\nu} \qquad \ldots (A1.1)$$

Thus, the three approximations become

$$k_1 = \frac{1}{4\pi\tilde{\nu}d} \ln\left\{\frac{(1-R)^2 + \sqrt{(1-R)^4 + 4R^2\,\tilde{T}_L^2}}{2\,\tilde{T}_L}\right\} \qquad \ldots (A1.2)$$

$$k_2 = \frac{1}{4\pi\tilde{\nu}d} \ln\left\{\frac{(1-R)^2}{\tilde{T}_L}\right\} \qquad \ldots (A1.3)$$

and $$k_3 = \frac{1}{4\pi\tilde{\nu}(d_1 - d_2)} \ln\left\{\frac{\tilde{T}_2}{\tilde{T}_1}\right\} \qquad \ldots (A1.4)$$

where the subscripts 1, 2 or 3 on k refer to the particular approximation. These are functions of three variables, the real and imaginary parts of the refractive index, n and k, and a wavenumber-thickness product, $\tilde{\nu}x$ or $\tilde{\nu}(x_1 - x_2)$. For a given pair of values of n and $\tilde{\nu}x$ the true value of $\tilde{T}_L$ is

calculated from equation (4.13) for a range of values of k. Using equations (A1.2) to (A1.4) allows the approximate value of k_m to be determined from this $\tilde{T}_L$ and the R-value given by (4.34). From this the fractional error

$$\Delta_m = \frac{k_m - k}{k} \qquad \ldots (A1.5)$$

in k due to the m^{th} approximation is found.

In the calculation of $\tilde{T}_L$ from (4.13) the value of ϕ^r used will be the principal value of

$$\phi^r = \arctan \frac{-2k}{1 - n^2 - k^2} \qquad \ldots (A1.6)$$

This lies between $\pm \pi/2$ radians and is not the true phase change on reflection. As both n and k are positive this must lie in the third quadrant and is

$$\phi^r = \pi + \arctan \frac{-2k}{1 - n^2 - k^2} \qquad \ldots (A1.7)$$

ϕ^r only appears in the form $\cos 2\phi^r$ so the difference between (A1.6) and (A1.7) may seem irrelevant, but it is important to be aware of this distinction.

The range of values taken for the parameters used in the calculation was decided as follows. Refractive index values of 1.5, 2, 3 and 4 and wavenumber-thickness products of 1, 3,10, 30 and 100 were used as these correspond to values frequently met in practice. For a given pair of these n and $\tilde{\nu}x$ values Δ_m was computed over the range of k values giving the power transmission $\tilde{T}_L$ in excess of 0.01 as most measurements are made under this condition. For the third approximation which required two $\tilde{\nu}x$ products the calculation was performed for the pairs

$$\tilde{\nu}x \text{ and } \tilde{\nu}x/4, \quad \tilde{\nu}x \text{ and } \tilde{\nu}x/2, \quad \tilde{\nu}x \text{ and } 3\tilde{\nu}x/4$$

for each refractive index and $\tilde{\nu}x$ pair. These thickness ratios cover those most likely to be met in the application of the third approximation.

The results of these calculations are described below in turn for each approximation.

(i) First Approximation

This relies on the assumption that k is sufficiently small for

$$\left|-2k\right| \ll \left|1-n^2-k^2\right| \qquad \ldots (A1.8)$$

so that $\phi^r \to \pi$ radians. For most transparent materials this will be the case and the approximation is expected to be a good one. The results of the calculation summarised in figure A1.1 show this to be so. This plots the error Δ_1 in the calculated k value as a function of the measured power transmission $\tilde{T}_L$. Each of the four curves represents one of the refractive index values 1.5, 2, 3 and 4 together with the wavenumber-thickness product $\tilde{\nu}x = 3.0$. For power transmissions in excess of 0.01 the error in k is less than $\pm\ 10^{-4}$ except for $n = 1.5$ where the error rises to $\sim -3 \times 10^{-4}$ as the transmission decreases towards values 0.03. This increase with reducing transmission is expected as decreasing transmission corresponds to increasing k which makes the inequality A1.8 invalid. For increasing values of $\tilde{\nu}x$ the error , rapidly tends to zero for all refractive indices. The use of the first approximation can therefore be assumed to give k (and hence α) values that are correct to within $\pm\ 10^{-4}$. For most requirements this is tantamount to saying that the first approximation gives an exact solution for k as random errors would usually exceed 1 part in 10^{-4}

(ii) Second Approximation

In addition to the assumption of the first approximation this requires that

$$1 \gg a^4 r^4 \qquad \ldots (A1.9)$$

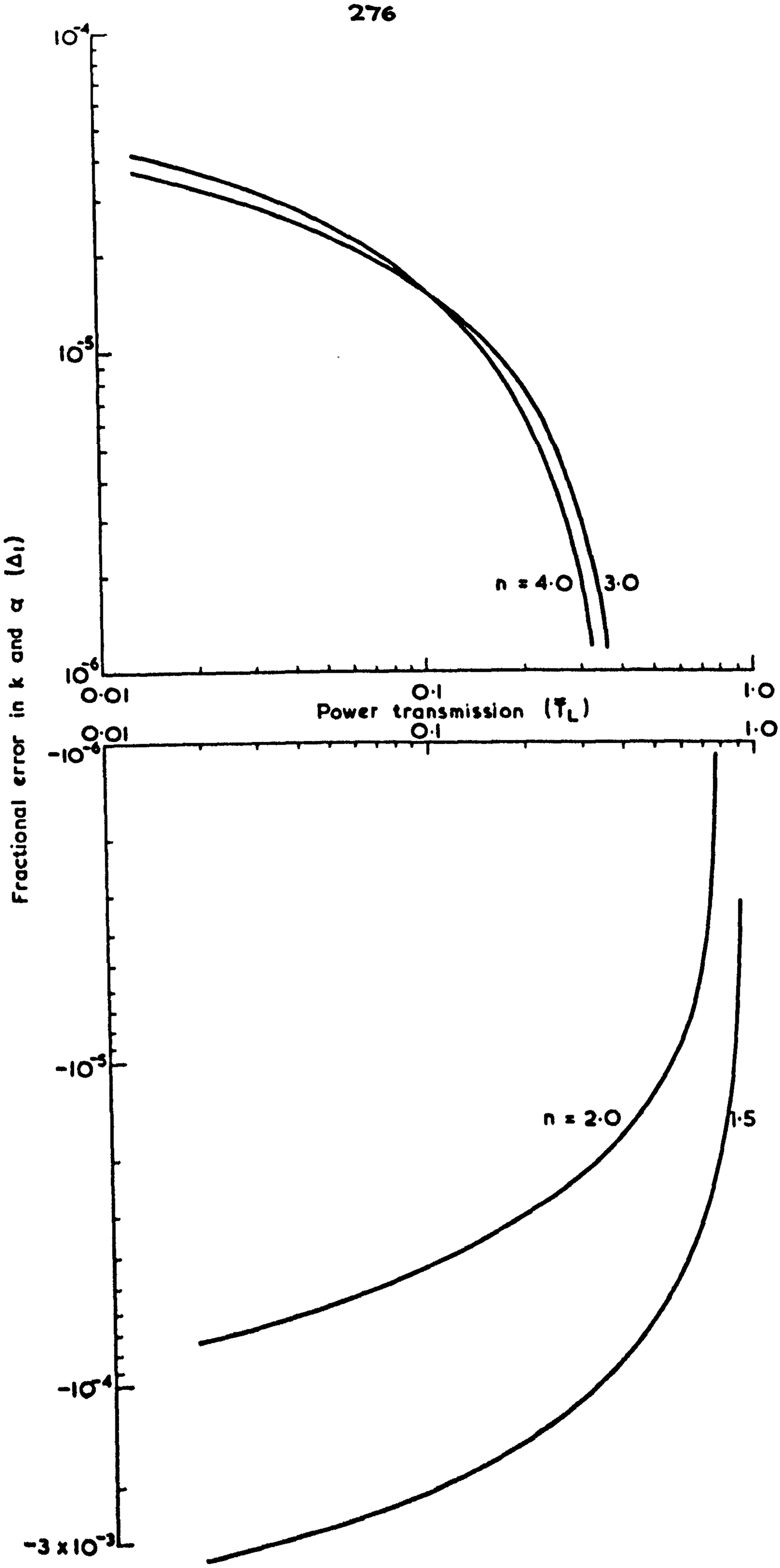

FIG.A1.1. The error in the calculated k- and α -values caused by the use of the first approximate expression. Curves are shown as a function of the measured transmission for refractive indices of 1.5, 2.0, 3.0 and 4.0. The wavenumber-thickness product is 3.0.

it would therefore be expected to hold in regions of low transmission with the error in k increasing with both $\tilde{T}_L$ and n, and the calculated values of figure A1.2 show this to be so. For a given refractive index the $\tilde{T}_L$ vs Δ_2 curves for $\tilde{\nu}x \gg 1.0$ lie on top of each other so that Δ_2 is independent of $\tilde{\nu}x$. This is a consequence of the fact that for $\tilde{\nu}x \gg 1.0$ the k-values required to give $0.01 \leqslant \tilde{T}_L \leqslant 1.0$ are small. Therefore $\cos 2\phi^r$ in equation 4.13 for $\tilde{T}_L$ goes to unity and $\tilde{T}_L$ becomes dependent on only n and $\tilde{\nu}xk$. For a given n-value Δ_2 thus depends only on $\tilde{\nu}xk$ and hence $\tilde{T}_L$.

Table A1.1 summarises the data of figure A1.2 by showing the maximum measured power transmission that may be used with this approximation if fractional errors in k of less than 0.1, 0.05 and 0.02 are to result. One sees that for the

Δ_2	REFRACTIVE INDEX 1.5	2	3	4
0.1	.91	.72	.42	.25
0.05	.90	.66	.35	.22
0.02	.86	.57	.285	.16

Table A1.1 Showing the maximum value of the power transmission to be used with the second approximation if the fractional error in k is to be less than Δ_2 for each refractive index.

higher refractive indices it is necessary to go to quite low transmissions to ensure low errors. The relatively large errors that can result from this approximation and the fact that the 'good' first approximation can be used if n is known means that this approximation should not be used.

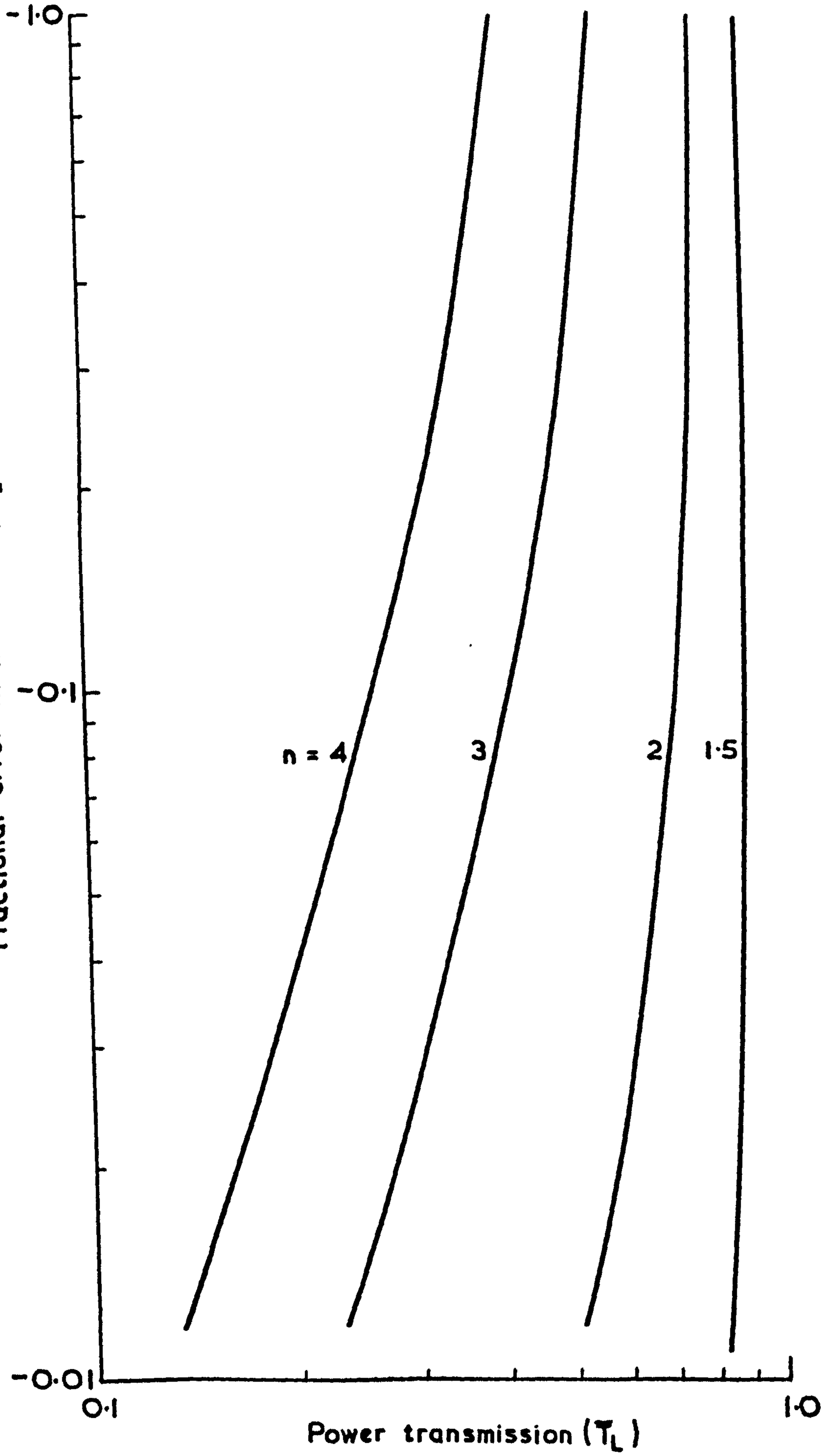

Fig.A1.2. The error in the calculated k- and α -values caused by the use of the second approximate expression. Curves are shown as a function of the measured transmission for refractive indices of 1.5, 2.0, 3.0 and 4.0.

(iii) Third Approximation

The third approximation assumes that the effects of the multiple internally reflected rays are independent of thickness and can be removed by ratioing measurements on different thickness specimens. The important variable in this analysis is the ratio of the two thicknesses used, and the role that this plays is illustrated in figure A1.3 which shows the error Δ_3 for $0.01 \lesssim \tilde{T}_L \lesssim 1.0$ and $n = 4.0$. The wavenumber thickness product of the thicker specimen was chosen as 30 and Δ_3 computed for a thinner specimen having $\tilde{\nu}x = 7.5$, 15 and 22.5. The abscissa represent the power transmission of the thicker specimen. All three curves tend to the same large error as the thicker specimen becomes more transparent, which follows from the increasing multiple reflection contribution as the absorption drops. The size of Δ_3 decreases as the ratio of the two thicknesses tends to 1.0 but if measurements were to be made on specimens having similar thicknesses, which is the only condition under which this approximation holds, the effects of random errors in the measurements would dominate. Therefore, choosing the ratio of the two thicknesses as 0.5 the curves of figure A1.4 were computed. These show the error Δ_3 as a function of the power transmission of the thicker specimen for the four refractive index values. It is again found that for a given refractive index Δ_3 is independent of $\tilde{\nu}x$ for $\tilde{\nu}x \gtrsim 1.0$. The error decreases with increasing absorption and in a similar manner to that used for the second approximation these curves are summarised in table A1.2 as the maximum measured power transmission that

Δ_3	REFRACTIVE INDEX 1.5	2	3	4
0.1	-	-	0.49	0.22
0.05	-	-	0.30	0.13
0.02	-	0.7	0.16	0.07

Table A1.2 Showing the maximum value of the power transmission to be used with the third approximation if the fractional error in k is to be less than Δ_3 for each refractive index. The dashes indicate that any transmission levels may be used with confidence.

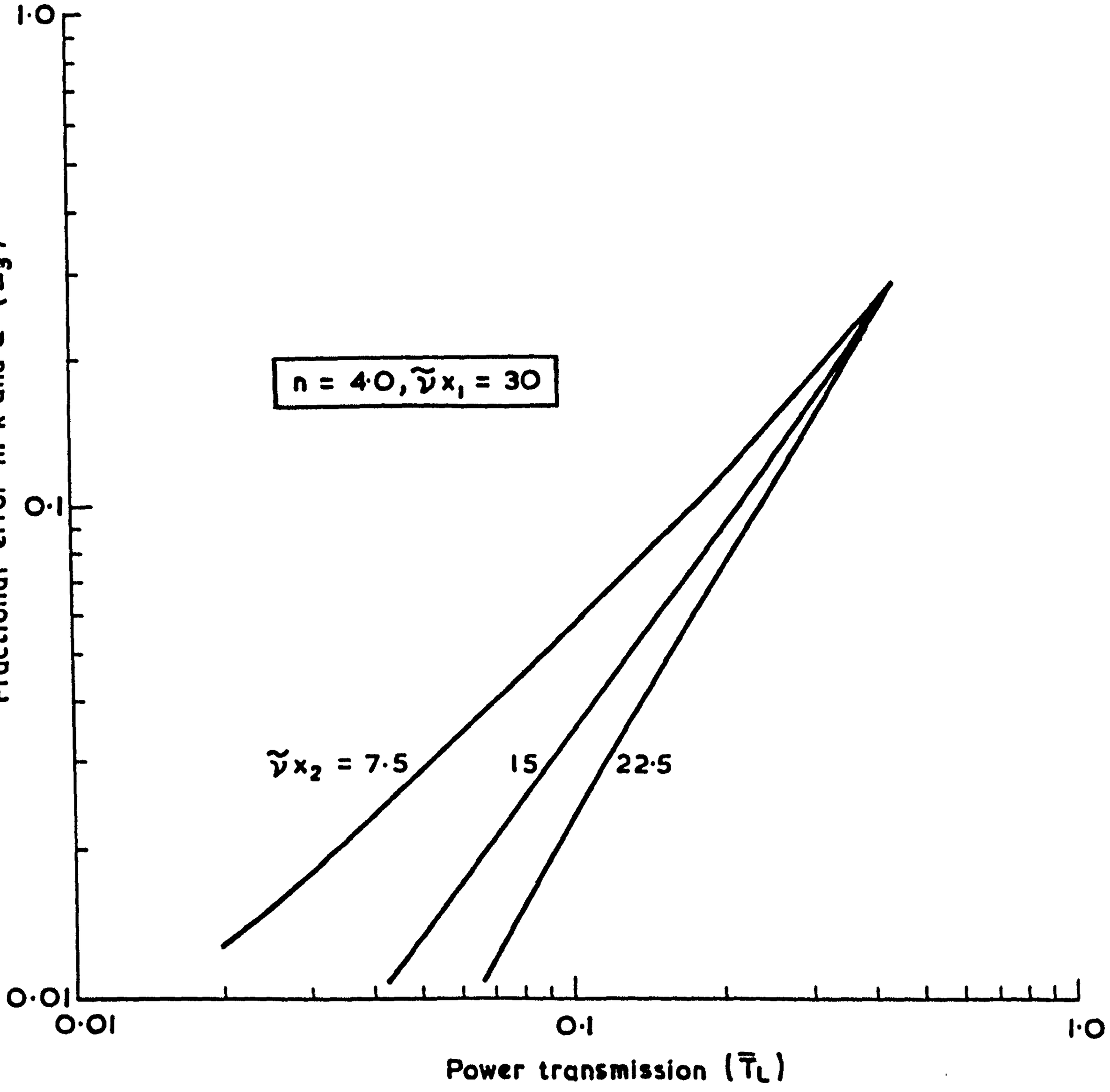

Fig.A1.3. The error in the calculated k- and α -values caused by the use of the third approximate expression. Curves are shown as a function of the measured transmission for wavenumber-thickness products of 7.5, 15 and 22.5 for the second specimen, that of the first specimen is 30. The refractive index is 4.0.

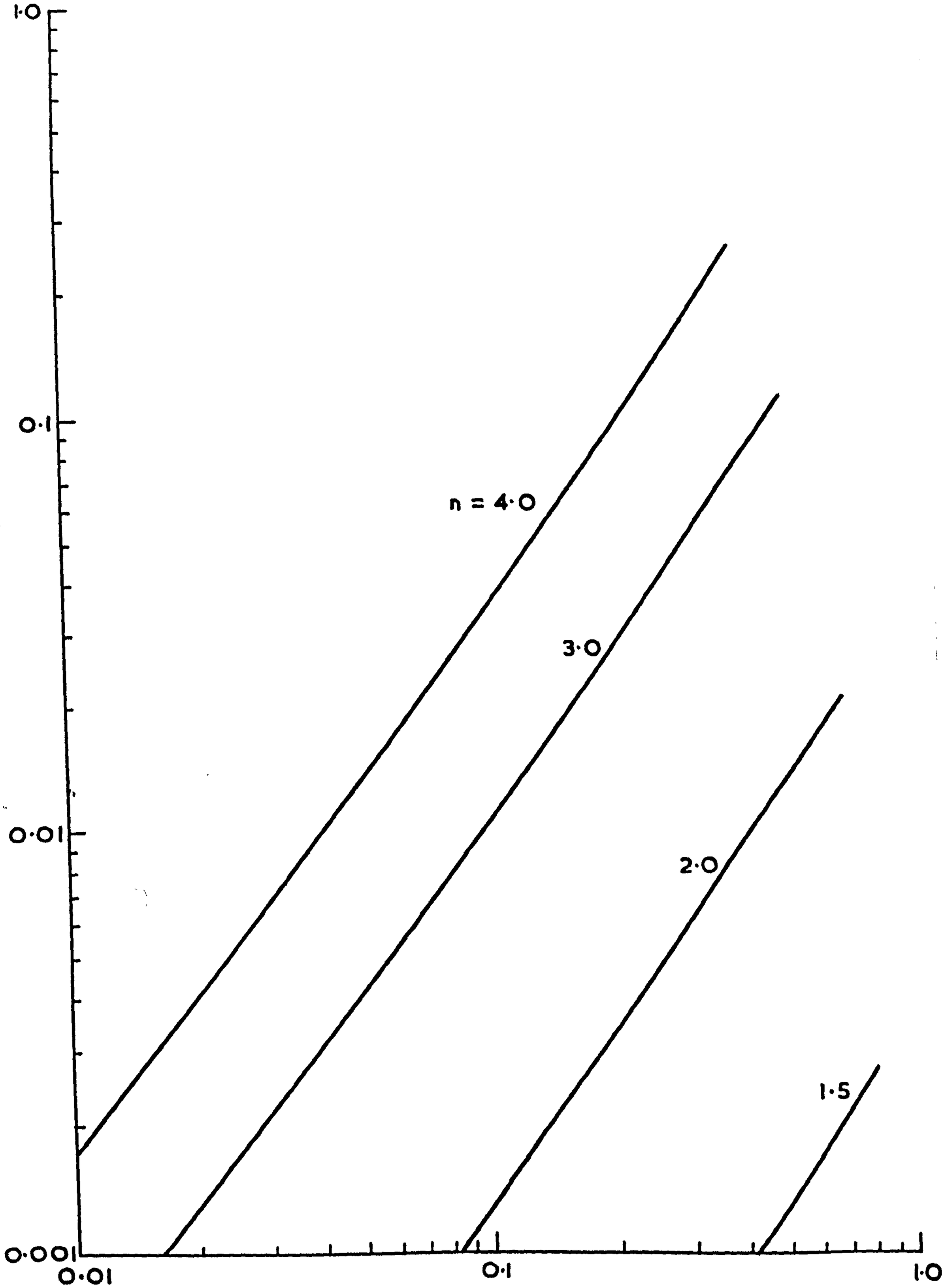

Fig.A1.4. The error in the calculated k- and α -values caused by the use of the third approximate expression. Curves are shown as a function of the measured transmission for refractive indices of 1.5, 2.0, 3.0 and 4.0. The ratio of the two thicknesses is 0.5.

can be used with this approximation if the fractional error in k is to be less than 0.1, 0.05 and 0.02. As expected the approximation is poor for high refractive indices and fairly low transmission levels must be used to avoid large errors. At the low refractive indices however the interface reflectivity becomes so low that almost any transmission level may be used with confidence. For $n = 2$, for instance, Δ_3 would be less than 0.02 for $\tilde{T}_L \lesssim 0.7$ while for $n = 1.5$ it would be less than 0.003 for $T_L \lesssim 0.8$.

From these calculations one may conclude that if the refractive index of a specimen is known its absorption index (and power absorption coefficient) may be computed using the first approximation to give k-values that contain a negligible systematic error due to the use of that approximation. If the refractive index is unknown measurements should be made on two specimens having thicknesses in the range of ratios 0.25 to 0.75 and the third approximation used. The thicker of the two specimens would be chosen from figure A1.4 so that its power transmission leads to the desired level of systematic error. The second approximation should not be used.

A1.3 THE EFFECT OF TRANSMISSION NOISE

The effect of transmission noise on the computed power absorption spectrum is most easily studied using the differential form of the appropriate expression (A1.2) - (A1.4). In this section only (A1.2) will be considered as the results of the previous section have shown it to be the preferred expression for the calculation of the absorption spectrum. Fleming and Chantry[238] have performed a similar analysis to the following for the case of the second expression and their conclusions will be considered at the end of this section.

Differentiating equation (A.2) with respect to $\tilde{T}_L$ leads to the following expression for the fractional error Δ in k or α corresponding to an error $\Delta\tilde{T}_L$ in the measured transmission

$$\Delta = -\frac{\Delta\tilde{T}_L}{\tilde{T}_L} \cdot \frac{(1-R)^4\left\{\left[(1-R)^4+4R^2\tilde{T}_L^2\right]^{-\frac{1}{2}}+1\right\}}{(1-R)^2+\left[(1-R)^4+4R^2\tilde{T}_L^2\right]^{\frac{1}{2}}} \cdot \left\{\ln\left[\frac{(1-R)^2+\left[(1-R)^4+4R^2\tilde{T}_L^2\right]^{\frac{1}{2}}}{2\tilde{T}_L}\right]\right\}^{-1} \quad \ldots (A1.10)$$

This was used to investigate numerically the effect of transmission noise and the results are shown in figure A1.5. This shows Δ plotted against transmission for refractive indices from 1.5 to 4.0 all for an error $\Delta\tilde{T}_L$ of 0.01. Δ increases steeply both at low transmission levels when the error in $\tilde{T}_L$ becomes an appreciable portion of $\tilde{T}_L$, and also at higher transmissions approaching the value $(1-R)^2$ when the error in $\tilde{T}_L$ dominates the absorption contribution to the transmission loss. For each refractive index the minimum Δ-value occurs close to the transmission value corresponding to

$$\alpha d = 1 \quad \ldots (A1.11)$$

in agreement with the result found by Fleming and Chantry[238] for the second approximate expression, although the sign of the fractional error Δ in that paper appears to be incorrect. The important result that follows from this analysis is that the error Δ due to transmission noise can very easily become quite large. The curves of figure A1.5 scale linearly with $\Delta\tilde{T}_L$ and therefore for a random noise level of only 0.03-0.04 in the transmission the power absorption coefficient for all materials having $n > 1.5$ would be in error by at least 10%. Random noise levels of a few percent are fairly typical of many transmission experiments and it is therefore important to be aware of considerable error that these introduce into the absorption spectrum.

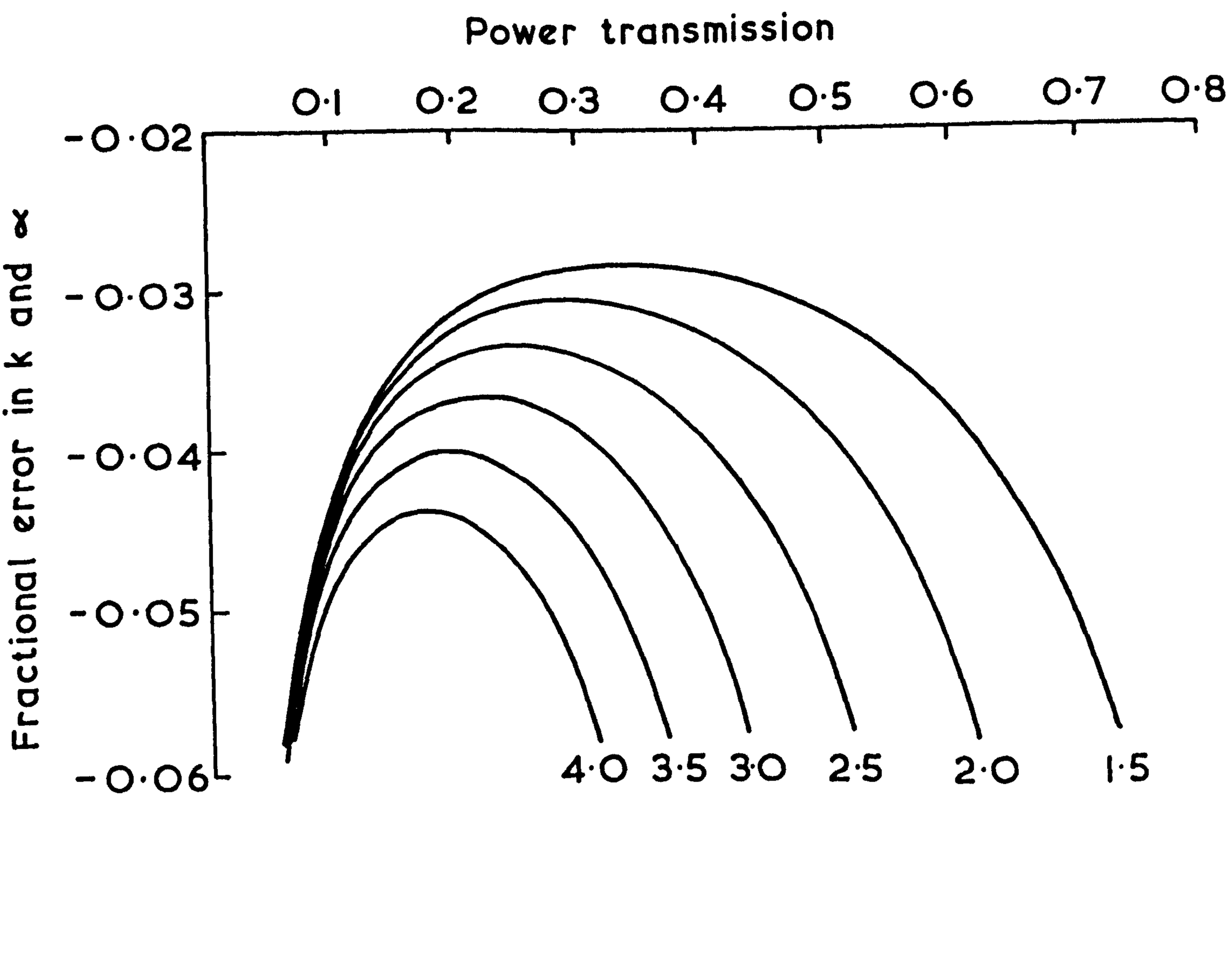

Fig.A1.5. The error in the k- and α -values calculated from the first expression due to an error of 0.01 in the measured transmission. Curves are shown for refractive indices between 1.5 and 4.0.

The same analysis applies to systematic errors in $\tilde{T}_L$, which represent a more serious problem. Random errors, by their very nature, would be apparent as noise on the absorption spectrum and can, to a certain extent, be removed by averaging of several spectra. This is not the case for systematic errors that could arise from stray-light or non-linearities in the detection system or channel spectrum effects, and for precise measurements considerable care must be taken to avoid or minimise such effects.

A1.4 THE EFFECT OF ERRORS IN THICKNESS AND REFRACTIVE INDEX

Thickness and refractive index errors will generally be systematic, with that of the refractive index arising from the thickness value used in its calculation. For the thickness error it is easily shown from equation (A1.2) that the fractional error in α is equal to minus one times that in the thickness. The consequences of a small error in refractive index may be found, in a similar manner to those of an error in transmission, by differentiating (A1.2) with respect to R, the reflectivity and using the relationship

$$\frac{\partial \alpha}{\partial n} = \frac{4(n-1)}{(n+1)^3} \cdot \frac{\partial \alpha}{\partial R} \qquad \ldots (A1.12)$$

The resulting expresssion for the fractional error in α is rather cumbersome and will not be reproduced here. Instead, the results of its application are shown in figure A1.6 which shows Δ, the fractional error in α and k plotted against transmission for refractive indices from 1.5 to 4.0 for an error in refractive index of 0.05. As with the error $\Delta\tilde{T}_L$ the fractional error in α scales linearly with this error in refractive index. At low transmission levels where absorption effects dominate, the fractional error in α is small but with increasing transmission Δ increases rapidly as the transmission approaches the value $(1-R)^2$. The magnitude of the fractional errors in α caused by small errors in refractive

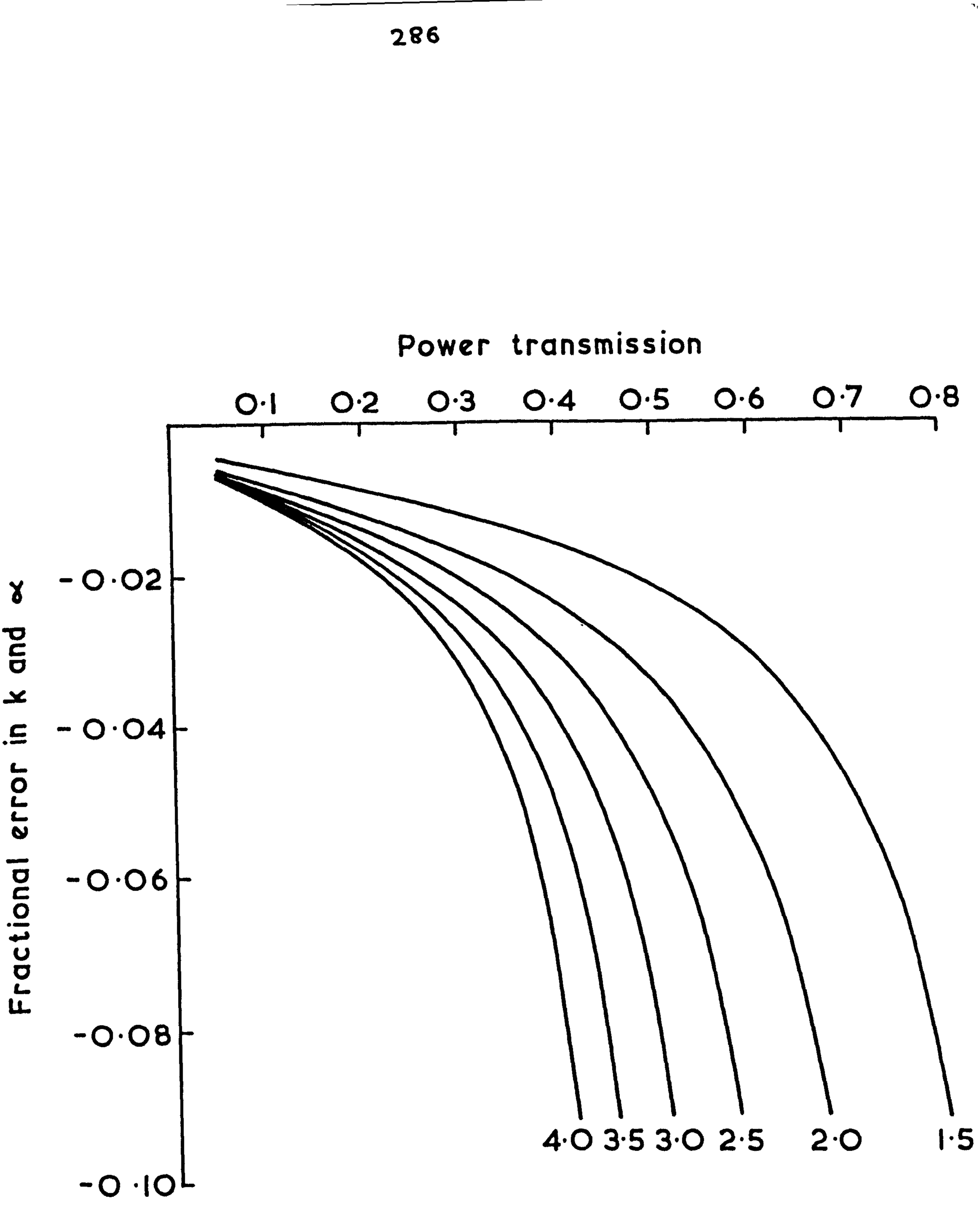

Fig.A1.6. The error in the k- and α -values calculated from the first expression due to an error of 0.05 in the refractive index. Curves are shown for refractive indices between 1.5 and 4.0.

index are seen to be relatively large and, in common with the conclusions of the previous section, to avoid errors in precise absorption measurement it is necessary to minimise random and systematic errors in the refractive index determination.

Appendix 2

Tabulated values of the complex refractive index, the power absorption coefficient and the complex relative permittivity of soda-lime-silica glass as determined in this work.

$\tilde{\nu}$ (cm^{-1})	n	k	α (cm^{-1})	ε'	ε''
(a) Microwave cavity resonator.					
1.1630	2.6081	.02237	.32700	6.8014	.11671
(b) Dispersive transmission spectrometry.					
2.9297	2.5852	.05970	2.1980	6.6796	.30869
3.9062	2.5767	.05323	2.6130	6.6366	.27433
4.8828	2.5726	.05397	3.3120	6.6154	.27772
5.8593	2.5710	.05653	4.1620	6.6069	.29066
6.8359	2.5700	.05731	4.9230	6.6015	.29457
7.8124	2.5685	.06156	6.0440	6.5932	.31625
8.7890	2.5670	.06563	7.2490	6.5854	.33697
9.7656	2.5665	.06578	8.0730	6.5825	.33767
10.742	2.5660	.06924	9.3470	6.5795	.35535
11.718	2.5653	.07310	10.764	6.5752	.37503
12.695	2.5647	.07677	12.247	6.5717	.39378
13.671	2.5648	.08091	13.900	6.5718	.41504
14.648	2.5654	.08510	15.665	6.5741	.43665
15.624	2.5650	.08889	17.453	6.5716	.45603
16.601	2.5649	.09379	19.565	6.5699	.48110
17.578	2.5660	.09925	21.923	6.5744	.50934
18.554	2.5664	.10362	24.159	6.5758	.53185
19.531	2.5671	.10801	26.509	6.5782	.55453
20.507	2.5686	.11341	29.226	6.5846	.58261
21.484	2.5693	.11938	32.231	6.5869	.61346
22.460	2.5699	.12360	34.884	6.5891	.63526
23.437	2.5724	.13251	39.028	6.5996	.68176
(c) Dispersive reflection spectrometry.					
20.000	2.5911	.12765	32.081	6.6975	.66149
22.000	2.6262	.17220	47.606	6.8672	.90445
24.000	2.6174	.13379	40.349	6.8330	.70035
26.000	2.6164	.13076	42.724	6.8282	.68425
28.000	2.5937	.18461	64.955	6.6934	.95763
30.000	2.5573	.17583	66.288	6.5086	.89930
32.000	2.5512	.16239	65.300	6.4821	.82856
34.000	2.5456	.16095	68.768	6.4544	.81945
36.000	2.5292	.20445	92.489	6.3551	1.0342
38.000	2.5310	.21601	103.15	6.3592	1.0934
40.000	2.5358	.19411	97.570	6.3926	.98445
42.000	2.5307	.22386	118.15	6.3543	1.1330
44.000	2.5310	.26436	146.17	6.3361	1.3382
46.000	2.5084	.29214	168.87	6.2067	1.4656
48.000	2.4431	.28273	170.54	5.8888	1.3815
50.000	2.4247	.30491	191.58	5.7862	1.4786
52.000	2.4625	.30640	200.22	5.9700	1.5090
54.000	2.4544	.32734	222.13	5.9169	1.6069
56.000	2.4558	.31736	223.33	5.9302	1.5587
58.000	2.4377	.34483	251.33	5.8235	1.6812

$\tilde{\nu}$ (cm^{-1})	n	k	α (cm^{-1})	ε'	ε''
60.000	2.3759	.33700	254.09	5.5313	1.6013
62.000	2.3841	.31835	248.03	5.5826	1.5179
64.000	2.4002	.34009	273.52	5.6453	1.6326
66.000	2.3864	.35067	290.84	5.5719	1.6737
68.000	2.3663	.33053	282.44	5.4901	1.5643
70.000	2.3544	.35121	308.94	5.4199	1.6538
72.000	2.3764	.37661	340.75	5.5054	1.7900
74.000	2.3989	.37111	345.10	5.6170	1.7805
76.000	2.4009	.35192	336.10	5.6405	1.6899
78.000	2.3842	.34615	339.29	5.5646	1.6506
80.000	2.3617	.35385	355.73	5.4524	1.6714
82.000	2.3413	.36779	378.99	5.3464	1.7222
84.000	2.3045	.36098	381.04	5.1804	1.6638
86.000	2.2912	.35850	387.43	5.1211	1.6428
88.000	2.3057	.38683	427.77	5.1666	1.7838
90.000	2.2615	.41930	474.22	4.9386	1.8965
92.000	2.2407	.38780	448.34	4.8703	1.7379
94.000	2.2845	.37197	439.39	5.0806	1.6995
96.000	2.3115	.37779	455.76	5.2003	1.7465
98.000	2.2838	.38396	472.85	5.0683	1.7538
100.00	2.2548	.39207	492.69	4.9304	1.7681
102.00	2.2626	.38314	491.10	4.9726	1.7338
104.00	2.3021	.37219	486.41	5.1611	1.7136
106.00	2.2903	.37757	502.93	5.1029	1.7295
108.00	2.2659	.37409	507.70	4.9944	1.6953
110.00	2.2141	.41348	571.56	4.7313	1.8310
112.00	2.2066	.41905	589.79	4.6935	1.8494
114.00	2.2237	.40868	585.46	4.7778	1.8176
116.00	2.2222	.39643	577.88	4.7810	1.7619
118.00	2.2201	.39435	584.76	4.7733	1.7510
120.00	2.1797	.41886	631.62	4.5757	1.8260
122.00	2.1711	.41177	631.29	4.5441	1.7880
124.00	2.1677	.40599	632.62	4.5341	1.7601
126.00	2.1717	.40803	646.06	4.5498	1.7722
128.00	2.1750	.38772	623.64	4.5803	1.6866
130.00	2.1746	.41129	671.90	4.5597	1.7888
132.00	2.1561	.45022	746.80	4.4461	1.9414
134.00	2.1345	.43066	725.18	4.3706	1.8385
136.00	2.1440	.40307	688.86	4.4343	1.7284
138.00	2.1572	.40632	704.62	4.4884	1.7530
140.00	2.1814	.42497	747.64	4.5779	1.8540
142.00	2.2007	.45603	813.75	4.6351	2.0072
144.00	2.1922	.47450	858.64	4.5806	2.0804
146.00	2.1565	.43531	798.65	4.4610	1.8775
148.00	2.1302	.39448	733.66	4.3821	1.6806
150.00	2.1176	.38436	724.50	4.3365	1.6278
152.00	2.1118	.41214	787.22	4.2898	1.7407
154.00	2.1325	.45879	887.86	4.3371	1.9567
156.00	2.1374	.45777	897.40	4.3589	1.9569
158.00	2.1439	.42184	837.56	4.4184	1.8088
160.00	2.1361	.45785	920.57	4.3533	1.9560
162.00	2.1186	.47878	974.67	4.2592	2.0287
164.00	2.1674	.47091	970.50	4.4759	2.0413
166.00	2.1466	.44212	922.26	4.4124	1.8981
168.00	2.1265	.42362	894.33	4.3425	1.8017
170.00	2.1275	.42956	917.67	4.3417	1.8278

$\tilde{\nu}$ (cm^{-1})	n	k	α (cm^{-1})	ε'	ε''
172.00	2.0995	.44079	952.73	4.2136	1.8509
174.00	2.0842	.43199	944.57	4.1573	1.8007
176.00	2.0911	.43592	964.11	4.1827	1.8231
178.00	2.0642	.43084	963.70	4.0753	1.7787
180.00	2.0481	.39690	897.76	4.0372	1.6258
182.00	2.0620	.39941	913.49	4.0923	1.6472
184.00	2.0765	.42252	976.95	4.1333	1.7547
186.00	2.0468	.44101	1030.8	3.9949	1.8053
188.00	2.0469	.40608	959.36	4.0249	1.6624
190.00	2.0677	.41250	984.89	4.1052	1.7059
192.00	2.0866	.42296	1020.5	4.1750	1.7651
194.00	2.0869	.43882	1069.8	4.1626	1.8316
196.00	2.0702	.43435	1069.8	4.0971	1.7984
198.00	2.0598	.43860	1091.3	4.0504	1.8069
200.00	2.0833	.45256	1137.4	4.1353	1.8856
202.00	2.1158	.42854	1087.8	4.2930	1.8134
204.00	2.0927	.41587	1066.1	4.2064	1.7406
206.00	2.0563	.41121	1064.5	4.0593	1.6912
208.00	2.0623	.36539	955.05	4.1196	1.5071
210.00	2.0744	.36636	966.81	4.1689	1.5200
212.00	2.0698	.37388	996.05	4.1443	1.5477
214.00	2.0077	.38945	1047.3	3.8792	1.5638
216.00	2.0025	.38201	1036.9	3.8641	1.5299
218.00	2.0467	.36733	1006.3	4.0540	1.5036
220.00	2.0383	.41612	1150.4	3.9815	1.6963
222.00	2.0385	.43104	1202.5	3.9697	1.7574
224.00	2.0471	.39146	1101.9	4.0374	1.6027
226.00	2.0452	.38088	1081.7	4.0378	1.5580
228.00	2.0389	.41635	1192.9	3.9838	1.6978
230.00	2.0384	.45632	1318.9	3.9468	1.8603
232.00	2.0361	.44471	1296.5	3.9479	1.8109
234.00	2.0184	.42411	1247.1	3.8941	1.7120
236.00	2.0177	.38544	1143.1	3.9225	1.5554
238.00	2.0177	.36228	1083.5	3.9399	1.4619
240.00	2.0638	.33754	1018.0	4.1453	1.3932
242.00	2.0663	.35764	1087.6	4.1417	1.4780
244.00	2.0334	.36081	1106.3	4.0045	1.4673
246.00	2.0248	.35661	1102.4	3.9726	1.4441
248.00	2.0264	.39490	1230.7	3.9503	1.6005
250.00	2.0234	.39795	1250.2	3.9358	1.6104
252.00	2.0062	.36561	1157.8	3.8912	1.4670
254.00	1.9691	.40453	1291.2	3.7137	1.5931
256.00	1.9463	.42251	1359.2	3.6096	1.6446
258.00	1.9657	.38904	1261.3	3.7126	1.5295
260.00	1.9916	.37169	1214.4	3.8283	1.4805
262.00	2.0195	.31375	1033.0	3.9799	1.2673
264.00	2.0500	.31310	1038.7	4.1045	1.2837
266.00	2.0242	.39843	1331.8	3.9386	1.6130
268.00	2.0228	.37877	1275.6	3.9483	1.5323
270.00	2.0519	.38430	1303.9	4.0626	1.5771
272.00	2.0504	.40792	1394.3	4.0377	1.6728
274.00	1.9935	.41894	1442.5	3.7985	1.6703
276.00	1.9476	.42796	1484.3	3.6100	1.6670
278.00	1.9497	.41105	1436.0	3.6324	1.6029
280.00	1.9650	.40661	1430.7	3.6959	1.5980
282.00	1.9861	.35993	1275.5	3.8150	1.4297

$\tilde{\nu}$ (cm^{-1})	n	k	α (cm^{-1})	ε'	ε''
284.00	2.0156	.36124	1289.2	3.9322	1.4562
286.00	2.0983	.36786	1322.1	4.2675	1.5438
288.00	2.1037	.35047	1268.4	4.3027	1.4746
290.00	2.0931	.30725	1119.7	4.2867	1.2862
292.00	2.1132	.35469	1301.5	4.3398	1.4991
294.00	2.0745	.39607	1463.3	4.1467	1.6433
296.00	2.0607	.38396	1428.2	4.0991	1.5825
298.00	2.1090	.35276	1321.0	4.3234	1.4879
300.00	2.1449	.34828	1313.0	4.4793	1.4941
302.00	2.1130	.39538	1500.5	4.3084	1.6709
304.00	2.0425	.36990	1413.1	4.0350	1.5111
306.00	2.0148	.33381	1283.6	3.9480	1.3451
308.00	2.0643	.33771	1307.1	4.1473	1.3943
310.00	2.1249	.31982	1245.9	4.4129	1.3592
312.00	2.1472	.31354	1229.3	4.5122	1.3465
314.00	2.1322	.30784	1214.7	4.4515	1.3128
316.00	2.1057	.24624	977.83	4.3733	1.0370
318.00	2.1005	.23549	941.06	4.3566	.98931
320.00	2.1518	.27041	1087.4	4.5571	1.1638
322.00	2.1868	.29226	1182.6	4.6967	1.2782
324.00	2.2098	.27385	1115.0	4.8082	1.2103
326.00	2.2427	.27352	1120.5	4.9549	1.2268
328.00	2.2188	.35815	1476.2	4.7948	1.5893
330.00	2.1902	.38448	1594.4	4.6492	1.6842
332.00	2.2183	.35239	1470.2	4.7967	1.5634
334.00	2.2187	.35805	1502.8	4.7944	1.5888
336.00	2.1977	.38235	1614.4	4.6837	1.6806
338.00	2.1733	.40959	1739.7	4.5555	1.7803
340.00	2.2110	.33844	1446.0	4.7740	1.4966
342.00	2.2755	.27254	1171.3	5.1036	1.2403
344.00	2.2841	.32097	1387.5	5.1141	1.4663
346.00	2.2396	.33862	1472.3	4.9011	1.5167
348.00	2.2254	.29494	1289.8	4.8654	1.3127
350.00	2.2881	.28780	1265.8	5.1526	1.3170
352.00	2.3426	.28716	1270.2	5.4053	1.3454
354.00	2.3449	.29994	1334.3	5.4086	1.4067
356.00	2.4531	.29479	1318.8	5.9308	1.4463
358.00	2.5635	.26892	1209.8	6.4992	1.3787

(d) Non-dispersive transmission spectrometry

As the refraction measurements were obtained from the period of a channel spectrum the wavenumbers of the refractive index values do not coincide with those of the corresponding absorption measurements and the two parts of the complex refractive index are therefore listed separately. The absorption spectrum is that of the 0.1991mm specimen shown in figure 5.22.

$\tilde{\nu}$ (cm^{-1})	n
2057	1.683
2166	1.639
2274	1.628
2384	1.623
2494	1.603
2606	1.585
2718	1.578

$\tilde{\nu}$ (cm^{-1})	n
2831	1.586
2944	1.575
3058	1.555
3172	1.576
3286	1.576
3400	1.550
3515	1.560
3629	1.552
3744	1.566
3859	1.550
3974	1.549
4090	1.552

$\tilde{\nu}$ (cm^{-1})	k	α (cm^{-1})
1300	0.014403	235.30
1350	0.009553	162.07
1400	0.007363	129.53
1450	0.006279	114.42
1500	0.005399	101.78
1550	0.005183	100.93
1600	0.005332	107.20
1650	0.004952	102.68
1700	0.004614	98.58
1750	0.004800	105.56
1800	0.004574	103.47
1850	0.003938	91.57
1900	0.003094	73.87
1950	0.002446	59.94
2000	0.001738	43.69
2050	0.001307	33.67
2100	0.001081	28.53
2150	0.000809	21.87
2200	0.000566	15.67
2250	0.000394	11.14
2300	0.000276	8.00
2350	0.000230	6.80
2400	0.000176	5.30
2450	0.000145	4.47
2500	0.000130	4.08
2550	0.000125	4.00
2600	0.000128	4.20
2650	0.000137	4.55
2700	0.000140	4.77
2750	0.000150	5.12
2800	0.000151	5.33
2850	0.000154	5.53
2900	0.000152	5.56
2950	0.000151	5.60
3000	0.000149	5.63
3050	0.000144	5.51
3100	0.000138	5.37

$\tilde{\nu}$ (cm^{-1})	k	α (cm^{-1})
3150	0.000128	5.08
3200	0.000127	5.10
3250	0.000125	5.12
3300	0.000127	5.28
3350	0.000129	5.46
3400	0.000138	5.91
3450	0.000147	6.39
3500	0.000153	6.73
3550	0.000154	6.89
3600	0.000118	5.33

References.

1. E.D.Palik, J.O.S.A. 50,1329,1960.

2. E.D.Palik, Naval Research Laboratory Bibliography No.21, 1963.

3. R.W.Wood, Phil.Mag. 20,770,1910.

4. H.Rubens and O.V.Baeyer, Phil.Mag. 21,689,1911.

5. E.F.Nicols and J.D.Tear, Phys.Rev. 21,587,1923.

6. A.G.Arkadiewa, Nature 113,640,1924.

7. H.A.Gebbie and G.A.Vanasse, Nature 178,432,1956.

8. J.Strong, J.O.S.A. 47,354,1957.

9. P.Jacquinot and C.Dufor, J.Rech.CNRS 6,91,1948.

10. P.Jacquinot, J.O.S.A. 44,761,1954.

11. P.Fellgett, Thesis, Cambridge University, 1951.

12. P.Fellgett, J.Phys.Radium 19,187,1958.

13. D.Bloor, Infrared Physics 10,1,1970.

14. J.S.Toll, Phys.Rev. 104,1760,1956.

15. F.Stern, 'Solid State Physics' Vol.15,
Ed. Seitz and Turnbull, Academic Press,New York 1963.

16. R.de L.Kronig, J.O.S.A. 12,547,1926.

17. H.A.Kramers, Atti.Congr.Intern.Fis., Como 1927.

18. M.Born and E.Wolf, 'Principles Of Optics' Third Edition,
Pergamon Press, Oxford 1965.

19. A.A.Michelson, Am.J.Science, Series 3, 22,120,1881.

20. J.E.Chamberlain, J.E.Gibbs and H.A.Gebbie, Nature 198,874,1963.

21. J.E.Chamberlain and H.A.Gebbie, App.Opt. 5,393,1966.

22. J.E.Chamberlain, H.A.Gebbie, G.W.F.Pardoe and M.Davies,
Chem.Phys.Lett. 1,523,1968.

23. J.E.Chamberlain and H.A.Gebbie, Nature 208,480,1965.

24. E.E.Bell, Jap.J.App.Phys. 4(Supp.I),412,1965.

25. E.E.Bell, Infrared Physics 6,57,1966.

26. E.E.Russell and E.E.Bell, Infrared Physics 6,75,1966.

27. R.B.Sanderson, App.Opt. 6,1527,1967.

28. J.R.Birch and C.C.Bradley, New Technology, July 1971.

29. C.C.Bradley, J.R.Birch and J.R.Stockton,
I.E.R.E. Conference on Infrared Techniques, Reading Sept.1971.
I.E.R.E. Conference Proceedings 22,187,1971.

30. J.R.Birch, Infrared Physics 12,29,1972.

31. D.H.Martin and E.Puplett, Infrared Physics 10,105,1970.

32. I.Simon, 'Modern Aspects of the Vitreous State',
Ed. J.D.Mackenzie, Butterworths, London 1960.

33. F.A.Jenkins and H.E.White, 'Fundamentals Of Optics'
Third edition, McGraw-Hill,New York 1957.

34. M.D.Mashkovich and A.I.Demeshina, Sov.Phys.Sol.St. 7,1323,1965.

35. A.Hadni, J.Claudel, X.Gerboux, G.Morlot and J-M.Munier,
Apt.Opt. 4,487,1965.

36. A.Hadni, 'Essentials Of Modern Physics Applied To The Study
Of The Infrared' Pergamon Press, Oxford 1967.

37. E.M.Dianov, N.A.Irisova and V.N.Timofeev, Sov.Phys.Sol.St. 8,2113,1967.

38. W.Bagdade and R.Stolen, J.Phys.Chem.Sol. 29,2001,1968.

39. G.J.Exharos and W.M.Risen, Sol.St.Comm. 11,755,1972.

40. J.R.Sweet and W.B.White, Phys.Chem.Glasses 10,246,1969.

41. J.R.Aronson and P.F.Strong, App.Opt. 14,2914,1975.

42. E.Ellis, P.H.Gaskell and D.W.Johnson, Symposium on the Electrical
and Optical Properties of Glasses and Ceramics, St.Andrews 1976.

43. G.J.Exarhos, P.J.Miller and W.M.Risen, J.Chem.Phys. 60,4145,1974.

44. J.C.Slater and N.H.Frank, 'Electromagnetism', McGraw-Hill,
New York 1947.

45. M.Born and E.Wolf, 'Principles Of Optics', Pergamon, Oxford 1965.

46. E.E.Bell, Handbuch der Physik, 25,1,1967.

47. G.W.Chantry, 'Submillimetre Spectroscopy', Academic Press, London 1971.

48. R.J.Bell, 'Introductory Fourier Transform Spectroscopy'
Academic Press, New York 1972.

49. J.E.Chamberlain, 'The Principles Of Interferometric Spectroscopy'
Ed. G.W.Chantry and N.W.B.Stone, Wiley, to be published.

50. J.E.Chamberlain, 'The Encyclopaedic Dictionary Of Physics'
Supp.Vol.4, Ed. J.Thewlis, Pergamon, Oxford 1971.

51. T.Hirschfeld, App.Opt. 16,3070,1977.

52. M.Harwit and M.H.Tai, App.Opt. 16,3071,1977.

53. R.R.Treffers, App.Opt. 16,3103,1977.

54. J.Strong and G.A.Vannasse, J.O.S.A. 49,844,1959.

55. J.Strong and G.A.Vannasse, J.O.S.A. 50,113,1960.

56. T.P.Sheahen and T.O.McCanney, J.O.S.A. 65,825,1975.

57. G.A.Vannasse and H.Sakai, Prog.Opt. 6,261,1967.

58. J.Connes, NAVWEPS Report 8099, US Naval Ordinance Test Station, China Lake 1963.

59. J.E.Gibbs and H.A.Gebbie, Infrared Phys. 5,187,1965.

60. M.L.Forman, W.H.Steel and G.A.Vanasse, J.O.S.A. 56,59,1966.

61. H.Sakai, Aspen Conference On Fourier Spectroscopy,1970. Air Force Cambridge Research Laboratories Special Report No.114, January 1971.

62. J.Connes, ibid.

63. E.V.Loewenstein, ibid.

64. J.W.Fleming, Infrared Phys. 17,263,1977.

65. J.E.Chamberlain, Infrared Phys. 12,145,1972.

66. R.Bracewell, 'The Fourier Transform And Its Applications', McGraw-Hill, New York 1965.

67. T.J.Parker and W.G.Chambers, Infrared Phys. 16,349,1976.

68. W.J.Burroughs and J.E.Harries, Infrared Phys. 11,99,1971.

69. R.H.Norton and R.Beer, J.O.S.A. 66,259,1976.

70. G.W.Chantry and J.W.Fleming, Infrared Phys. 16,655,1976.

71. M.F.Kimmitt, 'Far Infrared Techniques', Pion, London 1970.

72. G.W.Chantry, H.M.Evans, J.Chamberlain and H.A.Gebbie, Infrared Phys. 9,85,1969.

73. J.R.Birch, G.D.Price and J.Chamberlain, Infrared Phys. 16,311,1976.

74. T.J.Parker, W.G.Chambers and J.F.Angress, Infrared Phys. 14,207,1974.

75. M.N.Afsar, D.D.Honijk, W.F.Passchier and J.Goulon, I.E.E.E. Trans.Micro.Theory and Technique MTT-25,505,1977.

76. J.R.Birch and C.E.Bulleid, Conference On Precision Electromagnetic Measurement, Boulder Colorado June 1976. pp 48-49 Conference Digest, I.E.E.E. Cat.No.76CH1099-1 IM.

77. J.R.Birch, Infrared Phys. 18,275,1978.

78. J.W.Fleming, Spectrochimica Acta 32A,787,1976.

79. A.E.Costley, R.J.Hastie, J.W.M.Paul and J.Chamberlain, Phys.Rev.Lett. 33,758,1974.

80. N.W.B.Stone, J.E.Harries, D.W.E.Fuller, J.G.Edwards, A.E.Costley, J.Chamberlain, T.G.Blaney, J.R.Birch and A.E.Bailey, Proc.I.E.E. 122(10R),1054,1975.

81. D.G.Moss, J.Phys.E 10,1170,1977.

82. W.J.Burroughs and J.Chamberlain, Infrared Phys. 11,1,1971.

83. L.Genzel and K.Sakai, J.O.S.A. 67,871,1977.

84. J.Chamberlain and H.A.Gebbie, App.Opt. 10,1184,1971.

85. J.Chamberlain, Infrared Phys. 11,25,1971.

86. J.Chamberlain and H.A.Gebbie, Infrared Phys. 11,57,1971.

87. E.E.Russell and E.E.Bell, Infrared Phys. 6,75,1966.

88. R.J.Douglas and T.Timusk, App.Opt. 13,723,1974.

89. J.W.Fleming, NPL Report DMA 31,1974.

90. J.E.Chamberlain, G.W.Chantry, F.D.Findlay, H.A.Gebbie, J.E.Gibbs, N.W.B.Stone and A.J.Wright, Infrared Phys. 6,195,1966.

91. M.A.Kinch and B.V.Rollin, Brit.J.App.Phys. 14,672,1963.

92. P.E.Clegg and J.S.Huizinga, 'Infrared Detection Techniques For Space Research', pp132-140, Eds. V.Manno and J.Ring, Dordretch:Reidel 1972.

93. E.H.Putley, Proc.Phys.Soc.(London) 76,802,1960.

94. E.H.Putley, App.Opt. 4,649,1965.

95. J.W.Fleming, NPL Report DMA 27,1973.

96. M.Davies, G.W.F.Pardoe, J.Chamberlain and H.A.Gebbie, Trans.Faraday Soc. 66,273,1970.

97. J.Chamberlain, M.N.Afsar and J.B.Hasted, Nature 245,28,1973.

98. D.D.Honijk, W.F.Passchier and M.Mandel, Physica 59,536,1972.

99. D.D.Honijk, W.F.Passchier and M.Mandel, Physica 64,171,1973.

100. D.D.Honijk, W.F.Passchier and M.Mandel, Physica 68,457,1973.

101. W.F.Passchier, D.D.Honijk and M.Mandel, Infrared Phys. 15,95,1975.

102. D.D.Honijk, W.F.Passchier, M.Mandel and M.N.Afsar, Infrared Phys. 16,257,1976.

103. W.F.Passchier, D.D.Honijk and M.Mandel, Infrared Phys. 16,389,1976.

104. D.D.Honijk, W.F.Passchier, M.Mandel and M.N.Afsar, Infrared Phys. 17,9,1977.

105. W.F.Passchier, D.D.Honijk, M.Mandel and M.N.Afsar, Infrared Phys. 17,381,1977.

106. M.N.Afsar, J.B.Hasted and J.Chamberlain, Infrared Phys. 16,301,1976.

107. M.N.Afsar, J.Chamberlain and J.B.Hasted, Infrared Phys. 16,587,1976.

108. J.R.Birch, A.F.Harding, N.R.Cross and D.W.E.Fuller, Infrared Phys. 16,421,1976.

109. T.S.Moss, 'Optical Properties Of Semiconductors', Butterworths, London 1959.

110. E.V.Loewenstein and D.R.Smith, App.Opt. 10,577,1971.

111. E.V.Loewenstein, D.R.Smith and R.L.Morgan, App.Opt. 12,398,1973.

112. D.R.Smith and E.V.Loewenstein, App.Opt. 14,1335,1975.

113. D.R.Smith and E.V.Loewenstein, App.Opt. 15,859,1976.

114. H.W.Hohls, Ann.Physik 29,433,1937.

115. E.V.Loewenstein, J.O.S.A. 51,108,1961.

116. D.Malz, Exp.Tech.Phys. 13,257,1965.

117. S.Zwerdling, J.O.S.A. 60,787,1970.

118. I.Simon, J.O.S.A. 41,336,1951.

119. D.G.Avery, Proc.Phys.Soc. B65,425,1952.

120. R.E.Lyndquist and A.W.Ewald, J.O.S.A. 53,247,1963.

121. T.S.Robinson, Proc.Phys.Soc. B65,910,1952.

122. T.S.Robinson and W.C.Price, Proc.Phys.Soc. B66,969,1953.

123. D.W.Berreman, App.Opt. 6,1519,1967

124. M.Cardona, 'Optical Properties Of Solids', pp137-151,
Eds. S.Nudelman and S.S.Mitra, Plenum Press, New York 1969.

125. R.K.Ahrenkiel, J.O.S.A. 61,1651,1971.

126. W.G.Chambers, Infrared Phys. 15,139,1975.

127. R.H.Young, J.O.S.A. 67,520,1977.

128. J.Fahrenfort and W.M.Visser, Spectrochimica Acta 18,1108,1962.

129. J.Fahrenfort, Proc. 10th. C.S.I., Eds. E.R.Lippencott and
M.Margoshes, Spartan Books, Washington 1963.

130. N.J.Harrick, 'Internal Reflection Spectroscopy', Interscience,
New York 1967.

131. W.G.Spitzer and H.Y.Fan, Phys.Rev. 106,882,1957.

132. B.Lax and G.B.Wright, Phys.Rev.Lett. 4,16,1960.

133. G.B.Wright and B.Lax, J.App.Phys. 32(Supp),2113,1961.

134. D.F.Edwards and P.D.Maker, J.App.Phys. 33,2466,1962.

135. I.Kudman, J.App.Phys. 34,1826,1963.

136. T.S.Moss, T.D.F.Hawkins and G.J.Burrell, J.Phys.C 1,1435,1968.

137. J.R.Fitzpatrick and G.K.T.Conn, J.Phys.D 2,1407,1969.

138. R.P.Howson, J.Phys.D 3,863,1970.

139. N.K.S.Gaur, Physica 48,112,1970.

140. P.A.Schumann Jr., Sol.St.Tech. 13,50,1970.

141. M.A.Saifi and R.H.Stolen, J.App.Phys. 43,1171,1972.

142. V.Gopal, Phys.Stat.Sol.B 57,K69,1973.

143. V.Gopal, J.Phys.Chem.Sol. 36,343,1975.

144. J.Chamberlain, J.E.Gibbs and H.A.Gebbie, Infrared Phys. 9,185,1969.

145. J.W.Fleming, Infrared Phys. 10,57,1970.

146. R.J.Cook and C.B.Rosenberg, Conference on Dielectric Materials,
Measurements and Applications, Cambridge 1975.
IEE Conference Publication No.129.

147. G.W.Chantry, H.M.Evans, J.W.Fleming and H.A.Gebbie,
Infrared Phys. 9,31,1969.

148. J.D.Dromey and J.R.Birch, Infrared Phys. 18,243,1978.

149. K.D.Muller and R.V.McKnight, J.O.S.A. 53,760,1963.

150. A.C.Rose-Innes, 'Low Temperature Techniques', The English Universities Press, London 1964.

151. V.S.Vinogradov, Sov.Phys.Sol.Stat. 2,2338,1961.

152. E.Schlomann, Phys.Rev. 135,A413,1964.

153. G.K.White, Cryogenics, 4,2,1964.

154. J.Topping, 'Errors Of Observation And Their Treatment', Institute of Physics and The Physical Society, London 1963.

155. J.R.Birch and M.N.Afsar, Euromeas 77, Conference on Precise Electrical Measurement, Sussex 1977. IEE Conference Publication No.152.

156. J.Wong and C.A.Angell, 'Glass Structure By Spectroscopy', Marcel Dekker, New York 1976.

157. J.R.Birch and N.W.B.Stone, J.Phys.E 6,1101,1973.

158. J.R.Birch, R.J.Cook, A.F.Harding, R.G.Jones and G.D.Price, J.Phys.D 8,1353,1975.

159. D.W.E.Fuller, N.R.Cross and J.E.Chamberlain, Conference on Precision Electromagnetic Measurements, London 1974. I.E.E. Conference Publication No.113.

160. K.K.Mon, Y.J.Chabal and A.J.Sievers, Phys.Rev.Lett. 35,1352,1975.

161. A.J.Sievers, Conference on Fourier Transform Infrared Spectroscopy, Columbia, South Carolina 1977.

162. R.C.Zeller and R.O.Pohl, Phys.Rev.B 4,2029,1971.

163. R.B.Stephens, Phys.Rev.B 8,2896,1973.

164. S.Hunklinger,W.Arnold and S.Stein, Phys.Lett. 45A,311,1973.

165. B.Golding J.E.Graebner, B.I.Halperin and R.J.Schutz, Phys.Rev.Lett, 30,223,1973.

166. L.Piche, R.Maynard, S.Hunklinger and J.Jackel, Phys.Rev.Lett. 32,1426,1974.

167. M.von Schickfus, S.Hunklinger and L.Piche, Phys.Rev.Lett. 35,876,1975.

168. B.J.Blain and R.W.Douglas, Phys.Chem.Glasses 6,233,1965.

169. D.Crozier and R.W.Douglas, Phys.Chem.Glasses 6,240,1965.

170. R.V.Adams, Phys.Chem.Glasses 2,39,1961.

171. W.F.Passchier, D.D.Honijk, M.Mandel and M.N.Afsar, J.Phys.D 10,509,1977.

172. M.N.Afsar, J.Chamberlain and G.W.Chantry, I.E.E.E. Trans.Instr.Meas. IM-25,290,1976.

173. M.N.Afsar and G.W.Chantry, I.E.E.E. Trans.Micro.Theory and Tech. MTT-25,509,1977.

174. M.N.Afsar, NPL Report DES 42, June 1977.

175. E.E.Russell and E.E.Bell, J.O.S.A. 57,341,1967.

176. E.E.Russell and E.E.Bell, J.O.S.A. 57,543,1967.

177. E.E.Bell, J.de Physique 28,C2,1967.

178. J.R.Birch and D.K.Murray, Infrared Phys. 18,283,1978.

179. J.R.Birch and C.E.Bulleid, Infrared Phys. 17,279,1977.

180. J.Chamberlain, A.E.Costley and H.A.Gebbie, Spectrochimica Acta 25A,9,1969

181. H.W.Kroto, 'Molecular Rotation Spectra', Wiley, London 1975.

182. M.Cardona, W.Paul and H.Brooks, J.Phys.Chem.Solids 8,204,1959.

183. M.Cardona, W.Paul and H.Brooks, 'Solid State Physics In Electronics And Telecommunications', Vol.1 Part 1, Eds. M.Desirant and J.L.Michiels, Academic Press, London 1960.

184. C.M.Randall and R.D.Rawcliffe, App.Opt. 6,1889,1967.

185. A.J.Kemp, J.R.Birch and M.N.Afsar, Third International Conference on Submillimetre Waves and their Applications, Guildford 1978. Infrared Phys. in press.

186. H.A.Gebbie, N.W.B.Stone, F.D.Findlay and E.C.Pyatt, Nature 205,377,1965.

187. J.E.Chamberlain and H.A.Gebbie, Nature 206,602,1965.

188. J.I.Berg and E.E.Bell, Phys.Rev.B 4,3572,1971.

189. T.J.Parker, W.G.Chambers, J.E.Ford and C.L.Mok, Third International Conference on Submillimetre Waves and their Applications, Guildford 1978. Infrared Phys. in press.

190. R.J.Cook, 'High Frequency Dielectric Measurement',pp12-27, Eds. J.Chamberlain and G.W.Chantry, IPC, Guildford 1973.

191. J.E.Chamberlain, Infrared Phys. 5,175,1965.

192. J.E.Chamberlain, J.Quant.Spect.Rad.Transf. 7,151,1967.

193. U.Strom, J.R.Hendrickson, R.J.Wagner and P.C.Taylor, Sol.St.Comm. 15,1871,1974.

194. J.Chamberlain, Chem.Phys.Lett. 2,464,1968.

195. T.J.Parker, J.E.Ford and W.G.Chambers, Infrared Phys. Infrared Phys. 18,215,1978.

196. J.Gast and L.Genzel, Opt.Comm. 8,26,1973.

197. J.Gast, L.Genzel and U.Zwick, I.E.E.E. Trans.Micro.Theory and Meas. MTT-22,1026,1974.

198. U.Zwick, C.Irslinger and L.Genzel, Infrared Phys. 16,263,1976.

199. D.G.Mead, Infrared Phys. 18,257,1978.

200. D.G.Mead and L.Genzel, Third International Conference on Submillimetre Waves and their Applications, Guildford 1978. Infrared Phys. in press.

201. K.E.Gauss, H.Happ and G.Rother, Phys.Stat.Sol.B 72,623,1975.

202. K.E.Gauss and H.Happ, Phys.Stat.Sol.B 78,133,1976.

203. H.Happ and G.Rother, Phys.Stat.Sol.B 79,473,1977.

204. D.A.Ledsham, W.G.Chambers and T.J.Parker, Infrared Phys. 16,515,1976.

205. D.A.Ledsham, W.G.Chambers and T.J.Parker, Infrared Phys. 17,165,1977.

206. D.A.Ledsham, PhD Thesis, Westfield College, University of London, 1977.

207. T.J.Parker and R.P.Lowndes, Third International Conference on Submillimetre Waves and Their Applications, Guildford 1978. Infrared Phys. in press.

208. P.R.Staal and J.E.Eldridge, Infrared Phys. 17,299,1977.

209. M.N.Afsar, J.R.Birch and J.Chamberlain, Conference on Dielectric Materials,Measurements and Applications, Cambridge 1975. I.E.E. Conference Publication No.129.

210. J.E.Chamberlain, M.N.Afsar, D.K.Murray, G.D.Price and M.S.Zafar, I.E.E.E. Trans.Instr. and Measurement, IM-23(4),483,1974.

211. J.B.Scarborough, 'Numerical Mathematical Analysis', Second Edition, Oxford University Press 1950.

212. S.J.Fray, A.R.Goodwin, F.A.Johnson and J.E.Quarrington, J.Sci.Inst. 40,387,1963.

213. S.J.Fray, F.A.Johnson, J.E.Quarrington and N.Williams, Proc.Phys.Soc.(London) 85,153,1965.

214. D.Jones, A.H.Lettington and W.Richmond, J.Phys.E 2,623,1969.

215. B.Carli, J.O.S.A. 67,908,1977.

216. O.S.Heavens, 'Optical Properties of Thin Solid Films', Butterworths, London 1955.

217. A.W.Crook, J.O.S.A. 38,954,1948.

218. P.Rouard, Ann.d.Physique 7,291,1937.

219. K.Fuchs, Proc.Cambridge Phil.Soc. 34,100,1938.

220. K.L.Chopra, 'Thin Film Phenomena', McGraw Hill, New York 1969.

221. C.M.Randall and R.D.Rawcliffe, App.Opt. 7,213,1968.

222. E.J.Danielewicz and P.D.Coleman, App.Opt. 13,1164,1974.

223. R.H.Lyddane, R.G.Sachs and E.Teller, Phys.Rev. 59,673,1941.

224. T.Kurosawa, J.Phys.Soc.Jap. 16,1298,1961.

225. A.S.Barker Jr., Phys.Rev. 136,A1290,1964.

226. G.J.Exharos and W.M.Risen, Chem.Phys.Lett. 10,484,1971.

227. J.Reitzel, J.Chem.Phys. 23,2407,1955.

228. P.H.Gaskell and D.W.Johnson, J.Non-Crys.Sol. 20,153,1976.

229. R.J.Bell, N.F.Bird and P.Dean, J.Phys.C 1,299,1968.

230. J.R.Ferraro and M.H.Manghnari, J.App.Phys. 43,4595,1972.

231. E.Walley and J.E.Bertie, J.Chem.Phys. 46,1264,1967.

232. R.J.Charles, J.App.Phys. 32,1115,1961.

233. J.Chamberlain and G.W.Chantry, 'High Frequency Dielectric Measurement', IPC Press, Guildford 1973.

234. M.A.Bosch, Phys.Rev.Lett. 40,879,1978.

235. J.R.Birch and T.J.Parker, Infrared Phys. in press.

236. M.J.Wood, PhD Thesis, University of Bristol, 1971.

237. A.E.Clark and R.E.Strakna, Phys.Chem.Glasses 3,121,1962.

238. J.W.Fleming and G.W.Chantry, I.E.E.E. Trans.Inst.Meas. IM-23,473,1974.